

DEUTSCHES ELEKTRONEN-SYNCHROTRON
Ein Forschungszentrum der Helmholtz-Gemeinschaft



DESY-THESIS-2018-010

April 2018

**Design Study of a Laser-Driven X-Ray Source for
Medical Fluorescence Imaging**

by

T. Brümmer

ISSN 1435-8085

NOTKESTRASSE 85 - 22607 HAMBURG

DESY behält sich alle Rechte für den Fall der Schutzrechtserteilung und für die wirtschaftliche Verwertung der in diesem Bericht enthaltenen Informationen vor.

DESY reserves all rights for commercial use of information included in this report, especially in case of filing application for or grant of patents.

To be sure that your reports and preprints are promptly included in the
HEP literature database
send them to (if possible by air mail):

DESY Zentralbibliothek Notkestraße 85 22607 Hamburg Germany	DESY Bibliothek Platanenallee 6 15738 Zeuthen Germany
---	---

DESIGN STUDY OF A LASER-DRIVEN X-RAY
SOURCE FOR MEDICAL FLUORESCENCE IMAGING

DISSERTATION

zur Erlangung des Doktorgrades
des Department Physik
der Universität Hamburg

vorgelegt von

THERESA BRÜMMER

*19.04.1987

in Bonn

Hamburg

2017

Gutachter der Dissertation : Prof. Dr. Florian Grüner
Prof Dr. Wolfgang Hillert

Zusammensetzung der Prüfungskommission : Prof. Dr. Robin Santra
Prof. Dr. Florian Grüner
Prof. Dr. Wolfgang Hillert
Prof. Dr. Erika Garutti
Dr. Jens Osterhoff

Vorsitzender der Prüfungskommission : Prof. Dr. Robin Santra

Datum der Disputation : 30.10.2017

Vorsitzender des Fach-Promotionsausschusses Physik : Prof. Dr. Wolfgang Hansen

Leiter des Fachbereichs Physik : Prof. Dr. Michael Potthoff

Dekan der Fakultät MIN : Prof. Dr. Heinrich Graener

And then, there was light

- GENESIS 1:3

To my parents for their unconditional love and support

To my family, the source of my strength

Abstract

Thomson scattering, or inverse Compton scattering, is a technique holding the potential for the generation of X-radiation of high brilliance on the basis of the photon emission by relativistic electrons in optical laser fields. When combined with laser-plasma accelerators, purely laser-driven X-ray sources can be realised on a small scale compared to conventional accelerator-based sources. They therefore offer the prospect of high-resolution imaging, e.g. in the medical sector.

In this thesis, the applicability of such a Thomson source for the *in vivo* detection of gold nanoparticles via X-ray fluorescence imaging is examined. Through a detailed optimisation process, the required design parameters are identified. The design study is performed by means of trajectory-based simulations of the classical radiation, as well as theoretical calculations.

On the one hand, the existing theory is applied and extended for the optimisation of the number of emitted photons and bandwidth at the required energy and for a small observation angle to enable high spatial resolution. One focus is the role of the electron-bunch properties with respect to the resulting energy spectrum. Optimised low bunch widths at moderate divergences lead to a reduction of the X-ray bandwidth with a simultaneous increase of the photon number. As the choice of the electron-bunch parameters is linked to the laser configuration, an investigation of the latter is an important aspect of the optimisation process.

On the other hand, the electron-bunch focusing via active plasma lenses is investigated. The chromatic focusing of these lenses leads to a reduction of the effective energy spread of the electron spectrum and thus of the X-ray spectrum. Furthermore, varying the timing and spatial overlap between accordingly focused electron bunches and the Thomson laser is found to be a method for adjusting the source energy. Such bandwidth reduction of the source as well as a small observation angle generally result in photon loss. High repetition rate lasers represent a means of compensating for this aspect.

This thesis demonstrates that the bandwidth of the X-ray source is controllable through laser and electron optimisation, as well as chromatic focusing. This paves the way for the application of such sources in medical imaging and further research fields.

Zusammenfassung

Thomson-Streuung, auch Inverse Compton-Streuung, ist eine Methode zur Erzeugung hoch-brillanter Röntgenstrahlung und basiert auf der Photonenemission von relativistischen Elektronen im Feld eines optischen Lasers. In Kombination mit Laser-Plasma-Beschleunigern lassen sich rein Laser-betriebene Röntgenquellen mit im Vergleich zu konventionellen Beschleunigern geringem räumlichen Ausmaß realisieren. Solche Quellen ermöglichen hochauflösende Bildgebung, zum Beispiel im medizinischen Bereich.

Diese Arbeit untersucht solche Thomson-Quellen im Hinblick auf ihre Anwendung in der *in vivo* Bildgebung mittels Röntgenfluoreszenz von Gold-Nanoteilchen. Die hierfür benötigten Designparameter werden in einer detaillierten Studie ermittelt. Diese wird unter Verwendung von theoretischen Berechnungen, sowie trajektorien-basierten Simulationen der klassischen Abstrahlung der Elektronen durchgeführt.

Zum Einen wird die bestehende Theorie angewendet und für den hier betrachteten Spezialfall einer geringen Quellen-Divergenz durch Einschränkung des Öffnungswinkels erweitert. Letzteres ermöglicht eine verbesserte räumliche Auflösung. Für die Optimierung der Anzahl der emittierten Photonen und der Bandbreite ist der Einfluss der Elektronenbunch-Parameter ein zentraler Aspekt. Es zeigt sich, dass geringe Bunch-Breiten bei moderaten Divergenzen zu einer Reduktion der Bandbreite bei gleichzeitiger Erhöhung der Anzahl emittierter Photonen führen. Da die Wahl der Elektronenbunch-Parameter durch die Laser-Konfiguration bedingt ist, ist auch eine Untersuchung der Laser-Parameter wichtiger Bestandteil des Optimierungsprozesses.

Zum Anderen wird der Einfluss von aktiven Plasma-Linsen zur Elektronenbunch-Fokussierung untersucht. Die chromatische Fokussierung dieser Linsen führt zur Reduktion der effektiven Bandbreite des Elektronenspektrums und damit der Bandbreite des Röntgenspektrums. Des Weiteren bietet sie eine Möglichkeit zur Variation der Quellen-Energie mittels zeitlicher und räumlicher Verschiebung des Laserfokusses relativ zum Fokus des Elektronenbunches. Im Allgemeinen führt die Bandbreitenreduktion der Quelle, sowie der geringe Öffnungswinkel, zu Photonenverlust. Laser mit hoher Repetitionsrate stellen hier eine Möglichkeit der Kompensation dar.

Diese Arbeit zeigt, dass die Bandbreite der Röntgenquelle durch Laser- und Elektronen-Optimierung, sowie durch die chromatische Fokussierung kontrollierbar ist. Somit ist der Weg für die Anwendung solcher Quellen in der medizinischen Bildgebung sowie in weiteren Forschungsbereichen geebnet.

CONTENTS

1 Introduction	1
2 Introduction to Laser-Wakefield Acceleration and Synchrotron Radiation	7
2.1 High-Power Lasers	7
2.1.1 Laser Profile	8
2.1.2 Electron Dynamics in Electromagnetic Fields	9
2.1.3 Ponderomotive Force	10
2.2 Laser-Wakefield Acceleration	11
2.2.1 Basics of the Wakefield Generation	11
2.2.2 Emittance Conservation and Divergence Reduction	12
2.3 Synchrotron Radiation	13
2.3.1 Electrons in Alternating Electromagnetic Fields: The Hertzian Dipole	14
2.3.2 Undulator Radiation	15
2.3.3 Thomson Radiation	18
3 Design Target Parameters and Simulation Tools/Method	23
3.1 X-ray Fluorescence Imaging of Gold Nanoparticles	23
3.1.1 Target Source Parameters	24
3.2 Proposition of a Possible Thomson Source Setup	26
3.3 Simulation Tools	28
4 Design Study for a Thomson Source	33
4.1 Basics of Thomson Photon Yield and Bandwidth	34
4.1.1 Thomson Radiation Spectrum	34
4.1.2 Total Yield	36
4.1.3 Optimum Laser Waist and Duration	37
4.1.4 Optimum Electron-Beam Waist for the Total Yield	38
4.1.5 Yield within a Confined Cone	38
4.1.6 Bandwidth	38
4.2 Electron-Bunch Parameter Study	45

4.2.1	Initial Parameters for the Simulations	46
4.2.2	Optimising the Laser Parameters	47
4.2.3	Optimising the Electron-Bunch Parameters	48
4.2.4	Electron Bunch without Energy Spread and Emittance	49
4.2.5	Electron Bunch without Emittance or Energy Spread in a Linearly Chirped Laser	57
4.2.6	Electron Bunch without Emittance, with Energy Spread	59
4.2.7	Electron Bunch with Emittance, without Energy Spread	63
4.2.8	Geometrical Tolerance Study	66
4.2.9	Collision Angle between Electron Bunch and Laser	70
4.2.10	Electron Bunch with Emittance and Energy Spread	70
4.2.11	Summary	72
4.3	Yield and Bandwidth Optimisation	73
4.3.1	Yield Dependence of Electron Divergence and Diameter Ratio for Different Laser and Bunch Configurations	73
4.3.2	Analysis of the Waist Relation and Divergence Effect on the Total and Cone Yield	79
4.3.3	Bandwidth	83
4.3.4	Summary	84
4.4	Laser Parameter Study and Design Parameters	86
4.4.1	Optimum Laser Waist and a_0 at Constant Laser Pulse Duration	87
4.4.2	Optimum Laser Waist and Pulse Duration at Constant Laser Strength Parameter	89
4.4.3	Optimum Laser Strength Parameter and Pulse Duration at Con- stant Laser Waist	89
4.4.4	Summary	90
4.5	Nonlinear Effects and Higher Harmonics	90
4.6	Space-Charge Effects at High Bunch Charge	92
4.7	Conclusion	94
5	Discharge-Capillary Active Plasma Lens	97
5.1	Basics of the Active Plasma Lens	98
5.2	Lens Focusing	100
5.2.1	Theoretical Treatment	100
5.2.2	Parameter Scans - Focusing via an Active Plasma Lens	103
5.3	Thomson Source without Focusing Optics	106
5.4	Thomson Source with Plasma-Lens Focusing	110
5.4.1	Chromatic Focusing Effect on the Thomson Spectrum	110
5.4.2	Electron Bunch Offset and Pointing	117
5.5	Conclusion	122

6 Application-Oriented Source Design	125
6.1 Design Process	125
6.2 Thomson Source with $E_\gamma = 90$ keV	126
7 Conclusions and Outlook	129
A Appendix	135
A.1 Undulator Radiation	135
A.1.1 Emitted Wavelength, Bandwidth and Opening Angle	135
A.2 Thomson Bandwidth	138
A.3 Supplementary plots	140
Bibliography	157
Acknowledgements	160
Eidesstattliche Versicherung / Declaration of oath	161

CHAPTER 1

INTRODUCTION

Laser-plasma acceleration (LPA) in combination with Thomson scattering (TS) enables the generation of X-rays of high energy and quality while significantly reducing the spatial requirements in comparison to X-ray sources driven by conventional accelerators. Such brilliant light sources find application in numerous fields of research, such as material science, nuclear physics, and medicine, and their reduced size makes them accessible to small research and medical facilities. In medical diagnostics, they pave the way for functional imaging methods of high resolution. X-ray fluorescence imaging (XFI) allows to locate and quantify nanoparticles of high-Z elements in the human body, where the signal quality is highly dependent on the quality of the X-ray source. This thesis aims at the design of a dedicated LPA-driven X-ray Thomson source for the application in XFI of gold nanoparticles (GNPs).

Light represents an essential instrument in the acquisition of knowledge, as it reveals the structure of objects/matter. With their short wavelengths, X-rays can resolve structures on the atomic level, and penetrate deep into or through materials, allowing for a look into closed systems, e.g. the human body. Since the discovery of X-rays by Conrad W. Röntgen in 1896 [1], the quality of X-ray sources has increased, and in recent years, light sources of high brilliance are a promoted field of research. Originally, synchrotron radiation was merely an unwanted side-effect of accelerator facilities. After discovering their potential to serve as X-ray sources for scientific research, they were no longer only used parasitically, but synchrotron and later also linear accelerators were built with the main purpose of providing high-brilliance radiation, especially in combination with undulators or free-electron-lasers (FLASH, XFEL, LCLS, BESSY). The brilliance of a light source is a measure for its quality and describes the ratio of the radiation flux within a small area, divergence, and bandwidth. Nowadays, light sources exist with brilliances of $10^{17} - 10^{35}$ [2, 3].

In medical imaging, X-ray tubes have been, and are still state-of-the-art light sources in the

field of *structural imaging*. There, the generation of X-rays is based on Bremsstrahlung, resulting in radiation of large divergence with a highly polychromatic energy spectrum. By that, they do not meet the requirements for X-ray-based *functional imaging*.

Functional imaging in general describes the imaging process on the basis of physiological characteristics of cells, tissue or organs of interest. XFI utilises nanoparticles of elements with high atomic numbers (Z) as markers whose fluorescence signals lie within the X-ray regime. Opposed to optical fluorescence methods which are strongly limited in penetration depth of the radiation, XFI thus enables full-body *in vivo* imaging.

A prominent element of choice for XFI is the noble metal gold [4, 5, 6], as it is not naturally present in the human body, possesses a low reactivity and toxicity, and is not radioactive. GNPs can thus serve as functionalised diagnostic agents (FDA). Functionalisation refers to the conjugation of the NPs to specific biological molecules with the required functionality, so that the FDA couples to the cells of interest [7, 8]. XFI aims at the localisation and determination of the concentration of the GNPs. The detection quality is highly dependent on the quality of the X-ray source exciting the NPs [9].

In general, the characteristic energy of the fluorescence signal allows to distinguish the fluorescence signal from the signal of other materials. However, for *in vivo* imaging, photon-matter interaction within the surrounding tissue gives rise to a background signal mainly from Compton scattering. Extensive studies on the XFI on the basis of GNPs have been conducted, with the goal to optimise the detection, and to determine a detection limit [9]. Preliminary results showed that the required X-ray source for the optimum fluorescence-signal generation and detection should have an incident photon energy of $E_\gamma = 150$ keV at a bandwidth of ≤ 15 % FWHM [10]. In order to achieve a high spatial resolution of ~ 1 mm, the divergence of the radiation has to be confined to a cone of 1 mrad opening angle. It has to be noted, that, as the gold XFI is a novel technology, it is a work in progress and the source parameters presented here are object to constant optimisation. Recent results showed an increased significance in a specific detector geometry for incident energies of 90 keV [9]. This thesis is based on the earlier findings, but will give an outlook onto the effects of varying source requirements.

With regard to the clinical application, the number of incident photons marks a trade-off between dose limitations and signal quality. In order to enable clinical applications by reducing the treatment time, either the shot frequency, i.e. the laser repetition rate, or the number of photons per shot has to be sufficient to provide a total photon number of $\approx 10^9$ photons per second. A high photon yield within a small opening angle and bandwidth disqualifies conventional X-ray tubes with their broad spectrum and divergence for the application and requires a dedicated X-ray source of high brilliance.

Thomson sources promote an intrinsically small divergence (\sim mrad) at large photon energies (~ 100 keV) and low bandwidths, and are often referred to as "quasi-monochromatic" sources [11, 12, 13], making them a promising candidate for XFI. In difference to undu-

lators, Thomson scattering produces photons within the hard X-ray regime, orders of magnitude higher than undulators. Prove-of principle experiments without specific application have been conducted on conventional accelerators [14, 15, 11], and also in combination with LPA [16, 17, 18]. Dedicated laser-based X-ray sources for medical applications have been investigated, including Thomson sources driven by linear accelerators [19, 20] and an LPA-based betatron source [21], i.e. where the electron-laser interaction within the plasma-accelerator is used as X-ray source. These sources are limited by the provided photon energy of 30 – 40 keV [20, 21]. The combination of a linac with a high-repetition-rate laser, however, was shown to provide X-rays of up to 90 keV at a promising flux of 10^{12} photons per second in 5 % bandwidth, within an opening angle of ± 1.5 mrad. In case of the LPA-driven betatron source, an average flux of 10^5 photons/s/mrad is obtained. A low bandwidth at high photon yield within a small cone from an LPA-driven Thomson source has not been realised, so far.

While the process of Thomson scattering has been intensively examined theoretically [12, 22, 23, 24, 25] and efforts have been made to theoretically reduce the bandwidth [26, 27], literature lacks dedicated source design studies. Optimisation processes of the photon yield are often limited to maximising the emission in the full solid angle, and bandwidth calculation is only completely described for the on-axis bandwidth.

From the intrinsic source characteristics, another issue arises. Within the cone of radiation, the bandwidth is large (≥ 50 % FWHM), due to the energy-emission-angle relation, leading to the highest photon energies radiated into the electron propagation direction and an energy reduction with increasing deviation from that axis. In turn, this allows to reduce the source bandwidth by collimation, i.e. cutting low-energy contributions via dismissing larger observation angles [12]. The radiation cone decreases with increasing electron energy $1/\gamma$. Consequently, the divergence and bandwidth control is realised by a lower electron energy, adjusted to obtain 150 keV for the TS with a head-on colliding laser pulse, and a confinement via a pin hole. An important aspect in the application of X-ray sources, especially in medical imaging and in the motivation of this thesis, is the number of photons and the bandwidth within such a confined cone. This requires the evaluation of the Thomson theory with respect to the specific case of a 1 mrad cone opening angle and a dedicated design study for XFI which is thus the central aspect of this thesis.

Furthermore, the number of emitted photons is limited by the available electron bunch charge and the number of laser photons, as well as the overlap of the bunches, rendering Thomson sources poor candidates for high-yield applications. An increase in photon yield, however, can be moderated by a high repetition rate of the driving laser, while the bandwidth cannot be arbitrarily small. Therefore, the latter represents the more crucial parameter in the design of a Thomson source for XFI.

Both LPA and TS are driven by lasers, making their combination an appealing concept, and the development of the necessary lasers of high repetition rate and power a vital step

towards the improvement of such sources. LPAs, providing short-length electron beams [28, 29] of high quality on a short scale, significantly reduce the spatial requirements in comparison to conventional-accelerator-based light sources [30, 31]. The accelerating gradients within the plasma are order of magnitude larger than possible in conventional accelerators, allowing to accelerate electrons to energies in the GeV regime on a cm scale [32]. The size of a LPA-driven Thomson source is then determined predominantly by the size of the driver laser.

Driving both LPA and TS by a single high-power laser limits the available laser power for the Thomson interaction, as most pulse energy is required for the electron acceleration. In general, the Thomson laser is obtained via splitting the driver laser, so that it inherits its characteristics. Source optimisation, however, requires the laser parameters to be tuneable. This calls for beam optics for the laser, i.e. chirped pulse amplification [33] and/or chirped mirrors to manipulate the laser duration, as well as according focusing optics. Theory and existing Thomson sources neglect the opportunity to manipulate the electron parameters and in general, the electron bunch is assumed to be much smaller than the laser [12]. A fundamental understanding of the role of different geometrical electron parameters could thus lead to further improvement of the source quality. Consequently, the influence of the electron parameters on the resulting Thomson spectrum within the confined opening angle represent another major aspect of the source design. A foundation of possible source optimisation via electron beam optics was laid by Fuchs et al. [34], where chromatic electron focusing reduces the on-axis bandwidth of undulator-produced X-rays. This idea is adopted in this thesis, in that the desired electron parameters are achieved via focusing by a discharge-capillary active plasma lens [35]. Such lenses are of increasing interest, as they provide symmetric focusing by a single optical element at low focal lengths.

The thesis is structured, as follows. Chapter 2 provides an overview on the physics of LPA and synchrotron radiation. There, the general characteristics, as well as differences of undulator and Thomson radiation are explained. The design parameters, as determined by the XFI requirements, and a possible pump-probe source setup combining LWFA and Thomson, are given in chapter 3. This chapter also introduces the utilised simulation tools. The main part of this thesis is the investigation of a Thomson source within the given parameter regions, with respect to the confined cone angle and the effect of the underlying electron and laser parameters in chapter 4. In section 4.1 the existing Thomson theory in terms of photon yield and bandwidth is presented in detail and evaluated regarding its applicability for the source design. Thereupon, an extensive design study is performed in sections 4.2-4.4, with respect to the optimum electron and laser parameters, aiming at a deeper understanding of the interaction process and the resulting photon yield and bandwidth within the confined cone. An outlook onto the effects of high laser power and bunch charge, in terms of nonlinear effects and space charge, in sections 4.5-4.6 concludes the chapter. In chapter 5 the implementation of electron beam optics,

i.e. the active plasma lens, is investigated. The application of chromatic focusing is evaluated with respect to a setup without electron beam optics, on the basis of the optimum laser and electron parameters determined in the previous chapter. Chapter [6](#) provides the general guideline for the optimisation process of a Thomson source. Thereupon, this process is applied to the design of a 90 keV source, as required according to recent XFI studies, and the consequences of the different target source energy are briefly discussed. This thesis closes with a summary of the results, including an outlook onto further source improvements, as well as prospects for the application, in chapter [7](#).

CHAPTER 2

INTRODUCTION TO LASER-WAKEFIELD ACCELERATION AND SYNCHROTRON RADIATION

The X-ray source proposed for the X-ray-fluorescence imaging (XFI) of gold nanoparticles is an all-laser-driven Thomson source on the basis of laser-wakefield-accelerated electrons. This chapter gives an overview of the physics of electron acceleration and X-ray generation. High-power lasers and the dynamics of electrons within their fields represent the basis of both processes and are introduced in chapter [2.1](#). Thereupon, chapter [2.2](#) briefly explains the basic principle of laser-wakefield acceleration (LWFA) and discusses the beam quality of such accelerated electron bunches. Chapter [2.3](#) presents the general process of synchrotron radiation emission by electrons in external fields. Undulator radiation and Thomson radiation, two highly related applications of synchrotron radiation of high brilliance, are discussed and compared.

2.1 High-Power Lasers

State-of-the-art lasers provide high pulse energies at short pulse durations, thereby reaching powers above the TW regime. One example is the ANGUS laser at the LUX facility [\[36\]](#): With 5 J pulse energy in 25 fs FWHM pulse duration, it reaches a power of 200 TW. These high-power lasers achieve such high intensities in their focus, that partial or even full ionisation of a gas is obtained by a single pulse or even by the rising flank of the main pulse. This paves the way for their application in laser-plasma acceleration. Even more so, they hold the possibility for pump-probe experiments where a small part of the driver laser is used as probe, while the driver laser still retains enough power to accelerate the electrons. Therefore, the prospect of high power lasers driving both, laser wakefield acceleration (LWFA) and a Thomson scattering (TS), is promising for the realisation of an all-laser-driven X-ray source of high brilliance. In this chapter, the general properties

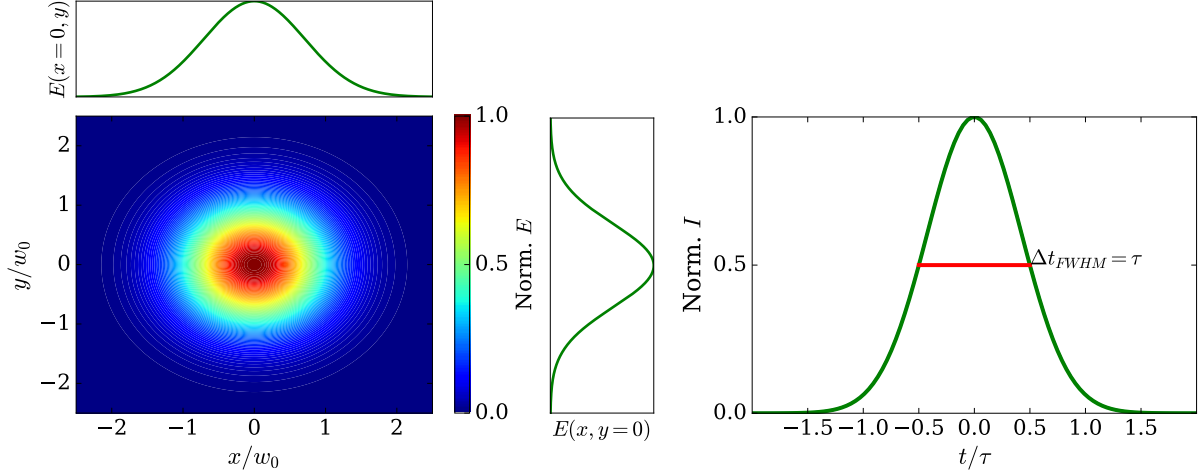


Figure 2.1.1: Gaussian laser profile. Left: Transversal Gaussian profile of the laser field E , where the spatial coordinates are expressed in units of w_0 . The line-outs along x for $y = 0$ and along y for $x = 0$ are displayed at the top and on the right, respectively. Right: Temporal Gaussian intensity profile with the FWHM laser pulse duration τ .

of high-power lasers and their interaction with (relativistic) electrons are presented.

2.1.1 Laser Profile

This section gives a simplified mathematical description of the laser profile. In this thesis, a temporal and transversal Gauss profile is assumed for the laser. The mathematical description hence should include a quantification of the temporal and transversal width of the laser, along with the maximum amplitude of the electric field E_0 , and the wavelength λ . The definitions of temporal and spatial extent are linked either to the field envelope $E(x, y, z)$ or the laser intensity $I \propto |E|^2$.

Typically, the transversal shape of the laser is described by its focal waist w_0 which is defined as the distance from the laser's central axis (x_0, y_0) , where the field amplitude has dropped to $1/e$ ($\approx 37\%$), and the intensity to $1/e^2$ ($\approx 14\%$) of their respective maximum values. The evolution of the laser waist along the longitudinal coordinate z is given as

$$w(z) = w_0 \sqrt{1 + \left(\frac{z - z_0}{z_R} \right)^2} \quad (2.1.1)$$

where

$$z_R = \frac{\pi w_0^2}{\lambda} \quad (2.1.2)$$

is the Rayleigh length and z_0 is the longitudinal position of the focus. The transverse shape of the laser field follows a Gaussian profile and is depicted in figure [2.1.1](#) (left).

In the following, the pulse duration τ refers to the FWHM width of the temporal intensity profile, shown in figure [2.1.1](#) (right), unless stated otherwise.

2.1.2 Electron Dynamics in Electromagnetic Fields

For LWFA, as well as for TS, the motion of electrons in an electromagnetic field is the fundamental process. The equation of motion of an electron is given by the Lorentz force:

$$\vec{F} = \frac{d}{dt}(\gamma m \vec{v}) = -e(\vec{E} + \vec{v} \times \vec{B}) \quad (2.1.3)$$

where γm denotes the relativistic mass with the electron's Lorentz factor $\gamma = E_{\text{kin}}/E_0 + 1$, e the electric electron charge, \vec{E} and \vec{B} the electric and magnetic field vectors, and \vec{v} the electron velocity. A good measure for the strength of the laser fields, and thereby for the force acting on the electron, is the dimensionless laser strength parameter a_0 . It is the normalised vector potential A_0 of the laser and is defined as [37]:

$$a_0 = \frac{eA_0}{mc^2} = \frac{eE_0}{\omega m_e c} = \frac{eE_0 \lambda}{2\pi m_e c^2} \quad (2.1.4)$$

with E_0 the laser field amplitude in the focus, λ the laser wavelength, m_e the electron rest mass, and c the speed of light. In a Gaussian laser with $E_0 = \sqrt{2I_0/c\varepsilon_0}$, with the vacuum permittivity ε_0 , a first estimate is obtained by

$$a_0 = \frac{e}{2\pi m_e c^2} \sqrt{\frac{2}{c\varepsilon_0}} \lambda \sqrt{I_0} \simeq 8.55 \times 10^{-6} \lambda \sqrt{I_0} \quad (2.1.5)$$

or, in a form more convenient for later simulations, using the relations $I_0 = 2P_0/\pi w_0^2$ and $P_0 = E_p/\tau$, with power P_0 , and pulse energy E_p :

$$a_0 = \frac{e}{2\pi m_e c^2} \sqrt{\frac{E_p}{c\varepsilon_0 \frac{\pi}{4} \tau}} \frac{\lambda}{w_0} \simeq \sqrt{\frac{E_p}{21.5 \times 10^9 \tau}} \frac{\lambda}{w_0} \quad (2.1.6)$$

The laser strength parameter a_0 determines the deflection strength, and thereby the maximum amplitude of the oscillation $A_x \propto a_0$, as well as the maximum deflection angle of the electrons with respect to their propagation axis [37]

$$\theta_D = a_0/\gamma. \quad (2.1.7)$$

With regard to the electron-laser interaction, this strength parameter marks two regimes important in LWFA, as well as in TS: The linear regime with $a_0 \ll 1$ and the nonlinear regime for $a_0 \geq 1$. In the linear regime, the deflection is $a_0/\gamma \ll 1$, as ($a_0 \ll 1$ and) $\gamma \gg 1$. Therefore, the transversal component of the velocity is negligibly small. The magnetic and electric field act in the same direction perpendicular to the electron propagation direction, via the Lorentz force, given in equation (2.1.3). In accordance with the naming of this regime, the motion of the electron is linear and it oscillates on

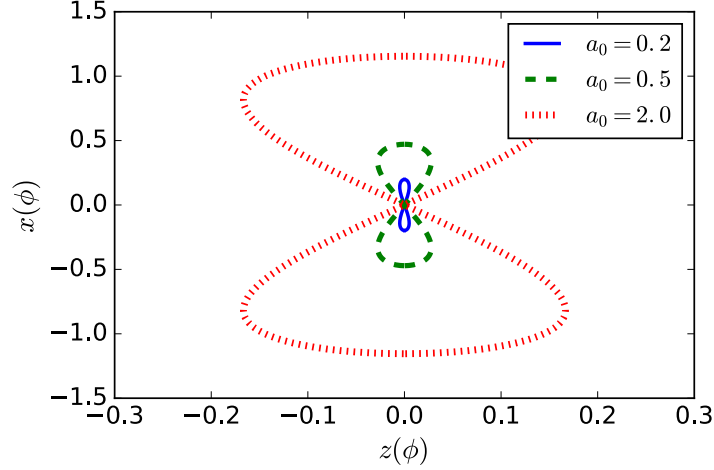


Figure 2.1.2: Figure eight motion of an electron in the average rest frame. For increasing laser strength a_0 , the longitudinal oscillation becomes increasingly pronounced.

a sinusoidal path. If a_0 approaches unity, the interaction becomes increasingly nonlinear. The deflection angle and thus the electron's velocity in transverse direction increases. In the nonlinear regime $a_0 \geq 1$, this leads to the coupling of the magnetic field to the transverse velocity component and results in longitudinal acceleration and deceleration. This behaviour is called figure-eight motion and is depicted for different laser strength parameters in figure [2.1.2](#).

2.1.3 Ponderomotive Force

An example for an effect increasing with the laser strength, is the ponderomotive force. The ponderomotive force arises in a laser field with spatial dependence, e.g. of Gaussian shape, where the intensity decreases with increasing distance from the beam centre (transversally and longitudinally). If the electron starts oscillating in a higher laser field and thereby gets deflected away from the axis, it experiences a lower field and is not deflected back to the original z position. Consequently, its time averaged position starts to drift away from the axis (if no other focusing forces are in place). This is the ponderomotive force which is given by [38](#)

$$F_p = -\frac{e}{4m_e\omega} \nabla E^2 = -m_e c^2 \nabla \frac{a^2}{2} \quad (2.1.8)$$

in the non-relativistic approximation. In LWFA it is responsible for the formation of the wake, and thus essential for the acceleration process. In nonlinear (also in weakly nonlinear, i.e. $a_0 < 1$) Thomson scattering it represents an unwanted side effect: It leads to the deflection of electrons away from high fields on the laser's central axis, increasing their divergence and reducing their contribution to the spectrum.

2.2 Laser-Wakefield Acceleration

In this chapter, the basic principle of laser-wakefield acceleration (LWFA) is presented. Thereupon, the issue of emittance growth of the electron bunch at the plasma exit is discussed.

2.2.1 Basics of the Wakefield Generation

Laser-plasma acceleration denotes the acceleration of electron bunches to relativistic energies by a strong laser pulse within a plasma. A plasma is a gas with a high degree of ionisation. In LWFA, the ionisation of a gas is typically achieved via a pre-pulse of a driver laser, the rising flank of its main pulse, or a discharge current. Upon ionisation, the electrons are no longer bound to the ions and thus move freely with respect to the ion background. Intense laser pulses propagating through the plasma evoke charge separation by means of the ponderomotive force (Ch. 2.1.3). Electrons are driven away from the high-field region of the laser pulse. This transversal and longitudinal dislocation from their rest position induces an electron-depleted zone behind the laser pulse, as it travels through the plasma. Electrons behind the laser pulse are then pushed back¹ towards this zone, forming an enclosed ion cavity, called a bucket, which moves at a phase velocity of the same magnitude as the group velocity of the laser within the plasma $v_{\text{ph,e}} \approx v_{\text{gr,laser}}$. In order to accelerate electrons, they need to be placed in the accelerating (and the focusing) phase of the wakefield. This can be achieved in two ways: Either via internal injection [39, 40, 41, 36], where, as the name promotes, electrons from the plasma background are used, or alternatively, a pre-accelerated bunch can be injected externally [42, 43]. Electrons within such a bucket experience a strong electric field accelerating them towards the laser pulse. Depending on the laser intensity, one distinguishes between the linear ($a_0 \ll 1$) and the nonlinear wakefield regime ($a_0 \geq 1$) [38].

Consequent strong electromagnetic fields exist on a short length scale, given by the plasma period $\lambda_p = 2\pi c/\omega_p$ with $\omega_p = \sqrt{ne^2/m\epsilon_0}$ the plasma frequency, and n the plasma density given in particles per volume. The so-called *cold non-relativistic wave breaking field* is given as $E_0(\text{V/m}) \approx 96\sqrt{n_0(\text{cm}^{-3})}$ [38]. It represents a figure of merit for electric fields within plasmas and can be exceeded by wakefields. For example, a density of $n = 10^{18}\text{cm}^{-3}$ yields a wave-breaking field of 96 GV/m and a plasma period of $\approx 33 \mu\text{m}$. These large fields and field gradients distinguish wakefield accelerators from conventional linear accelerators, as the fields of the latter are orders of magnitude smaller ($\approx 100 \text{ MV/m}$).

¹The gas ions are distributed uniformly in the plasma, as they are hardly effected by the laser field, due to their large mass. The field from the electrons is thus responsible for driving electrons back to the electron-depleted zone.

2.2.2 Emittance Conservation and Divergence Reduction

An electron bunch is mathematically described by the positions (x, y, z) and velocities or momenta (p_x, p_y, p_z) of the individual electrons. These properties define a 6D phase space. The volume occupied by the electrons in this phase space is called the beam emittance. In the projected 2D subspace, e.g. $x - p_x$, the normalised rms emittance is defined as [44]

$$\varepsilon_{n,x} = \frac{1}{m_e c} \sqrt{\langle x^2 \rangle \langle p_x^2 \rangle - \langle x p_x \rangle^2}. \quad (2.2.1)$$

Introducing the Courant-Snyder parameters (α, β, γ) ² allows to parametrise the emittance in the following form:

$$\varepsilon = \gamma x^2 + 2\alpha x x' + \beta x'^2 \quad (2.2.2)$$

This quantity is called the Courant-Snyder invariant and it describes an ellipsis in the 2D subspace, spanned by the transverse position x and $x' = p_x/p_z$. The Courant-Snyder parameters are defined as [45, 46]

$$\alpha = -\frac{\langle x x' \rangle}{\varepsilon}$$

$$\beta = \frac{\langle x^2 \rangle}{\varepsilon} \quad (2.2.3)$$

$$\gamma = \frac{\langle x'^2 \rangle}{\varepsilon}$$

$$\gamma\beta - \alpha^2 = 1 \quad (2.2.4)$$

so that β describes the bunch size, γ the divergence and α the correlation of the two.

The normalised emittance ε_n can serve as a measure for the beam quality, in that it quantifies the spatial extent and its evolution. In that way, the phase-space ellipsis is small for small bunch size and divergence. In the focus, i.e. where $\alpha = 0$, the following relation holds:

$$\varepsilon_n = \gamma \sigma_{r,0} \sigma_\theta \quad (2.2.5)$$

where $\sigma_{r,0}$ denotes the transversal electron rms waist in the focus and σ_θ is the electron divergence. Here and in the following, the term divergence is used to denote the standard deviation of the trajectory angles of the single particles in the bunch from the mean propagation axis. Other than the mean divergence, it stays constant in the transition through the focus.

A low bunch divergence is of importance for applications, such as undulators and Thomson sources, as well as for the beam optics guiding the bunch to the designated experiment. In plasma wakefields, the strong accelerating fields coincide with strong

²The Courant-Snyder parameters are not to be confounded with the Lorentz parameters γ and β .

focusing fields [38]. The consequent small beam sizes lead to high divergences at the transition from plasma to vacuum.

In order to achieve small electron focal waists at low divergences, the bunch emittance has to be kept as small as possible. Within the plasma, the finite bunch length and the longitudinal dependence of accelerating fields induces an energy spread in the bunch.

A bunch of non-zero energy spread experiences focusing forces depending on the single particle position³ and energy which can lead to an emittance growth due to betatron decoherence [47]. This emittance growth is reduced by matching the electron bunch size function to the focusing forces. However, this requires small beta functions, i.e. small beam sizes which in turn increases the divergence. A large divergence in combination with a finite energy spread gives rise to another issue which is the emittance growth within a drift space, given by [44]:

$$\varepsilon_{n,x}(z) = \frac{1}{m_e c} [\langle x_0^2 \rangle \langle p_x^2 \rangle - \langle x_0 p_x \rangle^2 + m_e^2 c^2 \sigma_\gamma^2 (2z \langle x_0 x' \rangle \sigma_{x'}^2 + z^2 \sigma_{x'}^4)]^{1/2} \quad (2.2.6)$$

where σ_γ is the energy spread, and $\sigma_{x'} = \langle x'^2 \rangle^{1/2}$ is the divergence in x direction. For zero divergence or energy spread, the emittance stays constant in a drift, as the z -dependent term vanishes. If either the energy spread, the divergence or both factors are of significant magnitude, they lead to an emittance growth in the drift space. While the energy spread is not easily reduced, adiabatic matching sections at the end of the plasma channel propose a means of reducing the beam divergence [48]. Such dedicated matching sections aim at reducing the focusing strength at such a low rate that the beam size can adapt adiabatically, i.e. grow without emittance increase. The change in focusing strength can either be obtained from a reduction of the plasma density or through an increase of the laser envelope. The shortest adiabatic profile for the focusing force dictates the profile for the laser envelope or plasma density change [49]. Simulations have shown promise in reducing the divergence and conserving the emittance during the transition from the plasma cell into vacuum [48].

For the topic of this thesis, the possibility of a low-divergent electron beam is exploited to justify the initial beam parameters, presented in section 3.2. However, the exact technique is not explicitly applied in the simulations.

LWFA provides relativistic electrons which are the basis of X-ray generation, explained in the following chapter.

2.3 Synchrotron Radiation

An electron at relativistic velocity which is accelerated by an external field emits electromagnetic radiation. If the electron is deflected from its original propagation direction, the

³In case of a spatial dependence of the focusing fields.

direction of emission is tangential to the electron propagation [50]. This phenomenon is called synchrotron radiation and is the basis of high-brilliance X-ray sources. If the external fields are aligned in an alternating order, the electron exhibits an oscillating motion. The intensity of the radiation is then confined to a small opening angle with respect to the electron propagation direction and X-ray pulses of high brilliance are produced.

This method is used in undulators, where electrons are deflected by magnets, i.e. by a physical component. A strongly related process is inverse Compton scattering or Thomson Scattering⁴ where the electromagnetic field of a laser is used to induce the oscillatory motion. Due to their similar processes of undulator and Thomson sources, the latter are also denoted optical undulators. In this chapter, both methods are presented and their similarities and fundamental differences are worked out.

2.3.1 Electrons in Alternating Electromagnetic Fields: The Hertzian Dipole

In alternating magnetic or electromagnetic fields, an electron performs an oscillating motion and emits synchrotron radiation along its trajectory. Both, a magnetic field (undulator) and an electromagnetic field (Thomson) in the laboratory frame correspond to an electromagnetic field in the rest frame of the electron. Therefore, the following description holds for both processes.

The transformation into the electron's average rest frame reveals the classical analogy of the emission of electromagnetic radiation: In its rest frame the electron, initially at rest, perceives an electromagnetic field, causing it to oscillate along the direction of the electric field. It then represents a Hertzian dipole with a frequency f' according to the Lorentz-transformed frequency of the external field which, in this image, travels towards the electron at relativistic velocity [50, 51]. The Lorentz-contracted wavelength $\lambda_{\text{field}}/\gamma$ of the field oscillation determines the emitted wavelength by the dipole in forward and backward direction with respect to the propagation. A Hertzian dipole emits radiation into the total solid angle, except for the direction of the oscillation axis, i.e. π . The same amount of photons is emitted in the forward and backward direction. Figure 2.3.1 (left) shows a schematic of the Hertzian dipole radiation in the electron rest frame (black dashed lines) and transformed to the laboratory frame (red straight lines). The Lorentz transformation back into the laboratory frame gives the opening angle in forward direction, the so-called synchrotron angle $\theta_{\text{synch}} = \pm 1/\gamma$. However, the emission still is directed into the whole solid angle except for the direction of the synchrotron angle. The angular intensity distribution of the relativistic-dipole radiation is depicted in figure 2.3.1 (right). In the x direction, the intensity drops at the synchrotron angle $\theta_x = 1/\gamma$. As the radiation into angles $> 1/\gamma$ is of much less energy - due to the Lorentz transformation, the highest

⁴In this thesis, the process will be addressed to as Thomson scattering or interaction.

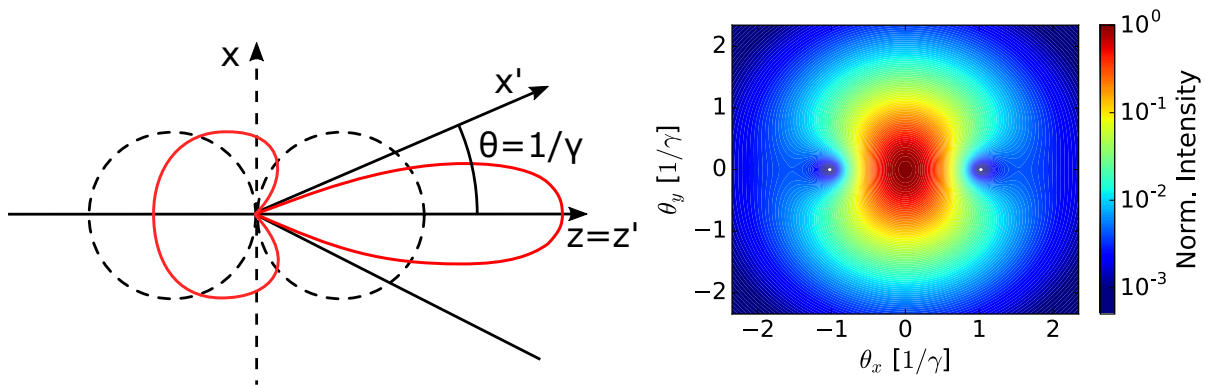


Figure 2.3.1: Left: Schematic depiction of the Hertzian dipole radiation in the average rest frame of the electron ($x - z$ plane, dashed black lines) and in the laboratory frame (x', z' , red lines). The emission in the laboratory frame in forward direction (z, z') is confined to the Lorentz-contracted synchrotron angle $\pm 1/\gamma$. Right: Angular intensity distribution of the radiation from an electron in an electromagnetic field simulated via ASTRA [52] and Clara [17]. In the x direction, the intensity vanishes at the synchrotron angle.

energy is emitted in the electron propagation direction - the major portion of the intensity is emitted into this angle. Consequently, the synchrotron angle is referred to as opening angle. However, in a relativistic dipole, this confinement only holds in the direction of the oscillation. In the transversal axis orthogonal to the oscillation, no such angle can be defined.

The longitudinal oscillation of double frequency in the nonlinear regime, when the magnetic field couples to the transversal velocity component (see figure 2.1.2), can be translated into a Hertzian dipole, as well: It oscillates with a frequency of $2f$ orthogonally to the first dipole oscillation. This gives rise to the emission of the second harmonic frequency in the emitted spectrum. As a Hertzian dipole does not emit radiation in the direction of its oscillation, such even harmonics are not perceived on axis, i.e. in the direction of the electron propagation.

2.3.2 Undulator Radiation

In this section, reference [50] is used as reference, if not cited otherwise.

An undulator is a periodic arrangement of electric or permanent dipole magnets. If the propagation direction of the electron is z , and the magnetic field is oriented along the y axis, the magnetic field on the z axis is

$$B_y(z) = B_0 \sin(2\pi/\lambda_u z) \quad (2.3.1)$$

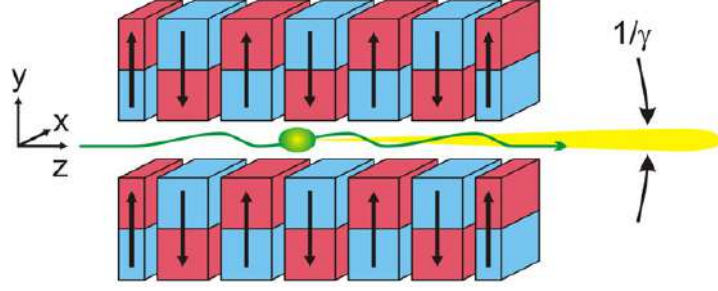


Figure 2.3.2: Schematic of the periodic dipole-magnet configuration in an undulator. The magnetic field is oriented along the y axis (arrows). The electron bunch travels on a sinusoidal path (green), oscillating in the $x - z$ plane, through the undulator. The emitted radiation in forward direction (yellow) is concentrated in a cone of opening angle $1/\gamma$. The image is adapted from reference [17].

with λ_u the period of the undulator and B_0 the maximum magnetic field on axis. An electron traveling through this assembly is deflected by the Lorentz force (Eq. (2.1.3)):

$$\vec{F} = -e\vec{v} \times \vec{B} \quad (2.3.2)$$

with $v = v_z$ and $B = B_y$, so that $F = F_x$. Consequently, the electron oscillates in the $x - z$ plane and emits radiation (Ch. 2.3.1). A schematic of an undulator and the electron trajectory is depicted in figure 2.3.2.

A measure for the deflection strength of an undulator is K , the so-called undulator strength parameter or deflection parameter. It represents the undulator analogue to the laser strength parameter a_0 in the case of an electromagnetic field (Eq. (2.1.4)) and is defined as

$$K = \frac{B_0 e \lambda_u}{m_0 c 2\pi} \approx 93.36 B_0 \lambda_u \quad (2.3.3)$$

The undulator strength parameter defines the maximum deflection angle θ_D and amplitude A_x in x , analogously to a_0 : $\theta_D = K/\gamma$, and $A_x = \frac{K \lambda_u}{\gamma 2\pi}$. It also distinguishes the linear from the nonlinear regime for $K \ll 1$ and $K \geq 1$, respectively. The latter is also called the wiggler regime.

Undulator Radiation Characteristics

While the synchrotron angle is not an undulator-typical property but, as the naming suggests, inherent to synchrotron radiation, an important characteristic of the undulator spectrum arises from its periodicity. Assuming a perfect sinusoidal trajectory ($K \ll 1$), electrons emit radiation of equal wavelength at equivalent positions along their path. These wavefronts interfere according to their delay and their emission angle (Bragg condition). A detailed derivation of the following formulae is given in the appendix A.1.1. From the constructively interfering wavelength, the undulator equation is obtained which gives the wavelength emitted by an undulator of λ_u and K by an electron with Lorentz

factor γ into the emission angle θ :

$$\lambda = \frac{\lambda_u}{2n\gamma^2} \left(1 + \frac{K^2}{2} + \gamma^2\theta^2\right) \quad (2.3.4)$$

where n denotes the n^{th} harmonic.

The interference condition when applied to a whole undulator device of N periods yields another characteristic feature: The bandwidth of the on-axis radiation is very small and scales with the undulator length $N\lambda_u$

$$\frac{\Delta\lambda}{\lambda} = \frac{1 + nN - nN}{1 + nN} = \frac{1}{1 + nN}. \quad (2.3.5)$$

Furthermore, the opening angle, i.e. the angle over which a wavelength can be observed is given by the angle of constructive interference of this wavelength θ and the angle at which it interferes destructively θ^* :

$$\theta^{*2} - \theta^2 = \frac{2\lambda}{N\lambda_u} \quad (2.3.6)$$

For the on-axis radiation, i.e. at $\theta = 0$, one obtains the opening angle

$$\Delta\theta = \frac{2\lambda}{N\lambda_u} = \frac{1}{\gamma} \sqrt{\frac{1 + K^2/2}{Nn}} \quad (2.3.7)$$

In the linear regime, where $K \ll 1$, this gives the so-called undulator opening angle, defining the opening angle of the central, thus maximum, emitted wavelength

$$\Delta\theta = \frac{1}{\gamma\sqrt{N}} \quad (2.3.8)$$

The angle-wavelength relation of undulator radiation can be summarised as follows: Different wavelengths are emitted into different angles. Due to the angular spread given by interference of the emitted light, these angles overlap, resulting in the according bandwidth at a fixed angle.

Therefore, an undulator emits a strongly spatially confined energy spectrum of small bandwidth, when regarding the central wavelength. This characteristic marks a substantial advantage of undulator radiation over synchrotron radiation from a bending magnet, i.e. a single dipole magnet. For a typical undulator of $\lambda_u = 1$ mm, $N = 100$, and electrons of 80 MeV, a central wavelength and photon energy ($n = 1$, $K \ll 1$, $\theta = 0$) of

$$\lambda_\gamma = 20.44 \text{ nm}$$

$$E_\gamma = 60 \text{ eV}$$

are obtained with a bandwidth of $\Delta\lambda_\gamma/\lambda_\gamma \approx 1$ % and an undulator opening angle of 0.6

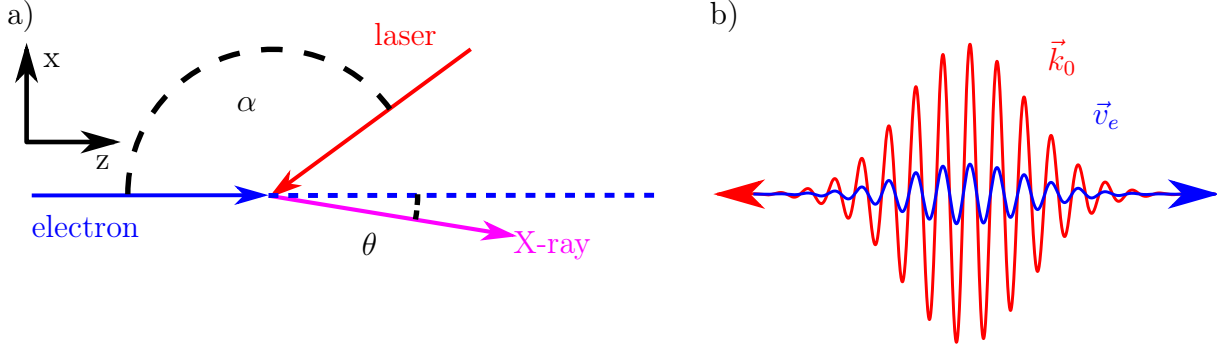


Figure 2.3.3: Schematic of the scattering of an electron and laser photon in the particle image (a) with the collision angle α and emission angle θ of the radiated X-ray photon. Head-on collision ($\alpha = \pi$) in the classical image (b) of a laser with wave vector \vec{k}_0 and a relativistic electron of velocity \vec{v}_e .

mrad. An estimate on the total number of photons N_γ , i.e. the photon yield in the full solid angle and at all wavelengths obtained from such a source is

$$N_\gamma = \frac{2\pi}{3} \alpha_f N_e N K^2 \quad (2.3.9)$$

with the fine structure constant α_f , the number of electrons N_e , the number of undulator periods N and the undulator parameter K . This lays the foundation for high brilliance undulator X-ray sources.

2.3.3 Thomson Radiation

In this section, the fundamental physics of Thomson scattering is introduced. A detailed description of the underlying theory with regard to the photon yield and spectral bandwidth is given in chapter [4.1](#).

Thomson scattering is a means of producing highly energetic photons within the hard X-ray regime based on the interaction of highly relativistic electrons and the electromagnetic field of a laser.

Thomson scattering may also be referred to as inverse Compton scattering. The latter naming provides a more descriptive image of the process in the particle regime, depicted in figure [2.3.3a](#)). Highly relativistic electrons scatter with laser photons, typically in the optical range. In comparison to the standard Compton interaction, where a photon transfers part of its energy to an electron at rest, this process is reversed here. Inverse Compton scattering denotes the low-photon-energy limit regime of Compton scattering. Due to the low photon energy compared to the relativistic kinetic energy of the electron, the electron's energy is transferred to the photon. Consequently, the photon's wavelength is reduced by several orders of magnitude.

In the classical picture, Thomson scattering may well be regarded as the optical equivalent to undulator radiation. While an undulator is a physical object (arrangement of

magnets), no material is required in Thomson scattering, as the laser itself is used as an optical element. In the electromagnetic field of the laser, the electrons oscillate and thus emit synchrotron radiation, as depicted in figure 2.3.3b) for a head-on collision. As described in chapter 2.3.1, the motion is similar to that in the magnetic field of an undulator. However, due to the smaller wavelength of lasers ($< \mu\text{m}$) compared to typical undulator periods ($\sim \text{mm}$) and the Lorentz-contracted laser wavelength owed to its relativistic motion relative to the electrons, significantly higher photon energies are reached. The photons' relative velocity with respect to the laser, and thus the emitted energy, scale with the collision angle α . Given a laser of wavelength λ_L interacting with electrons of energy described by the Lorentz factor γ , the photon energy⁵ E_γ reached in this process is given as [22]

$$E_\gamma = \frac{2\gamma^2[1 - \beta \cos(\alpha)]E_L}{1 + \frac{a_0^2}{2} + \gamma^2\theta^2} \quad (2.3.10)$$

where $E_L = hc/\lambda_L$ is the laser photon energy, with the Planck's constant h and speed of light c , and a_0 is the laser strength parameter. $\beta = \sqrt{1 - 1/\gamma^2}$ and θ is the observation angle with respect to the mean electron propagation direction.

In the nonlinear regime, higher harmonics are emitted, and the longitudinal average velocity of the electron is reduced, so that the emitted maximum energy decreases, as well, according to equation (2.3.10).

Equivalence of Thomson and Undulator Physics

The equivalence of Thomson and undulator radiation is revealed by the direct comparison of the undulator formula (2.3.4) and the Thomson formula (2.3.10).

$$\lambda_u \rightarrow \lambda_L/[1 - \beta \cos(\alpha)] \quad (2.3.11)$$

$$K \rightarrow a_0 \quad (2.3.12)$$

The difference between this optical undulator and a standard undulator is found in the electric field of the laser and its relativistic motion in contrast to an undulator at rest in the laboratory frame. The strength parameters K and a_0 , however, appear to be equivalent. The laser strength parameter (Eq. (2.1.4)) is defined via the vector potential \vec{A} :

$$\vec{a} = \frac{e\vec{A}}{m_0c^2}$$

to be

$$a_0 = \frac{eE_0}{m_0c^2k_0}$$

⁵In Thomson theory, the convention is to give the emitted photon energy (or frequency), rather than the wavelength.

and the undulator parameter (Eq. (2.3.3)):

$$K_u = \frac{eB_0}{k_u m_0 c}$$

with k_0, k_u the spatial angular frequency of the laser and undulator, respectively. An undulator equivalent to an optical undulator thus has a wavelength according to eq. (2.3.11) to account for relativistic motion and an undulator parameter $K_u = a_0$ to obtain equal deflection strength.

Using these relations, one can easily determine the electron oscillation amplitude A and the maximum emitted photon energy $E_{\gamma, \max}$ for equivalent systems. The amplitude in a magnetic undulator field for an electron propagating in z direction and a magnetic field $B = B_y = -B_0 \sin(k_u z)$:

$$A_{x,u} = \frac{K_u \lambda_u}{2\pi\gamma}$$

with (2.3.11) and (2.3.12), one obtains:

$$A_{x,l} = \frac{a_0 \lambda_0}{2\pi\gamma(1 + \beta)}$$

which is the amplitude for an electron in the electromagnetic laser field [37].

Difference between a_0 and K_u

While equation (2.3.11) follows directly from the Lorentz transformation, the equivalence of a_0 and K_u requires further explanation and the difference regarding the effect on the underlying fields has to be pointed out. Equal electron deflection in an undulator or laser field, i.e. $a_0 = K_u$, does not translate to equal laser and undulator fields.

As previously explained, in the linear regime, the electric and magnetic field act in the same direction, so that with the relation $B = \frac{E}{c}$ and $\beta \approx 1$, the Lorentz force in the electromagnetic field is

$$F_{L,em} = -e(E + \beta cB) = -e(E + \beta E) \approx -2eE \quad (2.3.13)$$

For an electron in a magnetic field, one obtains:

$$F_{L,m} = -e\beta cB = -e\beta E \approx -eE \quad (2.3.14)$$

Consequently, the force on the electron in a magnetic field is half as large as the force in an electromagnetic field if the according B fields (or assumed E fields) are of the same magnitude.

Equivalently, when setting a_0 equal to K_u :

$$\frac{eE_{0,l}}{m_0c^2k_0} = \frac{eB_{0,u}}{m_0ck_u} \quad (2.3.15)$$

Now, using $B = \frac{E}{c}$ and eq. (2.3.11) yields:

$$\frac{eE_{0,l}}{m_0c^2k_0} = \frac{eE_{0,u}}{m_0c^2} \frac{1}{2k_0} \quad (2.3.16)$$

$$\Rightarrow E_{0,u} = 2E_{0,l} \quad (2.3.17)$$

Imposing an identical deflection strength parameter for an undulator and an optical undulator demands that the equivalent undulator field has to be a factor 2 larger to obtain an equivalent laser field. Consequently, the third condition for a magnetic undulator which is to give the same emission as an optical undulator is:

$$B_{0,u} = 2B_{0,l} = 2E_{0,l}/c \quad (2.3.18)$$

Differences in Undulator and Thomson Radiation

A major difference between undulator and Thomson radiation lies in the transversal and longitudinal shapes of the respective fields. In an undulator, the transversal field is shaped parabolically with its minimum being on axis. Consequently, electrons with increasing distance from the central axis are deflected back. This is called transversal trapping [53]. In the Thomson case, the opposite effect occurs, owed to the ponderomotive force (cp. Ch. 2.1.3). As the transversal profile of the laser is typically of Gaussian shape with the maximum field on axis, electrons drift away from the central axis. The increasing electron divergence and their drift into lower fields reduce the photon yield.

Another aspect is the longitudinal shape of the laser. The pulsed nature of the laser leads to a longitudinally varying laser strength. Consequently, electrons emit radiation of less intensity at the beginning and end of the interaction region. Furthermore, as they emit radiation of different energy depending on the field, this also leads to an increased bandwidth in the Thomson spectrum. While in undulator radiation, the periodicity and thus emittance of equal wavelengths at equivalent points along the trajectory leads to an interference-based bandwidth reduction (cp. Eq. (2.3.5)), this is not or only partially the case in the temporally changing laser field. In Thomson scattering, another phenomenon appears: During the interaction, an electron experiences some laser field values twice and thus emits the same frequency at two points in time. This is illustrated in figure 2.3.4. The electron trajectory $z(\eta)$ is depicted within the field of the laser a . At two different points in time and space (z_1, z_2), the electron experiences the same laser field ($a(\eta_1) = a(\eta_2)$) and thus emits the same frequency ω . Depending on the temporal delay, these signals either interfere constructively or destructively, giving rise to oscillations in

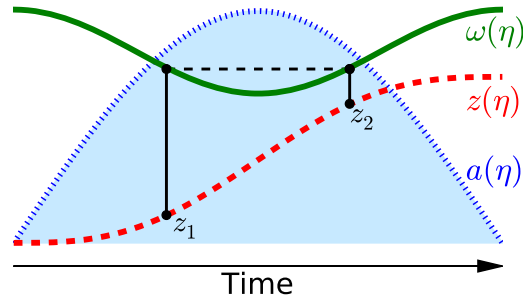


Figure 2.3.4: Schematic of the origin of the oscillations in the on-axis spectrum for small electron waists σ_r . The laser field a (blue) is time-dependent. An electron with trajectory z travelling through the field experiences the same field value $a_1 = a_2$ at the positions z_1 and z_2 . Consequently, it emits radiation of the same frequency $\omega_1 = \omega_2$ at these two points separated in time (and space). The image is adapted from [27].

the spectrum [26, 27, 54]. The oscillations are a nonlinear effect in Thomson scattering and the number of oscillations rises with increasing a_0 .

Yield maximisation techniques in undulator and Thomson sources feature differences, as well. Closely following equation (2.3.9)

$$N_\gamma \propto N_u K^2,$$

increasing the photon yield via the undulator/laser parameters can either be achieved by increasing the deflection strength (a_0 or K) or by increasing the interaction length i.e. N_0 or N_u . Unfortunately, the spectral broadening increases with increasing laser strength parameter [12], so that the gain of an increased yield ($\propto a_0$) comes at the cost of a larger bandwidth.

Increasing the photon yield via the interaction length is a further issue and disadvantage of the Thomson process in comparison with an undulator. While the undulator length can simply be increased to achieve higher photon yield ($\propto N_u$), the interaction with a laser is confined by the Rayleigh length (Eq. (2.1.2)) [12], where w_0 is the transversal laser waist. Therefore, by increasing the laser strength a_0 via stronger focusing reduces the longitudinal interaction range.

Finally, the timing of laser and electron bunch is crucial. This, however is facilitated by the proposed pump-probe setup (Ch. 3.2), where the electrons are driven by the same laser pulse that feeds the Thomson laser.

CHAPTER 3

DESIGN TARGET PARAMETERS AND SIMULATION TOOLS/METHOD

In this chapter, the target parameters and simulation methods for the design study are presented.

The principle of X-ray fluorescence imaging (XFI) is elaborated in section [3.1](#) and the consequent target source parameters are provided. Thereupon, a possible pump-probe setup, i.e., an all-laser driven LWFA-Thomson X-ray source, is proposed in section [3.2](#). This setup represents the basis of the following chapters as it sets the conditions for the electron and laser parameter regions for the design study. The simulation tools employed for the design study (Ch. [4](#)), as well as for the investigation of electron focusing via an active plasma lens (Ch. [5](#)), are presented in section [3.3](#).

3.1 X-ray Fluorescence Imaging of Gold Nanoparticles

In this section, reference [9](#) is used, if not specified differently.

X-ray fluorescence imaging (XFI) is a method of interest in medical functional imaging, as it in general could allow for full-body *in vivo* imaging.

Fluorescence denotes the spontaneous emission of light by a previously excited atom, where the energy of the emitted photons is characteristic to the material. The fluorescence signal of elements of high atomic number (Z) lies within the X-ray regime. Hence, such high- Z elements can be excited and detected within the human body rendering them appealing candidates for medical tracers.

In this work, an X-ray source for the X-ray fluorescence of gold nanoparticles (GNPs) is designed. Gold is a prominent choice for this medical application [4](#), [5](#), [6](#), as it is not naturally present in the human body, neither toxic¹, nor radioactive. With its atomic

¹The toxicity of nanoparticles in general is discussed controversially. Due to their small size, they can potentially invade into cells, and cause damage on the cellular level. However, in general, the material gold is not toxic, as opposed to lead and some heavy metals.

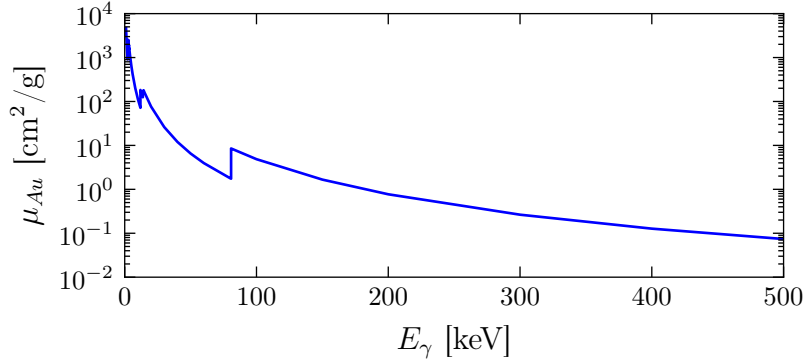


Figure 3.1.1: Gold attenuation coefficient μ_{Au} [55] as a function of the incident photon energy E_γ .

number of $Z = 79$, it possesses a high fluorescence energy of ≈ 70 keV [55], and thus a high transmission rate for fluorescence photons exiting the human body. Furthermore, GNPs offer a broad spectrum of application, as they can be functionalised, i.e. conjugated to numerous specific biological molecules with the required functionality. As a consequence, the GNPs couple to the cells of interest [7, 8], making them detectable through XFI. Among the possible applications are the detection of damaged neural cells [7], cancer research, and studies on pharmacokinetics.

3.1.1 Target Source Parameters

The specific demands on the X-ray source are given by this application. The excitation of gold fluorescence of the K shell requires source energies in the hard X-ray regime, given by the energy-dependent attenuation coefficient of gold [55], displayed in figure 3.1.1.

In general, the characteristic energy of the fluorescence signal allows to distinguish the fluorescence signal from the signal of other materials. However, for *in vivo* imaging, photon-matter interaction within the surrounding tissue gives rise to a background signal, where Compton scattering is the dominant effect. Extensive studies on the XFI of GNPs are conducted, with the goal to optimise the detection, and to determine a detection limit.

Apart from the detector design, the detection limit has been shown to be highly dependent on the quality of the applied X-ray source. Among the demands are the photon energy and bandwidth, the photon number, and the beam size. These are not based on the fluorescence response alone, but require the consideration of background signal in the surrounding tissue, as well as the detector type and geometry. On the basis of the correlation of the incident photon energy and the fluorescence cross section, one can deduce the amount of gold from the signal height. The latter is quantified by the dose-normalised signal-to-noise ratio, given as [10]

$$S = \frac{CT_i T_o}{ND} \quad (3.1.1)$$

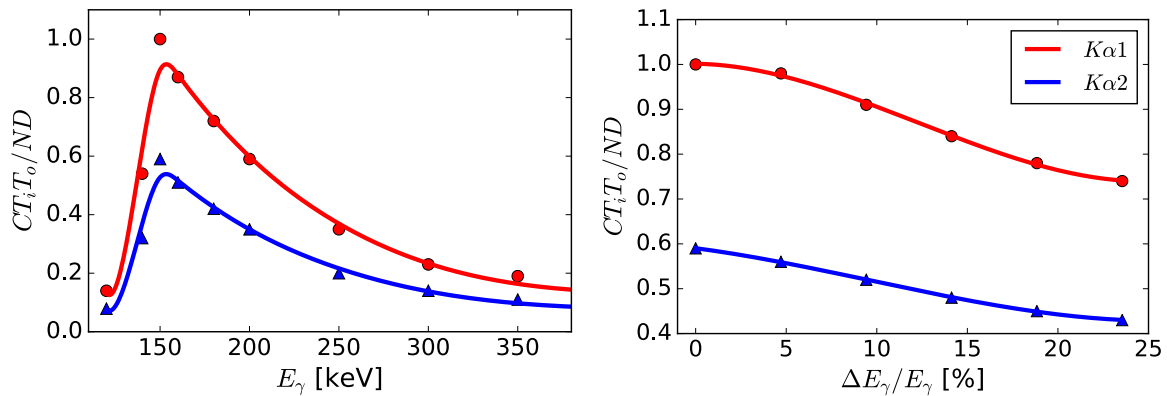


Figure 3.1.2: Dose-normalised signal-to-noise ratio over incident photon energy (left) and FWHM bandwidth (right) for the $K\alpha$ fluorescence lines of gold. (Courtesy of Oliver Schmutzler)

where C is the fluorescence cross section, T_i and T_o are the transmission coefficients for the incident photons and outgoing fluorescence photons, N is the noise, and D the deposited radiation dose. These quantities are dependent on the incident photon energy, yielding an optimum of ≈ 150 keV and a reduction of the significance with increasing source bandwidth, as displayed in figure 3.1.2. This determines the energy of the dedicated X-ray source, and limits the required bandwidth to $\lesssim 15$ % FWHM. It has to be noted, that, as the GNP-based XFI is a technology of currently high interest, its development is a work in progress and the source parameters presented here are object to constant optimisation. Recent results showed an increased significance in a different detector geometry for incident energies of 90 keV.

In order to localise the GNPs, the X-ray beam needs to be spatially confined at the region of interest (ROI). The detection and quantification via line scans requires a beam of small divergence and size, i.e. a pencil beam. A target opening angle of 1 mrad renders a source size of 1 mm at 1 m distance from the source. This gives a comparable or even higher spatial resolution than today's medical imaging techniques, such as PET (< 4 mm) [56, 57], CT (\sim mm) [57], SPECT, etc. Especially, the comparison to PET is of interest, as it also provides functional imaging.

The reconstruction of a 3D image of the ROI requires several line scans. For that, a photon number of 10^9 per line is desirable, which would result in an applied dose of ≈ 10 mG, comparable to CT or PET imaging². In general, the maximisation of photons per shot is of interest for the design study, to reduce the treatment time and thus enable clinical applications.

The target parameters for the source design are listed in table 3.1.1.

²The number of photons rendering a certain dose depends on the tissue depth.

E_γ	150 keV
$\Delta E_\gamma/E_\gamma$	$\leq 15\%$ FWHM
σ_θ	≤ 1 mrad
N_γ	10^9

Table 3.1.1: Required parameters for the X-ray source.

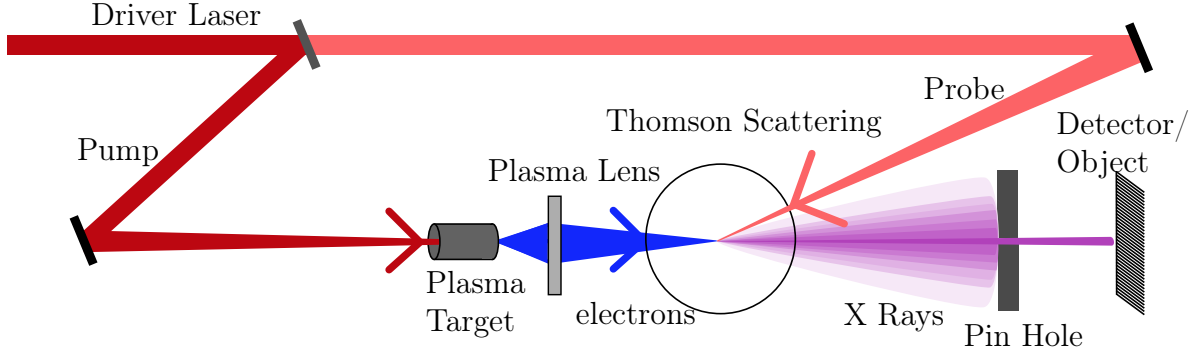


Figure 3.2.1: Schematic of the all-laser-driven Xray source combining LWFA and TS. The driver laser is divided into the pump laser and the probe laser, where the latter obtains only a small fraction of the driver lasers pulse energy. The pump laser is directed into the plasma target where it drives the wake and accelerates electrons (blue). The electron bunch is divergent behind the plasma and is focused by a plasma lens (see Ch. 5) onto the interaction region with the probe laser focus. The Thomson scattering process of electrons and the probe laser photons generates a cone of X-rays (purple) emitted in the electron propagation direction. Highest intensity and energy are emitted on axis (dark purple). This part of the X-ray beam is cut out by a pin hole.

3.2 Proposition of a Possible Thomson Source Setup

The proposed setup for the Thomson source is a pump-probe configuration where a single high-power laser drives both, a laser-wake-field accelerator (LWFA) providing the electrons for the interaction and the Thomson source (TS) itself. A schematic of this setup is shown in figure 3.2.1.

Numerous parameters influence the results of the Thomson interaction. Thus, the parameter region needs to be confined. Here, the laser and electron parameter regions assumed for the simulations are motivated. They are presented in table 3.2.1. The general driver-laser properties are adapted from the ANGUS laser at the LUX experiment [36]. For the accelerated electrons, parameters are taken from published experimental data of LWFA.

The normalised electron bunch emittance (cp. Ch. 2.2.2) is optimistically assumed to be $\varepsilon_n = 0.2$ mm mrad [58, 59]. The charge of the electron bunch is estimated to range from 5 to 200 pC. However, for initial simulations, a low charge of 10 pC is investigated. Typical energy spreads can extent from 1 to 10 % rms.

The Thomson laser is obtained from the driver laser, e.g. via a beam splitter. It therefore inherits its wavelength of 800 nm and pulse frequency of 5 Hz. Further parameters are influenced by the optics in the path and underly the possibility and necessity of

Driver Laser	$\lambda = 800 \text{ nm}$ $P \leq 200 \text{ TW}$ $\tau_D = 25 \text{ fs FWHM}$ $f = 5 \text{ Hz}$
Electrons	$Q \approx 5 - 200 \text{ pC}$ ($Q_{\text{sim}} = 10 \text{ pC}$) $\sigma_\gamma/\gamma \approx 1 - 10 \%$ $\varepsilon_n = 0.2 \text{ mm mrad}$ positional jitter = $1 - 6 \mu\text{m rms}$ pointing jitter = 0.3 mrad rms
Thomson Laser	$\lambda = 800 \text{ nm}$ $E_p = 0.5 \text{ J}$ $f = 5 \text{ Hz}$

Table 3.2.1: Parameters of the driver laser, the electron bunch, and Thomson laser in the proposed pump-probe setup.

optimisation. However, they are still subject to the initial driver laser's parameters. The driver laser has a power of $P_D \leq 200 \text{ TW}$ and a pulse duration of 25 fs. Its bandwidth is Fourier-limited, hence is given by the time-bandwidth product to be $\approx 40 - 60 \text{ nm}$ ³. The larger part of the driver laser's pulse energy $E_{p,D} = 5 \text{ J}$ is required for the electron acceleration. This limits the Thomson laser pulse energy E_p , and thereby the laser photons available for the interaction. For a first experiment, the laser pulse energy is assumed to receive $E_p \leq 1/10 E_{p,D} = 500 \text{ mJ}$. The use of a beam splitter leads to an elongation of the Thomson laser with respect to the driver laser. As the transmission through a dispersive material leads to a wavelength dependent group delay, the laser obtains a (linear) chirp, i.e. a longitudinal linear dependence of the frequency, and thereby a longer pulse duration. The boundary condition fixes the pulse energy, while the Thomson laser focal waist, pulse duration and laser strength parameter (linked by Eq. (2.1.6)) are subject to the optimisation process. For this, both the duration and the waist have to be adjustable parameters in the setup. The desired focal waist is achieved by according focusing optics, e.g. a parabola. The variation of the laser pulse duration is enabled via chirped pulse amplification [33] or by chirped mirrors which can stretch the pulse by increasing the longitudinal chirp. In the simulations, different pulse durations with the according longitudinal linear chirp are examined. For optimum Thomson interaction, a good overlap of electrons and probe laser needs to be provided. This is disturbed by position and pointing jitters of laser or electrons. Assuming the electrons to inherit the jitters from the pump laser, they have a position jitter of $3 - 6 \mu\text{m}$, as measured at ANGUS [60]. As this is dependent on the laser focusing, a more optimistic approach is to assume $1 \mu\text{m}$. As a reference for the pointing jitter, experimental data from reference [61] is consulted to assume 0.3 mrad rms .

³Taking fluctuations into account and non-ideal effects in transport, e.g. through the decoupling via a beam splitter, the Thomson laser's bandwidth can be slightly increased.

3.3 Simulation Tools

A detailed design study requires a simulation tool that enables the determination of the number of emitted photons, their emission angle and energy. Interference effects, as well as higher harmonic generation have to be included, as well. Depending on the bunch charge, space charge effects have to be taken into account. Moreover, the simulation tool has to allow the manipulation and design of the laser and electron parameters for the Thomson interaction to a high degree. In this thesis, trajectory-based Thomson radiation calculators, the Clara [17] and Clara2 [62] (Classical Radiation) codes are used. The trajectories are provided by either ASTRA (A Space-charge TRacking Algorithm) [52] or GPT (General Particle Tracer) [63]. In this chapter, the numerical modelling and the simulation chain are presented.

Radiation Calculation

In general, the energy dW emitted per unit solid angle $d\Omega$ and frequency $d\omega$ is given by the electric field at the observer $E(\omega)$ [50]:

$$\frac{dW}{d\omega d\Omega} = 2\varepsilon_0 c R^2 |E(\omega)|^2 \quad (3.3.1)$$

with ε_0 the vacuum permittivity, c the speed of light, and R the distance to the observer. A solution for the electric field $E(t)$ is obtained by introducing the Liénard-Wiechert potentials which determine the electromagnetic radiation from an electron of a given arbitrary trajectory $\vec{r}(t)$. With that, the energy emitted by a single electron into the far field⁴ is fully determined by this trajectory, i.e. the position \vec{r} , the velocity $\vec{\beta}$ and acceleration $\dot{\vec{\beta}}$ of the electron and the observation direction [17, 62, 64]:

$$\frac{d^2W}{d\omega d\Omega} = \frac{e^2}{16\pi^2\varepsilon_0 c} \left\| \int_{-\infty}^{\infty} \frac{\vec{n} \times [(\vec{n} - \vec{\beta}) \times \dot{\vec{\beta}}]}{(1 - \vec{\beta} \cdot \vec{n})^2} e^{i\omega(t - \vec{n} \cdot \vec{r}(t)/c)} dt \right\|^2 \quad (3.3.2)$$

For multiple electrons, i.e. for a bunch, the total electric field determines the radiated intensity

$$\vec{E}_{tot}(\omega) = \sum_j \vec{E}_j(\omega) \quad (3.3.3)$$

Adding up the intensity distributions of all electrons would ignore the phase relation and consequent interference effects. Therefore, the summation over all particles j in the bunch has to be executed within the norm brackets:

$$\frac{d^2W}{d\omega d\Omega} = \frac{e^2}{16\pi^2\varepsilon_0 c} \left\| \sum_j \int_{-\infty}^{\infty} \frac{\vec{n} \times [(\vec{n} - \vec{\beta}_j) \times \dot{\vec{\beta}}_j]}{(1 - \vec{\beta}_j \cdot \vec{n})^2} e^{i\omega(t - \vec{n} \cdot \vec{r}_j(t)/c)} dt \right\|^2 \quad (3.3.4)$$

⁴This assumption is valid, as the interaction region is much smaller than the distance to the observer.

The Clara code exploits the similarity of the integral to a Fourier integral by utilising a fast Fourier transform (FFT) to calculate the radiation spectrum and thereby reduce computational time. In order to further decrease the demand on time, as well as memory and storage space, several electrons are combined to a macro particle. Consequently, instead of a summation over 6×10^7 electrons (≈ 10 pC), the bunch is represented by N_{sim} macro particles (e.g., 2000 macro particles for a 10 pC bunch). In this case, the summation over the number of macro particles requires to account for the degree of coherent radiation emitted by all physical electrons represented by a single macro particle. When assuming a fully incoherent radiation, the phase information can be neglected and the emitted energy is proportional to the bunch charge. This assumption is valid, as the bunch length ($\sim 1 \mu\text{m}$) is larger than the wavelength of the emitted radiation (~ 10 pm). The number of emitted photons in a fully incoherent case is proportional to the number of emitted electrons $N_{\text{inc}} \propto N_e$, whereas for the fully coherent case, $N_{\text{coh}} \propto N_e^2$ holds. In case of coherent radiation, the radiation of each simulated particle is associated with the same phase information, so that the norm and the sum are interchangeable. Consequently, one obtains for the coherent case

$$\frac{d^2 n_{\text{phot,coh}}}{d\omega d\Omega} = N_e^2 \cdot \frac{e^2/(\hbar\omega)}{4\pi^2 c} \left\| \int_{-\infty}^{\infty} \left(\frac{\gamma \vec{n} \times [(\gamma \vec{n} - \gamma \vec{\beta}) \times \gamma \dot{\vec{\beta}}]}{(\gamma - \vec{n} \cdot \gamma \vec{\beta})^3} \right) \cdot e^{i\omega t_{\text{ret}}} dt_{\text{ret}} \right\|^2 \quad (3.3.5)$$

The number of electrons may be expressed as

$$N_e = Q/e = \frac{Q/e}{N_{\text{sim}}^2} \left(\sum_j^{N_{\text{sim}}} 1 \right)^2 \quad (3.3.6)$$

where the number 1 within the sum assumes equal phase information, i.e. coherence. To return to the incoherent case, several steps are performed. Firstly, the phase-dependence within the sum is reintroduced for velocities and accelerations. Secondly, equation (3.3.6) is inserted into (3.3.5) and in dividing by N_e one arrives at the incoherent case [17]

$$\frac{d^2 W}{d\omega d\Omega} = \frac{Q/e}{N_{\text{sim}}^2} \frac{e^2}{16\pi^2 \epsilon_0 c} \left\| \sum_j^{N_{\text{sim}}} \int_{-\infty}^{\infty} \frac{\vec{n} \times [(\vec{n} - \vec{\beta}_j) \times \dot{\vec{\beta}}_j]}{(1 - \vec{\beta}_j \cdot \vec{n})^2} e^{i\omega(t - \vec{n} \cdot \vec{r}_j(t)/c)} dt \right\|^2 \quad (3.3.7)$$

Clara2 is based on the same physics as the Clara code, but allows parallelised computing on CPU clusters, using the communication protocols MPI and OpenMP.

Trajectory Generation

As Clara and Clara2 are trajectory-based codes, GPT or ASTRA are applied to model the laser-electron interaction and calculate the resulting electron or macro-particle trajectories. Both codes allow to include space-charge effects. Throughout this thesis, mostly GPT is used, if not denoted otherwise. This is due to the C-based input-file structure

of GPT which allows to quickly alter electron and laser models individually by the user. Furthermore, apertures, such as the capillary discharge lens used in chapter 5 are easily included. This is also possible in ASTRA, where 3D field maps can be read in. However, this requires a further step of writing (and storing) the field maps.

The laser modelled in GPT is a temporal and spatial Gaussian beam which either has a Fourier-limited bandwidth or, if the bandwidth is specified, an according linear longitudinal chirp. The electron bunch is represented by a Gaussian distribution, as well. It is mathematically described via the Courant-Snyder parameters, thus defining its properties at any given longitudinal position. This allows to match or manipulate the electron focal point with regard to that of the laser. The temporal resolution of the trajectories is $\lambda/80/c$, so that higher harmonics oscillations can be resolved. The laser and electron bunch at the beginning of the tracking have a temporal delay of 1.5τ with τ the FWHM of the laser pulse duration. This ensures that at the beginning end end of the simulation, the respective positions of electron bunch and laser are well separated, so that the laser field at the electron position is negligible. Therefore, the total interaction distance recorded is 3τ . Consequently, for a laser of $\tau = 4$ ps FWHM, GPT generates the 6D electron phase space for 360.000 sampling points.

Clara/Clara2 Output and Analysis Scripts

Clara and Clara2 are C++ programs which calculate the radiation $dW/(d\omega d\Omega)$ for pre-defined observation angle θ and frequency ω bins. The output has the form of a 2D array of length and width according to the number of bins in θ and ω . In general, two files are created, for azimuthal angle $\phi = 0$ and $\phi = \pi$. This gives the radiation along the horizontal and vertical line of pixels through the centre $\theta_x = \theta_y = 0$, and the respective radiated frequency. Within the code, the number of output axes can be changed, e.g. to form a grid which yields a "full" angular detector image, as shown in figure 2.3.1 (right). However, the interpolation results are representative and require shorter computational time and obviously less storage. Furthermore, a single-trajectory analysis can be performed to calculate the radiation from each macro particle, separately.

The analysis is performed by different python scripts which read in the Clara output files. From these arrays, energy spectra and their bandwidth, angular distributions of photon energy and intensity, as well as photon numbers in arbitrary parameter regions (within the simulated parameter set) are calculated.

Further analyses in this thesis, including theoretical models and approximations, have been performed via python.

Computational Time and Storage

To record a simulation scenario with a total of 360.000 electron phase spaces via GPT takes ≈ 10 h on a cluster using 4 nodes and 32 processors per node⁵. A second program creates the trajectories from the phase-space output by GPT in ≈ 3 h. The parallelised Clara2 code then calculates the radiation in ≈ 2 h. This leads to a total of 15 h of calculation time, not counting preparation of the simulation and evaluation of the Clara2 results. For longer interaction regions, e.g. due to longer laser durations, or for higher sampling, this time is exceeded.

Storing the trajectories in form of ASCII files as required by Clara/Clara2 requires a large storage space, depending on the number of sampling points and macro particles. As the trajectories can be restored from the GPT output, they can be deleted after the radiation calculation. However, a simulation as regarded so far will take ≈ 30 GB per scenario run, even after the trajectory deletion. Assuming 10 scenarios with 10 runs thus requires a permanent storage of 3 TB. With the trajectory files in tact, the temporal storage space needs to exceed this value.

Consequently, although the GPT-Clara2 combination represents a fast way of calculating the radiation of a Thomson interaction, a space for data storage has to be found. The simulations were conducted on the cluster of the Helmholtz-Zentrum Dresden-Rossendorf (HZDR) which allowed a temporal storage of ≈ 15 TB. Consequently, data had to be moved to another (DESY) storing place, frequently. These were the limiting factor for the simulations in this thesis.

⁵This is the time for one job. Other jobs can, of course, run parallely on different nodes.

CHAPTER 4

DESIGN STUDY FOR A THOMSON SOURCE

The medical application motivating this thesis requires an X-ray source with the maximum possible photon yield at a certain bandwidth within a confined cone of small opening angle (cp. Sec. 3.1). In this chapter, simulations are employed to determine the influence of laser and electron parameters, as well as of the confined cone angle, on the resulting Thomson spectrum, in terms of photon yield and bandwidth. The initial parameters of the setup are given in section 3.2.

The characteristics of Thomson sources have been thoroughly studied [12, 37] and are well described in terms of total photon yield, energy- and intensity-angle dependence and on-axis bandwidth. However, in our case, the yield, as well as the bandwidth, within a cone of a certain confined opening angle are relevant. Optimisation of the total yield typically underlies assumptions that are not or only partially valid for this scenario. Furthermore, while the yield within a cone is theoretically describable, optimisations of this scenario have not been investigated, yet. Another issue poses the determination of the bandwidth where the topic of the bandwidth within a cone has not been visited, either. The source bandwidth reduction by employing a chirped laser has also been a topic of investigation [26, 27] but has not been quantified, so far.

In this chapter, the existing theory on photon yield and bandwidth is presented and discussed with regard to electron focal size and divergence, as well as the source divergence via a confining cone (Sec. 4.1). The applicability of the theory and its limits with regard to the XFI application are elaborated by means of comparison with simulations of the yield and bandwidth (Sec. 4.2). The simulations primarily aim at establishing an understanding of the Thomson spectrum and the underlying effects and, on this basis, at finding the optimum laser and electron parameters for the interaction. Given a pulse energy E_p of the Thomson laser, optimum laser strength parameter a_0 , laser waist w_0 and duration τ need to be determined. As for the electron bunch, the relevant parameters are the waist σ_r and divergence σ_θ at a given normalized emittance ε_n . The influence of the energy spread of a bunch of non-zero emittance is investigated in the following chapter 5.

4.1 Basics of Thomson Photon Yield and Bandwidth

A short introduction to Thomson scattering was given in section [2.3.3](#). Here, the underlying theory with focus on the source's photon yield and bandwidth is presented in detail. Furthermore, where possible, first assumptions on the effect of electron focal spot size and divergence, as well as the source divergence given by the confined observation angle, are drawn from the existing theory.

Note on Terminology

In the following, it has to be distinguished between the total *radiation cone*, θ_{synch} , and the confined *observation cone*, given by the maximum observation angle θ_c . The radiation cone is defined by the opening angle of synchrotron radiation $\theta_{\text{synch}} = 1/\gamma$. It is thus fixed by the electron energy, whereas the observation cone is an independent parameter.

4.1.1 Thomson Radiation Spectrum

Typical Thomson Spectra

For the design of a Thomson source, knowledge on its properties such as the angular energy and intensity distribution are of fundamental necessity. A typical Thomson angular spectrum is presented in figure [4.1.1\(a\)](#). The normalised number of photons is depicted depending on the observation angle $\gamma_e\theta$ and the normalised photon energy $y = E_\gamma(\theta)/E_{\gamma,\text{max}}$, where $E_{\gamma,\text{max}} = 4\gamma^2 E_L$ is the theoretical maximum photon energy. Due to non-ideal effects, such as an electron energy spread, values with $y > 1$ are possible. In accordance with the Thomson energy equation ([2.3.10](#)), shown as the white dashed line, the energy decreases with observation angle further from the electron-beam propagation axis. For large angles, as well as photon energies deviating from the results of this formula, the photon intensity drops. This angular energy and intensity dependence is an intrinsic property of Thomson (and undulator) sources (cp. Sec. [2.3.1](#)). Within the total opening angle ($\approx 1/\gamma$), the spectrum has a large bandwidth while its on-axis bandwidth may be small. Therefore, bandwidth reduction requires the confinement of the opening angle, i.e. the collimation of the radiation. Such a reduction in bandwidth is hence intrinsically linked to a reduction in photon yield, as well. Thus, the simple application of the theoretical approach for maximising the total yield does not necessarily lead to the expected results within a confined cone angle. Formulae to account for the yield within a certain bandwidth have been presented only for the ideal case (see below). The goal of this thesis is not the maximisation of the total yield, but the yield within a confined angular and energetic spread, making collimation a twofold necessary tool. Photons at energies deviating too much from the target energy would not benefit the fluorescence-signal photon yield (cp. Sec. [3.1](#)), but only increase the dose on the patient. Consequently, the collimation which

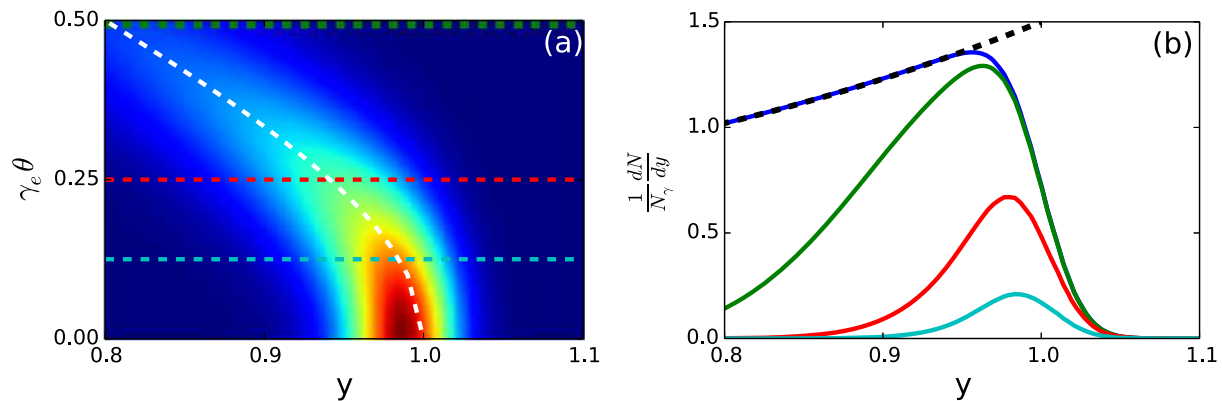


Figure 4.1.1: Typical angular energy and intensity distribution of a Thomson source (a) and the source collimation effect (b) as functions of the normalised photon energy $y = E_\gamma/E_{\gamma,\max}$. In (a) the vertical axis represents the observation angle $\gamma_e\theta$, where 0 is the electrons' propagation direction. The white dashed line shows the angular dependence of the photon energy as obtained from the Thomson energy equation (2.3.10). The spectra obtained from different collimation angles (coloured dashed lines in (a)) are depicted in the according colours in (b), and for the uncollimated case (blue). The black dashed line in (b) represents the ideal, uncollimated case. Both plots are adapted from reference [12].

is necessary in the first place to reduce the source's angular spread and thereby increase the spatial resolution in medical imaging, also removes photons of undesired energy from the spectrum. Energy spectra resulting from different collimation angles in figure 4.1.1(a) are shown in according colours in figure 4.1.1(b). In this realistic case (including electron beam divergence and energy spread), the collimation also cuts photons at the target energy emitted into larger angles.

Ideal Case

In order to obtain a basic understanding of the aforementioned yield-bandwidth relation, the ideal case is visited: Here, an electron beam without divergence or energy spread interacts with a plane-wave laser of zero bandwidth and constant laser strength a_0 . The total photon yield emitted in the full solid angle is given as [12]

$$N_\gamma = \frac{2\pi}{3}\alpha_f N_e N_0 a_0^2 \quad (4.1.1)$$

with the fine structure constant $\alpha_f \approx 1/137$, the number of electrons N_e in the bunch, the number of oscillations N_0 , i.e. laser periods within the interaction range, and the laser strength parameter a_0 (cp. Sec. 2.1). Figure 4.1.2 shows the photon number and intensity energy spectra in the linear regime ($a_0 \ll 1$). In the full solid angle, the photon number (blue) follows a parabolic shape. The intensity spectrum (green) displays that electrons at highest energy are emitted in the forward direction, i.e. the direction of electron propagation. The minimum photon number is reached at $y = 1/2$, corresponding to $E_\gamma(\theta = 1/\gamma)$, i.e. at the so-called Thomson opening angle. The photon yield within a

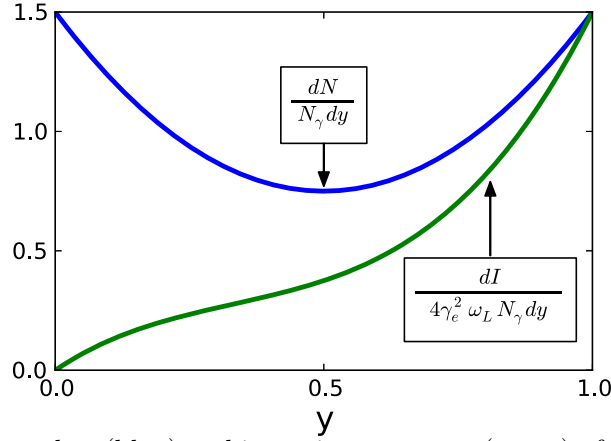


Figure 4.1.2: Photon number (blue) and intensity spectrum (green) of a linear Thomson source without non-ideal effects. Both functions are displayed in dependence of the normalised photon energy $y = E_\gamma/E_{\gamma,\max}$. This figure is adapted from reference [12].

bandwidth κ is given as [12, 19]

$$N_\kappa = N_\gamma \kappa (\kappa^2 - 3/2\kappa + 3/2) = N_\gamma \sigma(\kappa). \quad (4.1.2)$$

This bandwidth κ in the ideal case represents the integration boundary in y acquired by collimation. According to this formula, within a bandwidth of 10 % FWHM, 13.6 % of all photons are included.

4.1.2 Total Yield

In case of a head-on collision of a Gaussian laser and electron beam without relative longitudinal, transverse and temporal displacements, the total yield can be estimated on the basis of the Thomson cross section $\sigma_T = 8\pi/3r_e^2$ with the classical electron radius $r_e = e^2/mc^2$, the number of electrons and photons in the interaction N_e and N_p , respectively, as well as the beam sizes in the focus ($\sigma_{e,0}$ and $\sigma_{p,0}$) and their β functions (β_e^* and β_p^*) [12]:

$$N_\gamma = \frac{\sigma_T N_e N_p F(x)}{\sqrt{2\pi}\sigma_l \sqrt{\sigma_{e,0}^2 + \sigma_{p,0}^2}} \frac{1}{\sqrt{\frac{\sigma_{e,0}^2}{\beta_e^{*2}} + \frac{\sigma_{p,0}^2}{\beta_p^{*2}}}} \quad (4.1.3)$$

where

$$F(x) = e^{x^2} [1 - \text{erf}(x)], \quad (4.1.4)$$

$$x = \frac{\sqrt{2}}{\sigma_l} \sqrt{\frac{\sigma_{e,0}^2 + \sigma_{p,0}^2}{\frac{\sigma_{e,0}^2}{\beta_e^{*2}} + \frac{\sigma_{p,0}^2}{\beta_p^{*2}}}}, \quad (4.1.5)$$

$$\sigma_l = \sqrt{\sigma_{l,e}^2 + \sigma_{l,p}^2}, \quad (4.1.6)$$

and $\beta^* = \sigma_0^2/\varepsilon_t$, $\varepsilon_{t,p} = \lambda_L/2 = \lambda_L/(4\pi)$. From this, conditions for maximum total yield are derived.

4.1.3 Optimum Laser Waist and Duration

For first assumptions on obtaining the maximum yield, we follow the formula for the ideal case (4.1.1) demanding to maximise the number of electrons in the bunch N_e , the number of electron oscillations, i.e. laser periods N_0 and the laser strength parameter a_0 . This is true in general, however, this formula is only valid for the ideal case, i.e. for a laser of constant a_0 . Consequently, the length of the laser has to be increased to obtain a higher yield. For a given laser pulse energy, elongating the pulse requires stronger laser focusing to obtain a smaller focal waist and thereby a constant or higher laser strength parameter. The latter decreases the Rayleigh length $z_R = \pi w_0^2 / \lambda_0$ of the laser pulse. The first step in maximising the yield roots in confining the available laser photons to the interaction region, thus implementing conditions for the optimum laser waist and duration. The interaction length is given as [17]

$$L_{\text{int}} = \frac{(\tau_{\text{Laser}} + \tau_{\text{bunch}})c}{2} \quad (4.1.7)$$

which is clearly dominated by the laser pulse length, as it is typically several orders larger than that of the electron bunch. Requiring this interaction region to lie within the Rayleigh range z_R of the laser [12, 17], the optimum duration of the laser pulse from $L_{\text{int}} \leq z_R$ is

$$\tau_0(w_0) = \frac{2\pi w_0^2}{c\lambda_0} - \tau_e \quad (4.1.8)$$

Or, for electron bunches much shorter than the laser pulse [12]:

$$\tau_0(w_0) \approx \frac{2z_R}{c} \quad (4.1.9)$$

$$\sigma_l \approx 2\beta_p^* \quad (4.1.10)$$

Furthermore, the laser duration and the laser strength parameter are in the following relation (cp. Eq. (2.1.6)):

$$a_0 = \sqrt{\frac{E_p}{21.5 \times 10^9 \tau_0} \frac{\lambda_0}{w_0}}$$

For a constant a_0 , increasing the laser waist results in decreasing the laser duration. Solving the latter equation for τ_0 and setting it equal to equation (4.1.8), gives:

$$w_0 \approx 0.217 \frac{E_p^{1/4} \lambda^{3/4}}{\sqrt{a_0}} \quad (4.1.11)$$

4.1.4 Optimum Electron-Beam Waist for the Total Yield

For optimum overlap, luminosity considerations demand the electron beam size to match that of the laser in the focus [17]:

$$\sigma_{x,y} \leq w_0/2 \quad (4.1.12)$$

However, this assumption neglects that electrons in higher laser fields, i.e. at the centre of a Gaussian laser, emit more photons. Furthermore, as the diameters of a focused electron beam and laser pulse change in space and time during the interaction, their respective beta functions β^* have to be taken into account and the optimum mean overlap is determined for the entire interaction. In other words, the electron diameter influences both the transversal overlap and its temporal development. Consequently, not a two-dimensional overlap has to be optimised, but rather the interaction overlap volume. Another approach is to neglect the electron waist in the first place by assuming it to be orders of magnitude smaller than the laser waist [12]¹. The role of the electron beam waist and the according electron divergence on the total yield, as well as on the cone yield will be investigated in section 4.3.1.

4.1.5 Yield within a Confined Cone

While the total yield does not set absolute constraints on the electron divergence, but only in relation to the laser parameters, thus in terms of overlap, this is not the case when regarding the photon emission into a cone of confined opening angle. As electrons emit the radiation of highest intensity into their propagation direction, their divergence becomes a crucial parameter for the photon yield within a cone. The relative yield per energy and angular element for an electron bunch of rms divergence σ_θ is [12]

$$\frac{1}{N_\gamma} \frac{d^2 N}{\theta d\theta dy} = \frac{3}{2\sigma_\theta^2} [1 - 2y(1 - y)] \times \exp\left(-\frac{\theta^2 + \tilde{\theta}^2}{2\sigma_\theta^2}\right) I_0\left(\frac{\theta\tilde{\theta}}{\sigma_\theta^2}\right) \quad (4.1.13)$$

with the modified Bessel function I_0 , $\tilde{\theta}^2 = (1 - y)/\gamma^2 y$, the observation angle θ , and the energy of the emitted photon y normalised to the maximum energy of the first harmonic.

4.1.6 Bandwidth

Above, the bandwidth of the Thomson energy spectrum was already briefly discussed as to its effect on the photon yield and its dependence on the cone angle. Here, the single contributions to the bandwidth by a single electron, as well as electron-bunch effects and laser properties will be presented in detail.

¹For laser waists of several 10 μm , and an electron waist of $\sim 1 \mu\text{m}$.

Single Electron Spectrum and Observation Angle

There are two contributions to the bandwidth of the Thomson energy spectrum of a single electron in a continuous-wave laser field. The first contribution is owed to the intrinsic energy-angle correlation of the spectrum, as discussed before. Therefore, even in the ideal case, i.e. a single electron in an electromagnetic field of a plane-wave laser of constant field and infinite spatial extent in transverse and longitudinal direction, the Thomson energy spectrum possesses an intrinsic bandwidth. The effect of the observation angle on the bandwidth can be deduced from the Thomson formula (2.3.10) to be

$$\frac{\Delta E_\gamma(\Delta\theta_{\text{obs}})}{E_\gamma} = 1 - \frac{1 + a_0^2/2 + \gamma^2\theta_{\text{obs}}^2}{1 + a_0^2/2 + \gamma^2(\theta_{\text{obs}} + \Delta\theta_{\text{obs}})^2}$$

where Δ denotes the FWHM uncertainties. Consequently, the larger the observed angular region ($\Delta\theta_{\text{obs}}$), the broader the spectrum. In order to obtain the FWHM value of the bandwidth, $\Delta\theta_{\text{obs}}$ has to be the FWHM observation angle, not the total opening angle of e.g. a cone. For sufficiently small angles ($\Delta\theta_{\text{obs}} < 1/\gamma$) around the electron propagation axis ($\theta_{\text{obs}} = 0$), however, the half cone size θ_c is a good estimate and the formula can be approximated as

$$\frac{\Delta E_\gamma(\theta_c)}{E_\gamma} \approx \frac{\gamma^2\theta_c^2}{1 + \gamma^2\theta_c^2} \quad (4.1.14)$$

Consequently, in the total Thomson radiation angle $\theta_c = 1/\gamma$, the FWHM bandwidth is 50 %.

As the total opening angle of the radiation is linked to the kinetic electron energy ($\theta_{\text{synch}} = 1/\gamma$), and due to the energy-angle relation, a higher kinetic electron energy leads to a narrower total radiation cone. Therefore, at constant maximum observation angle, more photons of lower energy are emitted into the observation cone, thus increasing the bandwidth. Typical angular intensity distributions in x and y direction are shown in figure 4.1.3. Due to the polarisation of the interacting laser, the intensity distribution in y is broader.

The second contribution arises in a finite laser beam. It is determined by the number of laser periods, i.e. electron oscillations N_0 , analogously to the undulator theory. Consequently, the following is only valid for a plane-wave laser without transversal or longitudinal field dependence. The following equations (4.1.15-4.1.17) are analogous to the undulator theory (cp. Sec. 2.3.2), and are adapted from reference [50]. A detailed derivation is included in appendix section A.1.1. At a fixed observation angle θ_{obs} , the bandwidth is

$$\frac{\Delta E_\gamma(N_0)}{E_\gamma} = \frac{1}{1 + N_0} \quad (4.1.15)$$

Accordingly, a certain wavelength can be observed within the opening angle $\Delta\theta_\lambda$ relative

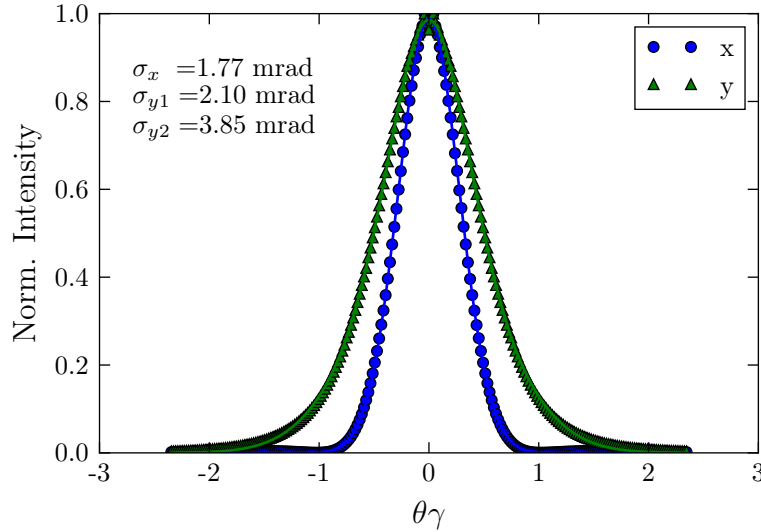


Figure 4.1.3: Angular intensity distribution of line-outs in x for $\theta_y = 0$ (blue circles) and in y for $\theta_x = 0$ (green triangles) as functions of the observation angle θ_γ . The laser strength parameter is $a_0 = 0.15$. The straight line curves are Gaussian fits to the simulation data. For the y distribution, a sum of two Gaussians is fitted. The according rms widths σ are given for all three functions.

to the angle θ_λ

$$\Delta\theta_\lambda = \sqrt{\theta_\lambda^{*2} - \theta_\lambda^2} = \sqrt{\frac{2\lambda}{N_0\lambda_u}} = \sqrt{\frac{4\lambda}{N_0\lambda_L}} \quad (4.1.16)$$

For the central wavelength $\lambda_{\min} = \lambda_L/(4\gamma^2)$, the opening angle is

$$\Delta\theta_{\lambda_{\min}} = \sqrt{\frac{1}{N_0}} \frac{1}{\gamma} \quad (4.1.17)$$

Both formulae are deduced from destructive interference conditions: The angle θ_λ^* is the angle at which a given wavelength interferes destructively. The angle θ_λ is the observation angle for which the Thomson formula gives the according wavelength. The observation angle forms a ring at $\theta_x^2 + \theta_y^2 = \theta_\lambda^2$ with the width given by $\Delta\theta_\lambda$. The angular distribution of four arbitrary wavelengths is illustrated in figure 4.1.4. For a given observation angle, a certain wavelength is observed. The bandwidth at this observation angle arises from the overlap of the opening angles of the wavelengths at neighbouring angles. Increasing the number of laser periods thus shrinks the angular distribution of each single wavelength and thereby the bandwidth at a given observation angle. If the total observation angle $\Delta\theta_{\text{obs}}$ is in the magnitude of $\Delta\theta_\lambda$, bandwidth reduction is obtained by increasing the number of laser periods. However, for sufficiently large observation angles and laser durations, the effect of N_0 becomes negligible:

$$\Delta E_\gamma/E_\gamma = \sqrt{\left(\frac{\Delta E_\gamma(\Delta\theta_{\text{obs}})}{E_\gamma}\right)^2 + \left(\frac{\Delta E_\gamma(N_0)}{E_\gamma}\right)^2} \quad (4.1.18)$$

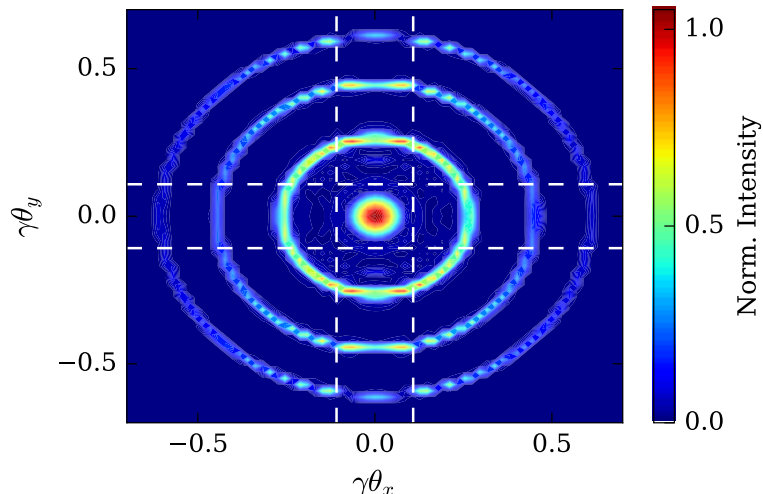


Figure 4.1.4: ASTRA-Clara Simulation of the angular intensity distribution of four arbitrary wavelengths. The maximum opening angles θ_x and θ_y of the central wavelength according to equation (4.1.17) with $N_0 = 100$ is indicated by the white dashed lines.

This is demonstrated in Fig 4.1.5. The simulated bandwidth $\Delta E_\gamma/E_\gamma$ of the Thomson radiation from an electron bunch within a plane-wave laser without longitudinal or transversal a_0 dependence, is shown in dependence of the cone radius for $N_0 = 20, 100$ and 200, and is compared to equation (4.1.18).

Electron-Bunch Effects

For an electron bunch, the divergence and energy spread of the electrons are important factors contributing to the Thomson bandwidth. As the electron energy $\Delta\gamma/\gamma$ enters the photon energy formula quadratically, it has a significant impact (cp Eq. (2.3.10)):

$$\frac{\Delta E_\gamma(\Delta\gamma)}{E_\gamma} \approx 2 \frac{\Delta\gamma}{\gamma} \quad (4.1.19)$$

The divergence of the electron bunch changes the on-axis bandwidth, as each electron emits the radiation into a cone centred around its own propagation axis. Consequently, an electron with a non-zero angle to the bunch propagation direction emits a smaller energy (and intensity) on axis. The on-axis bandwidth for a given FWHM divergence σ_{FWHM} is given as [12]:

$$\frac{\Delta E_\gamma(\sigma_{\theta,\text{FWHM}})}{E_\gamma} = \left(\frac{\gamma\sigma_{\theta,\text{FWHM}}}{2} \right)^2 \quad (4.1.20)$$

The effect of the electron divergence on the bandwidth via the according change in collision angle and thereby a change in the emitted energy (cp. Eq. (2.3.10)) is negligible in case of a head-on collision.²

²For head-on collision, $\alpha = \pi$. The cosine function is at an extremum and small changes in α lead to small changes in $\cos \alpha$. A more detailed discussion is included in the appendix section A.2

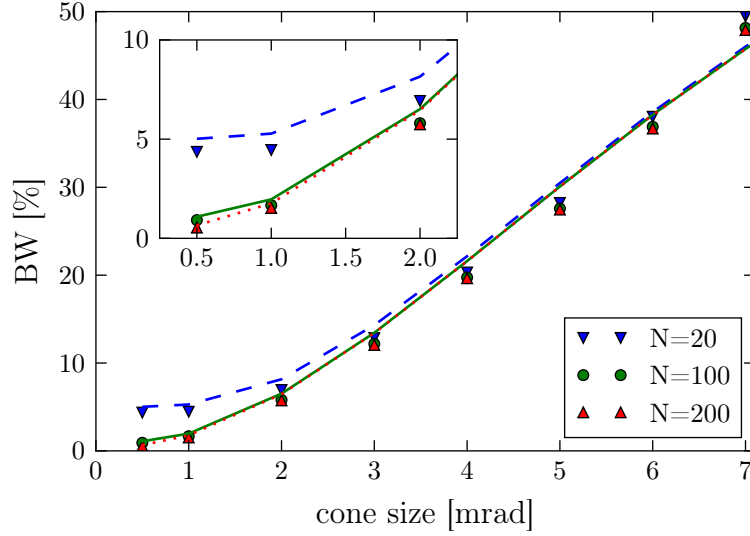


Figure 4.1.5: ASTRA-Clara simulation (markers) and analytical (lines) bandwidth $\Delta E_\gamma/E_\gamma$ in dependence of the cone radius for different number of laser periods N_0 , and thus laser duration $\tau = N_0\lambda/c$. The simulation results are obtained from the interaction of an electron bunch of zero energy spread and emittance with a plane-wave laser of constant a_0 . The analytical results are determined via equation (4.1.18). For a laser wavelength $\lambda = 800$ nm, the equivalent durations are obtained as $\tau(N_0 = 20) \approx 53$ fs (blue marker, dashed line), $\tau(N_0 = 100) \approx 267$ fs (green marker, solid line), and $\tau(N_0 = 200) \approx 533$ fs (red marker, dotted line).

Laser

In addition to the interference effect of the number of laser oscillations (see Eq. (4.1.15)), the bandwidth of the laser wavelength $\Delta\lambda$, the laser strength parameter a_0 , and the focusing of the laser³ contribute to the Thomson spectral bandwidth. Deriving the bandwidth from equation (2.3.10) yields

$$\frac{\Delta E_\gamma(\Delta\lambda)}{E_\gamma} = \frac{\Delta\lambda}{\lambda + \Delta\lambda} \approx \frac{\Delta\lambda}{\lambda} \quad (4.1.21)$$

$$\frac{\Delta E_\gamma(\Delta a_0)}{E_\gamma} = \frac{(\Delta a_0)^2/2 + a_0\Delta a_0}{1 + (a_0 + \Delta a_0)^2/2 + \gamma^2\theta^2} \quad (4.1.22)$$

For small Δa_0 and on-axis observation angle $\theta = 0$, the equation simplifies to

$$\frac{\Delta E_\gamma(\Delta a_0)}{E_\gamma} \approx \frac{a_0\Delta a_0}{1 + a_0^2/2} = \frac{a_0^2}{1 + a_0^2/2} \frac{\Delta a_0}{a_0} \quad (4.1.23)$$

An approximation for the on-axis bandwidth, given in reference [12], is independent of Δa_0 :

$$\frac{\Delta E_\gamma(a_0)}{E_\gamma} \approx \frac{a_0^2}{2} \quad (4.1.24)$$

³The divergence of the laser is again neglected with regard to its effect on the collision angle (appendix Sec. A.2).

number of (equivalent) laser periods	N_0	angular
observation cone	$\Delta\theta_{\text{obs}}$	angular
electron divergence	$\sigma_{\theta,e}$	angular
electron energy	γ	energetic + angular
electron energy spread	$\Delta\gamma$	energetic + angular
laser bandwidth	$\Delta\lambda$	energetic
laser divergence, spot size	$\sigma_{\theta,l}, w_0$	energetic
laser intensity	$a_0, \Delta a_0$	energetic
collision angle	$\alpha, \Delta\alpha$	energetic

Table 4.1.1: Angular and energetic contributions to the bandwidth. A quantitative analysis of the single contributions is given in table [4.1.2](#) and figure [4.1.6](#).

Interaction Geometry

The emitted energy depends on the relative velocity of the electron and laser which is dependent on the collision angle α : $E_\gamma \propto (1 - \beta \cos \alpha)$. The bandwidth contribution as derived from equation [\(2.3.10\)](#) reads

$$\frac{\Delta E_\gamma(\Delta\alpha)}{E_\gamma} = \beta \frac{\cos(\alpha) - \cos(\alpha + \Delta\alpha)}{1 - \beta \cos(\alpha)} \quad (4.1.25)$$

For $\beta \approx 1$, the equation simplifies for $\alpha = \pi$ (head-on), and $\alpha = \pi/2$:

$$\frac{\Delta E_\gamma(\Delta\alpha)}{E_\gamma}(\alpha = \pi) = \frac{\cos(\Delta\alpha) - 1}{2} \quad (4.1.26)$$

$$\frac{\Delta E_\gamma(\Delta\alpha)}{E_\gamma}(\alpha = \pi/2) = \sin(\Delta\alpha) \quad (4.1.27)$$

In a counter-propagating interaction geometry, i.e. $\alpha = \pi$, small deviations $\Delta\alpha$ from the collision angle only have a negligible effect on the emitted photon energy. For collision angles approaching the slope of the cosine function at $\alpha = \pi/2$, $\Delta E_\gamma(\Delta\alpha)$ increases. Therefore, the divergence of the electron bunch, as well as pointing effects are more significant to the spectrum at non-head-on Thomson interaction.

Overview

The total bandwidth of the Thomson scattered energy spectrum is:

$$\frac{\Delta E_\gamma}{E_\gamma} = \sqrt{\left(\frac{\Delta E_\gamma(\Delta\gamma)}{E_\gamma}\right)^2 + \left(\frac{\Delta E_\gamma(\Delta\lambda_0)}{E_\gamma}\right)^2 + \left(\frac{\Delta E_\gamma(\Delta\alpha)}{E_\gamma}\right)^2 + \left(\frac{\Delta E_\gamma(\Delta a_0)}{E_\gamma}\right)^2 + \left(\frac{\Delta E_\gamma(\Delta\theta_{\text{obs}})}{E_\gamma}\right)^2 + \left(\frac{\Delta E_\gamma(N_0)}{E_\gamma}\right)^2} \quad (4.1.28)$$

The bandwidth contributions, ordered in the two categories angular and energetic, are listed in table [4.1.1](#). The divergence and the observation angle are contributions to

parameter	Eq.	parameter range	bandwidth range [% FWHM]
N_0	for $\tau = 10$ ps–25 fs	(4.1.15) 3750 – 9	0.03 – 11.0
$\Delta\theta_{\text{obs}}$	at $\gamma = 156.4$	(4.1.14) 0.5 – 1.0 mrad	0.6 – 2.4
$\sigma_{\theta,e}$	at $\varepsilon_n = 0.2$ mm mrad, $\gamma = 156.4$, for $\sigma_r = 6 - 0.6$ μm	(4.1.20) 0.2 – 2.0 mrad	0.1 – 13.6
γ	at $\Delta\theta_{\text{obs}} = 0.5$ mrad	(4.1.14) 120 – 160	0.4 – 0.6
$\Delta\gamma/\gamma$		(4.1.19) 1 – 20 % FWHM	2.0 – 40.0
$\Delta\lambda/\lambda$		(4.1.21) 5 – 7.5 % FWHM	5.0 – 7.5
a_0		(4.1.24) 0.1 – 0.5	0.5 – 12.5
$\Delta\alpha$	at $\alpha = \pi$	(4.1.26) 0.3 – 2.0 mrad rms	~ 0 – ~ 0
$\Delta\alpha$	at $\alpha = \pi/2$	(4.1.27) 0.3 – 2.0 mrad rms	0.1 – 0.5
$\sigma_{\theta,l}$	at $\alpha = \pi$ for $w_0 = 20 - 5$ μm	(4.1.26) 0.01 – 0.05 rad	~ 0 – 0.06

Table 4.1.2: Parameter ranges and according bandwidth contributions, as obtained from the presented theory. The chosen parameter ranges are adapted from the design parameters in tables 3.2.1 and 3.1.1, and from the following design study.

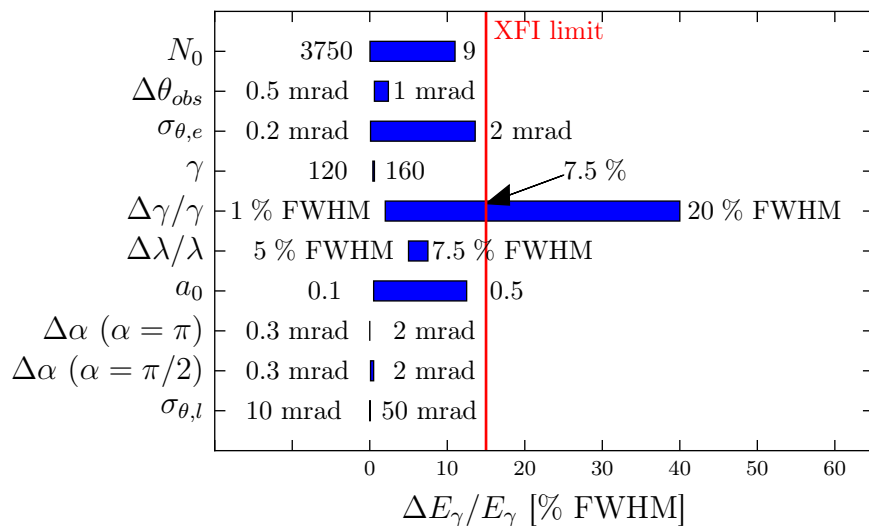


Figure 4.1.6: Graphic presentation of the theoretical bandwidth contributions obtained from the respective parameter ranges. The dominant contributions are the electron energy spread $\Delta\gamma/\gamma$, the electron divergence $\sigma_{\theta,e}$, the laser strength parameter a_0 , and the number of laser periods N_0 . The following section 4.2 shows that large a_0 values do not necessarily lead to a large bandwidth. Furthermore, the role of the laser periods in a Gaussian laser pulse, as well as the electron divergence within a cone demonstrate deviations from this theory. In chapter 5, chromatic focusing is utilised as a means to reduce the effective energy spread of electron bunches.

the bandwidth of purely angular nature, arising from the choice of magnitude of these parameters. Regarding the total solid angle, the divergence, as calculated here, will have no impact on the bandwidth. In section 4.2, the effect of the divergence-dependent overlap on the Thomson bandwidth will be discussed. This is, however, not taken into account in the on-axis bandwidth theory [12]. The bandwidth originating from the observation angle is the intrinsic bandwidth of a single electron with respect to its propagation axis. Therefore, it is only applicable in the case of zero or negligible electron divergence. The residual contributions are predominantly changing the energy of the emitted radiation. Their applicability is thus independent of the divergence and observation angle. Solely the electron energy and thus the electron energy spread require special mentioning, as the intrinsic radiation opening angle scales with $1/\gamma$, and thereby bears a small angular component.

In table 4.1.2, the contributions are quantified on the basis of the parameter ranges of the single contributions. The chosen parameter ranges are based on the design parameters in tables 3.2.1 and 3.1.1, as well as parameters from the following design study. A graphic of the contributions is shown in figure 4.1.6. In the presented theory, the electron bunch energy spread $\Delta\gamma/\gamma$ represents the dominant bandwidth contribution. According to equation (4.1.19), the energy spread is limited to $< 7.5\%$ FWHM to not exceed the XFI bandwidth limit of 15% FWHM. A means for the reduction of the effective electron energy spread is discussed in chapter 5, rendering bunches with initially large energy spreads no limit for the application, in terms of the bandwidth. The theory further suggests bandwidth increase from the laser's pulse duration, i.e. N_0 [4], strength parameter a_0 , and bandwidth $\Delta\lambda/\lambda$, as well as from a large electron divergence, hence a small electron waist. However, the following section 4.2 shows that in terms of a_0 , $\sigma_{\theta,e}$, and $\Delta\lambda$, appropriate optimisation strongly reduces the bandwidth contributions, as obtained from the theory.

4.2 Electron-Bunch Parameter Study

As pointed out in section 4.1 the theory on Thomson scattering is well established in terms of the estimation of the total yield and its optimisation. However, the theoretical description lacks optimisation with respect to a small opening angle, a central aspect of the medical application. Furthermore, assumptions such as a negligible electron bunch focal waist are made to optimise the total yield. This section presents the parameter study, where the effect of the electron bunch parameters on the total yield and, especially, on the cone yield is investigated.

⁴The equation for the N_0 bandwidth contribution (4.1.15) is based on interference effects in a laser of transversally and longitudinally constant strength, and is not applicable for a Gaussian laser.

4.2.1 Initial Parameters for the Simulations

In section 3.1 the required parameters for the X-ray source have been stated: For K -shell fluorescence, an incident photon energy of ≈ 150 keV at a maximum tolerable bandwidth of $\lesssim 15$ % FWHM is desired⁵. To achieve high spatial resolution, the divergence is limited to a cone of opening angle ± 0.5 mrad. In order to render medical application possible in the future, i.e. reduce the necessary imaging time to a minimum, the rate of fluorescence-signal photons per time, and thus of the X-ray photons per time has to be increased. While the repetition rate of a Thomson source is given by that of the driver laser, the number of photons per shot is a property to be optimised in Thomson interaction design. As a suitable starting point for the parameter study, the aim is the maximisation of the yield and the minimisation of the source bandwidth at the desired photon energy. The parameter set of the proposed pump-probe setup is listed in table 3.2.1.

The photon energy emitted by a Thomson source is determined by equation (2.3.10):

$$E_\gamma = \frac{2\gamma^2[1 - \beta \cos(\alpha)]E_L}{1 + \frac{a_0^2}{2} + \gamma^2\theta^2}$$

In case of a head-on collision, i.e. laser and electrons counter-propagate with an angle of $\alpha = \pi$, the maximum emitted photon energy on axis is $E_{\gamma,\max} = 4\gamma^2 E_L$ in the linear case ($a_0 \ll 1$). By choosing this interaction geometry, the photon energy is tuned via the kinetic energy of the electrons. The laser photon energy $E_L = hc/\lambda$ is prescribed by the driver laser's wavelength ($\lambda = 800$ nm). A photon energy of 150 keV is achieved by electrons of Lorentz factor $\gamma = 156$ or $E_{\text{kin},e} = 79$ MeV. Following from the required electron energy, the full radiation opening angle in forward direction is $\theta_{\text{synch}} = \pm 1/\gamma = \pm 6.4$ mrad, thus exceeding the required divergence of 1 mrad. Such a low divergence is obtained from a Lorentz factor of $\gamma = 1000$. However, as the intrinsic bandwidth within the full opening angle is ≈ 50 % FWHM (cp. Fig. 4.1.2), bandwidth reduction requires collimation. Consequently, an intrinsic opening angle larger than the required divergence is a necessary feature. Moreover, $\gamma = 1000$ would have to be mitigated by a decreased collision angle to arrive at $E_\gamma = 150$ keV which would decrease the overlap of laser and electron bunch and consequently reduce the yield, significantly.

A first orientation for the yield requirements is given by equation (4.1.3): The maximum yield is obtained for maximum number of electrons N_e and photons N_p , and for optimum overlap of the two beams. However, the laser pulse energy $E_p = hc/\lambda \cdot N_p$, as well as the electron bunch charge $Q = eN_e$ are limited by the conservative estimates of first field studies of LPAs. The electrons are accelerated via laser-plasma acceleration. Typical bunch charges achieved by this acceleration scheme are in the pC region [40, 41, 58, 59]. As a starting point for the parameter scans, a bunch charge of 10 pC is assumed. This

⁵Recent results corrected this value to $E_\gamma = 90$ keV (cp. Ch. 3.1). This design study is performed exemplarily for 150 keV. An outlook onto the change in photon energy to 90 keV is given in section 6.2

holds the advantage of being a realistic, yet low enough value, so that initially, space charge effects can be neglected. Higher electron-bunch charges will increase the Thomson photon yield linearly. An outlook on consequent space-charge effects will be given in chapter [4.6](#). In the pump-probe setup combining LWFA and TS with a single high-power laser, the Thomson laser pulse can only inherit a fraction of the driver laser's energy. $E_p = 500$ mJ is assumed to be a feasible value for the pulse energy of the Thomson laser.

The Thomson-interaction geometry determines the electron-laser overlap and hence represents the main aspect of the following optimisation studies. The relevant parameters include the interaction angle α , laser focal spot size w_0 , pulse length τ and resulting laser strength parameter a_0 . The relevant electron parameters are the transversal size σ_r and the divergence σ_θ defined by the emittance ε_n and the electron energy γ . Closely following equation [\(4.1.1\)](#), the number of laser oscillations N_0 , hence the laser duration and a_0 need to be maximised for highest photon yield. The latter, however, stands in contrast to minimising the bandwidth which requires a small a_0 (cp. Eq. [\(4.1.24\)](#)). The linear regime of an optical undulator is given for $a_0 \ll 1$. If a_0 approaches 1, i.e., the nonlinear regime, higher harmonics become more likely. To prevent the bandwidth from increasing dramatically, and from losing photons in the required energy range (first harmonic), the value of the laser strength parameter is limited to $a_0 \leq 0.15$ where 5 % of energy is lost to higher harmonics, according to reference [\[17\]](#).

The main aspects of the following simulations is to establish an understanding of electron-laser overlap effects with focus on the electron focal waist and divergence. These are then evaluated in terms of the total photon yield and the yield and bandwidth within a cone.

The base parameters for the optimisation process are:

$$\begin{aligned}
 E_p &= 500 \text{ mJ} \\
 a_0 &= 0.15 \\
 \lambda_0 &= 800 \text{ nm} \\
 \gamma &= 156.4 \\
 \tau_e &= 11.77 \text{ fs FWHM}
 \end{aligned}
 \tag{4.2.1}$$

4.2.2 Optimising the Laser Parameters

In order to maximise the photon yield of a Thomson source, many parameters have to be taken into consideration: Electron and laser parameters, as well as geometrical parameters describing the interaction. Those parameters are all inter-linked. In a head-on geometry, the laser duration is the dominant factor in defining the interaction region. In the proposed setup, the laser duration and waist are manipulated via the appropriate optical elements, rendering these two variable parameters. Therefore, a good starting point for the simulations is to define an initial laser configuration.

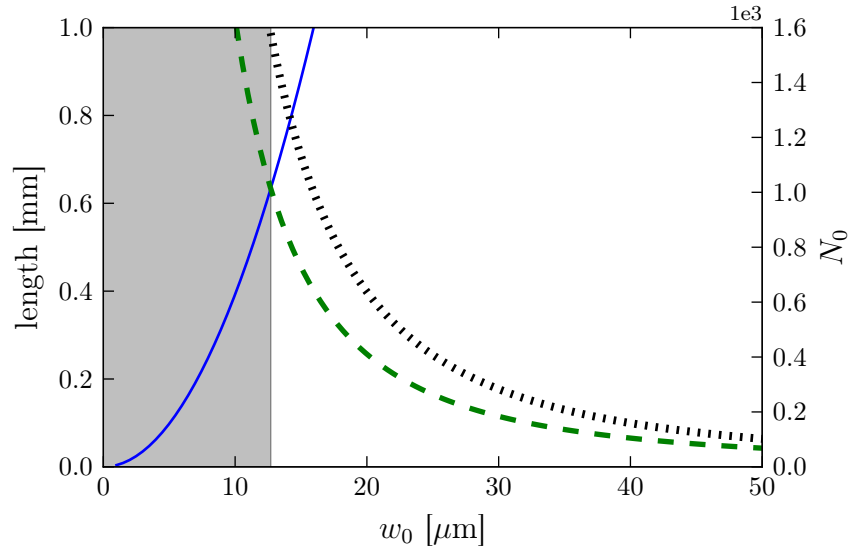


Figure 4.2.1: Rayleigh length z_R and interaction length L_{int} in dependence of the laser waist for the parameters given in equation (4.2.1). The grey area marks the unfavourable region, where the interaction length exceeds the Rayleigh length. While the Rayleigh length increases with increasing w_0 , the interaction length, limited by $a_0 = 0.15$, rapidly decreases. The optimum is found for $z_R = L_{\text{int}}$ at $w_0 = 12.7 \mu\text{m}$ and $N_0 = 1575$.

The number of laser oscillations N_0 , hence the laser duration, needs to be maximised within the interaction region for highest photon yield (Eq. (4.1.1)). For the initial laser strength parameter $a_0 = 0.15$, the interaction region and number of laser oscillations within the laser duration is shown as a function of the laser waist w_0 in figure 4.2.1. In accordance with equation (4.1.11), the plot shows an optimum laser waist at $12.7 \mu\text{m}$, and therefore, the optimum laser duration is $\tau = 4.2 \text{ ps}$. As an illustration: Increasing the laser waist to receive a larger Rayleigh length while keeping the laser duration constant would result in a decreased laser field in the interaction region and a decrease of the number of laser oscillations, as well. Adapting the laser duration to the increased w_0 would increase the number of oscillations, but also decrease a_0 . Consequently, there would be no gain. Hence, for a given a_0 , there exists an optimal w_0 - τ relation, defined by interaction and Rayleigh length.

In the following, as laser of $w_0 = 12 \mu\text{m}$ and $\tau = 4 \text{ ps}$ is assumed, rendering $a_0 = 0.156$. Such low laser waists are generally achievable via appropriate focusing optics.

4.2.3 Optimising the Electron-Bunch Parameters

In order to maximise the yield, the overlap of electrons and laser has to be optimised. Supposedly, optimum transversal overlap is obtained for equal electron and laser waist, i.e. $\sigma_r = \sigma_l$ [17]. In reference [12], yield optimisation concerns the laser parameters and is based on the condition $\sigma_r \ll \sigma_l$. As these approaches differ, the role of the electron waist on the Thomson spectrum is to be examined in the following parameter scans. An

electron bunch is characterised among others by its emittance, waist, divergence and its energy spread. In order to quantify the single effects separately, at first an electron bunch with zero energy spread and emittance is simulated. Thereupon, emittance and energy spread effects are evaluated. Concerning the laser parameters, different laser bandwidths are examined, as well, and the effect of the chirp is investigated. Further geometrical effects are analysed, i.e. the collision angle and longitudinal and transversal offset of electrons and laser.

4.2.4 Electron Bunch without Energy Spread and Emittance

At first, the interaction of an electron bunch without emittance or energy spread with a Gaussian laser is investigated. The transversal bunch size is varied and the spectral shape, photon yield and bandwidth are determined from simulations and compared to the theory. In order to analyse the effect of the bunch size on the spectrum, it has to be isolated from different effects, such as the laser chirp and bandwidth. Consequently, a laser of zero chirp and Fourier-limited bandwidth is simulated. With a duration of $\tau = 4$ ps, the latter is small enough ($\Delta\lambda = 0.23$ nm) to neglect its effect on the Thomson spectrum. A chirp, and a significant bandwidth will be included in the following section [4.2.5](#).

Yield

For a bunch of zero emittance, the total yield N_γ can be estimated via equation [\(4.1.3\)](#) by setting the electron bunch emittance very small (10^{-20} mm mrad). The cone yield is determined via equation [\(4.1.2\)](#) with $\kappa = \gamma^2\theta_c^2/(1 + \gamma^2\theta_c^2)$. The comparison of the yield within a cone of 0.54 mrad (> 0.5 mrad, due to angular sampling in the simulation) as obtained by simulation and theory are shown in figure [4.2.2](#). The results for a chirped laser are addressed in the following section [4.2.5](#). For a laser bunch of focal size $w_0 = 12$ μm , the Thomson yield within a cone is plotted against the electron bunch size σ_r . The deviation of the zero chirp simulation from the theoretical results for a 0.5 mrad cone value is due to sampling. The dashed line presents the results for a slightly larger cone, adapted to the simulation sampling. For increasing electron waist σ_r the yield decreases. The number of photons emitted by a single electron depends on the amplitude of the electric field (a_0) experienced by the electron: $N_\gamma \propto a_0^2$ for $a_0 < 1$. Due to the transversal field profile of the laser, for smaller bunch waists, more electrons are concentrated in the region of higher a_0 , thus increasing the photon yield. When comparing the photon yield to the ideal case (Eq. [\(4.1.1\)](#)[\(4.1.2\)](#)), an effective a_0 can be estimated:

$$a_{0,\text{eff}} = \sqrt{N_{\text{sim}}/N_\kappa} a_0 \quad (4.2.2)$$

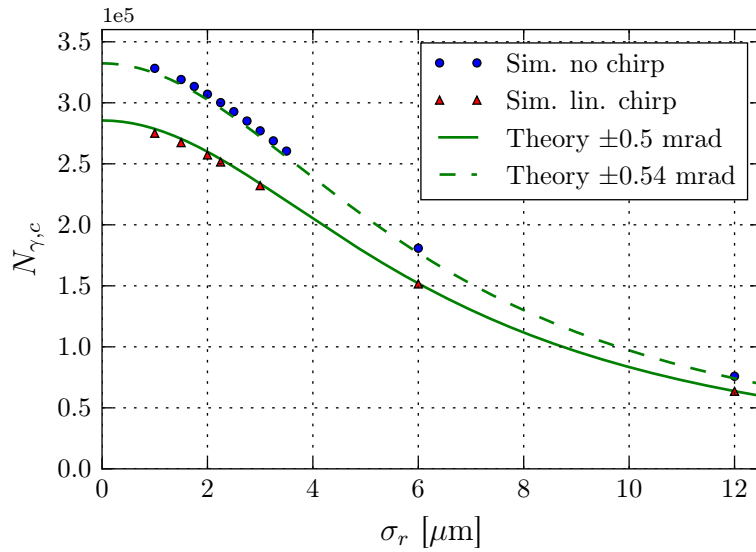


Figure 4.2.2: Thomson photon yield $N_{\gamma,c}$ as a function on the electron waist σ_r . The yield is simulated within a ± 0.5 mrad cone for an ideal electron bunch (no energy spread, no emittance). Blue: Simulation of a zero chirp interaction laser, red markers: Chirped laser, Green: Theory according to equations (4.1.3) and (4.1.2). The laser has a waist of $w_0 = 12 \mu\text{m}$, a duration of $\tau = 4$ ps, and $a_0 = 0.156$.

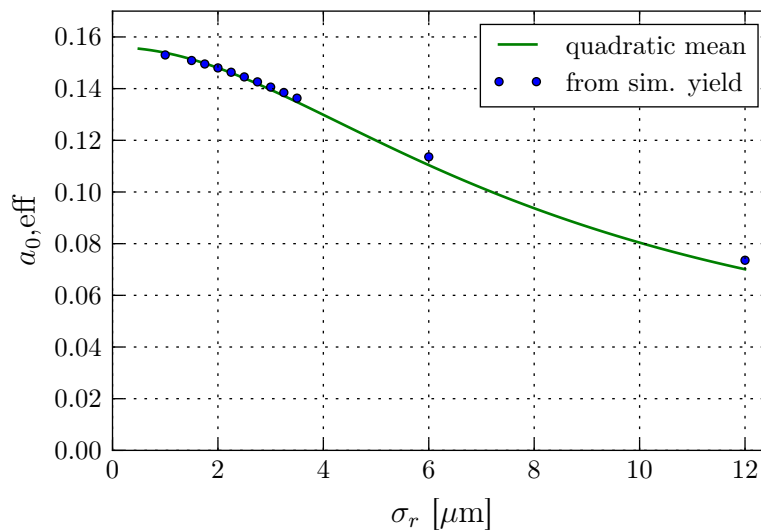


Figure 4.2.3: Effective a_0 as a function of the electron bunch waist. The markers represent the results obtained from equation (4.2.2) applied to the simulation. The straight line shows the results of overlap calculations of two 2D Gaussian functions.

where κ refers to the intrinsic cone bandwidth. This effective a_0 is the laser strength parameter that corresponds to a laser of constant a_0 , i.e. where all electrons in a bunch experience the same field, which gives equal photon yield. This holds as long as the number of electrons N_e that contribute to the Thomson spectrum can be approximated as constant. For $\sigma_r > \sigma_l$, the reduction of N_e to $N_{e,eff}$ would have to be taken into consideration, as well. The effective a_0 as a function of the electron waist is shown in figure 4.2.3. The theoretical comparison is drawn by calculating the mean a_0 from the overlap

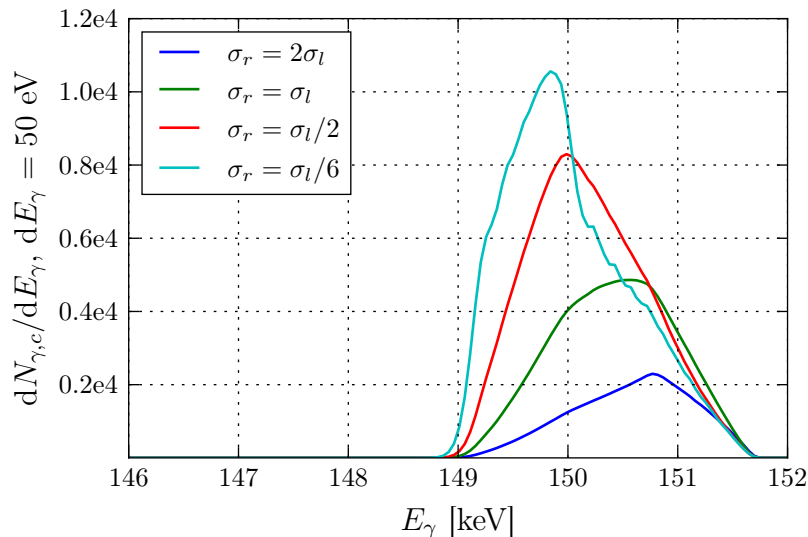


Figure 4.2.4: Total energy spectra within ± 0.5 mrad cone (azimuthal angle $0-2\pi$). Laser $\sigma_l = 6 \mu\text{m}$, $\tau = 4$ ps. For decreasing electron radius σ_r , the photon yield increases while the peak energy of the spectrum decreases.

of 2D Gaussian distributions, representing the mean transversal laser distribution within the interaction range and the transversal electron bunch distribution (see appendix [A.2](#)). The calculation neglects the transversal bunch waist change due to the ponderomotive force, as is it assumed to be too small (cp. Eq. [\(2.1.8\)](#)).

The decrease in a_0 also has an effect on the shape of the energy spectrum. Figure [4.2.4](#) demonstrates the change in the energy spectra within a cone of ± 0.5 mrad for different electron beam waists. For decreasing waist, the high-energy slope hardly changes, while the number of photons emitted into lower energy bins increases. As the lower energy signal arises from higher a_0 , this is in agreement with the reduction of the effective a_0 for increasing beam waist.

Bandwidth

Qualitative assessment and spectral analysis

The bandwidth of the simulated spectra is generally determined as FWHM bandwidth. This is convenient, as the bandwidth theory is based on FWHM characterisation. However, FWHM neglects the shape of the spectra, so that it is not always representative for the distribution. In order to analyse the bandwidth thoroughly, investigation of the angular energy and intensity distribution of the Thomson spectrum is advised.

The according line spectra for different bunch waists σ_r and observation angles θ are displayed in figure [4.2.5](#). These spectra are referred to as line spectra, as they do not include the total azimuthal angle of 2π , i.e. the total cone spectrum, but that of the line of pixels through $\theta_y = 0$ rad in one direction and $-\theta_c \leq \theta_x \leq \theta_c$ in the other.

Spectra of the smallest cone (\approx on axis, right column) show no angular dependence,

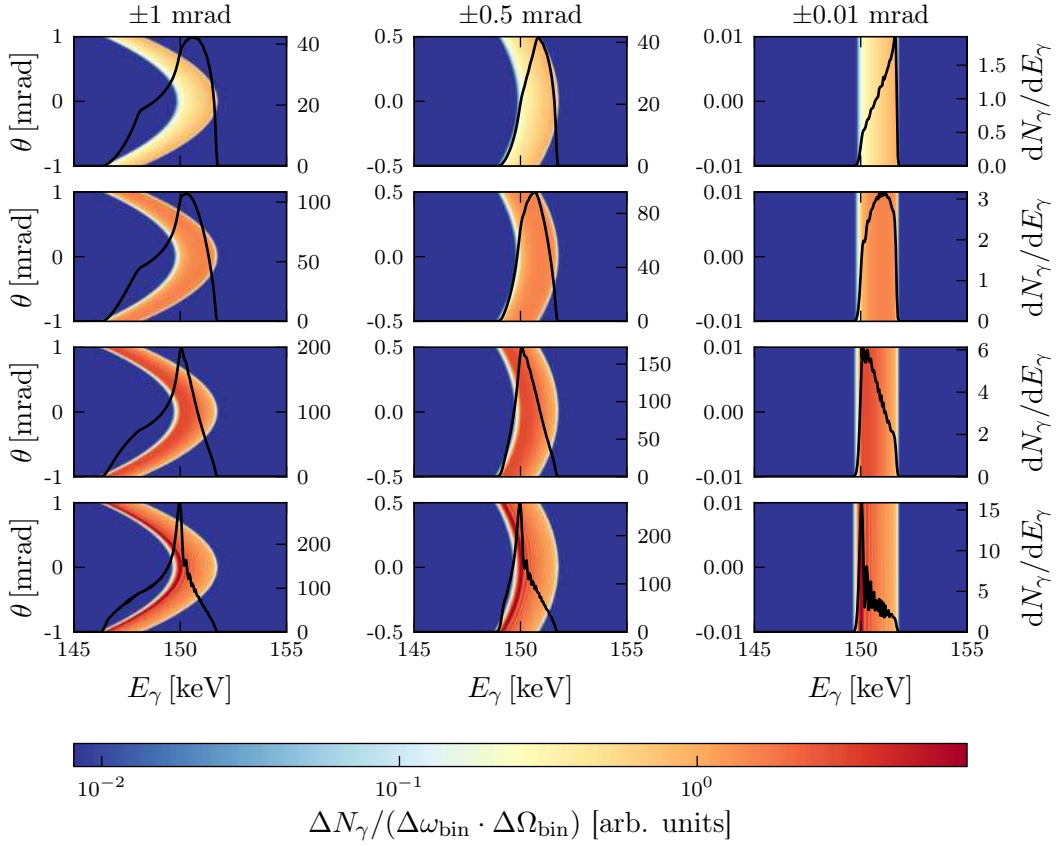


Figure 4.2.5: Line spectra for a non-divergent zero energy spread electron bunch in a zero chirp Gaussian laser of $\tau = 4$ ps and $w_0 = 12 \mu\text{m} \leftrightarrow \sigma_l = 6 \mu\text{m}$. The electron bunch waist is varied from top to bottom: $\sigma_r = 12 \mu\text{m}$, $6 \mu\text{m}$, $3 \mu\text{m}$, $1 \mu\text{m}$. Left column: Opening angle of 1 mrad, centre column: 0.5 mrad, right column: 0.01 mrad.

so that the observation-angle influence on the bandwidth can be neglected. Consequently, they allow to isolate the overlap effect of electrons and laser on the effective laser field $a_{0,\text{eff}}$, as experienced by the electrons: The total range of emitted photon energies is obviously independent of the bunch size which indicates the same for the range of a_0 . Due to the pulsed nature and the head-on collision geometry, the electron bunch interacts with all laser fields from $a_0 > 0$ to $a_{0,\text{max}}$, longitudinally. According to equation (2.3.10), the minimum energy is reached for $a_0 = a_{0,\text{max}}$, and the maximum energy for $a_0 > 0$, yielding the observed energy range: $E_\gamma(a_{0,\text{max}}) = 149.8$ keV to $E_\gamma(0) < 151.7$ keV. The peak energy $E_{\text{peak}} = E_\gamma(a_{0,\text{peak}})$ and the FWHM bandwidth, on the other hand, display a strong dependence on σ_r . For decreasing bunch size, the peak energy of the line spectrum decreases as well. This is explained by the increasing $a_{0,\text{eff}}$ with decreasing σ_r/σ_l : The emitted photon energy is proportional to $1/(1+a_0^2/2)$ (Eq. (2.3.10)), so that an increased a_0 leads to a lower emitted energy. For $\sigma_r = \sigma_l$ (second row), the on-axis spectrum is rather symmetric and the bandwidth is largest in comparison to the on-axis spectra of different σ_r/σ_l ratio. For $\sigma_r = 2\sigma_l$ (first row), the low- a_0 contribution increases as less electrons oscillate in the peak laser field. Consequently, an asymmetric spectrum with a smaller bandwidth peaked at higher photon energy is obtained. The opposite effect

occurs for $\sigma_r < \sigma_l$ and the bandwidth significantly decreases for $\sigma_r = \sigma_l/6$.

With larger cone size, the peak energy of the spectra is reduced and they obtain an increasing low-energy tail. In the high-energy part of the spectrum, i.e. where $E_\gamma > E_{\gamma,\text{peak}}$, the dependence on the electron bunch waist is more dominant in the alteration of the spectral shape than for $E_\gamma < E_{\gamma,\text{peak}}$: In case of a large bunch waist compared to the laser (first row, $\sigma_r/\sigma_l = 2$), the peak of the on-axis spectrum is at the maximum energy. Therefore, by increasing the cone, energy spectra of equal shape which are shifted towards lower energies in total, are added to the spectrum ($E_\gamma \propto 1/(1 + a_0^2/2 + \gamma^2\theta^2)$). In consequence, the high-energy flank is smoothed. For $\sigma_r = 1/6\sigma_l$ (last row), the on-axis spectrum peaks at the lower end of the energy range. Therefore, by increasing the cone angle, the added line spectra of $\theta > 0$ only contribute to the high-energy tail with a low intensity, hardly altering the FWHM of the spectrum.

Furthermore, it is observed that the change in opening angle is not a symmetric bandwidth contribution, as indicated in the theory. While the low-energy contributions increase with the opening angle, the intensity at higher energies quickly drops to zero. This means that for each observation angle > 0 , a lower energy band with according bandwidth is added to the spectrum. Therefore, the cone angle represents an asymmetric contribution to the bandwidth. The 1 mrad cone energy spectra (black lines, left row) start to display the characteristic low-energy parabola shape, presented in figure [4.1.2](#).

Oscillations in the spectrum for $\sigma_r \ll \sigma_l$

The last row in figure [4.2.5](#), where $\sigma_r/\sigma_l = 1/6$, displays oscillations in the intensity, most pronounced in the on-axis spectrum on the right. These oscillations are a well-known nonlinear effect in Thomson scattering [\[26, 27, 54\]](#). This interference phenomenon arises from the pulsed nature of the laser leading to a temporal a_0 -dependence in the pulse (Sec. [2.3.3](#)). This effect weakens for increasing σ_r/σ_l and for larger observation angles. With increasing electron focal waist this is due to the transversal change in a_0 . For larger cones, the oscillations are still present for each observation direction. The energy shift of the single angular spectra due to the energy-angle dependence of the emitted energy smears out the oscillations. Therefore, this effect is only observed in the case of a small electron waist compared to the laser waist and for on-axis spectra. Even though it is attributed to the nonlinear regime, i.e. $a_0 \geq 1$, it is already observed here, where $a_0 = 0.156$. This shows that nonlinear effects start to emerge already in this intermediate regime. The on-axis bandwidth, is decreased, as it refers to the major oscillation. For increased cone angles, it induces a reduced bandwidth, inherited from the small spectral width, as broadening due to the low-energy angular edges is below the half maximum boundary.

Quantitative assessment of the on-axis bandwidth and analysis of the a_0 contribution

As the theory is based on quantifying the on-axis bandwidth, spectra within the smallest cone will be evaluated and compared to the theory, before including the effect of the

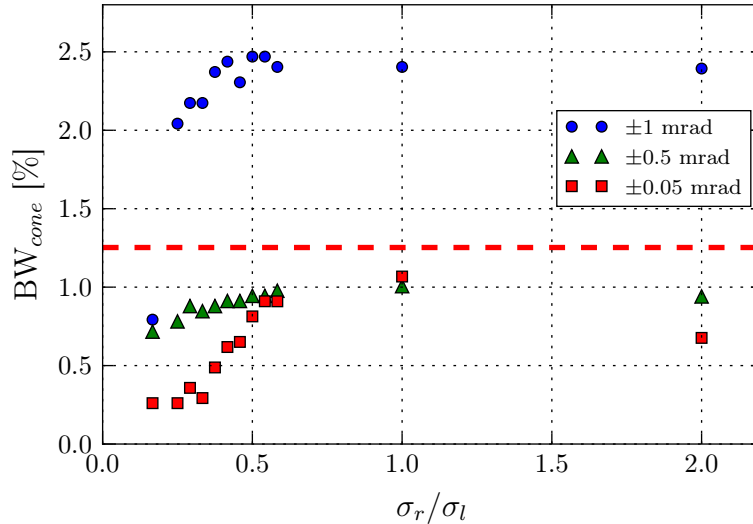


Figure 4.2.6: FWHM cone bandwidth as a function of the electron bunch laser waist relation σ_r/σ_l for a constant laser focal waist of $\sigma_l = 6 \mu\text{m}$. The results for different cone sizes are displayed: 1 mrad (blue circles), 0.5 mrad (green triangles), 0.05 mrad (red squares). The red dashed line indicates the theoretically determined on-axis bandwidth value.

opening angle.

The on-axis bandwidth in the discussed case (electron energy spread $\Delta\gamma = 0$, electron divergence $\sigma_\theta = 0$) is composed of the laser bandwidth $\Delta\lambda$, the number of laser periods N_0 , and the laser strength parameter contribution Δa_0 . For a laser of $\tau = 4$ ps FWHM at $\lambda = 800$ nm, the Fourier-limited bandwidth is $\Delta\lambda/\lambda = 0.29$ %. The number of laser oscillations can be approximated to $N_0 = c\tau/\lambda \approx 1500$ ⁶. Due to the pulsed nature of the laser and the transversal field dependence the number of oscillations N_0 does not give the contribution to the on-axis bandwidth, as the different oscillations are not equivalent and thus do not lead to equivalent photon emission (see chapter 2.3.3). Assuming the spectral broadening according to theory, $a_0^2/2 = 0.22$, this effect is implied, so that a constant on-axis bandwidth is obtained:

$$\frac{\Delta E_\gamma}{E_\gamma} = \sqrt{\frac{a_0^4}{4} + \left(\frac{\Delta\lambda}{\lambda}\right)^2} = 1.25 \text{ \%} \quad (4.2.3)$$

However, the previous analysis showed the dependence of the peak and mean effective laser field on the electron waist. Consequently, a constant contribution of a_0 is no valid assumption, on the one hand due to the transversal effect via the electron waist, on the other hand, due to the longitudinal effect arising from the pulsed nature of the laser (cp. Fig. 2.3.4). The bandwidth for different opening angles as functions of the electron laser waist ratio σ_r/σ_l is displayed in figure 4.2.6. The latter will be referred to as on-axis spectrum, as the according line spectra show no angular dependence. From the theory,

⁶This assumption is applicable, as the laser's Rayleigh length is matched to the interaction length. Therefore, one can assume that each electron undergoes the full number of laser oscillations.

one would expect a constant bandwidth, independent of the electron waist. However, with increasing electron bunch waist, the on-axis bandwidth increases, until laser and electrons possess equal transversal spread ($\sigma_r = \sigma_l = 6 \mu\text{m}$). For $\sigma_r > \sigma_l$, the bandwidth decreases. This electron waist dependence is not included in the theory. In the following, an explanation, as well as a quantification of the bandwidth in dependence of the bunch waist is attempted.

Deduced from the qualitative assessment of the spectra, it is assumed that the electron waist dependence arises from the different a_0 values an electron encounters along its path. In this case, the effective a_0 is no appropriate quantity, as an electron emits radiation of intensity $I(a_0)$ at photon energy $E_\gamma(a_0)$ for each perceived laser field along its propagation. Consequently, the a_0 distribution of each individual electron and thereupon of the bunch has to be determined. Again assuming a Gaussian transversal electron bunch profile, the electric laser field at each time step and transverse coordinates x and y is calculated and weighted with the number of electrons at these coordinates. The resulting a_0 distributions are displayed in figure 4.2.7 (top, straight lines) for three scenarios: $\sigma_r \ll \sigma_l$, $\sigma_r \approx \sigma_l$ and $\sigma_r \gg \sigma_l$. On the basis of equation (4.1.1), the photon yield is obtained from $N_\gamma \propto a_0^2 N_e$. The emitted energy E_γ is calculated according to equation (2.3.10). The resulting energy spectra are shown in figure 4.2.7 (bottom, straight lines). In order to compare the results with the simulation, the above-mentioned procedure is reversed to obtain the a_0 distribution (top, dashed lines) from the simulated energy spectra (bottom, dashed lines).

If the electron waist σ_r is larger or of same size as the laser waist σ_l , the majority of electrons experience low laser field values during the interaction. Consequently, the a_0 distribution peaks at low values. At this point, it is important to clarify the difference of the calculated and simulated results at $a_0 < 0.05$ (top, inset) and above the maximum laser strength $a_{0,\text{max}} = 0.156$ for the simulation. In the calculations, electrons outside the laser or at low fields will render the according a_0 value. An electron in zero field will not contribute to the Thomson spectrum ($N_\gamma \propto a_0^2$). Therefore, in the a_0 distribution reconstructed from the simulation, such low fields do not occur. Furthermore, the simulated on-axis spectra are broadened according to the laser bandwidth, allowing for higher field values $a_0 > a_{0,\text{max}}$ in the reconstruction, that are not taken into account by the calculation. Summarising, the simulation gives the a_0 distribution actually contributing to the energy spectrum, while the calculations give the distribution as experienced by the electron bunch. As this approach does not incorporate the interference of emitted wavefronts, one cannot deduce the spectral bandwidth from the obtained a_0 distribution. The spectral oscillations in the on-axis spectrum for low electron waist are of this origin, and are thus not included in the calculation results. Unfortunately, the calculation of the energy spectra from the a_0 distribution is very sensitive: While the a_0 distributions are in good agreement, the small difference at $a_0 \approx 0.1 \pm 0.025$ for $\sigma_r \gg \sigma_l$ leads to a strong difference in the spectra. Consequently, the bandwidth cannot be reconstructed. As the reconstruction of the energy spectrum is less sensitive to small changes at larger a_0 values,

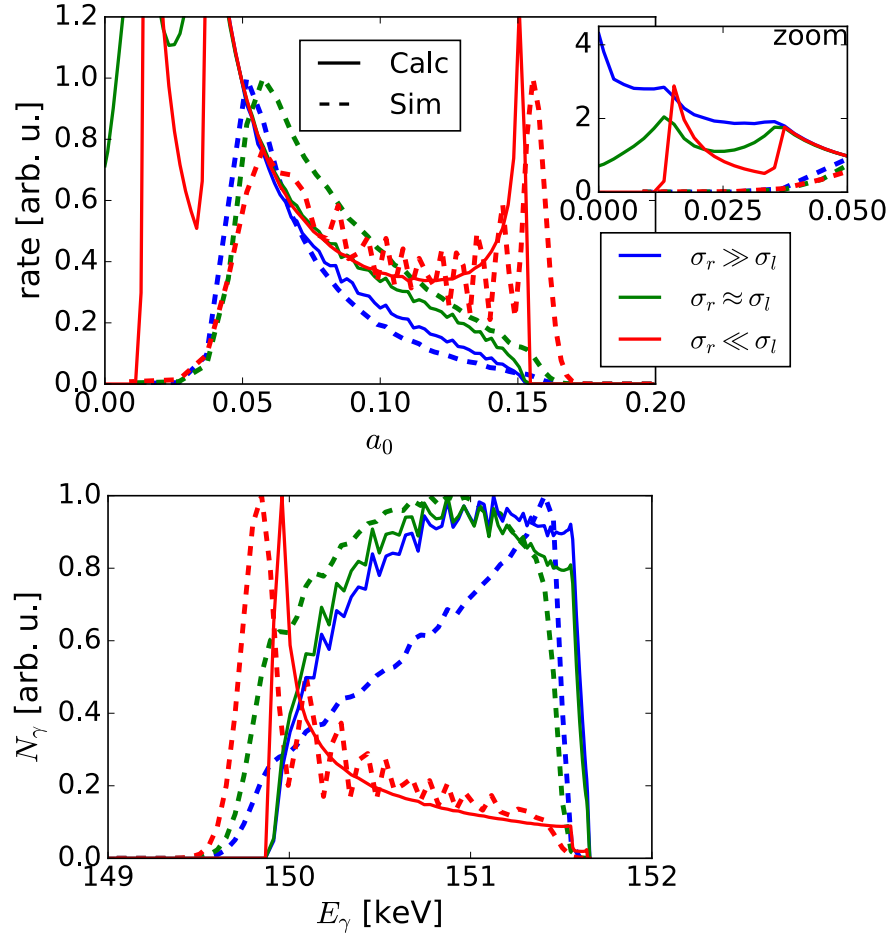


Figure 4.2.7: a_0 distributions (top) and according energy spectra dN_γ/dE_γ (bottom). The results from calculations (straight lines) and simulations (dashed lines) are displayed for different electron-laser waist relations: $\sigma_r \gg \sigma_l$ (blue), $\sigma_r \approx \sigma_l$ (green), $\sigma_r \ll \sigma_l$ (red). The inset in the left plot shows a zoom into the low- a_0 region. The rate is given in arbitrary units and refers to the number of electrons and oscillations at which a certain a_0 value is encountered. In the case of the calculations, the energy spectra are reconstructed from the a_0 distribution. The a_0 distribution for the simulations is drawn from the according on-axis spectra.

in case of smaller electron waist, the calculated and simulated energy spectra coincide, if one neglects the shift in E_γ . Especially in the case of a small electron waist compared to the laser, the shift in energy due to the higher experienced a_0 values is visualised. Furthermore, a small bandwidth arising from the small width of the a_0 distribution is observed. The dependence of the bandwidth on the electron waist via the experienced laser field values underlines the advantage of a small electron waist. While in Thomson sources, bandwidth reduction is typically linked to reducing the yield, the optimisation of the electron waist represents a means of improving the bandwidth while increasing the yield due to higher effective laser fields.

Analysis of the cone bandwidth

According to theory, when introducing an opening angle to the emission by a non-divergent

electron beam, the bandwidth arising from the cone angle is $\gamma^2\theta_c^2/(1 + \gamma^2\theta_c^2)$, leading to

$$\Delta E_\gamma/E_\gamma(\theta_c = 0.5 \text{ mrad}) = \sqrt{\left(\frac{\gamma^2\theta_c^2}{1 + \gamma^2\theta_c^2}\right)^2 + \left(\frac{\Delta E_\gamma}{E_\gamma}(\theta = 0)\right)^2}$$

This approach appears to be valid, as the contribution to the bandwidth obtained from the bandwidth of the laser, is symmetric. The time-bandwidth product yields a bandwidth of 0.23 nm for an 800 nm laser of 4 ps FWHM pulse duration. This bandwidth is sufficiently small to apply the formula, even though it was formulated for the interaction with a plane wave with zero bandwidth.

The angular spectra in figure [4.2.5](#) demonstrate that the angular contribution to the bandwidth is constant for all σ_r/σ_l . Consequently, when calculating the cone bandwidth from the simulated on-axis bandwidth according to the above-mentioned formula, one should arrive at the simulated cone bandwidth.

However, as the opening angle gives rise to lower energies in the spectrum, the angular broadening is not a symmetric contribution, as indicated in the theory. Furthermore, the peak energy of the spectrum decreases with the electron-laser waist relation (best seen in figure [4.2.4](#)). As the FWHM bandwidth is calculated with respect to this maximum energy, the same total width of the spectrum results in a smaller relative bandwidth for higher peak energy.

Again, consulting the line spectra for the analysis, we see that spectral broadening at low electron waist, broadening appears to be mainly below the FWHM. In case of $\sigma_r = 6 \mu\text{m}$ (second row), there is no bandwidth increase from the on-axis (right) to the 0.5 mrad cone spectrum (centre), also seen in figure [4.2.6](#).

4.2.5 Electron Bunch without Emittance or Energy Spread in a Linearly Chirped Laser

While the electron properties are identical to those in the previous chapter, a larger bandwidth $\Delta\lambda/\lambda$ is introduced to the laser parameters, and thereby a linear longitudinal chirp according to the duration of 4 ps. The remaining laser parameters (w_0 , τ , a_0) are kept as before.

Yield

The yield within a ± 0.5 mrad cone is not affected by the introduction of the laser bandwidth, as shown in figure [4.2.2](#). This is due to the linear character of the longitudinal chirp. In a symmetric head-on interaction geometry⁷, an electron propagates through the full longitudinal extent of the laser, so that the mean wavelength, and thus the mean a_0 is uninfluenced.

⁷Head-on collision of laser and electrons, where laser and electron focus have no spatial displacement.

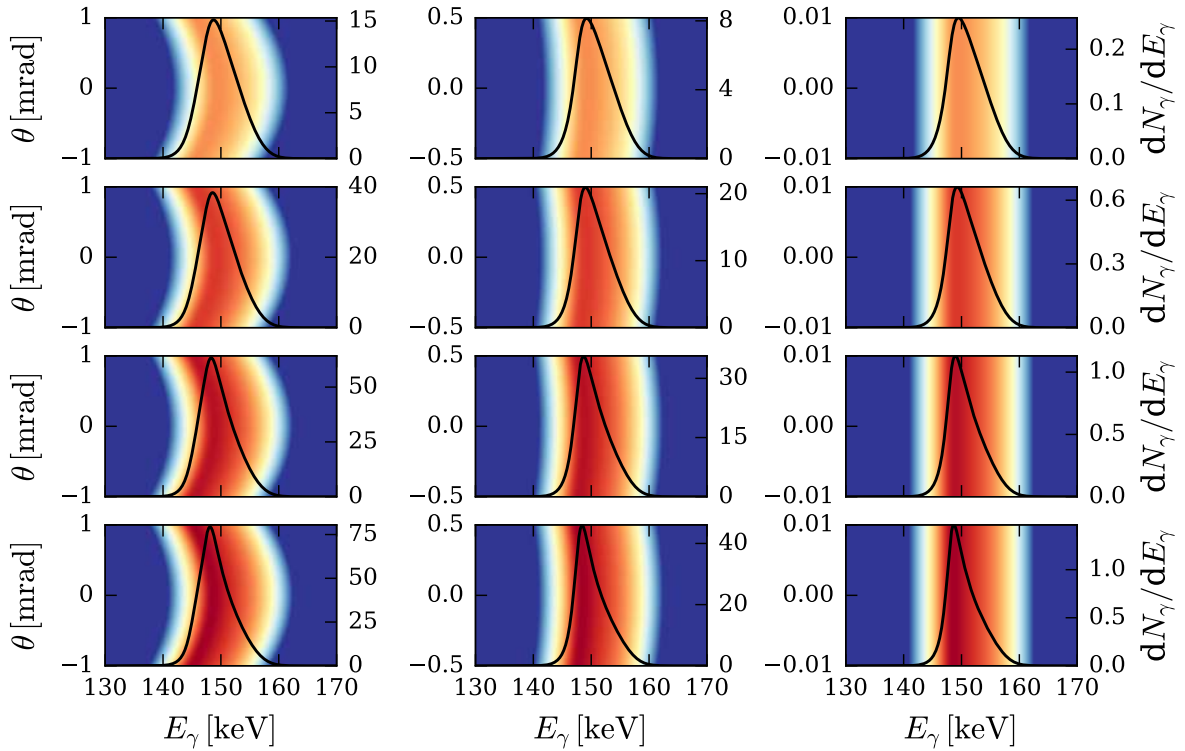


Figure 4.2.8: Line spectra for a non-divergent zero energy spread electron bunch in a linearly chirped Gaussian laser of $\Delta\lambda = 40$ nm, $\tau = 4$ ps and $w_0 = 12$ μm . The electron bunch waist is varied. From top to bottom: $\sigma_r = 12$ μm , 6 μm , 3 μm , 1 μm . Left column: Opening angle of 1 mrad, centre column: 0.5 mrad, right column: 0.01 mrad.

Bandwidth

According to theory, the relation between relative laser bandwidth and Thomson photon energy bandwidth is linear: $\Delta E_\gamma/E_\gamma = \Delta\lambda/\lambda$. For an FWHM bandwidth of $\Delta\lambda = 40$ nm and 60 nm⁸, the expected bandwidth contribution is therefore $\Delta E_\gamma/E_\gamma = 5\%$ and 7.5%, respectively. These are well above the previously obtained spectral bandwidth values dominated by a_0 and the opening angle. Again, the line spectra support the analysis process, shown in figure 4.2.8 for $\Delta\lambda = 40$ nm. The line spectra for $\Delta\lambda = 60$ nm are included in the appendix figure A.3.2. Obviously, the laser bandwidth has a dominant effect on the spectral shape. Neither a change in the opening angle nor in the electron bunch waist lead to a significant alteration. In direct comparison of the spectra, as displayed in figure 4.2.9, a slight reduction in bandwidth results from reducing the electron bunch waist. As expected, a small reduction in peak energy is observed, as before, for smaller electron bunch waist, as well as for increasing observation angle, as can be seen in figure 4.2.10. Moreover, the smallest spectrum is obtained for the smallest electron bunch waist.

Figure 4.2.11 displays the relative photon bandwidth within a ± 0.5 mrad cone for

⁸These values are based on the fourier-limited bandwidth expected from the driver laser ANGUS with $\tau = 25$ fs.

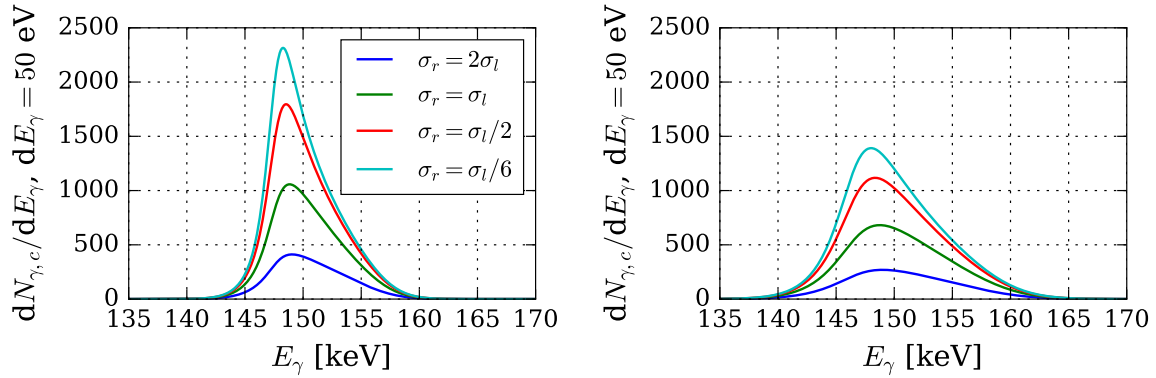


Figure 4.2.9: Total spectra within a cone of ± 0.5 mrad for $\Delta\lambda = 40$ nm (left) and 60 nm (right). Laser $\sigma_l = 6$ μm , $\tau_{\text{FWHM}} = 4$ ps. For decreasing electron radius σ_r , the photon yield increases while the peak energy of the spectrum decreases.

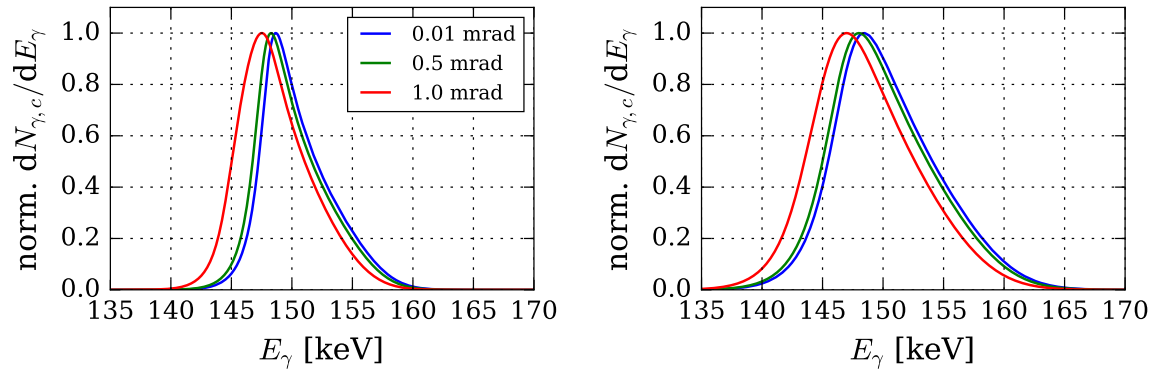


Figure 4.2.10: Normalised spectra for $\sigma_r = 1$ μm for different cone angles for $\Delta\lambda = 40$ nm (left) and $\Delta\lambda = 60$ nm (right). With increasing cone angle, the peak energy decreases, as well as the bandwidth.

the different laser bandwidths. The bandwidth lies well below the theoretical values and decreases with decreasing waist relation. Different to the previous scenario with no laser chirp and smaller laser bandwidth, the Thomson bandwidth rises also for electron waists larger than the laser waist. Before, the bandwidth decrease at large electron waist was owed to the shift of the peak energy to larger values and the reduction of the number of electrons and oscillations in fields exceeding $a_0 = 0.05$. Due to the larger laser bandwidth, this effect is not observed here.

4.2.6 Electron Bunch without Emittance, with Energy Spread

Yield

The radiation cone is determined by the synchrotron angle $\theta_{\text{synch}} = 1/\gamma$. Consequently, a different electron energy changes the size of the radiation cone, and thereby the number of photons emitted into the observation cone of opening angle $\theta_c < 1/\gamma$. The introduction of an energy spread to the electron bunch, however, is a symmetric distribution, so that

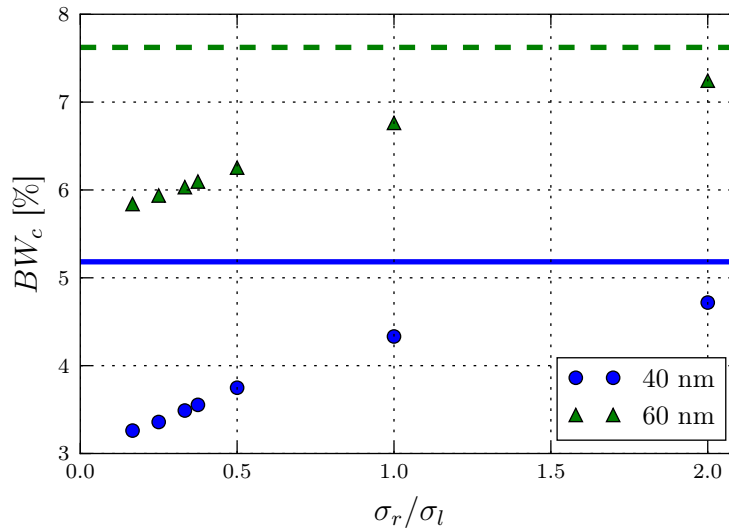


Figure 4.2.11: Cone bandwidth as a function of the electron laser waist ratio σ_r/σ_l for the interaction with a chirped laser. The simulation results for a laser bandwidth of $\Delta\lambda = 40$ nm (blue circles) and 60 nm (green triangles) are compared with the respective theoretical values (blue straight line, green dashed line).

the gain from smaller opening angles $1/(\gamma + \Delta\gamma)$ cancels out the loss due to larger opening angles $1/(\gamma - \Delta\gamma)$. The photon yield as a function of the electron waist coincides with the results for zero energy spread in figure [4.2.2](#).

Bandwidth

The effect of the electron energy spread on the Thomson bandwidth is straight forward, as well. Assuming no longitudinal or transversal bunch chirp, the interaction of electrons of different energies is distributed randomly. Consequently, the line spectra in figure [4.2.12](#) obtain a symmetric broadening, according to equation [\(4.1.19\)](#). For an energy spread of 1 % rms (2.35 % FWHM), this leads to a Gaussian bandwidth contribution of 4.7 % FWHM bandwidth, dominating the asymmetric effects described so far, and therefore, the total bandwidth. The Thomson bandwidth within a cone of 0.5 mrad is shown in figure [4.2.13](#) for an energy spread of 1 % rms, and 5 % rms. The electron bunch waist has no influence on the bandwidth.

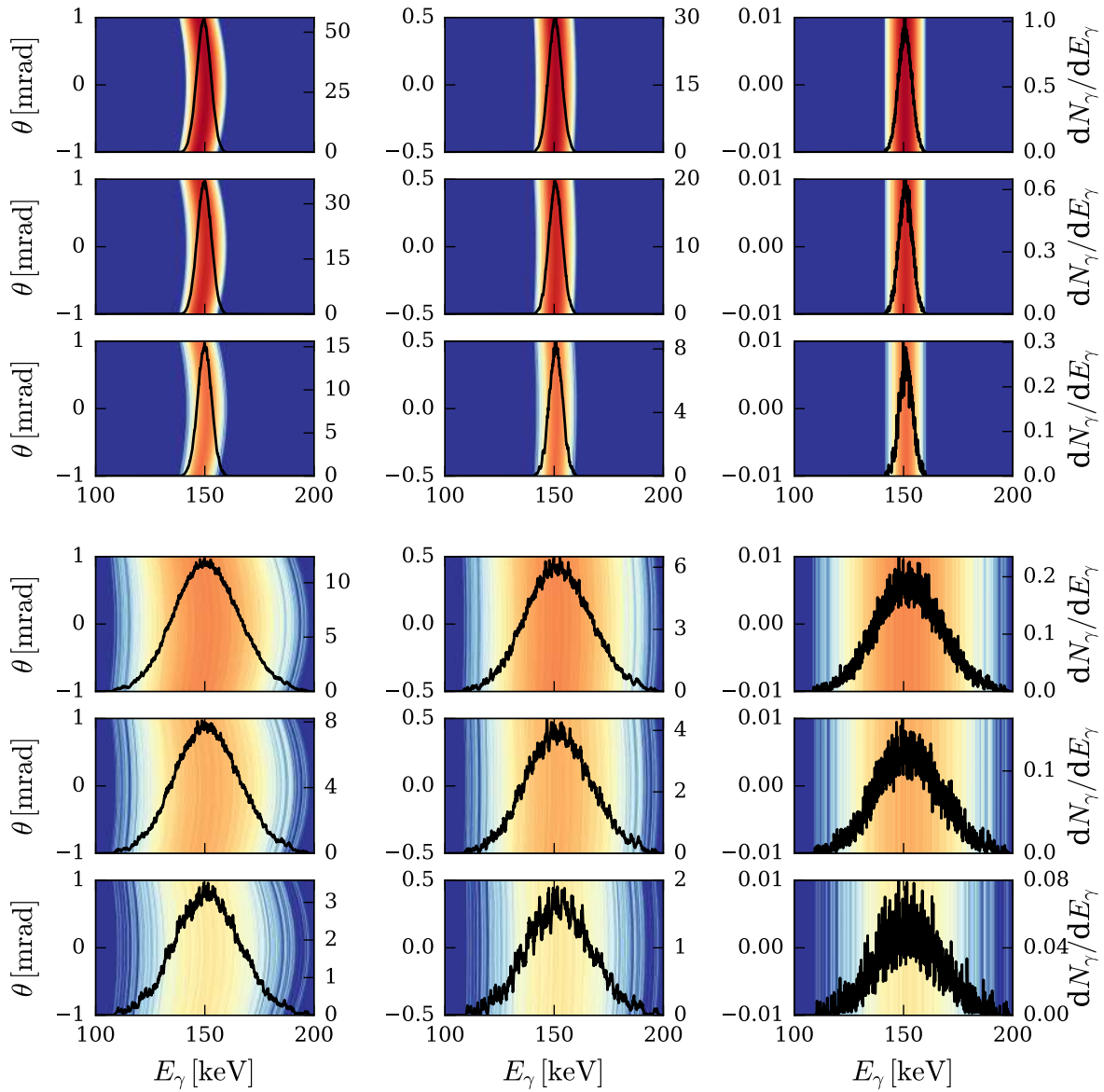


Figure 4.2.12: Line spectra for a non-divergent electron beam with 1 % rms energy spread (row 1-3) and 5 % rms energy spread (row 4-6) in an Gaussian laser beam of zero chirp. The electron bunch waist is varied: $\sigma_r = 12 \mu\text{m}$ (row 1, 4), $6 \mu\text{m}$ (row 2, 5), $3 \mu\text{m}$ (row 3, 6). Left column: Opening angle of 1 mrad, centre: 0.5 mrad, right: on axis. The laser waist and duration are constant at $w_0 = 12 \mu\text{m}$ and $\tau = 4 \text{ps}$.

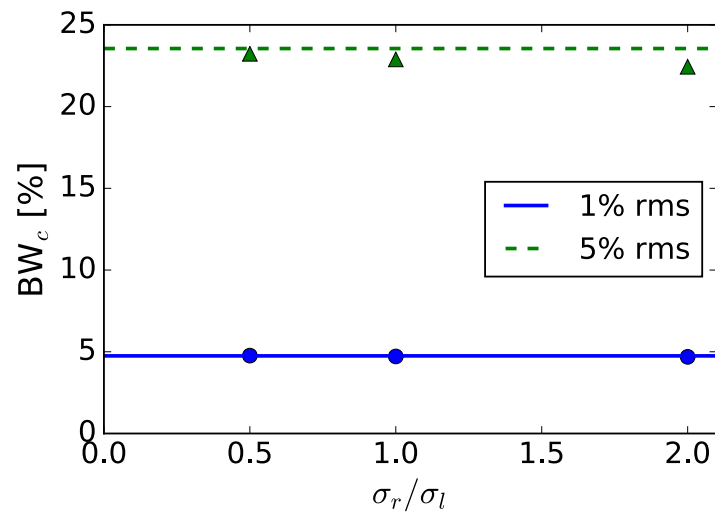


Figure 4.2.13: Bandwidth within a cone of 0.5 mrad as a function of the electron waist for an electron bunch of 1 % rms energy spread (blue) and 5 % rms energy spread (green) from simulation (markers) and theoretical calculation (lines).

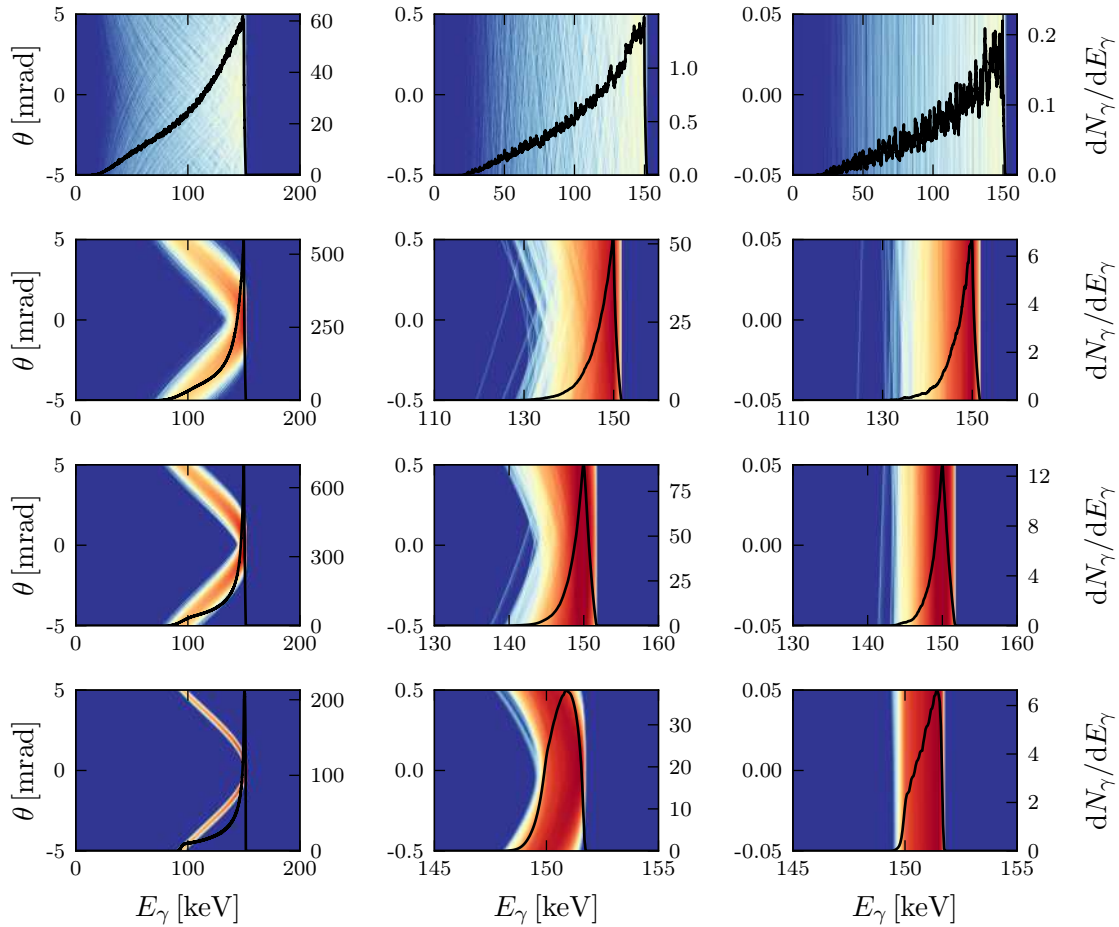


Figure 4.2.14: Line spectra for a divergent electron beam without energy spread in a Gaussian laser beam of zero chirp and vanishing bandwidth. Electron waist and divergence from top to bottom: $\sigma_r = 0.25, 1.75, 3, 12 \mu\text{m}$, accordingly $\sigma_\theta = 5.12, 0.73, 0.43, 0.11 \text{ mrad}$. The laser waist and duration are $w_0 = 12 \mu\text{m}$, and $\tau = 4 \text{ ps}$. Left column: Opening angle of 1 mrad, centre: 0.5 mrad, right: on axis. The energy bin size is $dE_\gamma = 50 \text{ eV}$.

4.2.7 Electron Bunch with Emittance, without Energy Spread

At constant bunch emittance, the divergence of the bunch is dependent on the bunch focal waist (Eq. (2.2.5)). The resulting line spectra are displayed in figure 4.2.14, for different electron bunch waist and according divergence. In order to recognise the effect of different propagation directions and hence radiation direction from these electrons, a larger opening angle is regarded. In a cone of 5 mrad (left), the typical curved shape of the angular energy function is observed for small divergence, i.e. large electron waist (bottom). With increasing divergence (decreasing waist), several of such curved functions with different central emission angle overlap and thus induce a smearing along the vertical axis. For divergences below the cone angle, the shape of the spectrum is hardly altered (left column, row 2-4). For larger divergence (top), the centre of the single-electron radiation contributions with larger angle to the propagation axis is no longer emitted into the angle of interest. The result from a single electron with an angle > 0 to the beam propagation

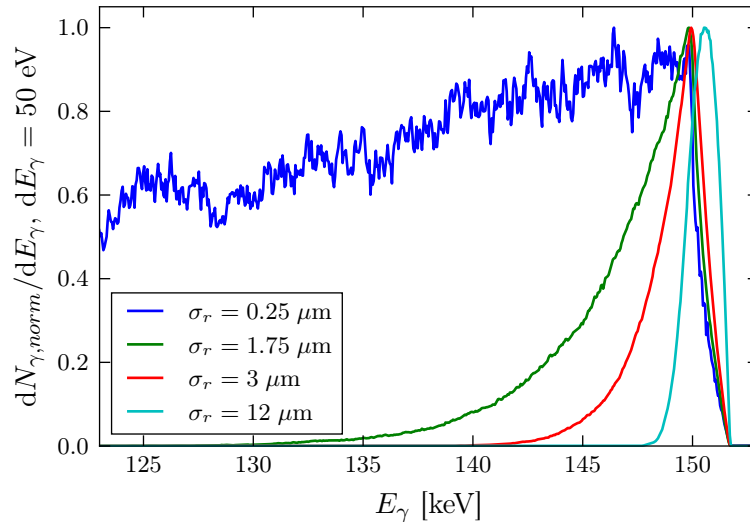


Figure 4.2.15: Normalized energy spectra within a 0.5 mrad cone for different electron bunch waists. For smallest waist (blue), the bunch inherits the largest divergence. With increasing bunch waist (decreasing divergence), the peak energy drift towards higher energies and the bandwidth decreases.

axis is equivalent to that of an on-axis electron where the observation cone is shifted in transverse direction⁹. The greater this shift, the smaller the intensity at high energies of the line spectrum, and the low-energy tail contributes increasingly. The consequence of a large electron divergence on the spectrum within a smaller cone becomes obvious when regarding the line spectra in the first row for 0.5 mrad (centre) and 0.05 mrad (right): The confinement of the angle no longer results in a decreased bandwidth. The normalised spectra within 0.5 mrad (Fig. 4.2.15) illustrate the bandwidth increase with decreasing waist, as well as a decrease in peak energy. This is attributed to the shift in the central emission angle.

Yield

The total and the 0.5 mrad cone yield as functions of the divergence are presented in figure 4.2.16. For very small waists, the divergence increase leads to a worse electron-laser overlap, thus reducing the total yield significantly. Therefore, in contrast to the above findings, the photon yield will drop again below a certain laser-bunch-waist relation. For larger waists and smaller divergences, the total yield only slightly drops. At ≈ 2.5 mrad, the maximum total yield is reached. This, however, is not the optimum divergence regarding the cone yield. Here, two effects are encountered: On the one hand, the changes in laser-electron overlap, influencing the total yield and the cone yield identically. On the other hand, the reduced cone size which is not, as in case of a non-divergent electron beam, determined by a constant factor according to equation (4.1.2). Due to the angular

⁹In the counter-propagating geometry, a small a change in the collision angle due to the electron divergence has a negligible effect on the emitted energy spectrum.

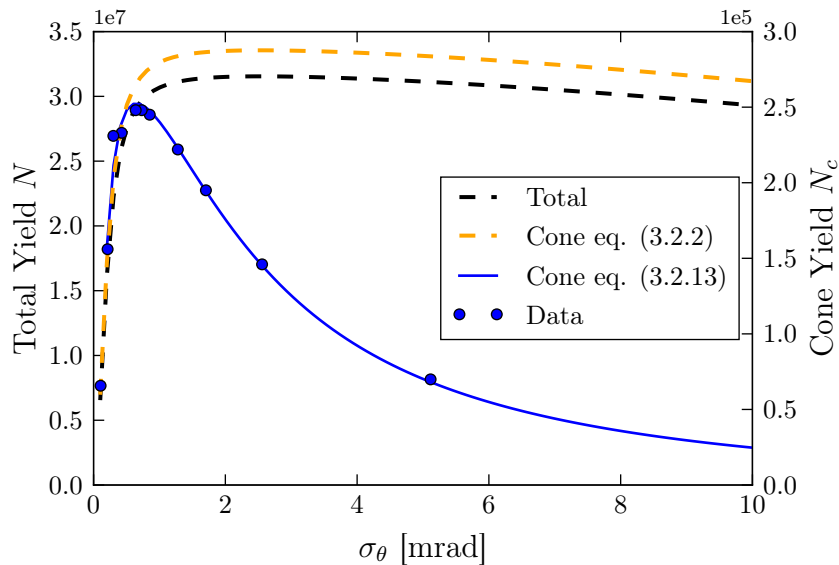


Figure 4.2.16: Total (black dashed line) and cone yield (yellow dashed line) as functions of the electron divergence. Eq. (4.1.2) describes the ideal case, hence neglects divergence effects and only accounts for the cone angle (green dashed line). It therefore scales as the total number of photons. Eq. (4.1.13) accounts for the divergence and cone angle (blue straight line) and coincides with the data markers).

smearing of the intensity-energy distribution the cone does not cut out symmetrically from the contribution of each electron. Thus, equation (4.1.13) has to be applied. The result of the numerical integration fits well with the simulation. For $\sigma_r = 2.1 \mu\text{m}$ and $\sigma_\theta = 0.6 \text{ mrad}$, the maximum yield within $\pm 0.5 \text{ mrad}$ cone is reached.

As the cone yield does not scale linearly with the total yield, maximisation techniques of the latter are not adequate in this case. This issue is approached in depth in the following section 4.3 and represents a major aspect of the investigation in this thesis.

Bandwidth

The energy bandwidth as a function of the divergence and waist of the electron bunch is displayed in figure 4.2.17 for the opening angles discussed: $\theta_c = 0.05 \text{ mrad}$, 0.5 mrad , and 5 mrad . The progression of the bandwidth with the electron waist strongly depends on the regarded cone size. For the on axis cone and the 0.5 mrad cone, the bandwidth decreases with increasing bunch waist. The functions saturate above $\sigma_r \approx 2 \mu\text{m}$, i.e. at divergences below 0.5 mrad , the bandwidth is not further decreased. The on-axis bandwidth value at $\sigma_\theta \approx 5 \text{ mrad}$ is not representative. Here, the divergence is so large that the simulation data on axis is too low to estimate the FWHM from the spectral distribution (see also Fig. 4.2.14, top right). Also, as mentioned before and illustrated by the identical course of the functions, the further reduction in opening angle has no effect on the spectral bandwidth. The bandwidth within the 5 mrad cone displays a reversed dependence: The bandwidth grows with increasing waist and decreasing divergence. As the opening angle is larger

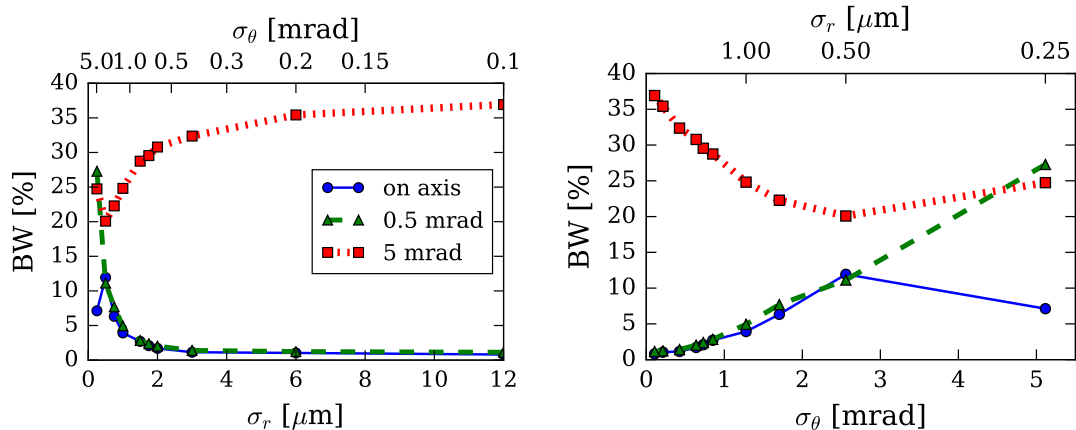


Figure 4.2.17: FWHM Thomson bandwidth as a function of the electron divergence σ_θ and waist σ_r for the on-axis cone (blue straight line), 0.5 mrad (green dashed line), and 5 mrad (red dotted line).

than the divergence, the cone hardly cuts the spectrum. Consequently, the influence of the divergence is negligible and the behaviour is explained by the overlap-dependent a_0 distribution, as discussed in the case of a non-divergent electron beam (cp. Fig. 4.2.6). At lowest waist, the divergence is of the order of the cone angle, and the bandwidth drops again.

Consequently, at opening angles exceeding the electron divergence, the bandwidth of the spectrum is determined by the waist. It defines the overlap of laser and electrons and therefore the a_0 distribution. The large divergence should lead to a broader a_0 distribution, as well, and thereby to an increase of the bandwidth. However, the maximum a_0 contribution is at $\approx a_0^2/2 = 1.22\%$, and thus dominated by the large opening angle contribution at $\theta_c = 5$ mrad and $\gamma = 156.4$. Therefore, the total bandwidth is of the order of 20 %, rendering the change in a_0 insignificant. For cone angles below or in the magnitude of the electron divergence, the bandwidth is dominated by the divergence-induced non-ideal overlap of the single-electron spectra. This explains the rise of the bandwidth in the 5 mrad case. Nevertheless, the bandwidth within a cone of 0.5 mrad is significantly smaller than within a 5 mrad cone, for small electron divergence. A further reduction of the opening angle would only lead to yield loss, without improving the bandwidth. At large divergence, $\sigma_r \geq 4.5$ mrad, the same holds for the reduction from a 5 mrad opening angle to the 0.5 mrad cone.

4.2.8 Geometrical Tolerance Study

For ideal overlap, electron and laser focus have to meet at the same point in space and time. Hence, a longitudinal mismatch can occur in one of three ways: Firstly, if the electron bunch has a spatial delay, but no temporal delay, i.e. they meet at the laser focus, but with either a divergent or convergent electron beam for negative or positive

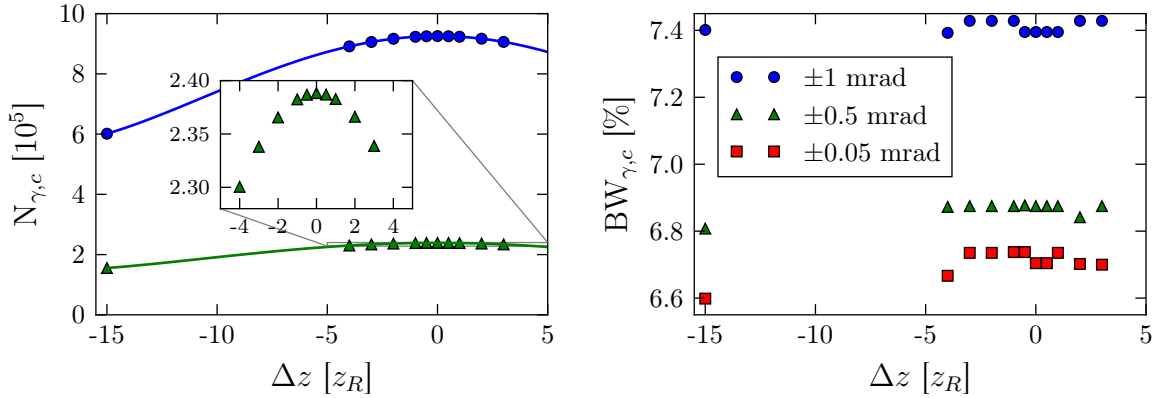


Figure 4.2.18: Yield (left) and bandwidth (right) as a function of the longitudinal spatial electron focus delay for different cone sizes of 1 mrad (blue circles), 0.5 mrad (green triangles), and 0.05 mrad (red squares). The yield functions display a parabolic behaviour (fitted lines).

delay, respectively. Secondly, laser and electron beam are displaced longitudinally in time and space, leading to a divergent (convergent) electron beam in a convergent (divergent) laser. Thirdly, they meet in the electron focus, with either a convergent or divergent laser. A transversal mismatch can occur due to pointing and positional electron jitter.

The simulated electron beam has an emittance of $\varepsilon_n = 0.2$ mm mrad and a focal waist of $\sigma_r = 2.1$ μm , according to the optimum found in the previous section for a laser of $\tau = 4$ ps and $w_0 = 12$ μm .

Spatial Delay

The timing is set in such a way that the interaction takes place in the laser focus, whereas the electron focus is shifted longitudinally in multiples of the laser's Rayleigh length. The according photon yield and bandwidth within cones of 1 mrad, 0.5 mrad and 0.05 mrad are displayed in figure 4.2.18. The inset on the left shows a decreasing effect on the photon yield with spatial delay, however, it is negligibly small. This is due to the fact that the electrons have a low emittance and their beam size hardly changes with distance from the focal point: For a spatial offset of $\Delta z = 3z_R$, the bunch size grows by 11 % to 2.3 μm , according to [46]

$$\sigma_r(z) = \sqrt{\left(\frac{\varepsilon_n z}{\gamma \sigma_0}\right)^2 + \sigma_0^2}.$$

Moreover, the divergence does not change¹⁰. Therefore, the effect is negligible for small longitudinal offset. The isolated beam size effect was discussed in chapter 4.2.4, and can be deduced from figure 4.2.2 for the photon yield. The bandwidth appears to be independent of the spatial delay, in first approximation. A small effect can be seen for the on-axis bandwidth (red) which decreases with spatial delay. The on-axis bandwidth

¹⁰Here, it is referred to the divergence given by the individual angle with respect to the propagation axis of each electron. The mean divergence of the bunch which would be zero in focus and grow with increasing longitudinal distance.

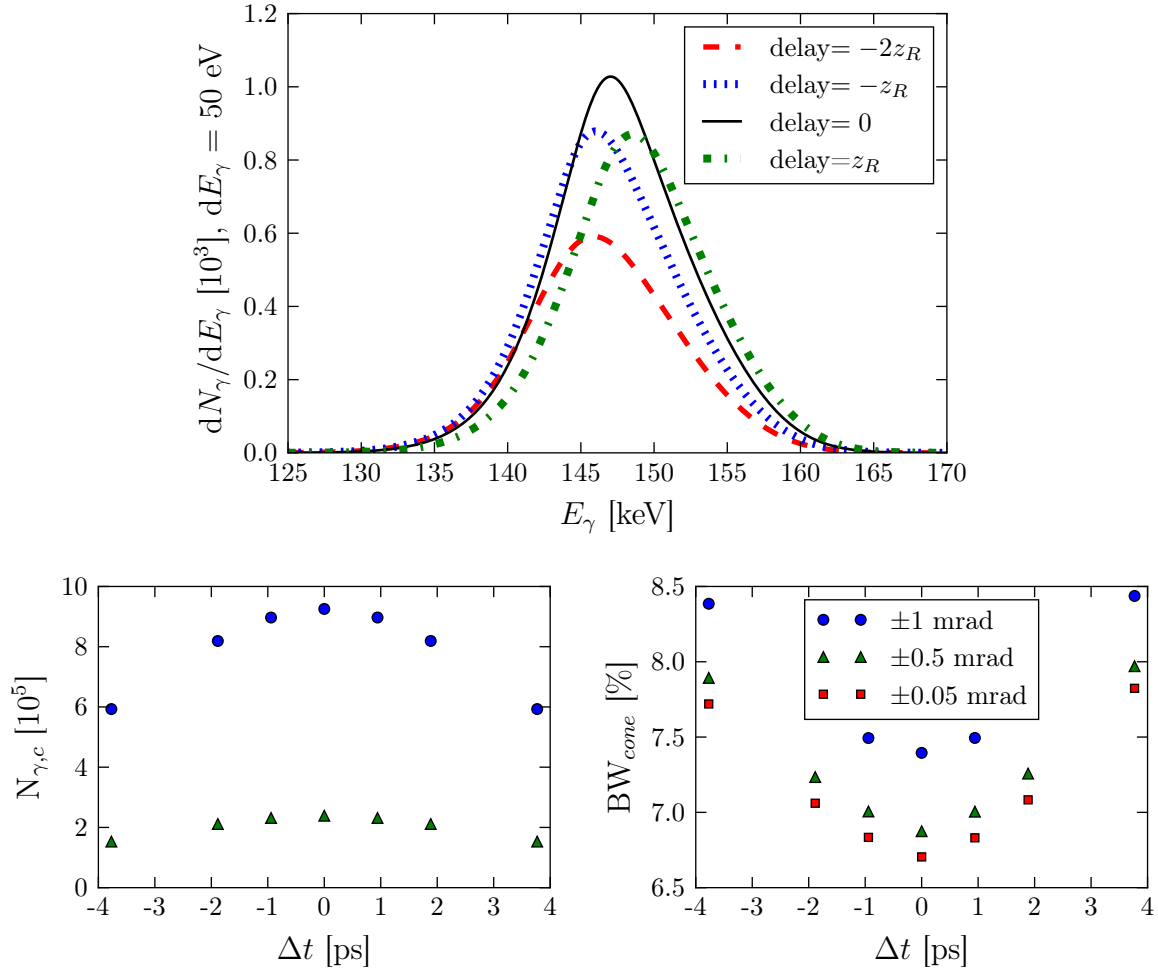


Figure 4.2.19: Top: 0.5 mrad cone spectra for different values of the delay. Bottom: Yield (left) and bandwidth (right) as a function of the delay for different cone sizes. The delay denotes the temporal delay between laser and electron focus. Zero delay refers to the case where laser and electron beam meet in their respective foci at maximum temporal laser intensity.

is dominated by electrons with zero divergence which travel on axis through the laser and thus experience less spectral broadening owed to the transversal change in a_0 .

Temporal Delay

If a temporal delay is imposed on the electron-laser interaction, neither electrons nor the laser are in their focus at the time of interaction. Furthermore, the laser pulse intensity is significantly decreased. Therefore, a large impact on the spectra, the photon yield, and the photon bandwidth is observed, as demonstrated in figure [4.2.19](#). The plot at the top displays the cone spectra for different temporal delays. The delay describes the starting point ($\Delta z_0 = c\Delta t$) and time of the electron bunch. A delay of $\Delta t = 0$ refers to the case where electron and laser starting points and time are set in such a way that they meet in their respective foci. For negative electron delay, the peak energy is shifted towards lower values, as the interaction with the chirped laser takes place at larger a_0 values and smaller

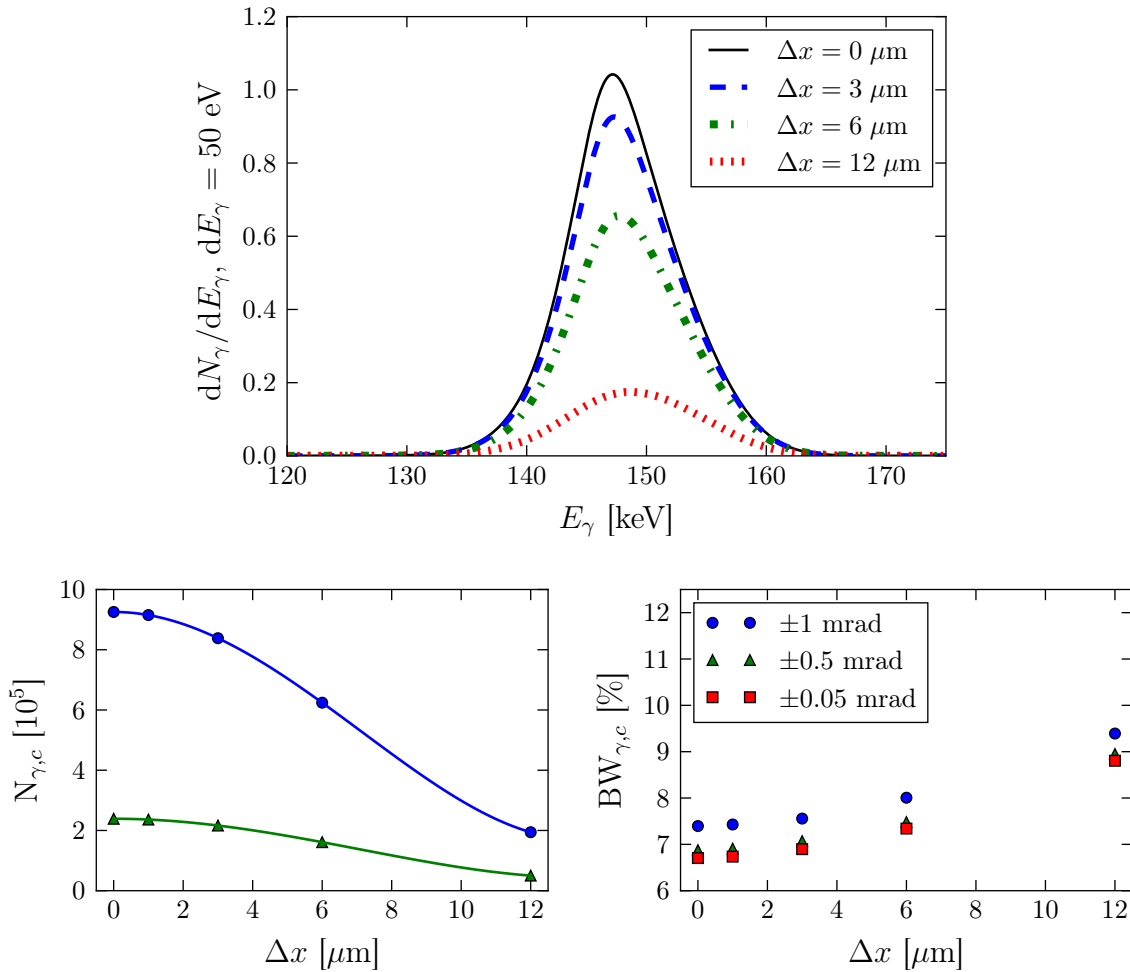


Figure 4.2.20: Top: Simulated cone spectra for different values of the transversal offset. Bottom: Simulated (markers) and interpolated (lines) cone yield (left) and bandwidth (right) as functions of the offset for different cone sizes. The interacting Thomson laser has a waist of $12 \mu\text{m}$.

λ_0 values of the laser wavelength. The symmetric behaviour in the opposite direction is obtained from a positive delay. The cone yield and bandwidth as functions of the delay (bottom left and right, respectively) demonstrate the worsening impact of the delay: With increasing delay, the yield decreases due to the decreased spatial and temporal overlap, and the bandwidth increases due to the increased Δa_0 .

Transversal Offset

A transversal offset of the respective electron and laser foci moves the bunch centre towards regions of lower laser fields. For a laser of sufficiently low a_0 , as regarded here, the ponderomotive force on the electrons is negligible¹¹. Therefore, the imposed initial offset stays constant with respect to the propagation axes, thus the counter-propagating geometry is maintained. The impact of the electron offset depends on the distance between

¹¹The angular deviation from the original propagation axis of the simulated bunch is $0.5 - 10 \mu\text{rad}$, i.e. $< 2\%$ of the half opening angle of the cone, at maximum.

detector and interaction centre, as well as on the transversal position of the pin hole with respect to the electron focus. For small distances (\sim cm) and a pin hole aligned with the laser focus, the central emission axis from an electron bunch with a transversal offset possesses a large angle > 0.5 mrad with respect to the laser axis at the pin hole position. Consequently, emission of highest intensity and energy is cut by the pin hole. In case of large distances of the pin hole from the interaction centre, or, if the pin hole is aligned with the electron propagation axis, the effect on the Thomson spectrum originate from the overlap. The resulting spectra are displayed in figure 4.2.20 (top), as well as the cone yield (left) and bandwidth (right) as functions of the transversal offset Δx . Interaction within lower fields resulting from this offset thus results in a slight increase in the peak photon energy (cp. Eq. (2.3.10)), as well as a loss in cone yield and a small bandwidth increase. The simulated Thomson laser has a waist of $12 \mu\text{m}$. Offsets of $\Delta x \leq w_0/4 = 3 \mu\text{m}$ result in a cone yield loss of $< 10 \%$ and a negligible cone bandwidth increase.

4.2.9 Collision Angle between Electron Bunch and Laser

Optimum overlap and highest emitted photon energy are obtained in a counter-propagation geometry of electron bunch and laser. The spectra obtained from a deviation in the collision angle $\Delta\alpha$, where $\Delta\alpha = 0$ refers to the counter-propagation, are displayed in figure 4.2.21 (top row) for a longitudinally chirped laser pulse (left) and a zero chirp Fourier-limited laser of equal strength and duration (right). The effect on the line spectra for collision angles deviating from the head-on geometry are shown in the appendix figure A.3.1. Figure 4.2.21 compares the photon yield (second row) and bandwidth (bottom row) as functions of the deviation in the collision angle $\Delta\alpha$ for a chirped laser (left) and a laser of zero chirp and vanishing bandwidth (right). Already at an angle of 5° the photon yield is reduced by over 50%. As observed before, the chirp has no impact on the cone yield (cp. figure 4.2.2). The bandwidth, on the other hand, reflects that with increasing collision angle, the spectra receive a lower spectral width, as the interaction length with respect to the laser duration decreases. Consequently, in case of a chirped laser, low- and high-wavelength parts are cut out of the interaction region, reducing the effective laser bandwidth and hence the bandwidth of the Thomson spectrum. Still, the bandwidth reduction does not compensate for the yield loss, as depicted in the inset in figure 4.2.21 (bottom left), where the ratio of the cone yield and the according bandwidth is plotted against the collision angle. For all cone angles, the head-on collision gives the best result. Even more so, the best result is obtained from the 1 mrad cone angle.

4.2.10 Electron Bunch with Emittance and Energy Spread

In order to combine emittance and energy spread, the means of propagation and/or focusing have to be determined. One possibility is to assume an electron beam starting in focus at the plasma exit. If beam transport and focusing is required, according beam

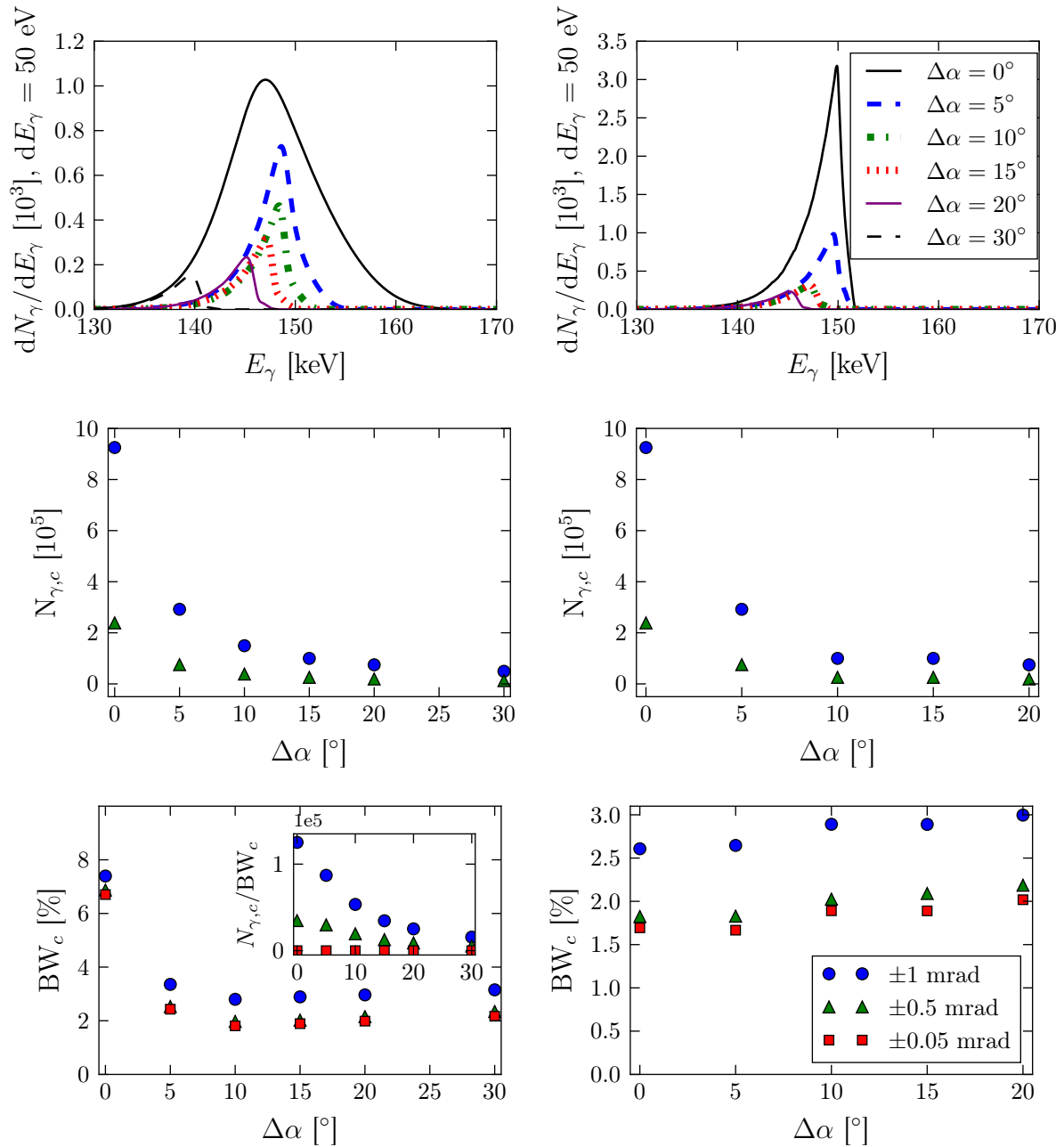


Figure 4.2.21: Energy spectra (top row), cone yield (central row) and bandwidth (bottom row) for different collision angles $\Delta\alpha$ with a chirped laser (left) and without chirp (right). $\Delta\alpha$ refers to the deviation from the counter-propagation ($\Delta\alpha = 0$). The inset displays the ratio of yield and bandwidth. The legend (bottom right) refers to all plots of the second and third row.

optics need to be applied. Typically, focal lengths of beam focusing optic are energy-dependent, as they operate on the basis of the Lorentz force on a charged particle e.g. in a magnetic field. This is the central aspect in the following chapter on electron focusing via a capillary discharge active plasma lens (Ch. 5). The effects of electron bunch energy spread and different focusing strength are discussed there, in detail.

4.2.11 Summary

The comparison of the parameter scans to the existing Thomson theory reveals that the numerically determined yield coincides with the cone yield from the simulations. However, two issues arise which are not covered by the theory: The electron bunch waist and divergence effects, as was anticipated, on the one hand. On the other hand, the impact of the effective a_0 as seen by the electrons, in case of non-ideal effects, such as a laser of longitudinally and transversally varying field strength, is not treated by the theory.

The parameter scans were conducted on the basis of a single set of laser parameters (a_0 , τ , w_0), according to theoretical optimisation. For all scenarios, the influence of the electron beam waist on the photon yield and bandwidth was investigated. With the exception of the tolerance and collision-angle studies, a counter-propagating geometry with no longitudinal and transverse delay between electrons and laser was simulated.

If the electron bunch waist is small compared to that of the laser, the electrons are assembled in the highest fields. The resulting high a_0 and low Δa_0 lead to an increased photon yield and a reduced bandwidth. For an electron bunch with non-zero emittance, a low waist is accompanied by a large divergence. Hence, the longitudinal development of the transversal overlap worsens with decreasing bunch waist. Simulations and theory show that an optimum electron divergence and waist can be determined in terms of yield maximisation. The photon yield is independent of a laser chirp and an electron energy spread. A significant yield reduction is obtained from large electron divergences in comparison to the cone angle, from large electron waists in comparison the laser waist, as well as from a temporal delay and transversal offset between laser and electrons. A deviation from the head-on geometry by 5° has shown to reduce the yield to 50 %.

The effect on the Thomson bandwidth depends on several other parameters. If an electron bunch energy spread is introduced, the bandwidth is dominated by this contribution and the electron waist has no significant influence. The regarded cone angle has an impact on the bandwidth as a function of electron waist and divergence. For cone angles exceeding the bunch divergence, only low-intensity parts of the spectrum are cut, thus hardly altering the spectrum. The bandwidth is dominated by Δa_0 , so that it rises with increasing electron waist. If the cone angle is of the order of or below the bunch divergence, it represents the dominant effect on the bandwidth. With increasing divergence, the bandwidth rises due to the overlap of the single-electron spectra. In this case, a low divergence is favourable over a low bunch waist.

Electron waist (and divergence) optimisation leads to an increased Thomson yield. Consequently, their optimisation is a central aspect in the following chapters. As the bandwidth is determined by several effects and as it can often not be theoretically determined, trajectory-based simulation proves to be an important tool in Thomson bandwidth determination and thus in Thomson source design.

4.3 Yield and Bandwidth Optimisation

The general electron parameter scans were conducted on the basis of a single laser parameter set, chosen according to theory (cp. Ch. 4.2.2). A first estimate on the role of bunch waist and divergence has been made for the chosen laser scenario. The electron waist and divergence were found to have an impact on the photon yield, especially in the special case of a confined opening angle. The theoretical optimisation of the laser (cp. Ch. 4.1.3) neglects the bunch parameters. Therefore, this chapter aims at providing an understanding of the impact of the electron-laser waist relation and the bunch divergence on the photon yield and bandwidth for different laser configurations.

Firstly, a detailed analysis of the electron bunch waist and divergence on the total yield and the yield within a cone is conducted for different laser parameter sets and an increased electron emittance. The theoretical yield results are obtained from equations (4.1.3)ff for the total yield and the numerical calculations via equation (4.1.13) for the yield within a confined cone. The cone bandwidth obtained from the simulations is presented and a quality criterion is used to quantify the results.

In the following, the cone refers to the opening angle of ± 0.5 mrad, unless stated differently.

4.3.1 Yield Dependence of Electron Divergence and Diameter Ratio for Different Laser and Bunch Configurations

There is no global optimal electron divergence or ratio of the electron-bunch and laser diameter, as these two represent rivalling effects. This is true for the total yield, but even more crucial to the case of a confined observation angle. In the previous chapter, it was shown that a smaller bunch diameter raises the effective laser field, thus inducing an increased emittance of photons. When the electron divergence is of the order of the opening angle of the cone, more photons are radiated into angles outside the observation angle. If the observation angle is not confined, the constraint on the divergence is less significant and a small electron waist is favourable. Within an angle of ± 0.5 mrad, the yield maximum is reached at $\sigma_\theta \approx 0.6$ mrad, i.e. $\sigma_r = 2 \mu\text{m} = 0.175w_0$ in the case of a laser of $w_0 = 12 \mu\text{m}$ and $\tau = 4$ ps (cp. Fig. 4.2.16).

As a different laser waist favours a different electron waist which then changes the divergence according to its emittance, the yield-dependence of the waist relation and

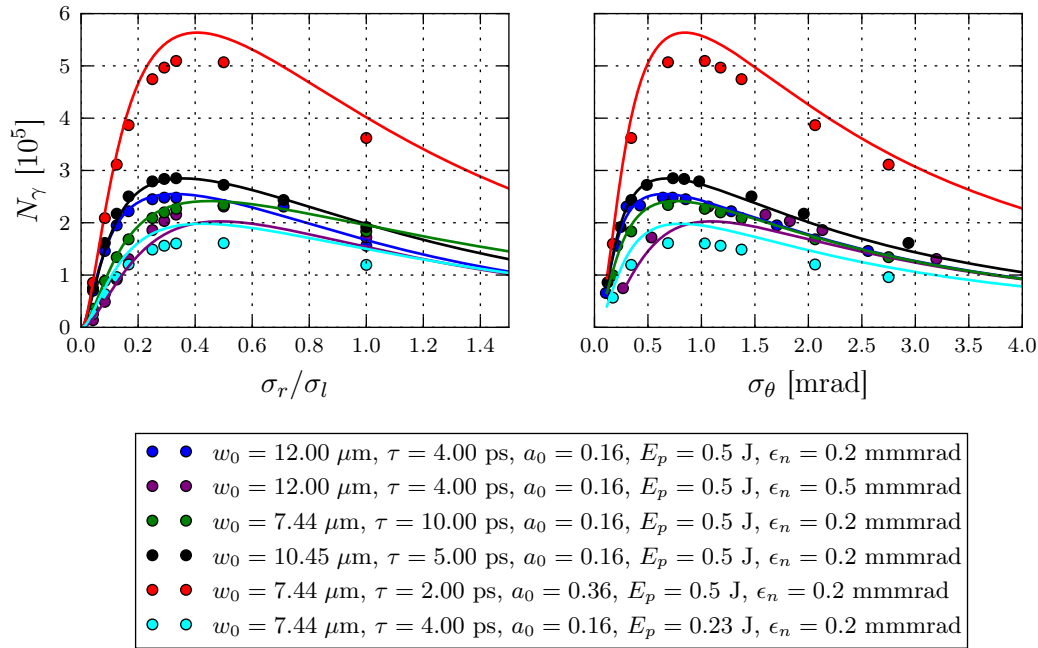


Figure 4.3.1: Simulated (markers) and theoretical (lines) cone yield as function of the laser-electron waist relation (left) and of the electron divergence (right) for different parameter sets (legend). The maximum yield values, as well as the electron waist and divergence values are listed in table [4.3.1](#).

electron divergence is simulated and calculated for different scenarios: On the one hand, the laser parameters are varied, and on the other hand, a higher electron emittance is investigated, as well.

In figure [4.3.1](#), the results of the cone yield for six different scenarios (legend) are plotted as functions of the waist relation (left) and the divergence (right). The basis for the parameter variation is the previously investigated scenario of $w_0 = 12 \mu\text{m}$, $\tau = 4 \text{ ps}$ and $a_0 = 0.16$, displayed in blue, which is the theoretically determined optimum laser configuration, in accordance with equation [\(4.1.10\)](#). The parameters at the respective photon yield maxima are listed in table [4.3.1](#). At first sight, it becomes apparent, that each scenario requires different electron parameters to reach the best photon yield. Neither for the electron waist or divergence, nor for the waist relation of electron and laser, the

colour	N_{max}	σ_r	σ_r/w_0	σ_θ
blue	2.55	1.97	0.164	0.649
purple	2.03	2.93	0.244	1.091
green	2.42	1.68	0.226	0.760
black	2.85	1.87	0.179	0.682
red	5.64	1.51	0.203	0.845
cyan	1.98	1.59	0.213	0.806

Table 4.3.1: Maximum yield values and respective values for the electron waist σ_r , the waist relation σ_r/w_0 , and the electron divergence σ_θ , as calculated for the scenarios plotted in figure [4.3.1](#) (straight lines).

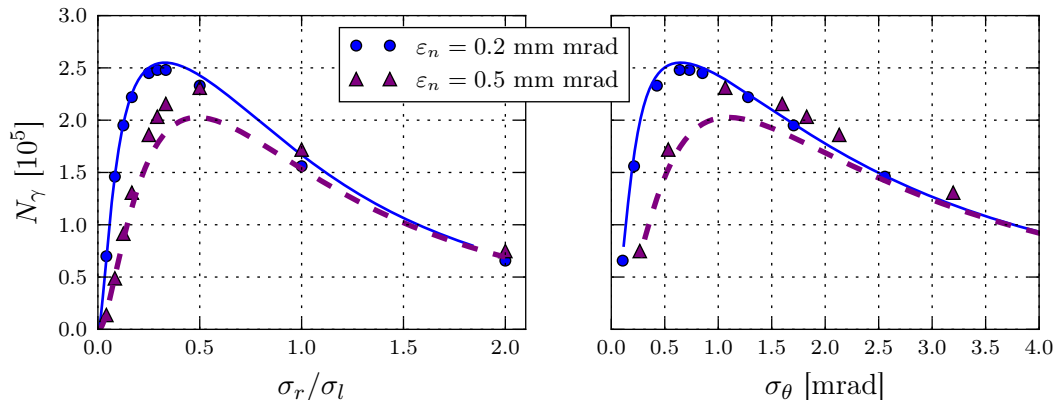


Figure 4.3.2: Simulated (markers) and theoretical (lines) cone yield as a function of the waist relation σ_r/σ_l (left) and electron divergence (right) for $\varepsilon_n = 0.2$ mm mrad (blue) and $\varepsilon_n = 0.5$ mm mrad (purple).

optimum values coincide. However, the deviations are small for all scenarios with a laser strength parameter of $a_0 = 0.16$, as long as the electron waist is $\approx 0.2w_0$ and the divergence is approximately of the magnitude of the cone size of 0.5 mrad. A significantly higher yield ($>$ factor 2) is obtained from an increased laser strength of $a_0 = 0.36$.

In the following, the single scenarios are evaluated and compared.

Electron Emittance

The comparison of the scenario of an electron bunch with $\varepsilon_n = 0.2$ mm mrad with that of identical laser parameters, but normalised emittance $\varepsilon_n = 0.5$ mm mrad visualises the consequence of the emittance increase. The respective yield as function of the waist relation and electron divergence is shown in figure [4.3.2](#). A larger emittance leads to a larger, hence worsened electron waist-divergence ratio. The optimum waist relation and divergence are both shifted towards higher values in the high-emittance case, where the optimum electron waist is $\sigma_r \approx 0.24w_0 = 2.9 \mu\text{m}$ and the according divergence $\sigma_\theta \approx 1.1$ mrad. Consequently, there is no global upper limit for the divergence, but photon loss due to higher divergence is moderated by the gain from the increased effective a_0 for smaller bunch waists. The maximum cone yield is reduced with respect to the low-emittance case by 20 %.

Constant Laser Strength Parameter a_0

The same laser strength parameter a_0 can be obtained from different laser waist and duration combinations. Figure [4.3.3](#) displays the resulting a_0 for different laser waist w_0 and duration τ of a laser with $E_p = 0.5$ J pulse energy. The optimum duration and according a_0 for a given laser waist are included as grey and red lines, respectively.

The green curve in figure [4.3.4](#) displays the result of a more strongly focused laser with $w_0 = 7.44 \mu\text{m}$ at longer laser duration $\tau = 10$ ps. From the theoretical description

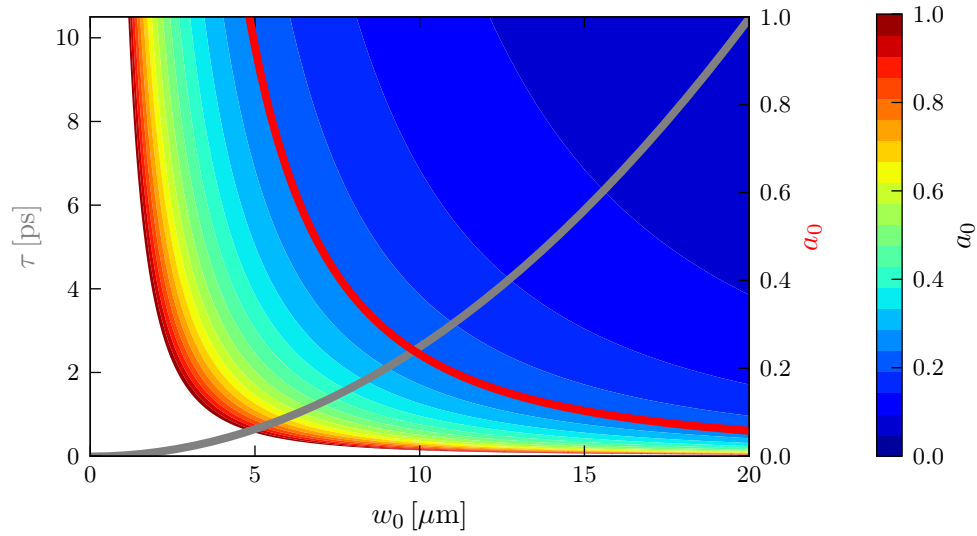


Figure 4.3.3: Laser strength parameter a_0 for different waist w_0 and duration τ configurations of a laser with pulse energy $E_p = 0.5$ J (colour plot), as obtained from equation (2.1.6). Laser FWHM duration τ (grey line) and strength parameter a_0 (red line) as functions of the laser waist w_0 for optimum laser waist-duration relation, according to equation (4.1.8).

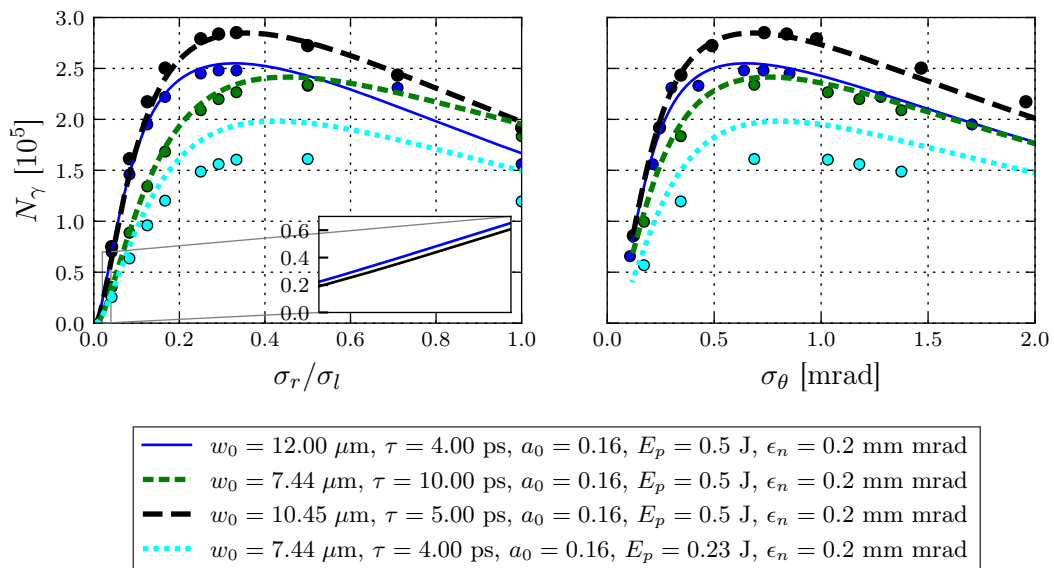


Figure 4.3.4: Simulated (markers) and theoretical (lines) cone yield as a function of the waist relation σ_r/σ_l (left) and electron divergence (right) for different laser parameter sets of equal $a_0 = 0.16$.

(Eq. (4.1.8)ff.), it is apparent that with the Rayleigh length $z_R = 0.217$ mm and pulse length $\tau \cdot c = 3$ mm, the interaction length is much larger than the Rayleigh range (cp. Eq. (4.1.10)). Nevertheless, this deviation from the theoretical ideal does not result in a significant yield reduction. Due to the long laser duration, the increased number of oscillations ($N_0 \approx 10 \text{ ps} \cdot c / \lambda = 3750$) mitigates the loss in the mean laser strength, experienced by the electrons. However, the smaller laser waist demands a stronger electron focusing at the cost of an increased divergence: The maximum yield is found at $\sigma_r \approx 0.23w_0 = 1.7 \text{ } \mu\text{m}$ and $\sigma_\theta \approx 0.8$ mrad. The laser-electron waist relation is increased with respect to the blue scenario, translating to a lower transversal effective a_0 .

Another theoretically non-ideal laser configuration with $w_0 = 10.45 \text{ } \mu\text{m}$ and $\tau = 5$ ps demonstrates a larger maximum yield than obtained by the theoretically optimised configuration. This example underlines the advantage of electron-waist and divergence optimisation. The comparison of the two curves shows that the optimum laser configuration depends on the electron waist. For $\sigma_r = \sigma_{r,\text{opt}}$, the black scenario in figure 4.3.4 leads to a higher yield. For electron waists much smaller than the laser waist¹², the theoretically optimal laser configuration yields a negligibly larger photon number within the cone, as displayed in the inset. For large electron waists ($> 10 \text{ } \mu\text{m}$), the curves coincide. This can be understood when regarding the simplified case, a non-divergent electron beam, and performing the effective a_0 analysis, equivalent to figure 4.2.3 in section 4.2.4: The mean transversal overlap gives the effective a_0 , as seen by the electrons. As the yield is proportional to $a_{0,\text{eff}}^2 N_0$, this magnitude is plotted against the electron waist in figure 4.3.5. Obviously, one has to bear in mind that without electron divergence, the divergence-related yield loss within the cone is not taken into account. Nevertheless, the respective compensation of $a_{0,\text{eff}}$ and N_0 becomes apparent, as well as the convergence of the yield curves for large electron waists, where the mentioned divergence effects are negligible.

Another possibility of achieving the same laser strength parameter, is to adjust the laser pulse energy to $E_p = 0.23$ J and laser waist $w_0 = 7.44 \text{ } \mu\text{m}$ while keeping the duration $\tau = 4$ ps as in the initial scenario¹³. The low- E_p curve lies (cyan) below the $E_p = 0.5$ J curve for equal divergence or electron waist (Fig. 4.3.4). This scenario underlines, as well, that not the maximum a_0 is the relevant parameter, but the effective a_0 which is reduced, as in the above-mentioned scenario with equal waist (black), but not mitigated by a longer laser duration.

Different Laser Strength Parameter at Constant w_0

An obvious gain in photon yield represents the increment in the laser strength parameter, achieved by decreasing the waist to $w_0 = 7.44 \text{ } \mu\text{m}$ and the duration to $\tau = 2$ ps as

¹²As mentioned before, an electron waist much smaller, i.e. negligible, with respect to the laser waist is assumed in the optimisation process [12].

¹³This is only discussed for the purpose of thoroughness. All other parameter scans assume a pulse energy of 0.5 J, as given in chapter 4.2.1

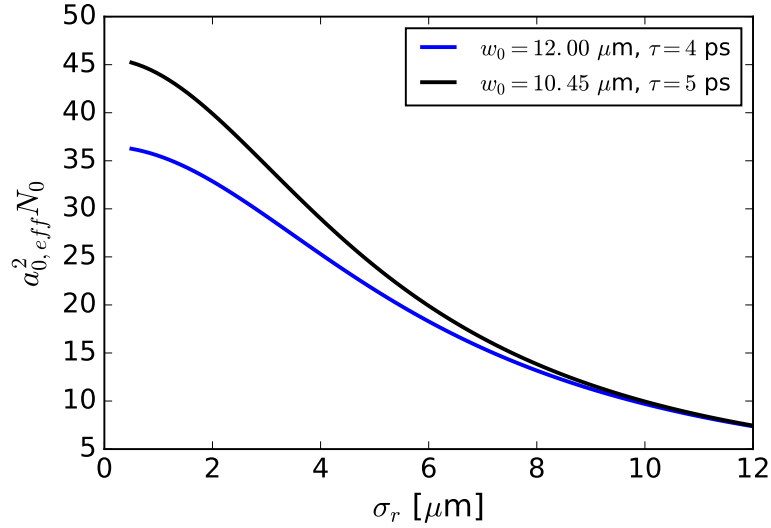


Figure 4.3.5: $a_{0,\text{eff}}^2 N_0$ as a function of the electron waist σ_r . The effective laser strength is obtained from transversal mean overlap calculations (cp. Sec. [4.2.4](#)), the number of oscillations is obtained from the laser duration as $N_0 = c\tau/\lambda$.

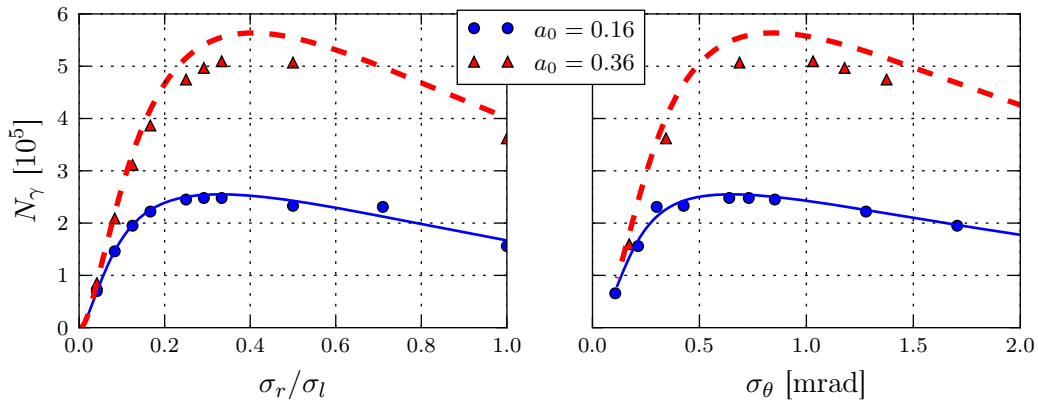


Figure 4.3.6: Cone yield N_γ as a function of the waist relation σ_r/σ_l (left) and electron divergence (right) for different laser parameter sets of different $a_0 = 0.16$ (blue) and $a_0 = 0.36$ (red). Simulation (markers) and Calculation (lines).

displayed in figure [4.3.6](#). The maximum yield is a factor 2.2 larger, yielding $N_\gamma = 5.64 \times 10^5$ which approximately coincides with the relation $a_{0,r}^2 N_{0,r}/a_{0,b}^2 N_{0,b} = 2.53$ at $\sigma_r = \sigma_{r,\text{max}}$. Interestingly, the maximum yield is reached for smallest electron waist, and therefore highest divergence, with respect to the other scenarios of equal electron emittance. As the high a_0 is obtained from shortening the pulse, the longitudinal overlap does not have to be maintained for a long range which would require a lower divergence. This example shows that not only the cone, but also the longitudinal overlap determines the optimum divergence.

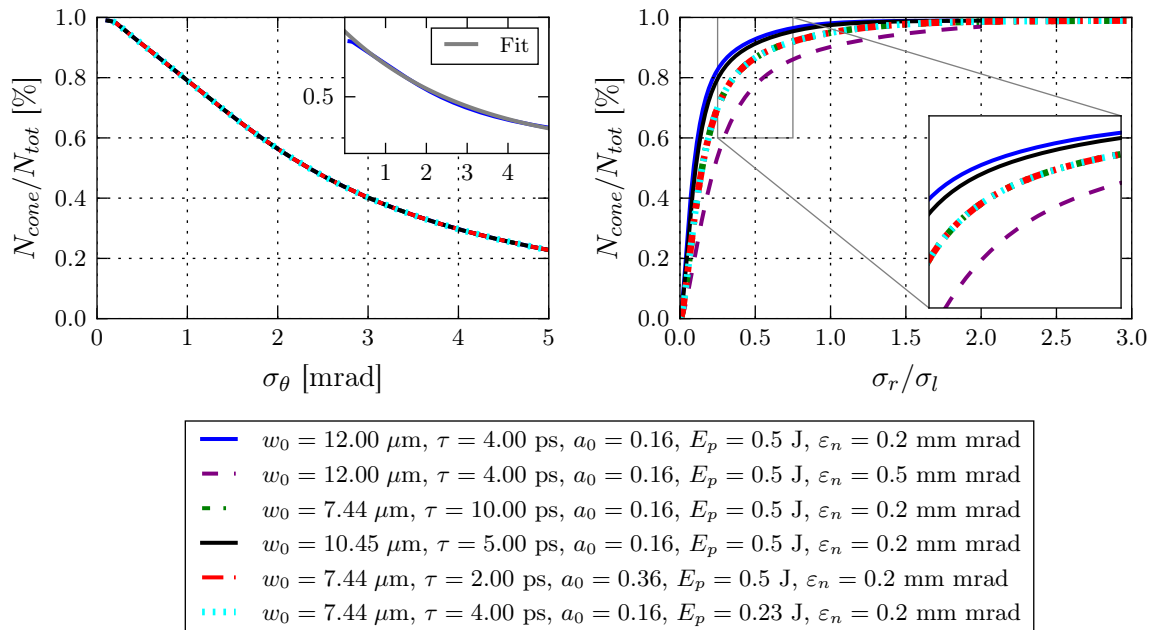


Figure 4.3.7: Relative photon yield $N_{\text{cone}}/N_{\text{tot}}$ within a cone of ± 0.5 mrad as a function of the electron divergence σ_θ (left) and of the electron-laser waist ratio σ_r/σ_l (right). The lines display the numerical results for the different scenarios (legend).

4.3.2 Analysis of the Waist Relation and Divergence Effect on the Total and Cone Yield

In order to understand the different optimal divergence and diameter values, the resulting effects are to be evaluated separately. They can be divided into the *overlap effect* on the one hand, obviously independent of the opening angle and thus identical for total and cone yield. On the other hand, the *cone effect* which is responsible for cutting photons emitted into angles exceeding the cone. In this section, only calculations are applied for the yield analysis, as they have shown to qualitatively coincide with the simulation results in the previous sections.

Cone Effect

In the non-divergent electron bunch case, the impact of the cone effect is trivial. Due to the symmetry, the cone yield is given by the factor $\sigma(\kappa)$ from equation (4.1.2). For a divergent electron beam, however, the cutting is no longer symmetric with respect to the individual propagation axes, owed to the fact that they are not identical. For an electron at large angle with respect to the mean electron-propagation axis, not only the low-energy and low-intensity tail are cut. On the contrary, for too large divergence, the maximum intensity and energy part might be cut, while the low-energy tail remains within the observation angle. This is equivalent to cutting the single-electron spectra via an off-axis observation cone. As figure 4.3.7 illustrates, the cone effect in the divergent-

electron bunch case is solely dependent on the bunch divergence. Here, the relative yield within the cone ($N_{\text{cone}}/N_{\text{tot}}$) is plotted against the divergence (left) and the diameter ratio (right). For zero divergence, the percentage of photons within the cone approaches the value given by $\sigma(\kappa)$ in equation (4.1.2). Note, that even in this case, only 1 % of the total yield is emitted into the cone. As expected, a small divergence is favourable. An identical divergence effect on the cone yield for all scenarios translates into different yield behaviour as function of the waist relation. Consequently, the relative photon yield is largest for the scenario of largest laser waist and lowest electron emittance (blue), and decreases with decreasing laser waist. The high emittance (purple) leads to the worst relative yield.

To summarise, the cone effect favours a large beam and a low divergence. For $0.5 \text{ mrad} \leq \sigma_\theta < 5 \text{ mrad}$, the empirical fit function (inset figure 4.3.7)

$$\frac{N_{\text{cone}}}{N_{\text{tot}}} = 0.01 \cdot 0.73^{\sigma_\theta [\text{mrad}]} \quad (4.3.1)$$

gives the relative cone yield.

Overlap Effect

Apart from the cone effect, the transversal and longitudinal overlap has to be investigated. Isolating the overlap effect from the cone effect is done by regarding the total yield as function of the waist relation and divergence. This is shown in figure 4.3.8. The bottom row displays the normalised total yield within the regions of highest yields for σ_r/σ_l (left) and σ_θ (right). The optimum waist relation lies between 0.04 and 0.07, the divergence between 2 and 4 mrad for all scenarios, the latter exceeding the cone opening angle. For the total yield, the optimum overlap has to be found. In case of a divergent electron beam, this translates into finding the lowest mean waist relation throughout the interaction. Consequently, for smaller laser waists, the electron waist needs to be decreased as well, to improve the transversal overlap in the focus. On the other hand, the longer the laser pulse, the lower is the required divergence of the bunch. Comparing the results for two laser configurations of equal size, but different durations of 10 ps (green), 4 ps (cyan) and 2 ps (red) reveals a dependence of the waist relation and divergence on the duration: With increasing duration, the divergence has to be reduced to maintain the overlap. This comes at the cost of the electron waist. For equal duration of 4 ps and different laser waists 12 μm (blue) and 7.44 μm (cyan), a smaller laser focus requires a smaller electron bunch. However, the optimum waist relation as found in the case of larger laser waist, cannot be maintained, as the divergence increase has to be controlled. Consequently, both, the divergence, as well as the waist relation are increased, hence a worse longitudinal and transversal overlap is obtained, resulting in a reduced total yield.

The optimum relation between laser and electron beam focal waist for the total yield

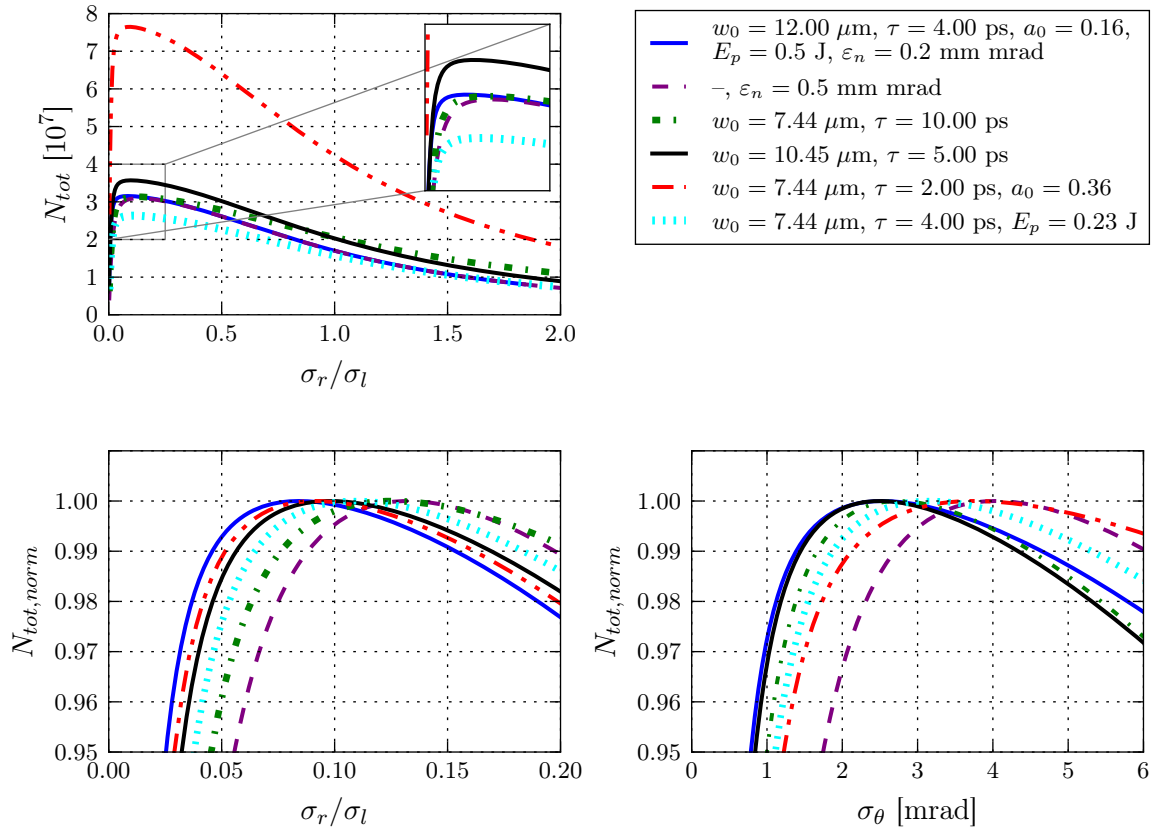


Figure 4.3.8: Calculated overlap effect on the total yield for a divergent electron beam. Total yield as a function of the waist relation σ_r/σ_l (top). The bottom row shows normalised total yield as functions of the waist relation (left) and the electron divergence (right).

may also be obtained from equations (4.1.3)-(4.1.5)¹⁴. Inserting the derived optimum relation for laser duration $c \cdot \sigma_{\text{long},l}$ and waist σ_l into equation (4.1.6) yields

$$\sigma_{\text{long}} = \sqrt{\sigma_{\text{long},e}^2 + \sigma_{\text{long},l}^2} \approx \sigma_{\text{long},l} = \frac{8\pi\sigma_l^2}{\lambda} \quad (4.3.2)$$

In rewriting equation (4.1.3) as $N_\gamma = \sigma_T N_e N_p F(x) \xi$ with

$$\xi := \frac{1}{\sqrt{2\pi}\sigma_{\text{long}}} \frac{1}{\sqrt{\sigma_r^2 + \sigma_l^2}} \frac{1}{\sqrt{\frac{\sigma_r^2}{\beta_e^2} + \frac{\sigma_l^2}{\beta_p^2}}} \quad (4.3.3)$$

the two terms $F(x)$ and ξ can be evaluated individually with regard to the optimum electron-laser waist relation. In order to investigate the influence of this relation, a parameter a is introduced, so that $\sigma_r := a \cdot \sigma_l$ with $a \in \mathbf{R}$.

The function $F(x)$ (eq. (4.1.5)) is maximal for minimal x . Expressed as a function of the

¹⁴So far, the laser parameters have been denoted with l , and the electrons with e , so the equations are adapted to match this notation.

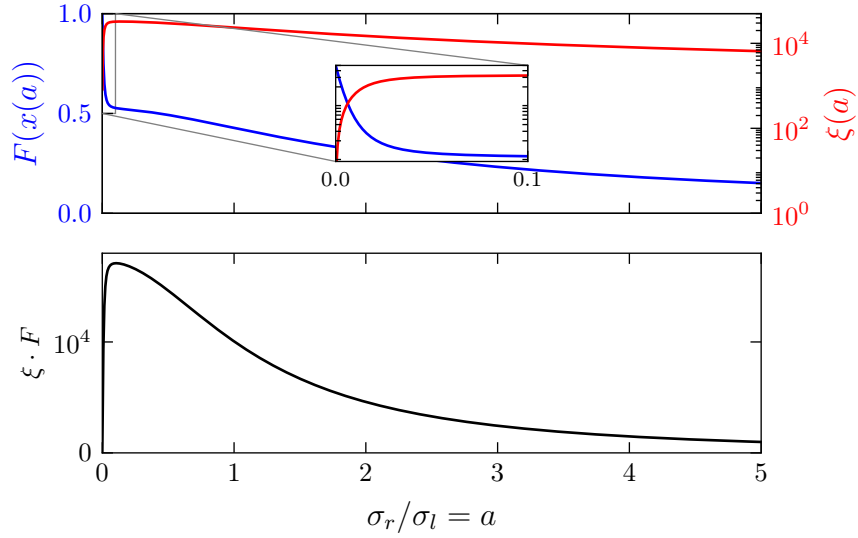


Figure 4.3.9: Overlap functions $F(x)$ (blue) and ξ (green), according to equations (4.1.5) with equation (4.3.4) and (4.3.5), and their product $F(x) \cdot \xi$ (black) as functions of the waist relation a .

waist relation parameter a , x then reads:

$$x(a) \propto a \sqrt{\frac{1 + a^2}{(4\pi)^2 \varepsilon_n^2 / \gamma^2 + \lambda^2 a^2}} \quad (4.3.4)$$

The function $x(a)$ is minimal for $a \rightarrow 0$, as $x \geq 0$ holds. Consequently, $F(x(a))$ demands a small bunch waist compared to the laser waist. Analogously, ξ can be expressed as a function of a , so that

$$\xi(a) \propto \frac{a}{\sqrt{1 + a^2}} \frac{1}{\sqrt{(4\pi)^2 \varepsilon_n^2 / \gamma^2 + \lambda^2 a^2}} \frac{1}{\sigma_l} \quad (4.3.5)$$

Obviously, $\xi(a = 0) = 0$. In figure 4.3.9 the single contributions $F(x(a))$ and $\xi(a)$, as well as their product $\xi \cdot F \propto N_{\text{tot}}$ are plotted against the waist relation a . $F(x)$ appears to be a measure for the transversal overlap, while ξ takes into account the decrease in longitudinal overlap with increasing divergence.

Considering the maximisation of the overlap volume requires to increase σ_r / σ_l for increasing emittance, in order to confine the electron divergence σ_θ , as displayed in figure 4.3.10 (left). This function, and thereby the optimum waist relation, is independent of the laser waist which directly translates to the matching of divergence of laser and electron beam: A more strongly focused laser with consequent smaller waist and larger divergence also allows for the electron bunch to have a larger divergence, hence a smaller focal waist. This is illustrated in figure 4.3.10 (right). For zero emittance, $\xi(a) \propto 1 / \sqrt{1 + a^2}$ and the maximum yield would be obtained for $a \rightarrow 0$, as well. For increasing electron emittance, the divergence increases at constant electron waist $\varepsilon_n \propto \sigma_r \sigma_\theta$.

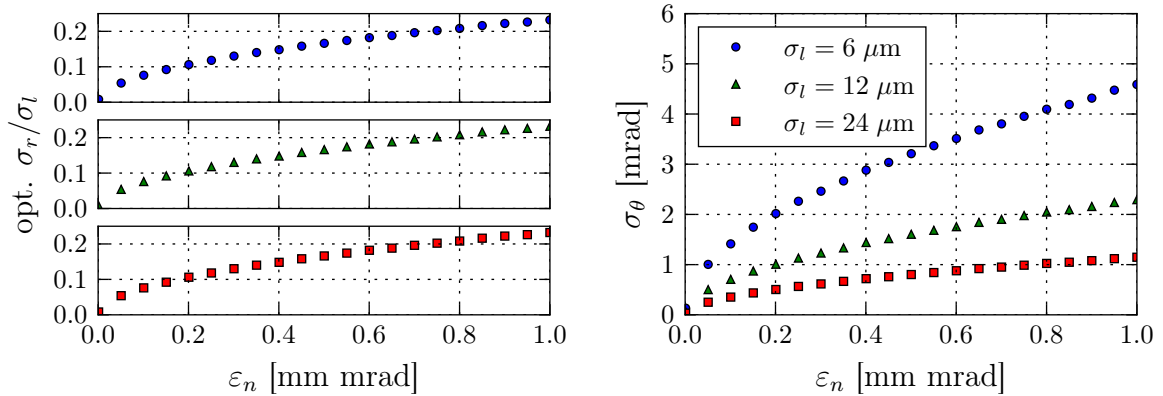


Figure 4.3.10: Emittance influence on the optimum electron-laser waist relation σ_r/σ_l (left) and on the optimum electron divergence σ_θ (right), as obtained from equations (4.1.13)ff.

4.3.3 Bandwidth

For the bandwidth analysis, simulations are employed, in combination with the calculations, as the theory has shown to deviate from the simulation in this respect. Figure 4.3.11 displays the simulated and theoretical cone bandwidth (according to the scenarios presented in figure 4.3.1) as function of the electron waist (left) and the electron divergence (right). In accordance with the findings in the parameter scans (Fig. 4.2.17), the cone bandwidth obtained from an electron beam with a non-zero emittance rises with decreasing electron waist and increasing divergence¹⁵. Within the regions of maximum yield, the theory and the simulations are in good agreement for low a_0 . This is because at small divergences, the divergence effect is not overestimated by the theory, but is still the main bandwidth contribution. The bandwidth for the $a_0 = 0.36$ case is over-estimated by the theory, as expected (see Ch. 4.2.4). This is due to the fact that the theory discards electron bunch optimisation and assumes a bandwidth defined by the maximum a_0 , rather than the actual a_0 distribution, as seen by the electrons. With $a_0 = 0.36$, this contribution exceeds that of the divergence (at low divergence values) and the theoretical divergence contribution rises quadratically with σ_θ (cp. Eq. (4.1.20)). This neglects that electrons of large propagation angle with respect to the main bunch direction emit radiation of very low intensity into the cone. If this angle approaches or exceeds the synchrotron angle $1/\gamma = 6.4$ mrad, the bandwidth will thus saturate. For $\sigma_r \gtrsim 1 \mu\text{m}$ and $\sigma_\theta \lesssim 2$ mrad, the bandwidth is below 10 %. This allows for an electron bunch of $\sigma_\gamma/\gamma \lesssim 1.5$ % rms energy spread without exceeding the boundary condition for the total bandwidth of $\Delta E_\gamma/E_\gamma \lesssim 15$ % FWHM.

In order to quantify the results of photon yield and bandwidth, a quality parameter Q is defined, so that for maximum yield at minimum bandwidth, this factor is largest:

$$Q = \frac{N_\gamma}{\text{BW}} \quad (4.3.6)$$

¹⁵Note, that no electron energy spread is included.

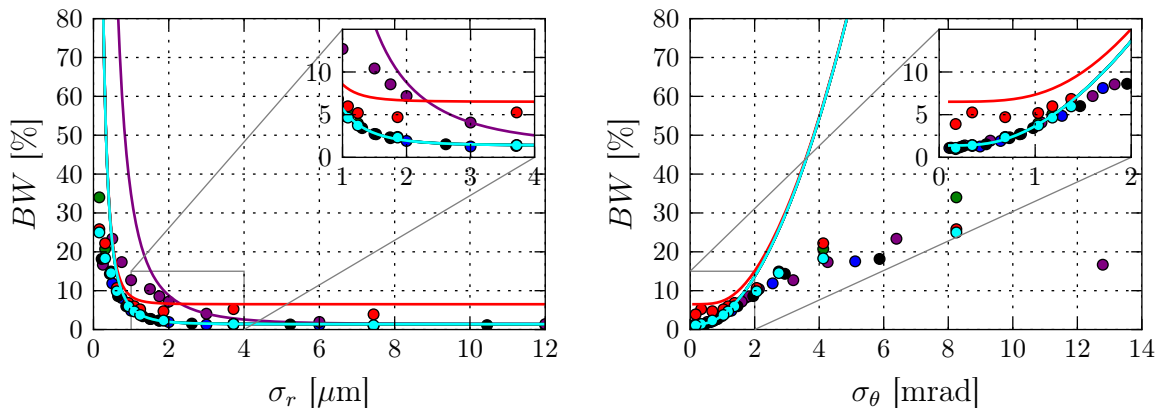


Figure 4.3.11: Simulated (markers) and theoretical (lines) cone bandwidth as functions of the electron waist (left) and of the electron divergence (right) for the different parameter sets.

However, while in general the yield should be maximised, a low-shot photon count could be moderated by a high-repetition rate laser. Therefore, the bandwidth is the more crucial parameter. The quality is thus not a definitive quantity, in that its maximum does not necessarily denote the optimum configuration. A modification of the definition, such as $Q = N_\gamma/BW^2$, would also neglect the bandwidth limit, and allow for quality maxima at too large bandwidth, due to a large enough yield. Consequently, for a given electron bunch energy spread, the quality parameter is modified in such a way as to exclude too large bandwidth values. This allows to define a region of acceptable bandwidth for which the maximum yield then defines the optimum:

$$Q_{\text{BW}} = \begin{cases} N/BW & \text{if } BW \leq BW_{\text{max}} \\ 0 & \text{else} \end{cases} \quad (4.3.7)$$

where BW_{max} denotes the maximum allowed bandwidth before including the electron energy spread.

The quality, as calculated from simulations and theory is displayed as a function of the electron divergence in figure [4.3.12](#). The highest qualities are achieved for the black and blue case. In the simulations, both qualities are identical, as the yield is higher in the black scenario, while it obtains a larger bandwidth, as well. Thus, in this case, the definition of the optimum laser parameter set would depend on the electron energy spread, in order to determine whether the yield should be maximised or the bandwidth should be minimised. The optimum can then be determined via the modified quality Q_{BW} which takes into account the bandwidth limit.

4.3.4 Summary

Bandwidth reduction of a Thomson source typically comes at the cost of the photon yield. The variation of the electron parameters, however, has shown that there exist an optimum

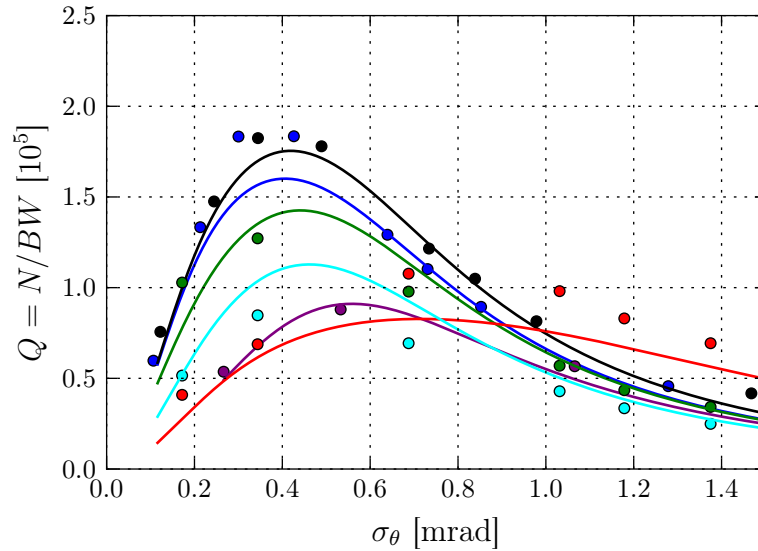


Figure 4.3.12: Simulation (markers) and theoretical results (lines) for the quality, defined as the yield-bandwidth ratio $Q = N_\gamma/BW$, as a function of the electron divergence.

electron waist and divergence, so that the spectral broadening due to the a_0 distribution is reduced. By cutting low- a_0 values from the laser, a yield increase can be achieved while the bandwidth is reduced. Consequently, this represents a way to improve both, the yield and the bandwidth.

The optimum electron waist and divergence depend on the laser waist and on the electron emittance. The optimum laser and electron configurations are those that give the highest effective a_0 over the whole interaction length. In other words, the best transversal overlap for the whole laser duration is to be determined. The simulations and calculations have shown that the optimum laser configuration is not necessarily the one given by the theoretical formulae for $a_0 = 0.16$. If the electron bunch is optimised with respect to the laser configuration, a laser of longer duration and smaller waist gives the better yield result. The confinement by the chosen cone reduces the photon yield significantly, especially with increasing divergence. As both, the temporal maintenance of the transversal overlap, and the confined cone require a low divergence, a laser with a longer duration is favourable. The photon yield within a cone can be explained and quantified by two aspects: The *overlap effect* and the *cone effect*. The latter is solely dependent on the electron divergence. The overlap effect can be explained simply by the mean a_0 , and therefore, it is only the mean electron and laser waist during the interaction that determine the total yield. It is hence the mean, and not the maximum a_0 , that defines the photon yield. Consequently, the total yield equation (4.1.3) can be applied to any scenario, given the mean waists. From this, an empirical formula was derived (Eq. (4.3.7)) to calculate the cone yield in dependence of the electron divergence for the given electron parameters. From these findings, the following consequences arise.

The analysis showed that an increased effective a_0 at small bunch waist can compensate

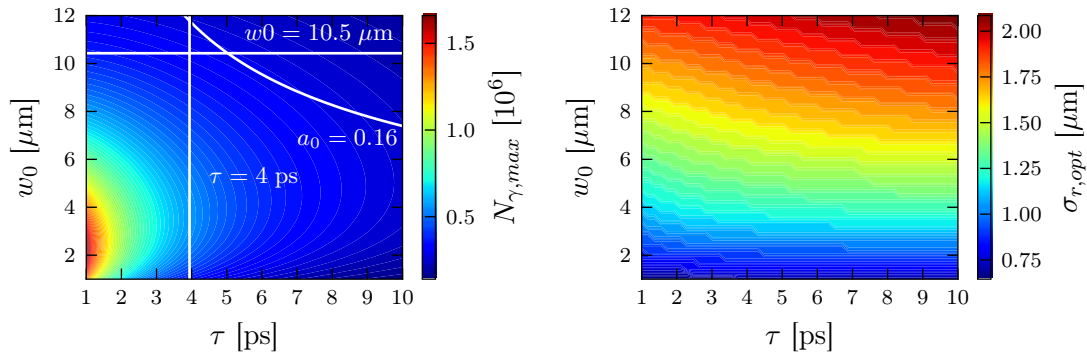


Figure 4.4.1: Maximum yield for different laser parameter duration τ , waist w_0 and according laser strength a_0 for a laser of pulse energy $E_p = 0.5$ J (left). The lines for constant τ , w_0 and a_0 , as investigated in sections 4.4.1–4.4.3, are shown in white. The according numerically determined optimum electron waist σ_{opt} is plotted as a function of τ and w_0 (right).

the photon loss due to large divergence. Furthermore, the increased number of oscillations in a longer laser moderates the loss in effective a_0 during the interaction. By decreasing the laser waist, a stronger electron focusing is favoured over a low divergence. If the laser pulse is sufficiently short, e.g. for purpose of increasing the peak a_0 , the longitudinal overlap does not have to be maintained over a long range. Consequently, a higher electron divergence is allowed in terms of the total yield.

The simulated bandwidth at low divergence and according large electron waist values coincides with the theory in case of small a_0 , i.e. where the theoretical spectral broadening is small enough. However, for increasing divergence and laser strength parameter values, the theoretical approximation is not valid.

As different laser configurations lead to similar quality Q , in the next section, an attempt is made to localise optimum laser parameter regions.

4.4 Laser Parameter Study and Design Parameters

In this chapter, the laser parameters a_0 , w_0 , and τ are varied and a bandwidth of $\Delta\lambda = 60$ nm, and hence a linear longitudinal chirp, is added to the laser configuration. The electron-waist parameter scans demonstrated that the optimum electron waist and divergence are well estimated by Rykovanov et al [12]. Therefore, the optimum electron waist for each laser parameter set is determined numerically, according to equations (4.1.3) for the maximum total yield and (4.1.13) for the divergence-dependent cone yield. At a given laser parameter set, the optimum electron waist $\sigma_{r,\text{opt}}$ is determined numerically, and the according maximum photon yield is calculated. The results are displayed in figure 4.4.1. The maximum yield is achieved for high laser strength parameter, i.e. at low waist and duration values. The optimum electron waist is hardly changed for constant w_0 , it slightly rises with increasing laser duration, as explained in the previous section.

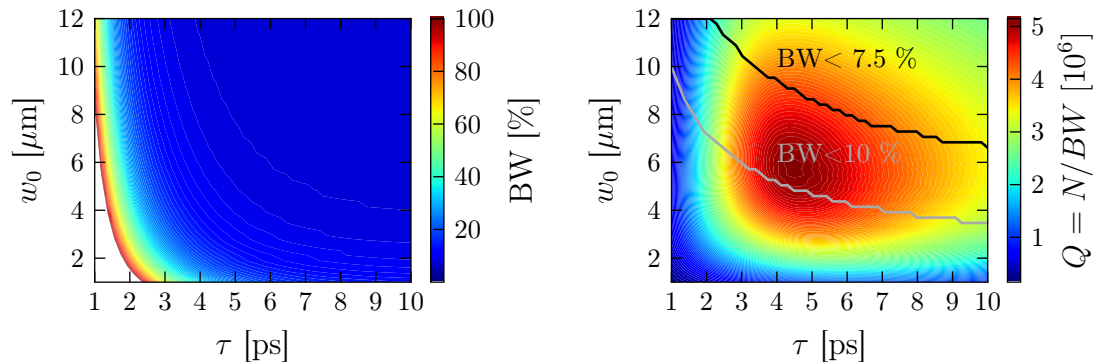


Figure 4.4.2: Theoretical bandwidth (left) and quality $Q = N/BW$ (right). Assuming a maximum acceptable bandwidth of 7.5 or 10 %, the results below the black or grey curve, respectively, are discarded.

The theoretical bandwidth calculation and the according quality, defined as $Q = N/BW$, are shown in figure [4.4.2](#). However, as the bandwidth estimation is inaccurate in case of low maximum a_0 , due to the negligence of the actual a_0 distribution, these calculations only serve as a first qualitative estimate. The region of highest quality is at $w_0 \approx 6 \mu\text{m}$ and $\tau \approx 4.5 \text{ ps}$. As these calculations exclude an energy spread of the electron bunch, not simply the quality as plotted defines the optimum parameter region. Depending on the effective energy spread of the bunch - which, as mentioned, is determined by the focusing technique - quality values below a certain threshold have to be discarded, according to equation [\(4.3.7\)](#). For effective energy spreads of 2.3 % rms and 2.8 % rms, the maximum bandwidth is 10 % FWHM and 7.5 % FWHM, respectively. Consequently, the region of highest quality might be cut, due to the bandwidth requirement.

Three scenarios are investigated in detail in comparison to simulation results of yield and bandwidth. They are indicated by the white lines (Fig. [4.4.1](#)) for constant laser duration, constant waist, and constant yield.

4.4.1 Optimum Laser Waist and a_0 at Constant Laser Pulse Duration

The investigated scenario is adapted to the case in figure [4.3.1](#) with $a_0 = 0.16$, $\tau = 4 \text{ ps}$. At constant τ , the laser waist w_0 is varied, and hence also a_0 , to find the optimum parameter set at constant laser duration. With a constant laser duration, the number of laser periods N_0 is kept constant, and thus also the demand on the electron divergence by the interaction length.

The theoretical and simulative results for the cone photon yield, the bandwidth and the resulting quality are displayed in figure [4.4.3](#) (top row). While for $a_0 < 1$ the simulated and calculated photon yield values are in good agreement, the main difference is found in the bandwidth. In the simulations, the bandwidth has a minimum at $w_0 = 7 \mu\text{m}$.

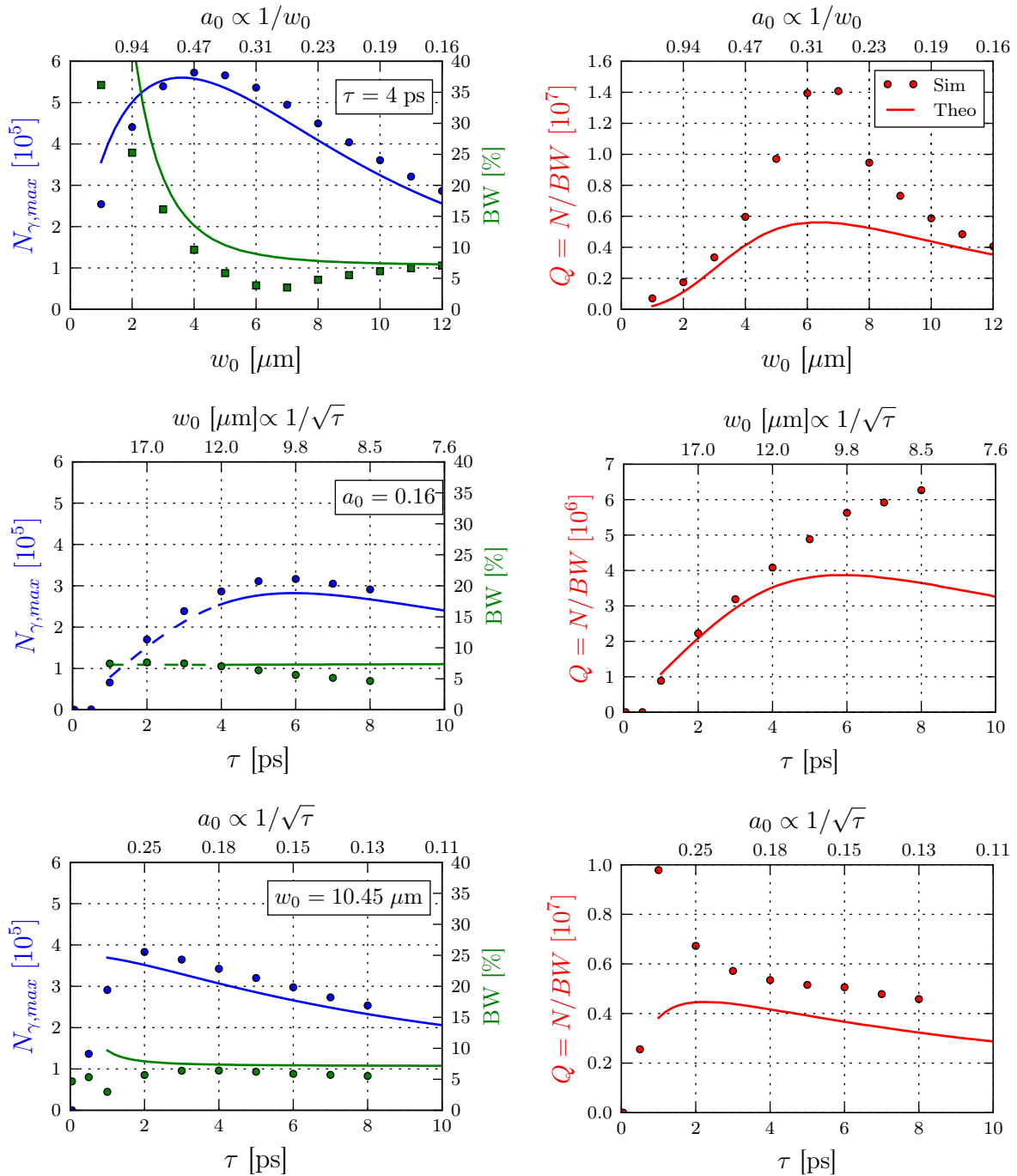


Figure 4.4.3: Simulated (markers) and theoretical (lines) results for the cone yield and bandwidth for the three scenarios indicated in figure 4.4.1 (white lines) are displayed in the left column. The according quality $Q = N/BW$ is shown in the right column. From top to bottom: Constant laser duration, constant laser strength parameter, and constant laser waist. The relations between a_0 , w_0 , and τ are given by equation (2.1.6). (The dashed lines indicate the zone which is not included in figure 4.3.1).

The theoretical bandwidth is dominated by the maximum a_0 and the electron-divergence effect and hence rises with decreasing w_0 and accordingly decreasing σ_r . The drop in the bandwidth is an effect which arises due to the longitudinal chirp of the laser (cp. Sec. 4.2.5). With decreasing laser and also electron waist, the laser's Rayleigh length decreases and the electron divergence increases. The interaction region is defined by the laser duration and thus stays constant. At the beginning and end of the interaction region, a large laser waist due to the short Rayleigh length, reduces a_0 , and thereby the contribution to the spectrum. The highest contribution is obtained from the interaction in the laser centre. Consequently, the effective laser bandwidth is reduced and low a_0 values are cut. This *chirp effect* thus leads to a bandwidth decrease at the high-energy side of the spectrum. As the pulse energy is kept constant, with decreasing laser waist at constant pulse duration, the maximum a_0 increases. Therefore, with further reduction of the waist, the spectrum is broadened at the low-energy side, i.e. for increasing a_0 , resulting in a bandwidth increase. The according spectra showing this development are included in the appendix figure A.3.3.

As a result of the bandwidth minimum, the simulated quality curve displays a maximum at $6 - 7 \mu\text{m}$, exceeding the theoretical maximum by more than a factor two.

4.4.2 Optimum Laser Waist and Pulse Duration at Constant Laser Strength Parameter

For varying duration τ and waist w_0 at constant laser strength parameter $a_0 = 0.16$, the theoretical and simulative results are displayed in figure 4.4.3 (centre row). Again, the photon yield from simulation and calculation agree well. The bandwidth, however, is constant in theory, as it is determined by the maximum a_0 . In the simulations, the a_0 distribution is taken into account, determined by the electron-laser overlap. In order to maintain a_0 , the laser waist has to be reduced for increasing laser duration. With smaller waist, the Rayleigh length (Eq. (2.1.2)) decreases, while the interaction length increases with the laser duration. The overlap at beginning and end of the laser pulse is worsened, leading to the same *chirp effect*, as described in the previous section. Consequently, for increasing laser pulse duration, the bandwidth decreases, leading to an increase in quality.

However, this deviation is rather small. With the maximum simulated quality at 6.5×10^6 , it is only half the value obtained in the previous section.

4.4.3 Optimum Laser Strength Parameter and Pulse Duration at Constant Laser Waist

In this section, the laser waist is kept constant, at $w_0 = 10.45 \mu\text{m}$, for different values of a_0 and τ . The results are presented in figure 4.4.3 (bottom). The bandwidth drop in the simulations at $\tau = 1 \text{ ps}$ is again attributed to the *chirp effect*. For durations below

$\tau = 1$ ps, and according $a_0 > 0.3$, the bandwidth is again dominated by the increasing laser strength, as in the scenario with constant laser duration. The spectra visualising the broadening of the low- or high-energy flanks of the distribution are displayed in appendix figure [A.3.4](#). The observed bandwidth minimum leads to a sharp peak in the quality at $\tau = 1$ ps. However, with $Q(1 \text{ ps}) \approx 1 \times 10^7$, this quality lies below the maximum quality at $w_0 = 7 \mu\text{m}$ and $\tau = 4$ ps, as well.

4.4.4 Summary

The laser parameter scans revealed that a theoretical maximum of the quality can be found for constant laser pulse energy. This maximum, however, does not take into account the demand on the bandwidth by the XFI, on the one hand, and the overlap-determined a_0 distribution, on the other hand. It was shown that a higher quality can be obtained for a relatively large $a_0 = 0.36$ at $\tau = 4$ ps and $5 \mu\text{m} < w_0 < 8 \mu\text{m}$.

It has to be distinguished between a high quality obtained from a large photon yield, and from a low bandwidth, where the latter represents the favourable configuration. Imposing another quality condition upon these results, namely maximising the yield while the bandwidth should lie below 10 % leads to the optimum configuration at $\tau = 4$ ps and $w_0 = 5 \mu\text{m}$. The quality value at these parameters exceeds that of the other simulations. Hence, this case is chosen as the basis for the lens focusing in the following chapter.

So far, the simulations only included the Thomson spectrum of the first harmonic. Due to the non-zero cone opening angle, the second harmonic, which is suppressed on axis, contributes to the spectrum. Bearing in mind the medical application for the Thomson source, higher harmonics generation should be suppressed, in order to minimise the radiation dose.

Moreover, the bunch charge of $Q = 10$ pC investigated up to now was chosen so that space-charge effects are negligible. In an effort to maximise the yield, the increase of the bunch charge is an important aspect.

In the following sections, quantifications of the second-harmonics generation and space-charge effects are briefly discussed, thus concluding this chapter on the general characteristics of a Thomson source.

4.5 Nonlinear Effects and Higher Harmonics

The nonlinear regime of Thomson scattering is defined via the laser strength parameter $a_0 \geq 1$. However, previous simulations showed that nonlinear effects start to emerge already in the intermediate regime where $0 < a_0 < 1$. So far, this has been quantified in terms of photon yield and bandwidth. Another effect of increasing laser strength is the excitation of higher harmonics. The application of the Thomson source in this thesis demands a certain photon energy. Radiation at multiples of the required energy (150 keV)

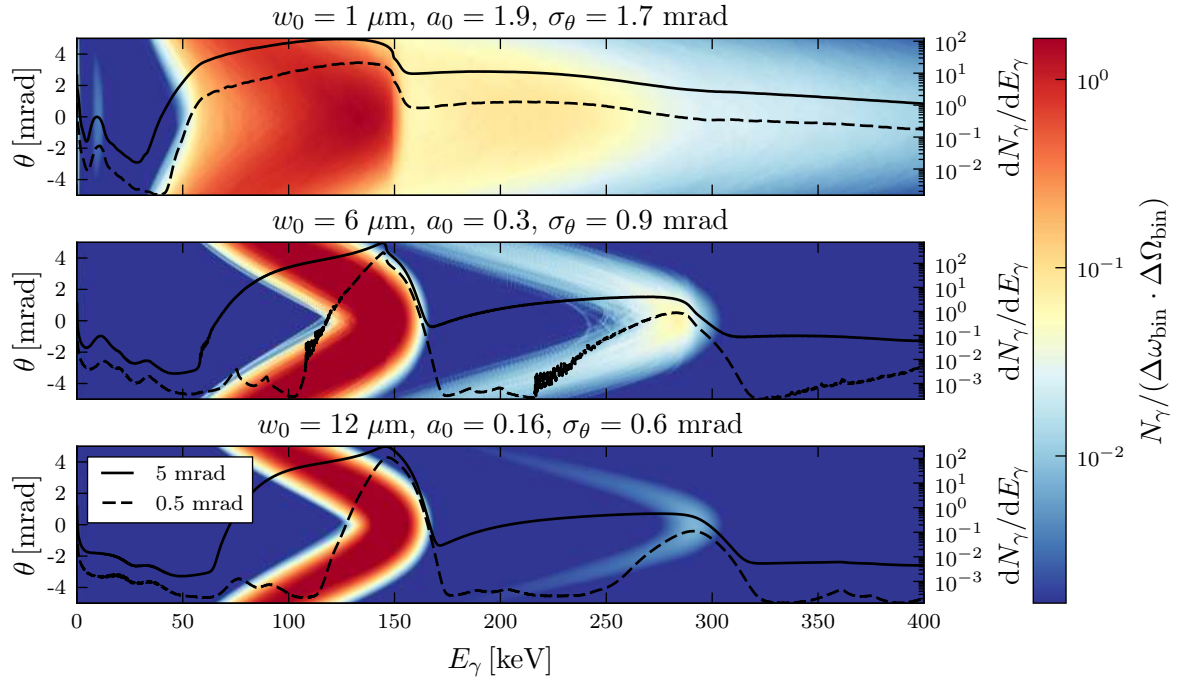


Figure 4.5.1: Line spectra within an opening angle of $\theta = \pm 5$ mrad (colour plot) and total spectra within 5 mrad (straight lines) and 0.5 mrad (dashed lines). Three parameter sets from the scenario of constant laser duration at 4 ps (Ch. 4.4.1) are displayed.

have a reduced fluorescence cross section (cp. Fig. 3.1.1). Furthermore, the dose deposited in tissue rises with increasing photon energy. Therefore, the quantification of radiation within higher harmonics is of twofold interest.

Figure 4.5.1 displays the line spectra within a cone of 5 mrad, as obtained from the parameter scan in section 4.4.1. The total spectra (dN_γ/dE_γ) for 5 mrad and 0.5 mrad are included. The laser duration is constant at 4 ps, and the laser waist and thereby the laser strength is varied. The electron waist is set according to the photon yield optimisation. Even harmonics arise from the longitudinally oscillating Hertzian dipole in the electron rest frame (cp. Sec. 2.3.1). Though they are suppressed on axis, the electron divergence and the non-zero cone angle lead to a contribution of the second harmonic ($E_{\gamma,2,max} = 300$ keV) to the spectrum. The following effects are observed. Firstly, a high laser strength leads to spectral broadening, so that, even on axis ($\theta = 0$), the first and second harmonic overlap. For smaller a_0 , this is only the case if the cone angle is large enough to include the low-energy tail of the second harmonic. Secondly, with higher a_0 , the second harmonic is more pronounced. This is due to the broadened figure-eight motion (cp. Fig. 2.1.2). Thirdly, the total spectra show that even at large laser strengths, the peak of the second harmonic in the spectrum is orders of magnitude smaller than that of the first harmonic. In figure 4.5.2, the percentage of photons within the second harmonic with respect to the number of photons in the first two harmonics is displayed as functions of the waist and laser strength (left). The number of photons within the two harmonics

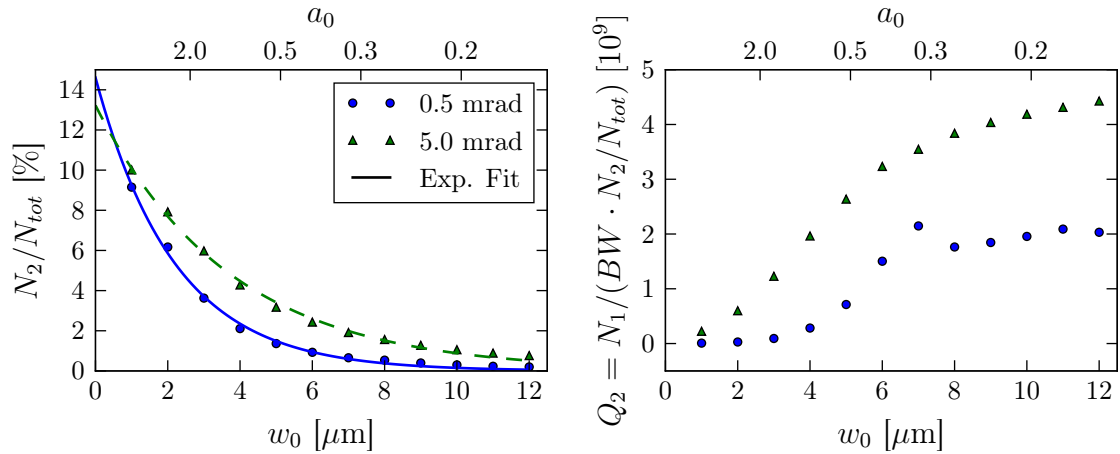


Figure 4.5.2: Percentage of photons within the second harmonic (left) and quality criterion including the second harmonic contribution (right) as functions of the laser waist w_0 and strength parameter a_0 for a cone angle of 0.5 mrad (blue circles) and 5 mrad (green triangles).

is denoted as the total yield^[16], N_{tot} . At the previously defined optimum at 6 – 7 μm , the second harmonic contributions is only at ≈ 1 % which is negligibly small. Defining a new quality criterion which demands a low contribution of the second harmonic, according to

$$Q_2 = \frac{N_1}{BW \cdot N_2/N_{tot}} \quad (4.5.1)$$

where N_i is the number of photons within the i^{th} harmonic, leads to an optimum at a laser waist of $w_0 \approx 7$ μm (Fig. 4.5.2, right).

In summary, it can be stated that the second harmonic contribution within a cone of 0.5 mrad opening angle is negligibly small, even at large laser strength parameters. The more significant nonlinear effect is the spectral broadening which dominates the quality functions.

4.6 Space-Charge Effects at High Bunch Charge

Space charge induces a transverse and longitudinal expansion of the electron bunch [65]. This effect increases with decreasing waist and increasing charge of the bunch. So far, simulations and calculations have been conducted with a relatively low bunch charge of 10 pC, where the effect of space charge is negligible. This section shall provide an estimation on the effect of space charge on the cone yield and bandwidth for electron bunches of increased charge.

The scenario under investigation is the parameter set from chapter 4.3.1 with $w_0 = 10.45$ μm , $\tau = 5$ ps, $a_0 = 0.16$ (black curve in Fig. 4.3.1). Electron bunch charges of $Q = 10, 100, 200,$ and 500 pC are simulated including the GPT space-charge model

¹⁶The contribution from the higher harmonics of order exceeding 2 is negligible.

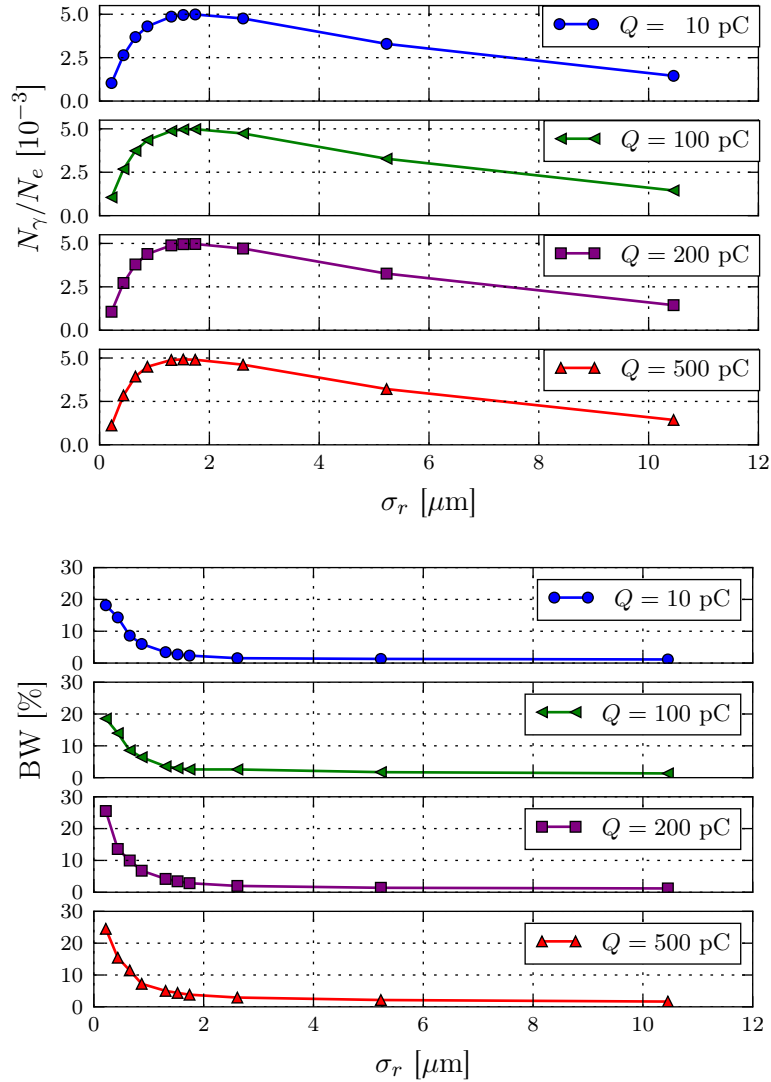


Figure 4.6.1: Cone yield and bandwidth results from simulations including space charge effects for different bunch charges $Q = 10, 100, 200$ and 500 pC.

spacecharge3Dmesh. The results of the Thomson interaction are displayed in figure [4.6.1](#). The yield is normalised to the number of electrons in the bunch. An influence of the space-charge-induced bunch expansion is found at 200 and 500 pC, where a small relative increase in the bandwidth at 200 pC and 500 pC can be observed for small electron bunch waists. However, at these parameters, the divergence of the electron bunch is large enough to dominate the bandwidth, so that it rises steeply for all scenarios. This region of small electron waist $\sigma_r < 0.75 \mu\text{m}$ is characterised by a too large cone bandwidth and is therefore no desirable parameter set. The space-charge-induced bunch deformation is therefore negligibly small¹⁷. For lower charges, no effect is detected with respect to yield, as well as to the bandwidth. Consequently, as it is not relevant within the parameter regions of interest for charges of 5 – 200 pC (cp. Tab. [3.2.1](#)), space-charge effects will be discarded in further simulations. Subsequently, a higher yield can be obtained from an

¹⁷This is shown for the case of $\sigma_r = 0.2 \mu\text{m}$ in figure [A.3.5](#) in the appendix.

increased bunch charge, resulting in 6×10^6 photons per shot in case of a 200 pC bunch.

4.7 Conclusion

This chapter was concerned with providing a deeper understanding of the effect of the different electron, laser and interaction geometry parameters on the Thomson interaction and the resulting spectrum. The parameter scans were conducted with respect to the possible source setup (Sec. 3.2).

While the photon yield is well estimated by the existing theory, it is formulated for a head-on collision without transversal or longitudinal focal offsets (Ch. 4.1.2). It was shown that in terms of the yield, the width of the effective a_0 distribution of the electron interaction with the laser is the determining parameter. Therefore, an extrapolation of the theory to different electron parameters and interaction geometries is possible. Yield calculation can then be performed, simply by means of the mean electron and laser waists.

The bandwidth was found to be well represented by the theory, in case of either low electron divergence, low a_0 , i.e. the linear regime, or in case that the electron energy spread dominates the total bandwidth. The theoretical description differs from the simulations, if the actual a_0 distribution, as experienced by the electrons, is relevant which is the case for increasing $a_{0,\max}$. This includes the value of a_0 for each electron at each point within the interaction region. The quantification of this distribution, however, includes extensive numerical calculations, so that this does not represent a valid alternative to the Clara simulations.

A central aspect of this chapter was the investigation of the role of the electron-laser waist relation and the electron divergence on the source parameters. Electron bunch parameter optimisation has proven to be a vital tool in the design of a dedicated Thomson source. Typically, Thomson bandwidth reduction comes at the cost of a lower yield. The reason is that even in the *ideal case*, i.e. a single electron in a counter-propagating laser field of constant laser strength parameter leads to the intrinsic Thomson bandwidth. However, bunch-waist and divergence optimisation can achieve an increased yield and reduced bandwidth, with respect to scenarios of electron bunches with waists much smaller than or equal to the laser waist as proposed by literature. The waist and divergence can be optimised, quantified by the quality parameter Q , introduced in this chapter as the ratio of photon yield and bandwidth. Thereby, optimisation refers to finding the best compromise between the interaction *overlap* and the *cone effect*, as these two represent rival effects.

Furthermore, the laser parameters in the presence of electron bunch optimisation have been investigated. It was revealed that the theoretically ideal laser does not necessarily give the best result in terms of the yield or bandwidth. Moreover, as the theory neglects the a_0 distribution, as experienced by the electrons, the bandwidth at increasing a_0 is often overestimated. This leads to an underestimation of the quality parameter. The

comparison of theory and bandwidth leads to the determination of a laser parameter configuration of large quality, i.e. at $\tau = 4$ ps, $w_0 = 5$ μm and $a_0 = 0.37$ which is the basis for the next chapter on lens focusing. For this configuration, emittance into higher harmonics was shown to be negligible. Furthermore, at the chosen bunch-waist and -divergence values, space-charge effects can be neglected within the chosen parameter range of the bunch charge $Q = 5 - 200$ pC.

Still, throughout this chapter, the laser pulse energy was fixed to $E_p = 0.5$ J, thus determining the relation between a_0 , w_0 and τ . From the findings, it can be stated that the optimum laser would be of higher pulse energy, so that a broad waist and a long duration still yield a large enough a_0 . Then, the broad waist would lead to a nearly constant transversal a_0 for moderately low bunch waists, and the weaker electron focusing would reduce the divergence, and hence photon yield and bandwidth impairment. For large a_0 , spectral broadening due to the longitudinal a_0 variation can be reduced by choosing a small deviation from the counter-propagating interaction angle. The yield reduction would still be large (up to 50 %), but due to the proposed higher pulse energy, the initial yield would be larger. In the proposed pump-probe setup the laser pulse energy is limited, future lasers with high repetition rates and higher power, however, might allow for this.

The simulations and calculations in this chapter with electron emittance did not include an electron-bunch energy spread, as this requires a specification on bunch propagation and focusing. This will be investigated in the next chapter, where the chromatic focusing effect of a discharge-capillary active plasma lens is applied to achieve the optimum electron parameters for a given laser configuration.

CHAPTER 5

DISCHARGE-CAPILLARY ACTIVE PLASMA LENS

Transport and focusing of laser-wakefield-accelerated electron beams is an important aspect of their application. As presented in the previous chapter, optimum photon yield of the X-ray Thomson source is obtained for rather small electron focal waists ($\sim \mu\text{m}$). As the electron beam is divergent when exiting the plasma, an appropriate beam optic has to be found, in order to focus the electrons onto the laser focus to obtain the optimum focal waist and according divergence.

Electron focusing is typically achieved via magnetic fields, hence on the basis of the Lorentz force. Due to the energy-dependence of the Lorentz force, electrons of different kinetic energy experience different focusing strengths. This leads to energy-dependent focal lengths, as well as focal spot sizes and divergences. According to the spatial overlap and electron focal parameters, electrons of different energy contribute more or less to the spectrum. An interesting prospect is therefore the use of this chromatic focusing effect, in order to decrease the effective electron energy spread, as experimentally confirmed by Fuchs et al. [34]. Electron beam focusing or collimation is conventionally achieved via solenoids or quadrupole triplets. However, solenoids are highly chromatic with a focusing strength proportional to $1/\gamma^2$. While, with a proportionality factor of $1/\gamma$, the chromaticity effect of quadrupole triplets is weaker, radially symmetric focusing requires an assembly of three lenses with different and opposite strengths. Consequently, despite their rather strong field gradients ($\approx 500 \text{ T/m}$), the total focusing length is tens of centimetres. Hence, the longitudinal extent of focusing lengths of an electron bunch with energy spread $\sigma_\gamma/\gamma > 0$ is also of the order of centimetres.

A discharge-capillary active plasma lens (APL) as proposed by van Tilborg et al. [35] holds the prospect of a chromatic focusing effect at short focusing lengths and thus smaller setups. The concept of such a lens is presented in detail in the following section 5.1. In section 5.2, the theoretical approximation of the focusing of a divergent electron beam (after plasma acceleration) and GPT simulations are presented. In order to assess

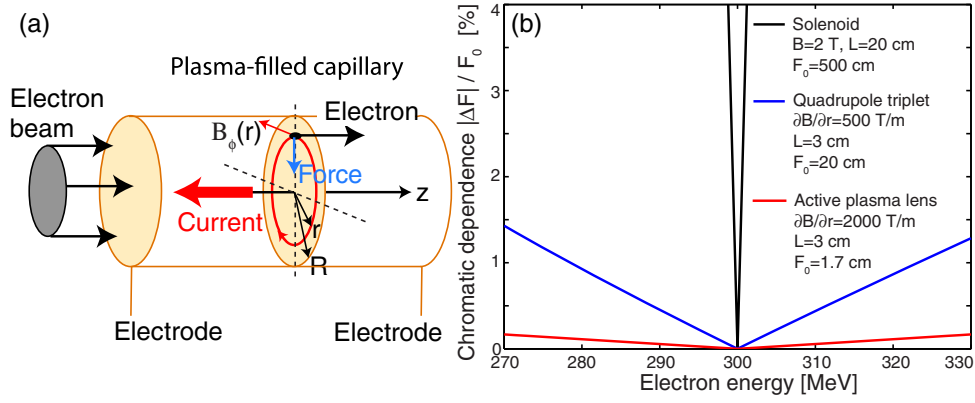


Figure 5.1.1: (a) Schematic display of a discharge capillary. (b) Chromatic dependence of the focal length for a solenoid (black), a quadrupole triplet (blue) and a discharge capillary active plasma lens. This figure is adapted from [35].

the effects of electron focusing on the Thomson spectrum, the interaction of a laser with a divergent electron beam behind the plasma is investigated, at first. The Thomson scattering simulation results of an divergent beam at the plasma exit, and of an APL-focused electron bunches are presented in chapters [5.3] and [5.4], respectively.

5.1 Basics of the Active Plasma Lens

A discharge-capillary plasma channel for focusing electrons is a gas-filled cylindrical tube with electrodes at either end (Fig. [5.1.1] (a)). A voltage is applied between the electrodes so that at breakdown, a discharge current flows axially through the tube. The current can be approximated as uniformly distributed in the capillary [66]:

$$J = \frac{I_0}{\pi r_0^2} \quad (5.1.1)$$

where I_0 is the peak current and r_0 is the capillary radius. According to Ampère's law, the magnetic field for a radius $r < r_0$ is given as:

$$B_\phi = \mu_0 J r / 2 \quad (5.1.2)$$

The index ϕ indicates the invariance of the magnetic field with respect to the azimuthal angle, and μ_0 is the vacuum permeability. With that, the magnetic field gradient reads

$$\frac{\partial B_\phi}{\partial r} = \frac{\mu_0 I_0}{2\pi r_0^2}. \quad (5.1.3)$$

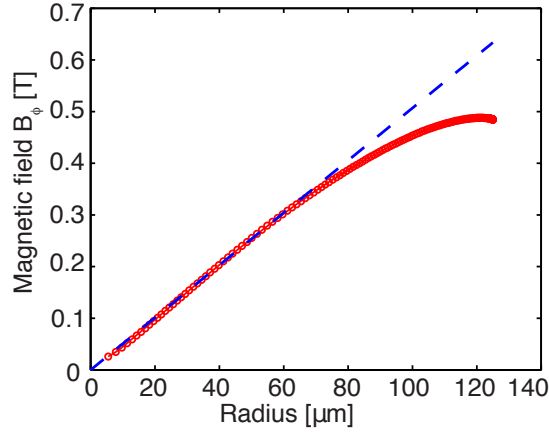


Figure 5.1.2: Radial dependence of the magnetic field within a capillary of $r_0 = 125 \mu\text{m}$. (Markers: Simulations, dashed line: Linear fit.) The figure is adapted from [35].

The focal length of a capillary-discharge active plasma lens (APL) in accordance with the thin-lens approximation¹ is given as

$$f = \frac{1}{kL} \quad (5.1.4)$$

with L the length of the capillary and k the strength parameter, defined as

$$k = \frac{e}{m_0\gamma c} \frac{\partial B_\phi}{\partial r} = \frac{e\mu_0}{2\pi m_0\gamma c} \frac{I_0}{r_0^2}. \quad (5.1.5)$$

Consequently, the following dependence of the focus arises:

$$f \propto \frac{\gamma r_0^2}{LI_0}$$

The focal length in terms of the longitudinal coordinates z_e the end of the capillary, z_F the focal point position, and L reads $f = L/2 + z_F - z_e$. The chromaticity effect on the focal length of a plasma lens, a solenoid, and a quadrupole triplet is displayed in figure 5.1.1(b). The longitudinal spread of the focal region is smallest in case of the plasma lens which also possesses the shortest focal length F_0 .

As shown in Fig. 5.1.2, field gradients are linear within the lens up to a radius of $\approx r_0/2$. Consequently, simulations are only representative, if the bunch size does not exceed this value.

¹In the thin-lens approximation the focal length of an optical element, i.e. the lens, is the distance from the lens centre to the focus. As the focusing effect of the capillary depends on its length, this parameter is included in the formula for the focal length.

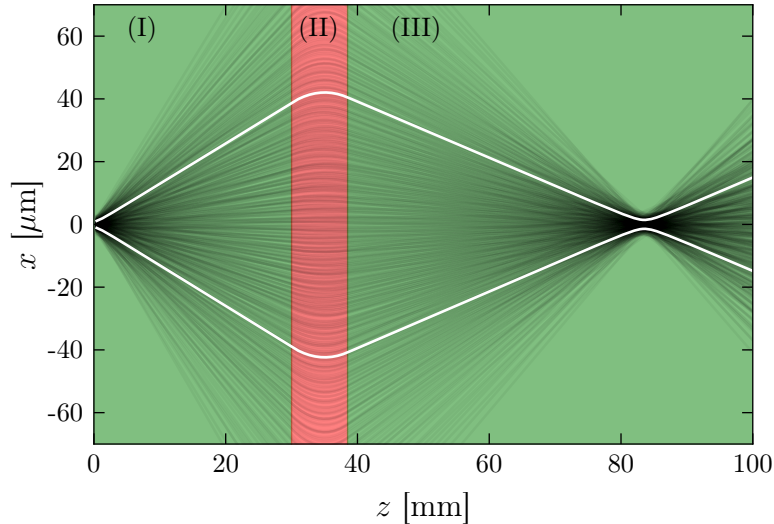


Figure 5.2.1: Active-plasma-lens focusing setup. The evolutions of the single electron trajectories (black), as well as of the bunch rms waist σ_r (white) in the $x - z$ plane are displayed in the free drift (green) and the plasma lens (red). The electron bunch starts in its focus at the plasma exit ($z = 0$). It drifts freely (I) towards the plasma lens (II) and reaches its second focal point in the following free-drift section (III).

5.2 Lens Focusing

This section presents the theoretical and GPT simulation results of the electron trajectories and bunch parameters upon focusing via an APL. In the first part, the theoretical approach for the lens focusing of a divergent electron beam is explained. In the second part, for several parameter scans, the simulation results are shown and compared to the theory.

5.2.1 Theoretical Treatment

The path of the electron bunch behind the plasma target can be divided into three sections, as displayed in figure 5.2.1. An electron bunch in its focus at the plasma exit drifts freely (I) towards the active plasma lens, where a radial magnetic field focuses the bunch (II). After a second drift distance (III), the bunch reaches its focal point.

Thomson yield and bandwidth optimisation determines the best electron beam waist in the focus for the Thomson interaction (Sec. 4.7). At each point along its path, the bunch is defined via the Courant-Snyder parameters (CSP, Sec. 2.2.2). This calls for a treatment via the matrix formalism [45, 46, 67, 68]. When given the according transfer matrix of form $([M_{11}, M_{12}], [M_{21}, M_{22}])$, the CSPs transform as follows:

$$\begin{pmatrix} \beta_1 \\ \alpha_1 \\ \gamma_1 \end{pmatrix} = \begin{pmatrix} M_{11}^2 & -2M_{11}M_{12} & M_{12}^2 \\ -M_{21}M_{11} & 1 + 2M_{12}M_{21} & -M_{12}M_{22} \\ M_{21}^2 & -2M_{22}M_{21} & M_{22}^2 \end{pmatrix} \begin{pmatrix} \beta_0 \\ \alpha_0 \\ \gamma_0 \end{pmatrix} \quad (5.2.1)$$

The free drift transition matrix is defined as [45]

$$M_{\text{FD}} = \begin{pmatrix} 1 & s \\ 0 & 1 \end{pmatrix} \quad (5.2.2)$$

Hence, according to equation (5.2.1) and $M_{11} = 1$, $M_{12} = s$, $M_{21} = 0$, and $M_{22} = 1$, one obtains the free-drift transformation matrix for the CSPs:

$$\begin{pmatrix} \beta_1 \\ \alpha_1 \\ \gamma_1 \end{pmatrix} = \begin{pmatrix} 1 & -2s & s^2 \\ 0 & 1 & -s \\ 0 & 0 & 1 \end{pmatrix} \begin{pmatrix} \beta_0 \\ \alpha_0 \\ \gamma_0 \end{pmatrix} \quad (5.2.3)$$

The influence of the active plasma lens can be determined in one of two ways. The first approach is the thin-lens approximation which is used by van Tilborg et al. [35] to determine the focal length. This approximation is applicable, if the length of the lens is much smaller than the focal length, i.e. $\frac{1}{kL} \gg L$. In this case, the lens thickness is negligible and an infinitesimally thin lens with the following transfer matrix acts on the beam parameters:

$$M_{\text{TL}} = \begin{pmatrix} 1 & 0 \\ -\frac{1}{f} & 1 \end{pmatrix} \xrightarrow{\text{eq. (5.2.1)}} M_{\text{TL}} = \begin{pmatrix} 1 & 0 & 0 \\ \frac{1}{f} & 1 & 0 \\ \frac{1}{f^2} & \frac{2}{f} & 1 \end{pmatrix} \quad (5.2.4)$$

The CSPs after a free drift, a thin active plasma lens and free drift to focus transform as follows:

$$\begin{pmatrix} \beta \\ \alpha \\ \gamma \end{pmatrix} = M_{\text{FDII}} \quad M_{\text{TL}} \quad M_{\text{FDI}} \quad \begin{pmatrix} \beta_0 \\ \alpha_0 \\ \gamma_0 \end{pmatrix} \quad (5.2.5)$$

$$= \begin{pmatrix} 1 & -2s_I & s_I^2 \\ 0 & 1 & -s_I \\ 0 & 0 & 1 \end{pmatrix} \begin{pmatrix} 1 & 0 & 0 \\ \frac{1}{f} & 1 & 0 \\ \frac{1}{f^2} & \frac{2}{f} & 1 \end{pmatrix} \begin{pmatrix} 1 & -2s_{II} & s_{II}^2 \\ 0 & 1 & -s_{II} \\ 0 & 0 & 1 \end{pmatrix} \begin{pmatrix} \beta_0 \\ \alpha_0 \\ \gamma_0 \end{pmatrix} \quad (5.2.6)$$

However, as the bunch needs to be small ($\sim \mu\text{m}$) for the Thomson interaction, small focal lengths are required. Therefore, the thin-lens matrix approach is no longer a suitable tool for a first approximation of the lens parameters necessary for the simulation (cp. Fig. 5.2.1).

The second approach is to derive the transfer matrix of the plasma lens from that of a quadrupole. As the quadrupole focuses in one direction and defocuses in the other, while the plasma lens focuses in both directions, only the focusing part of the quadrupole

transition matrix is used [46]:

$$M_{\text{APL}} = \begin{pmatrix} \cos(\phi) & \frac{1}{\sqrt{|k|}} \sin(\phi) \\ -\sqrt{|k|} \sin(\phi) & \cos(\phi) \end{pmatrix}$$

$$\xrightarrow{\text{eq. (5.2.1)}} M_{\text{APL}} = \begin{pmatrix} \cos^2(\phi) & -\frac{2}{\sqrt{|k|}} \cos(\phi) \sin(\phi) & \frac{1}{|k|} \sin^2(\phi) \\ \sqrt{|k|} \cos(\phi) \sin(\phi) & 1 - 2 \sin^2(\phi) & -\frac{1}{\sqrt{|k|}} \sin(\phi) \cos(\phi) \\ |k| \sin^2(\phi) & 2\sqrt{|k|} \cos(\phi) \sin(\phi) & \cos^2(\phi) \end{pmatrix}$$

with $\phi = L\sqrt{|k|}$, where L is the length of the plasma lens and k its strength parameter.

I. Free Drift

The initial electron beam size $\sigma_{r,i}$ at the plasma exit and its emittance determine the bunch size at entering the lens after a free drift of length z_0 according to equation (5.2.3):

$$\sigma_r(z_0) = \sqrt{\left(\frac{\varepsilon_n z_0}{\gamma \sigma_{r,i}}\right)^2 + \sigma_{r,i}^2} \quad (5.2.7)$$

with $\sigma_{\theta,i} = \varepsilon_n / (\sigma_{r,i} \gamma)$.

II. Active Plasma Lens

In the thin lens approximation, as utilised in reference [35], a first approximation on the bunch size development can be made.

a: Collimation

Now, as the beam is divergent, the formulae as given before need to be altered, as they hold for a collimated electron bunch. In the first part of the lens, the bunch is collimated over the distance L_{coll} . With the focusing strength k and eq. (5.1.4) it holds;

$$L_{\text{coll}} = \frac{1}{k f^*} = \frac{1}{k(z_0 + L_{\text{coll}}/2)}$$

with f^* the focal length of a collimated beam traveling in $-z$ direction with focus at the plasma exit. This yields the collimation length:

$$L_{\text{coll}} = -z_0 + \sqrt{z_0^2 + \frac{2}{k}} \quad (5.2.8)$$

b: Focusing

With the total length of the lens L and the collimation length L_{coll} the effective lens length for bunch focusing is obtained:

$$L_{\text{foc}} = L - L_{\text{coll}}$$

III. Free Drift to Focus

The focal length according to eq. (5.1.4) can then be calculated from the lens' total length reduced by the collimation length.

$$f = \frac{1}{kL_{\text{foc}}} = \frac{1}{k(L - L_{\text{coll}})} \quad (5.2.9)$$

The β function at position s , is given as:

$$\beta(s) = \beta_0 + \frac{s^2}{\beta_0} = \frac{\sigma_s^2}{\varepsilon}$$

with $\alpha_0 = 0$, $\beta_0 = \sigma_0/\varepsilon$ in the focus, $\varepsilon = \varepsilon_n/\gamma$ the emittance and σ_s the transversal rms beam size at position s , where σ_0 is the focal beam waist. A shorter focal length yields a smaller focal waist, according to:

$$f = \frac{\gamma\sigma_0}{\varepsilon_n} \sqrt{\sigma_s^2 - \sigma_0^2} \quad (5.2.10)$$

In the following, theoretical results via the matrix formalism are compared to GPT simulations. The influence of the individual lens parameters on focal length and waist is established.

5.2.2 Parameter Scans - Focusing via an Active Plasma Lens

The focusing strength and thus the focal length and waist obtained from an APL depend on several parameters. These are the lens parameters on the one hand, and the bunch parameters on the other hand. The lens is defined by its position after the plasma exit z_0 , its length L , the current I_0 , and its radius r_0 . The relevant bunch parameters are the emittance ε_n , the kinetic energy γ , and the bunch's energy spread σ_γ/γ . In this section, the influence of these parameters is analysed and the theoretical model is compared to the result of the GPT simulations.

Lens Parameters

The current I_0 and the capillary radius r_0 determine the magnetic-field gradient within the lens. Figure 5.2.2 displays the focal position z_f and the focal waist $\sigma_{r,0}$ as functions of the current (a) and the radius (b). The magnetic-field gradient increases with increasing magnitude of the current, leading to a shorter focal length and smaller bunch waist. For different capillary radii of 300 μm (dashed lines and triangles) and 200 μm (straight lines and circles), different lens currents lead to the same focal length and waist, as the focusing strength depends on the magnetic field gradient. Consequently, different parameter combinations can yield equal results. With increasing lens radius, the focusing strength decreases, so that larger focal lengths and waists are obtained. Again, equal

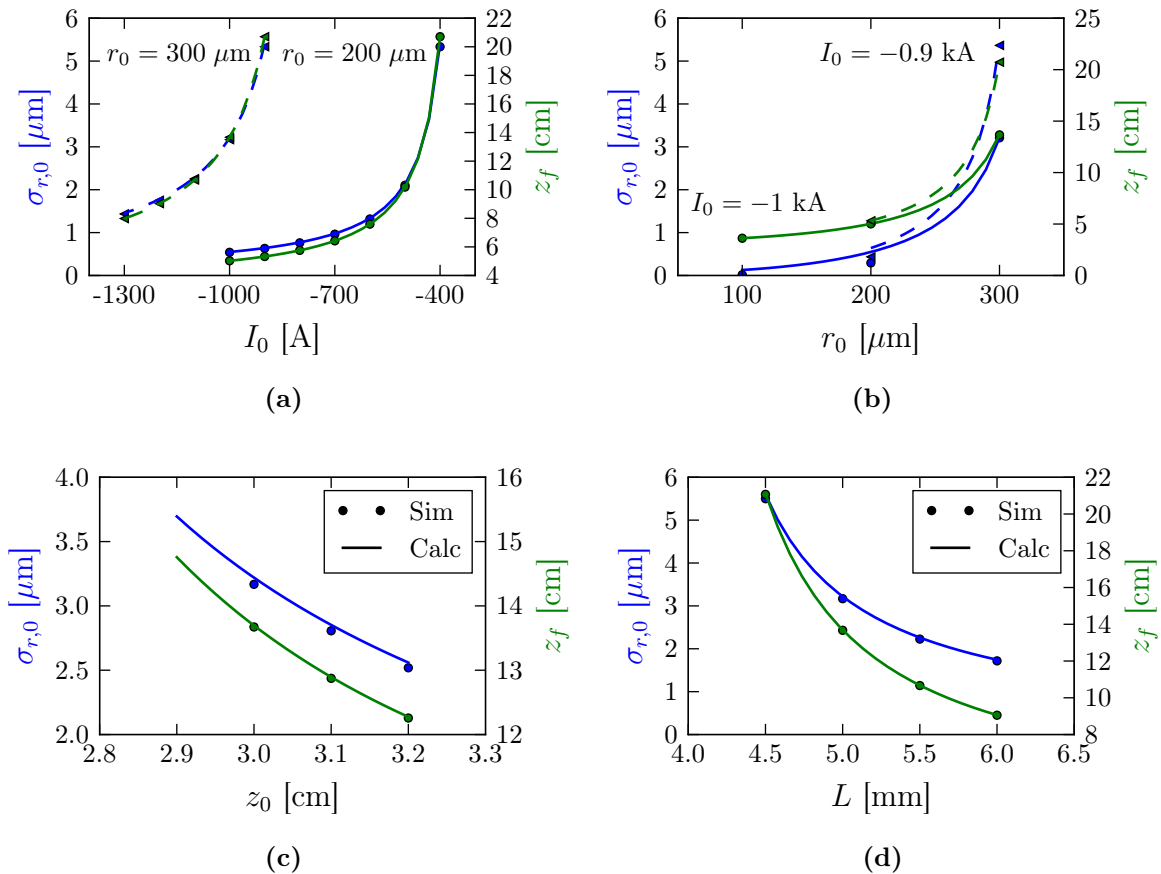


Figure 5.2.2: Electron bunch focal waist $\sigma_{r,0}$ (blue) and focus coordinate z_f (green) as a function of the lens current (a), radius (b), longitudinal capillary position (c), and capillary length (d). The simulative (markers) and theoretical (lines) results are presented for $r_0 = 200 \mu\text{m}$ (lines and circles) and for $r_0 = 300 \mu\text{m}$ (dashed lines and triangles) in the I_0 variation. For the variation of r_0 , the simulative (markers) and theoretical (lines) results are presented for $I_0 = -1 \text{ kA}$ (lines and circles) and for $I_0 = -0.9 \text{ kA}$ (dashed lines and triangles).

results are obtained from different lens currents -0.9 kA (dashed lines and triangular markers) and -1 kA (straight lines and circular markers).

The influence of spatial parameters, i.e., the capillary position z_0 and the capillary length L is displayed in figure 5.2.2 (c, d, respectively). With smaller distance from the plasma exit, i.e. the electron initial focal point, the focal length and waist increase. This is due to the smaller entrance bunch waist, while the bunch divergence is identical. The capillary length determines the distance over which the bunch experiences the magnetic field. Hence, with increasing length, the exit divergence is increased, leading to smaller focal lengths and waists with increasing length.

Bunch Parameters

The focal length of the APL is energy-dependent (cp. Eq. (5.1.5)): Electrons with higher kinetic energy experience a weaker focussing due to a lower strength parameter k of the lens, and vice versa. The focal length f is proportional to the kinetic energy of the

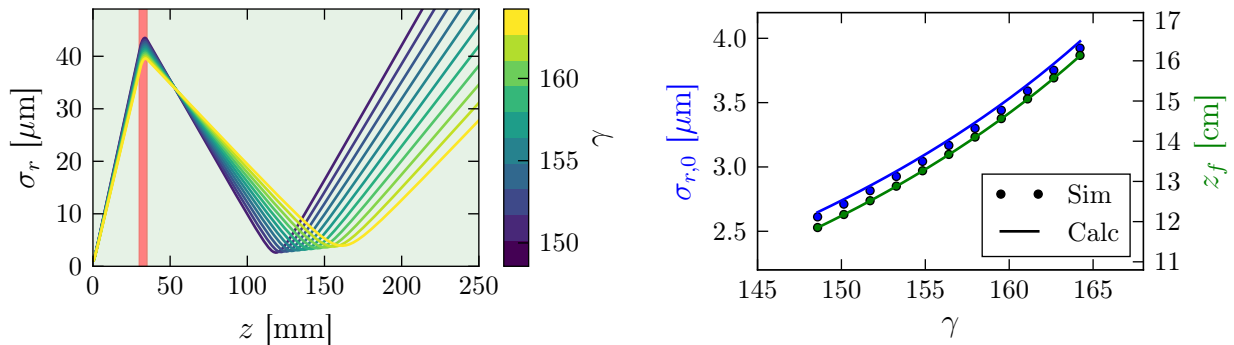


Figure 5.2.3: Left: Bunch size as a function of the distance z from the plasma target for electron bunches of different energy γ and energy spread $\sigma_\gamma/\gamma = 0$. The free drift is indicated by the green, the plasma lens by the red shaded area. Right: Focal length z_f (green) and focal electron waist $\sigma_{r,0}$ (blue) as functions of the bunch Lorentz factor γ . The plasma lens is positioned at $z_0 = 3$ cm behind the plasma target with parameters: $I_0 = 1$ kA, $L = 5$ mm, $r_0 = 300$ μm .

electron γ . Consequently, higher-energetic electrons have a larger focal waist than lower-energetic electrons. Figure 5.2.3 displays the evolution of the bunch waist σ_r in the APL setup (left) and the according simulated and calculated focal waists $\sigma_{r,0}$ and longitudinal focus coordinates z_f (right) for electron bunches of different kinetic energy and no energy spread. The APL parameters are $I_0 = -1000$ A, $r_0 = 300$ μm and $L = 5$ mm. The capillary is positioned at $z_0 = 3$ cm behind the plasma exit. The γ dependence of the lens focusing strength leads to a short focal length at accordingly smaller focal waist (cp. Eq. (5.2.10)) for electrons of lower energy. Higher-energetic electrons experience a weaker strength parameter and therefore obtain a larger focal waist at larger focal length.

Obviously, this energy-dependent focusing has an effect on electron bunches of non-zero energy spread. Figure 5.2.4 shows the development of the electron waist through a plasma-lens setup (a,c,d) for bunches of different energy spread and emittance values of $\varepsilon_n = 0.2$ mm mrad (solid lines), $\varepsilon_n = 0.5$ mm mrad (dashed lines). As a smaller focal length is accompanied by a larger divergence, the total bunch waist development is asymmetric. Behind the focal point² the bunch divergence is larger than before. The point of minimum bunch waist may be denoted as the total or mean focal point. However, due to the asymmetry, electrons of energy $\gamma = \bar{\gamma}$ are focused behind that point. The position of the total focus is thus dominated by low-energy electrons. Therefore, with increasing energy spread, the focal point is shifted longitudinally towards the lens and the mean focal waist increases. This is illustrated in figure 5.2.4(d). Figure 5.2.4(b) displays the total focal length \bar{f} (green) and the total focal waist $\bar{\sigma}_{r,0}$ (blue) as functions of the rms energy spread σ_γ/γ .

Different focusing strength for different electron energies lead to a chromatic emittance growth within the plasma lens (cp. Ch. 2.2.2). This is illustrated in figure 5.2.5 for different energy spread values of the bunch. Chromatic emittance growth, in this case, is not a negative effect, but a measure for the chromaticity effect. With different focusing

²The focal point of a bunch with energy spread is defined as the point of minimum bunch waist.

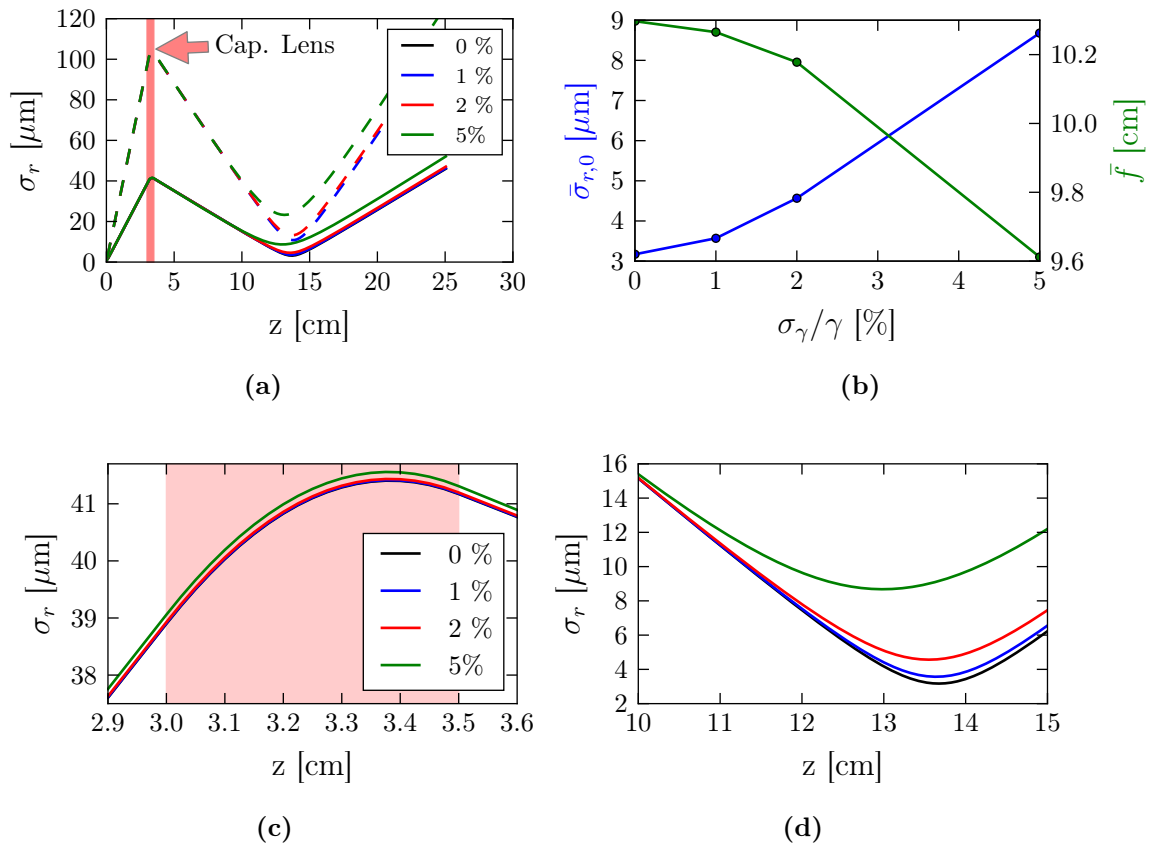


Figure 5.2.4: Electron bunch size as function of the distance from the plasma target for different electron energy spreads $\sigma_\gamma/\gamma = 0, 1, 2$ and 5% rms (a). The bunch was simulated with an initial emittance $\varepsilon_n = 0.2$ mm mrad (straight lines) and 0.5 mm mrad (dashed lines). (b) Total focal length \bar{f} (green, not to be confused with the focus position z_F) and focal spot size $\bar{\sigma}_{r,0}$ (blue) as functions of the bunch energy spread. The bottom row displays a zoom into the different bunch size evolution within the plasma lens (c) and the resulting focal waists (d).

strength, the electron waist and divergence of the electrons is energy-dependent. Consequently, the total bunch governs a larger area in the phase space, while the emittance, i.e. the phase-space area, of electrons at the mean energy is constant.

5.3 Thomson Source without Focusing Optics

The results of the design study (Ch. 4.2) show that electron-waist (σ_r) and -divergence (σ_θ) variation has a significant impact on the photon yield and bandwidth of the Thomson radiation spectrum within a cone. For most scenarios under investigation, the parameter region around $\sigma_r/w_0 \approx 0.1 - 0.2$ and $\sigma_\theta \approx 0.5 - 1$ mrad provides the best yield-bandwidth ratio. The electron bunch at plasma exit already possesses a low emittance at low divergence and bunch waist. Moreover, scans on the longitudinal spatial delay of the electron focus with respect to the laser focus display no significant yield loss (cp. Fig. 4.2.18). This motivates the comparison of the impact of an un-focused bunch, namely directly behind the plasma target, with a focused bunch on the Thomson-spectrum characteristic.

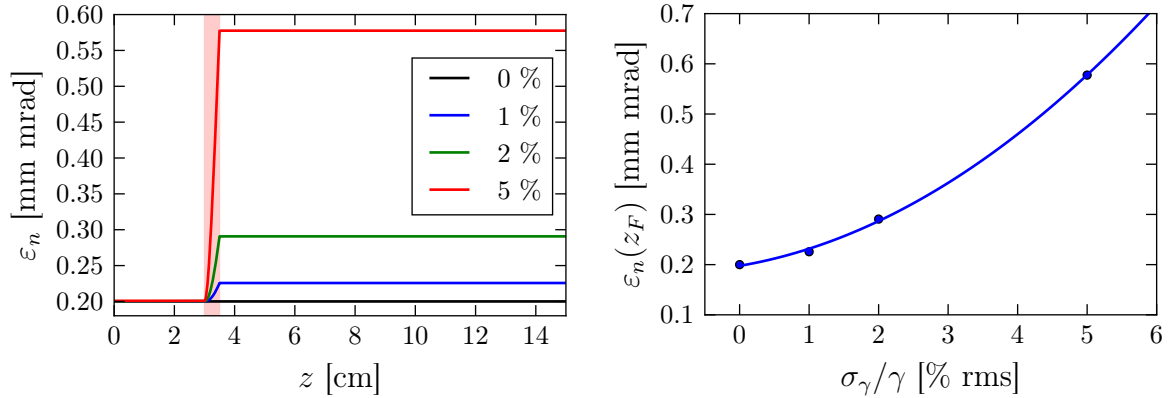


Figure 5.2.5: Chromatic emittance growth within the capillary. Left: Normalised emittance evolution as a function of the distance from the target z for an electron bunch of energy spread $\sigma_\gamma/\gamma = 0, 1, 2$ and 5 % rms. The capillary position is indicated as red shaded area. Right: Normalised emittance at the focus $\varepsilon_n(z_F)$ as a function of the electron bunch energy spread.

In this chapter, the X-ray spectra of an electron-laser interaction close to the plasma exit are presented and will later serve as a benchmark for the application of beam optics, in our case of chromatic focusing via a plasma lens.

For all simulation scenarios, the emittance is set to $\varepsilon_n = 0.2$ mm mrad. The simulated electron bunch starts in its focus with a focal waist of $\sigma_{r,0} = 1$ μm . From this, a divergence of 1.28 mrad is obtained. On this basis, different electron bunch energy spreads are compared. The laser has a constant FWHM duration of 4 ps and a bandwidth of 60 nm.

Depending on the accelerator beamline design, a Thomson source with its interaction immediately behind the plasma target might not be realisable. Therefore, an important issue is the dependence of the source parameters on the distance from the plasma exit, i.e. from the electron bunch's focal point. Typically, in the simulations the delay is chosen in such a way that the electromagnetic field of the laser at the initial bunch position can be assumed to be negligible. A delay of 1.5τ has shown to be a good criterion (cp. Sec. 3.3). Therefore, temporal delays of $\Delta t_1 = 1.5\tau = 6$ ps and $\Delta t_2 = 2\Delta t_1 = 12$ ps are simulated. The different scenario parameters, as well as photon yield and bandwidth within a ± 0.5 mrad cone, are given in table 5.3.1. For a laser of $w_0 = 5$ μm , the photon yield N_γ (blue) and the bandwidth (red) as functions of the rms electron bunch energy spread are displayed in figure 5.3.1 (left).

The photon yield displays no significant dependence on the bunch energy spread. This comes as no surprise, as the energy spread has no impact on the yield (cp. Sec. 4.2.6). Furthermore, it is assumed that for a drift on this short scale, the chromatic emittance growth (Sec. 5.2.2) is marginal, as well, thus excluding an energy-spread impact on the divergence. For a constant divergence, the longitudinal overlap of laser and electron bunch, as well as the fraction of photons emitted into the cone, is constant as well. There is, however, an obvious yield decrease with increasing delay. If the delay is twice as large,

scenario	w_0 [μm]	$\Delta\gamma/\gamma$ [% rms]	delay [ps]	N_γ [10^5]	BW [%]
1	12	1	6	1.92	11.42
2	12	1	12	1.45	10.46
3	5	1	6	3.37	8.48
4	5	1	12	1.97	7.23
5	5	5	6	3.38	23.89
6	5	5	12	1.97	23.69
7	5	10	6	3.26	45.04
8	5	10	12	1.88	43.98

Table 5.3.1: Parameter sets and photon yield and bandwidth within a ± 0.5 mrad cone for a Thomson interaction behind the plasma target. For all scenarios, the electron bunch has an emittance $\varepsilon_n = 0.2$ mm mrad and an initial focal waist at plasma exit of $\sigma_{r,0} = 1$ μm . The laser duration is $\tau = 4$ ps, and its bandwidth is $\Delta\lambda = 60$ nm. The laser waist w_0 , the electron bunch rms energy spread σ_γ/γ are varied, as well as the distance of the laser focus, which is the interaction centre, from the target exit. The distance is given as a temporal delay, denoting the time at which the electron bunch meets the laser centre.

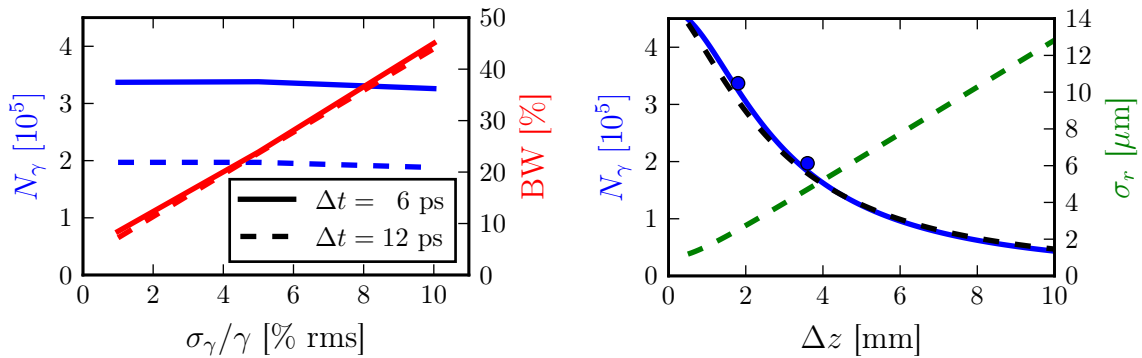


Figure 5.3.1: Left: Simulated cone photon yield N_γ (blue) and bandwidth (red) as functions of the electron bunch rms energy spread σ_γ/γ for a temporal delay of $\Delta t = 6$ ps (straight lines) and 12 ps (dashed lines). The delay is the electron bunch flight time for the distance from the target exit, i.e. the electron focus, to the Thomson interaction centre, i.e. the laser focus. (6ps $\hat{=}$ 1.8 mm, 12 ps $\hat{=}$ 3.6 mm.) Right: Calculated (lines) and simulated (markers) cone yield N_γ and calculated electron waist in the laser focus as functions of the distance from target Δz . The black dashed line represents the theoretical results applying the mean electron waist to equation (4.1.13), the blue line is obtained from the empirical formula (4.3.1).

the cone yield is reduced to 60 %. The opposite dependency is observed for the cone bandwidth. The delay has no impact, while the bandwidth increases with increasing energy spread. A large energy spread dominates the Thomson bandwidth, so that for increasing energy spread, it coincides with this bandwidth contribution, given by equation (4.1.19).

The yield loss due to an increased delay is explained by the worsened overlap of electron and laser. As established in the previous chapter 4, this is due to a larger electron beam resulting in decreased effective a_0 , and thus reduced photon emission. In the regarded scenario, the divergence is constant and not coupled to the bunch waist. The evolution of the latter with drift distance Δz is given by equation (5.2.3), so that for $\Delta z_1 = c\Delta t_1 = 1.8$ mm, $\sigma_r(\Delta z_1) = 2.5$ μm and for $\Delta z_2 = c\Delta t_2 = 3.6$ mm, $\sigma_r(\Delta z_2) = 4.7$ μm are obtained for the bunch size at the interaction centre. In section 4.2.4, it is shown that the yield depends on the effective a_0 , as seen by the electrons during the interaction. This effective a_0 is identical for a non-divergent beam of constant waist and for a divergent electron beam of equal mean waist, given by (5.2.7). For a divergent beam, the mean waist is the waist at the interaction centre, i.e. the laser focal point. Consequently, the total photon yield in dependence of the distance from the plasma-target exit can be calculated using equation (4.1.3) with $\sigma_{e,0} = \sigma_r(\Delta z)$ and a small emittance value $\varepsilon_n > 0$ to give the total yield $N_{\gamma,\text{tot}}(\Delta z)$. In order to determine the yield within the cone, the divergence needs to be taken into account, again. From section 4.3.1, it is established that the effect of the divergence on the cone yield is independent of the laser parameter (cp. Fig. 4.3.7), so that for an electron bunch of $\gamma = 156.4$ and a cone of ± 0.4 mrad, the cone yield can be estimated with help of the empirical formula (4.3.1). Alternatively, equation (4.1.13) can be used and numerically solved for a constant divergence $\sigma_\theta = 1.28$ mrad. The results are displayed in figure 5.3.1 (right) where the cone yield N_γ (blue: empirical formula, black: Eq. (4.1.13)) and the according electron waist (green dashed) are displayed as functions of the distance Δz from the plasma target. The cone yield values as obtained from the simulations are included for means of comparison (markers). As established in section 4.2.8, a spatial delay of the electron focal point with respect to the laser focal point hardly reduces the photon yield for small enough deviations. Therefore, for a distance of $c\tau/2 = c2$ ps = 0.6 mm from target, the Thomson source cone yield is equivalent to the optimum as obtained from figure 4.4.3 for constant $\tau = 4$ ps. This is because the electron waist at this point coincides with the determined optimum electron waist for a laser of $w_0 = 5$ μm (cp. Fig. 4.4.1).

The experimental realisation of a Thomson source with electron-laser interaction immediately behind the plasma target might be difficult. Apart from the possibly hindering position of other physical components of the beamline, it is typically aimed at prohibiting a laser pulse to enter the plasma target and the beamline in counter-propagating geometry. Unfortunately, already at small distances, the worsening overlap leads to a significantly decreased photon emission. The cone yield drops to more than half its value,

if the interaction centre is 3 mm behind the plasma exit. However, if experimentally possible, interaction behind the plasma, thus exploiting the already well-enough electron parameters at this point, gives the same photon yield. It consequently represents a simpler alternative to a Thomson setup including a focusing element, such as a plasma lens. Nevertheless, this applications is limited by the electron bunch's energy spread. With the application limiting the tolerable Thomson bandwidth to below $\approx 15\%$ FWHM, the electron energy spread must not exceed $\approx 2.5\%$ rms.

In the design of the dedicated Thomson source, the bandwidth represents the more crucial parameter. As described in this thesis' introduction, high-repetition lasers can increase the photon yield per time unit, thus compensating for a possibly low shot photon count. The Thomson bandwidth, on the other hand, is dominated by the electron bunch energy spread. Analogously to Fuchs et al. [34], chromatic focusing provides the possibility of decreasing the effective electron energy spread. There, a quadrupole lens doublet was implemented for bunch focusing, in a laser-plasma driven undulator source. In the following section, an active plasma lens is investigated in this regard.

5.4 Thomson Source with Plasma-Lens Focusing

In this section, the laser interaction with the APL-focused electron bunch is examined. The electron-bunch trajectory through the lens and in the laser field are determined with the General Particle Tracer (GPT). The Thomson radiation is then calculated via Clara2. In section 5.4.1, the chromatic focusing effect on the Thomson spectrum in dependence of the electron-bunch energy spread is examined. Thereupon, section 5.4.2 is concerned with non-ideal effects of the electron bunch, i.e. transversal offset and pointing.

5.4.1 Chromatic Focusing Effect on the Thomson Spectrum

Electron-Bunch Focusing

For the analysis of the effect of chromatic focusing via the plasma lens on the Thomson spectrum, electron bunches of $\sigma_\gamma/\gamma = 0, 1, 5$ and 10% rms energy spread are propagated through the setup (cp. Fig. 5.2.1). The maximum Thomson bandwidth is $\Delta E_\gamma/E_\gamma \leq 15\%$ FWHM. This requires the bandwidth of the simulation to fulfil the condition

$$\frac{\Delta E_\gamma}{E_\gamma} \Big|_{\sigma_\gamma/\gamma=0\%} \leq \sqrt{\left(\frac{\Delta E_\gamma}{E_\gamma}\right)^2 - \left(\frac{2\Delta\gamma}{\gamma}\right)^2} \quad (5.4.1)$$

with $\Delta\gamma/\gamma = 2\sqrt{2\ln 2}\sigma_\gamma/\gamma$. For 5% rms energy spread, the bandwidth must lie below 11% FWHM. In accordance with these demands, the laser configuration with $\tau = 4$ ps FWHM, $w_0 = 5$ μm , and $a_0 = 0.37$ is chosen, taken from figure 4.4.3. As electrons of different energy experience different focusing forces, introducing an energy spread to the

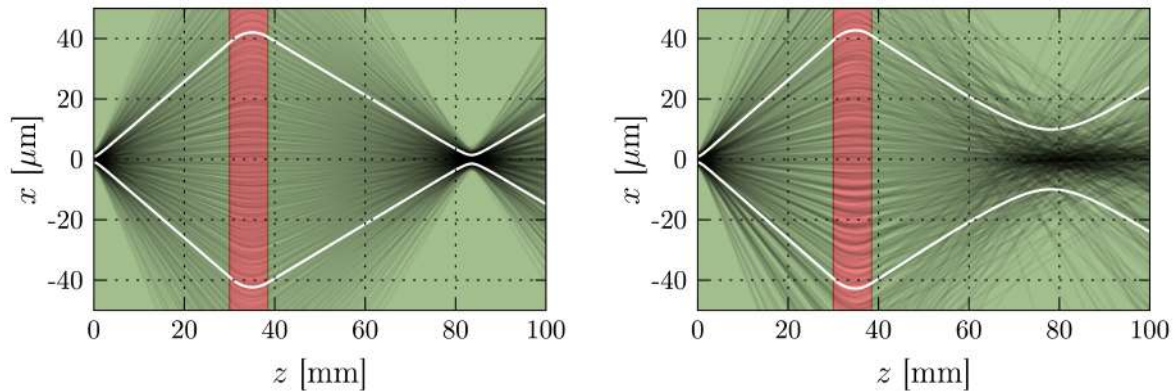


Figure 5.4.1: Electron trajectories (black) and rms bunch waist σ_x (white) evolution through the setup in the $x - z$ plane for an electron bunch without energy spread (left) and with 10 % rms energy spread. Sections of free drift are displayed in green, the capillary lens in red.

electron bunch results in an increase in the focal spot size at a decreased focal length (cp. Fig. 5.2.4b). In order to enhance the spectral response of the Thomson interaction at the target source energy of 150 keV, the contribution from the electrons of $\gamma = 156.4$ needs to be optimised. Therefore, the lens parameters (z_0, I_0, r_0, L) are set to give the determined optimum electron waist and divergence in the focus for the target electron energy which is also chosen as the mean bunch energy in the simulation:

$$I_0 = -750 \text{ A}$$

$$r_0 = 300 \text{ } \mu\text{m}$$

$$L = 8.5 \text{ mm}$$

$$z_0 = 3 \text{ cm}$$

The effect of different energy spreads at these lens parameters is shown in figure 5.4.1. For 0 % energy spread, the focal length is at $z \approx 84 \text{ mm}$, and the focal waist is small ($\sim 1.4 \text{ } \mu\text{m}$). If the energy spread is increased to 10 %, the different focusing of the electrons leads to a broadening of the region where the single trajectories cross $x = 0$. Consequently, the focal area appears to be smeared out. The focal length, defined as the point of minimum mean bunch waist is placed closer to the capillary lens for larger energy spread. A more detailed analysis of this focal region is based on figure 5.4.2. Colouring the trajectories according to their individual energy reveals that electrons of the target energy are in fact focused at the focal point of a 0 % rms energy spread electron bunch, and the total bunch focus shifts towards the lens. One can therefore distinguish between the *total* focal point and waist of the bunch, and the *target* focal point and waist including electrons at the target energy: With the lens parameters given above, the following focal

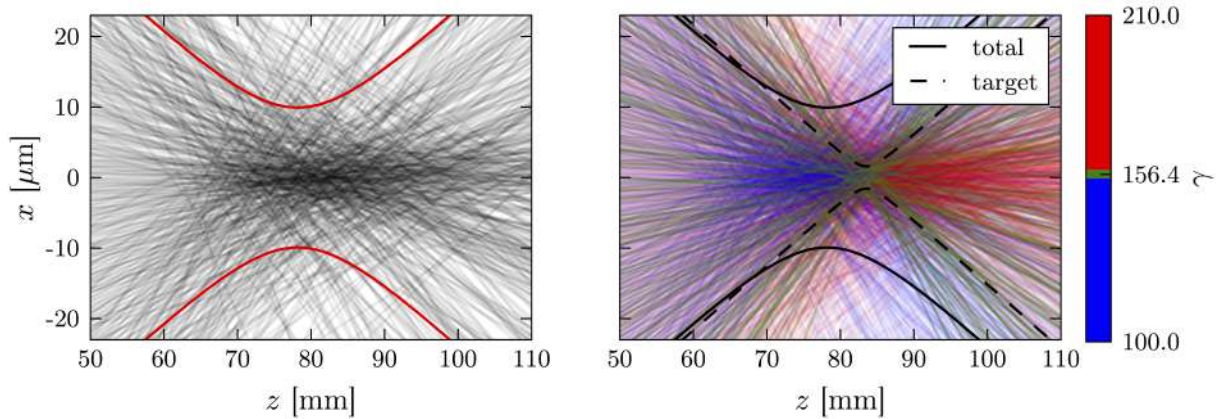


Figure 5.4.2: Zoom into the focus region of the electron bunch of $\sigma_\gamma/\gamma = 10\%$. On the left side, the trajectories are displayed in black and the rms bunch waist in red. On the right side, trajectories are coloured according to the kinetic energy of the electron, with electrons of kinetic energy equivalent to the mean kinetic bunch energy $\gamma_i = \bar{\gamma}_b$ in green, lower and higher energetic electrons in blue and red, respectively.

lengths and waists are obtained:

$$\begin{aligned}\sigma_{\text{tar}} &= 1.42 \mu\text{m} \\ f_{\text{tar}} &= 83.57 \text{ mm} \\ \sigma_{\text{tot}} &= 9.9 \mu\text{m} \\ f_{\text{tot}} &= 78.23 \text{ mm}\end{aligned}$$

This notation is used in the following for the analysis.

Thomson Interaction and Response Function

As established in the previous chapter [4](#), the electron bunch's mean waist and the divergence play an important role in the contribution to the Thomson spectrum within a cone. Furthermore, the synchrotron angle of the single-electron emission will increase with decreasing electron energy ($\propto 1/\gamma$). In addition to the decreased contribution due to the stronger focusing and thus higher divergence, single electrons of low energy will also contribute less due to the emission angle. Consequently, low-energy electrons will contribute the least to the spectrum. In order to quantify the contribution of the single electrons according to their energies, a response function is defined, analogously to Fuchs et al. [\[34\]](#). The response function is the normalised number of emitted photons as a function of the electron's Lorentz factor γ . The normalisation is performed with respect to the emission of a single on-axis electron at target energy. Figure [5.4.3](#) demonstrates the effect of the synchrotron-angle and divergence dependence of the photon emission due to different electron energies. In an unrealistic scenario, where all electrons are focused onto the same spot at identical spot size, electrons of highest γ contribute more to the spec-

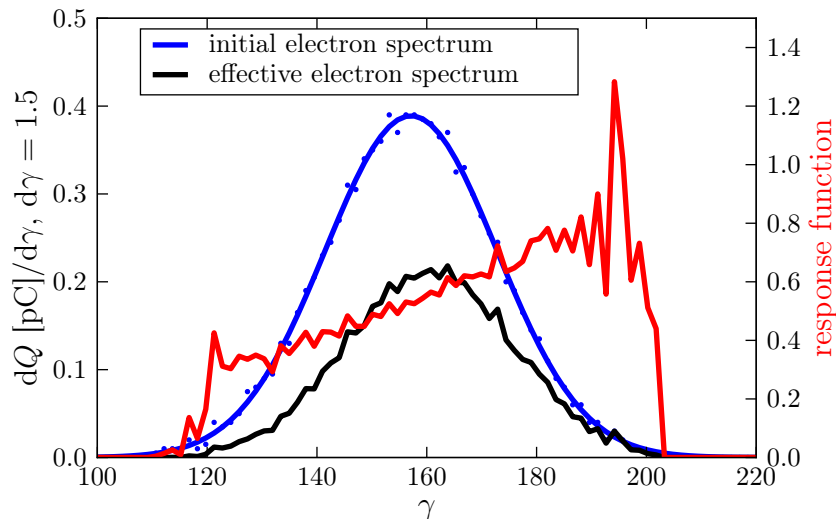


Figure 5.4.3: Electron spectra and response function for an energy-independent focus. Initial (blue) and effective (black) electron spectra with the according response function (red) are displayed as a function of the Lorentz factor γ . The electron bunch has an energy spread of $\sigma_\gamma/\gamma = 10\%$ rms. All electron energy slices of the bunch are focused onto the same focal point at equal spot size. This unphysical scenario is supposed to isolate the effect of the electron energy on the contribution to the Thomson spectrum.

trum, leading to an asymmetric response function. This is due to the smaller synchrotron angle and divergence for higher kinetic energy which both increase the yield within the confined cone (cp. Ch. 4).

The interaction with the laser and the lens-focused electron bunch is simulated in two scenarios. Firstly, the laser is configured so that its focal point coincides with the bunch's total focus, and secondly, it is set to coincide with the target focus. The respective response functions of an electron bunch with $\sigma_\gamma/\gamma = 10\%$ for the two scenarios are shown in figure 5.4.4. Here, the response function is normalised with respect to the response of an electron bunch of zero energy spread focused by the APL. Both response functions possess a sharp peak compared to the scenario with energy-independent focus. Consequently, due to the longitudinal spread of the focal points of electrons of different energies, as well as the optimisation of the target-energy electron parameters, their contribution is increased with respect to the other energies. The synchrotron-angle and divergence effect (cp. Fig. 5.4.3) is observable as well, as the response functions are asymmetric with a higher response at high energies than at lower energies. Shifting the laser focus to the total electron-bunch focus leads to a response function of lower peak response which is shifted towards lower energies. A central finding of the previous chapter was that the photon emission of a single electron is describable only by the effective a_0 it experiences, and this translates to the mean electron waist being the determining factor. This offers an explanation for the different total and target response functions. At the total focus, electrons of the target energy and of higher energies are convergent and their mean waist is larger than the determined optimum waist. Their contribution is thus lessened. The electrons of focal

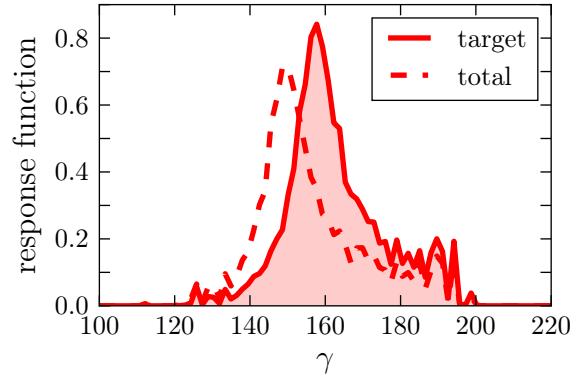


Figure 5.4.4: Response function, i.e. number of photons emitted into the cone as a function of γ of the electrons, for the Thomson interaction at the target focus (straight line, filled curve) and at the total bunch focus (dashed lines), as defined in figure [5.4.2](#).

point coinciding with the total focus have a Lorentz factor of $\gamma \lesssim 145$, determining the response function peak (cp. Eq. [\(2.3.10\)](#)). However, as they are at non-optimum electron waist, and, more importantly, as the charge of electrons at this energy is less than that at target energy, the response function peak is reduced, as well.

Effective Electron Spectrum and Thomson Spectrum

Multiplying the response function with the original electron spectrum returns the effective electron spectrum contributing to the Thomson spectrum. The effective electron spectra for target and total focus interaction are compared to the initial electron spectrum in figure [5.4.5](#) (left). The resulting Thomson spectra are shown for both interaction setups (right). The shape of the effective electron spectra mirrors that of the respective response functions with a peak at the electron energy of highest contribution:

$$\gamma_{\text{tar}} = 156$$

$$\gamma_{\text{tot}} = 145$$

On the one hand, it is observed that the energy spread of the effective spectra is significantly reduced with respect to the original spectrum of $\sigma_\gamma/\gamma = 10\%$ rms:

$$\frac{\sigma_\gamma}{\gamma}(f_{\text{tar}}) \approx 3\% \text{ rms}$$

$$\frac{\sigma_\gamma}{\gamma}(f_{\text{tot}}) \approx 4\% \text{ rms}$$

On the other hand, as expected, this is accompanied by a reduced total effective bunch

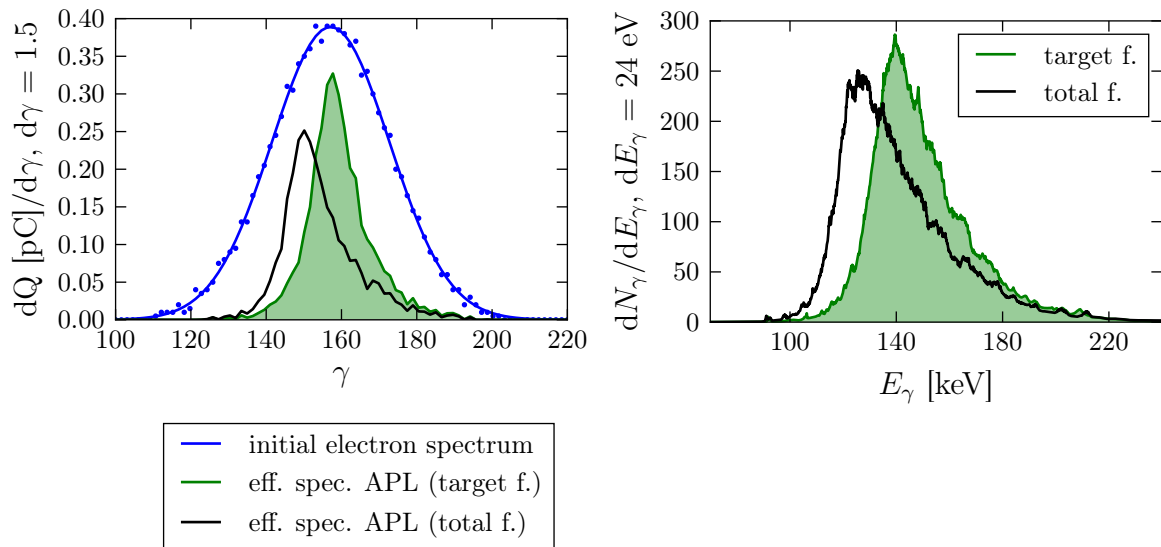


Figure 5.4.5: Initial (blue) and effective electron spectra for the interaction in the target (green) and total focus (black), given as the charge $dQ/d\gamma$ as a function of the electrons' γ parameter (left). The Gaussian electron spectrum of the initial electron bunch is compared to the effective electron spectra as obtained from the single-particle photon-emission analysis. On the right, the according Thomson spectra are shown.

charge:

$$Q_{\text{eff}}(f_{\text{tar}}) = 3.4 \text{ pC}$$

$$Q_{\text{eff}}(f_{\text{tot}}) = 2.9 \text{ pC}$$

The Thomson spectra inherit their shape from the effective electron spectra. Consequently, in case of the target interaction, the Thomson spectrum peaks at higher energies than for the total focus interaction, according to the peak γ parameter of the effective electron spectrum. With equation (2.3.10) and γ_{tot} one obtains:

$$E_{\gamma,\text{tar}} = \frac{4\gamma_{\text{tar}}^2 E_L}{1 + a_0^2/2} = 141 \text{ keV}$$

$$E_{\gamma,\text{tot}} = \frac{4\gamma_{\text{tot}}^2 E_L}{1 + a_0^2/2} = 122 \text{ keV}$$

with $a_0 = 0.37$ and $E_L = 1.55 \text{ eV}$ ³. Furthermore, the spectral height is reduced in the latter interaction scheme, due to the reduced effective bunch charge. From the reduced effective energy spread, a reduced bandwidth of the target-focus interaction spectrum is obtained.

The photon yield and bandwidth as functions of the bunch energy spread are displayed in figure 5.4.6. With increasing bunch energy spread, the cone photon yield drops, and

³Note that the photon energy is broadened predominantly by the a_0 distribution and the effective bunch energy spread. Consequently, these energies give approximately the peak, but not the maximum obtained energy.

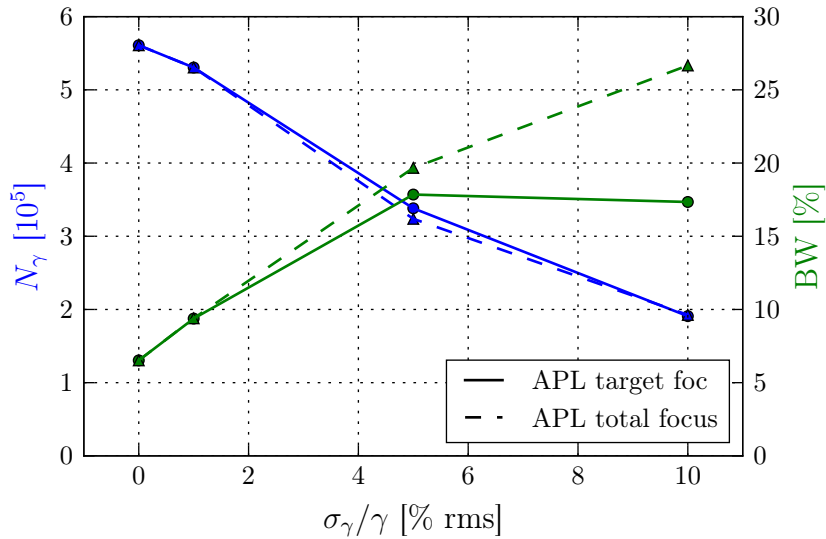


Figure 5.4.6: Cone photon yield (blue) and bandwidth (green) as functions of the electron bunch’s energy spread σ_γ/γ . The results from the target-focus interaction are displayed as straight lines, the dashed lines represent the total-focus interaction scheme.

the bandwidth rises. If the interaction region is set to the target focus, the bandwidth increase is reduced and appears to saturate above $\sigma_\gamma/\gamma = 5$ % rms. The reason for this saturation is that with further increasing bunch energy spread, electrons of even higher and lower energies are included in the initial spectrum. However, they hardly contribute to the spectrum, as they are focused even further away from the target focus, i.e. from the interaction centre. With increasing distance from the target focus, the contribution decreases, so that the Thomson bandwidth is not influenced by these electrons. Consequently, by selecting a smaller bandwidth contribution from the initial zero-energy spread configuration (Sec. 4.4), the saturation bandwidth can be adjusted to 15 %FWHM. As a result, there would be no limit on the initial bunch energy spread for the XFI application, in terms of the bandwidth. However, increasing the energy spread leads to a decrease in the number of electrons at the target energy, thus leading to the observed yield decrease. Despite the un-optimised parameters at the total focus, there is no yield loss in this case with respect to the target-focus interaction. The consequence is found in the increased Thomson bandwidth with respect to the target-focus interaction. Nevertheless, it has to be noted that independent of the position of the interaction centre with respect to the electron bunch, a significant Thomson bandwidth reduction is obtained, due to the chromatic focusing of the APL.

Summary

The chromatic focusing of the plasma lens leads to a longitudinal broadening of the focal region, according to the respective focal lengths for electrons of different energies. Optimising the electron bunch properties for electrons of the target energy (acc. to Sec. 4.4),

and choosing the target focal length as interaction centre, leads to an increased contribution to the spectrum by these target electrons, accompanied by a decreased contribution by electrons of different energy. Consequently, the effective electron spectrum, and thus the Thomson cone spectrum obtain a reduced bandwidth. The photon yield loss at increased bunch energy spread is accounted for by the reduced effective bunch charge. If the electron energy deviates enough from the target energy, the according electrons are focused too far from the interaction region to still contribute to the Thomson spectrum. This leads to a saturation bandwidth at bunch energy spreads exceeding ≈ 5 %rms. In the investigated scenario, this bandwidth saturation occurs at ≈ 17 % which is above the predefined threshold of 15 % FWHM. The maximum acceptable electron energy spread is thus $\sigma_\gamma/\gamma \lesssim 2$ % rms. If the initial electron spectrum exceeds that energy spread, this can be moderated via a different laser configuration of lower Thomson bandwidth at $\sigma_\gamma/\gamma = 0$ (Ch. 4.4). In case of a saturation bandwidth of 15 % FWHM, there is no limit on the allowed bunch energy spread by the XFI bandwidth requirements.

An interesting aspect is the tuneability of the Thomson spectrum's peak energy by means of varying the laser timing and focus position. In the case of an electron bunch of 10 % rms energy spread, a peak shift of $\Delta E_\gamma \approx 20$ keV is obtained by shifting the interaction region from the target to the total bunch focus without significant photon yield loss. The often advertised tuneability of a Thomson source is generally based on the Thomson energy equation (2.3.10). This requires to either be able to vary the electron energy, the laser wavelength, a_0 , or the observation angle. As analysed in detail in the previous chapter 4, the latter two measures either lead to a significant yield loss, a large bandwidth increase, while the first two are simply not manageable on a short time scale, as the total setup would have to be modified. Consequently, focusing via an APL holds a relatively simple possibility to change the photon spectrum by solely changing the laser focusing. Nevertheless, in case of this focal-position based source tuning, a larger energy spread has to be the accepted consequence.

These aspects are promising advantages in comparison with the results of an unfocused electron bunch (cp. Sec. 5.3). However, the application of electron beam optics is subject to non-ideal effects, such as position and angular jitter of the bunch. These are evaluated in the following section.

5.4.2 Electron Bunch Offset and Pointing

The electron bunch is accelerated by the driver laser which is subject to non-ideal effects, such as angular deviation (pointing) and spatial offset from the original propagation axis. The electron bunch is assumed to inherit the positional and pointing jitter from the driver laser (Sec. 3.2). In this section, the effect of an offset and pointing angle of the bunch in the plasma-lens setup for the Thomson source properties is examined.

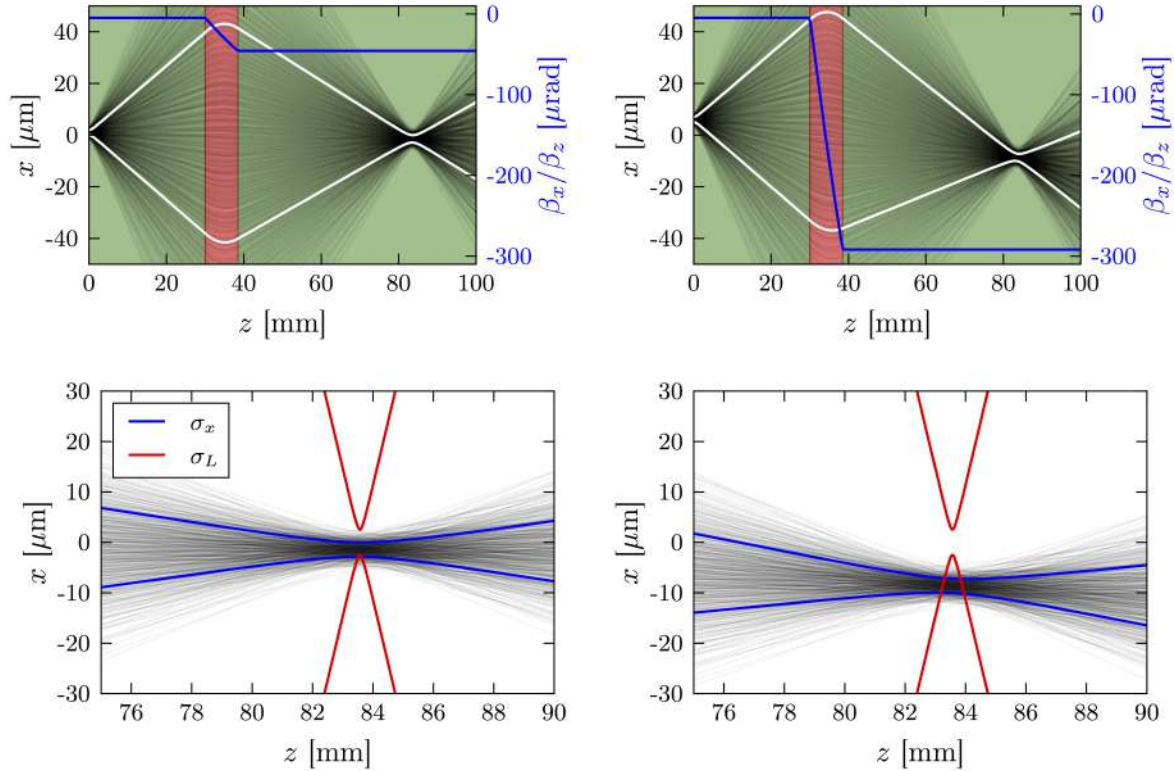


Figure 5.4.7: Electron trajectories (black) and bunch waist (white) through the setup for an electron bunch offset of $1 \mu\text{m}$ (left) and $6 \mu\text{m}$ (right) for an electron bunch of zero energy spread. The blue lines show the change in the mean angle of the bunch propagation with respect to the x axis. A zoom into the focal region shows the laser focal waist (red) and electron waist (blue) (bottom).

Transversal Bunch Offset

The positional jitter of the bunch may optimistically be assumed to be $1 \mu\text{m}$ (Sec. 3.2), but will be evaluated up to $6 \mu\text{m}$.

For this purpose, an offset is imposed onto the initial electron parameter set of a bunch with zero energy spread. The impact of an offset of $\Delta x_i = 1 \mu\text{m}$ and $6 \mu\text{m}$ on the electron trajectories, and the evolution of the mean bunch waist through the setup is displayed in figure 5.4.7 (top). With increasing offset, the bunch centre shifts transversally from the central lens axis and obtains an angle with respect to the initial propagation axis z . The radial dependence of the magnetic field within the lens results in a stronger focusing force on electrons further away from the axis. Consequently, the bunch is asymmetrically focused and the focal point is transversally shifted, as well. The initial longitudinal focus coordinate stays constant, as the focal length is not effected by the electron position within the lens. The transversal focus shift results in a shift with respect to the laser focus, and thereby in a worsening of the electron-laser overlap, as shown in the bottom row of the figure.

In figure 5.4.8, the transversal focus offset Δx , the pointing angle at the focus, as well as the focal bunch waist, are plotted as a function of the initial electron offset. The

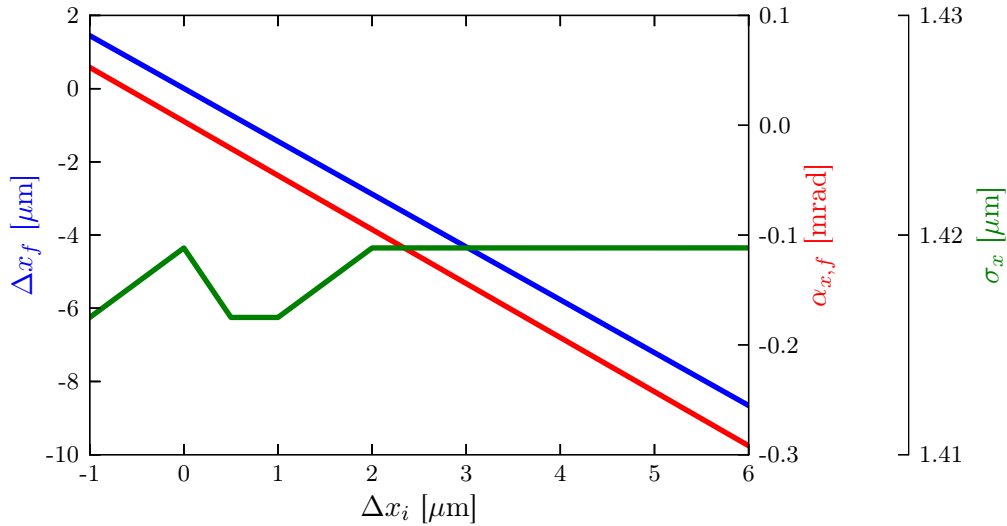


Figure 5.4.8: Focus offset Δx_f (blue), focus pointing angle $\alpha_{x,f}$ (red) and electron focal waist σ_x (green) as functions of the initial electron bunch offset Δx_i .

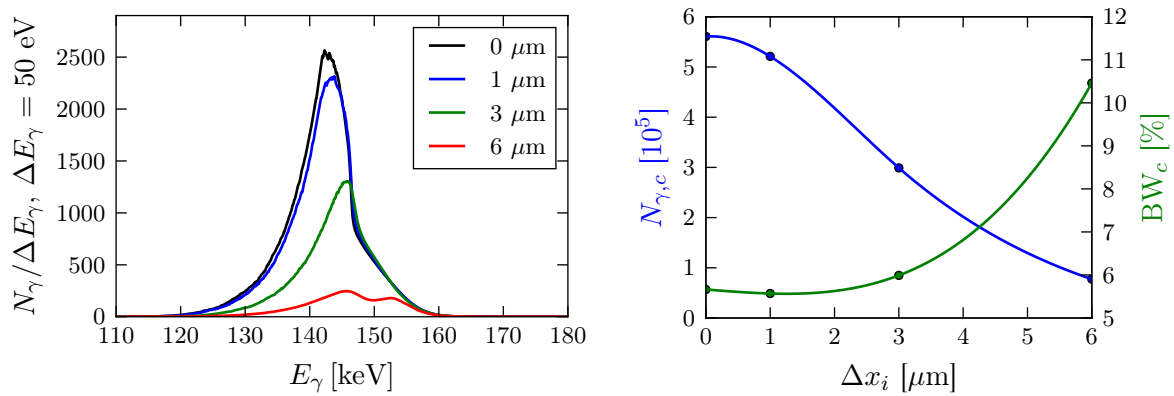


Figure 5.4.9: Thomson cone spectra for different offset values (left). Thomson yield (blue) and bandwidth (green) within the cone as functions of the initial electron bunch pointing angle (right).

focus offset and pointing angle decrease linearly with increasing initial electron offset. The bunch focal waist shows no dependence.

A transversal bunch shift with respect to the laser position can be translated into an increased mean bunch waist within the laser. Consequently, a yield reduction and bandwidth increase are the result of the focal offset. The additional change in collision angle was quantified in section 4.2.9 and leads to a further quality decrease. The decrease in the emitted photon energy due to the pointing angle, according to the Thomson energy equation (2.3.10), is negligible, as the collision angle deviation is $\Delta\alpha_x < 0.3$ mrad for an offset of 6 μm . A increase in the peak energy, however, is obtained, as the bunch centre is at lower a_0 in the interaction centre. The effects are displayed in figure 5.4.9, where the resulting Thomson spectra are compared for different initial bunch offset (left), and the cone yield and bandwidth as a function of the offset are presented (right). If the bunch

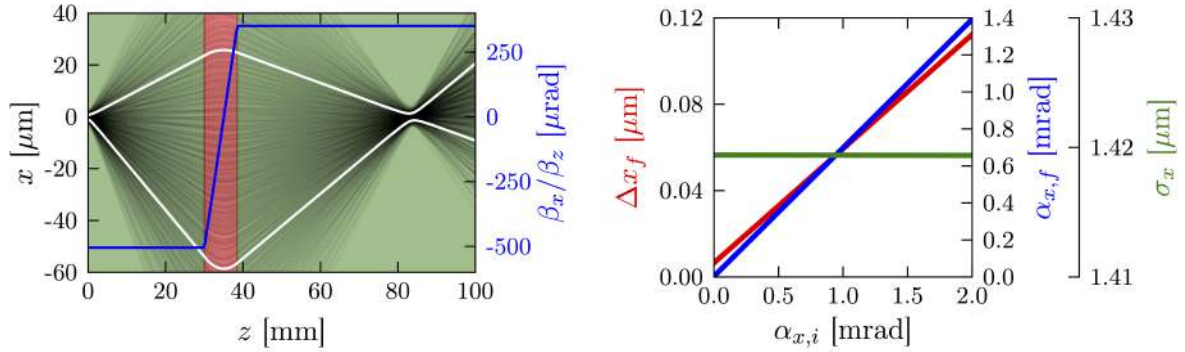


Figure 5.4.10: Electron trajectories (black) and bunch waist (white) evolution through the setup. The bunch pointing angle $\alpha_x = \beta_x/\beta_z$ is included in blue (right axis). Focus offset (red), focus pointing angle (blue) and electron focal waist (green) as functions of the initial electron bunch pointing angle (right).

has an offset of 3 μm , the photon yield drops to half its maximum value at zero offset. The bandwidth increase is negligible at small electron offsets. Assuming an effective electron bandwidth of 2 % rms, the required Thomson bandwidth before including this energy spread, would be 7.5 % FWHM, thus, allowing for a jitter of up to 3 μm . For an offset of 1 μm , the bandwidth does not increase and the yield loss is moderate. Consequently, such low positional jitters are tolerable.

Bunch Pointing Angle

Apart from the positional jitter, an angular jitter, i.e. pointing, is inherited from the driver laser. Again, assuming an optimistic value, a pointing of 0.3 mrad rms (cp. Ch. 3.2) is assumed, for purpose of evaluation, an angle of up to 2 mrad is investigated.

The trajectories and waist evolution through the setup for an initial beam-propagation angle of 0.5 mrad with respect to the z axis, is presented in figure 5.4.10 (left) for a bunch of zero energy spread. The focus position is hardly varied transversally, but the beam obtains a pointing angle. The focus offset, focus pointing angle and focal bunch waist are displayed as functions of the initial bunch pointing angle (right). The focus offset and pointing angle are in linear dependence of the initial pointing angle. The transversal offset, however, is negligibly small, with 100 nm at an initial pointing angle of 1.8 mrad, and the focal waist is not affected. The pointing angle in the focus, however, is almost of equal magnitude, as the initial pointing angle. The Thomson spectra, shown in figure 5.4.11 (left), display a decrease in the number of photons, owed to the decreased overlap (again, compare with Ch. 4.2.9). Due to the negligible transversal focus offset, the interaction centre and the bunch focus coincide, so that no increase of the spectral peak energy is obtained. A slight reduction in peak energy of the spectra is obtained from the decreased collision angle. The photon yield hardly decreases with increasing initial pointing angle (right), due to the maintained overlap at the interaction centre. The bandwidth hardly increases for low pointing angles. This is because, for a zero energy spread electron bunch,

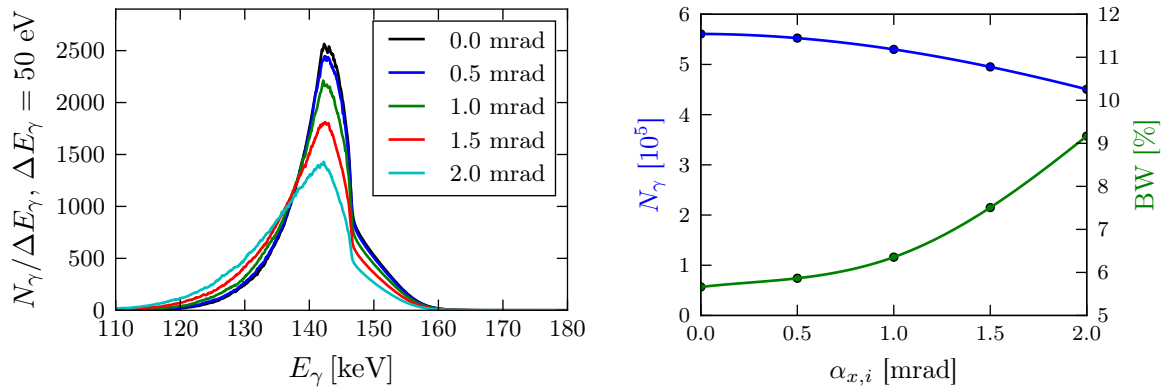


Figure 5.4.11: Thomson spectra for different pointing angles (left). Thomson yield (blue) and bandwidth (green) within the cone as functions of the initial electron bunch pointing angle (right).

an increased collision angle leads to a reduction of the effective laser bandwidth, due to the chirp, as shown in figure [4.2.21](#). Due to the increased propagation angle of the bunch, and the fact that photons are emitted into a cone centred around this direction, a bandwidth increase results. The observation angle is fixed, and centred at 0 mrad with an opening angle of ± 0.5 mrad. Consequently, a focal pointing angle of > 0.5 mrad results in the loss of photons at the maximum emitted energy, and an increase of the low-energy photon contribution. Therefore, the bandwidth increases with increasing pointing angle, and a dramatic increase is observed for focal pointing angles > 0.5 mrad, i.e. initial pointing angles of ≈ 1 mrad.

Consequently, the main reason for the yield loss and bandwidth increase in the presence of an angular jitter of the electron bunch, is due to the changed propagation direction of the bunch within the focus, with respect to the position of the cone. Assuming pointing angles of 0.3 mrad, as suggested, the worsening effects on yield and bandwidth are negligible.

Using the Pointing Angle Effect: Plasma-Lens Rotation

An interesting aspect in the effect of a large electron pointing angle is that the focal position in the transversal plane $x-y$ is hardly changed, while the angle of the mean bunch propagation increases with respect to the x -axis. If the angle of the laser is appropriately changed to again obtain a head-on collision, the extended laser propagation axis does not point to the plasma target. In the original setup without electron pointing, and also in the setup including electron offset, this is still the case, so that un-scattered laser-photons enter the target. Consequently, the pointing effect can be used as a feature. In rotating the plasma lens with respect to the initial bunch propagation axis, and adapting the laser propagation direction, a head-on collision is realisable. Furthermore, in case of an electron bunch with a significant energy spread, electrons of different energies will not only be separated longitudinally within the focal region, but a transverse separation will occur, as well. Figure [5.4.13](#) displays the resulting spectrum from the head-on collision

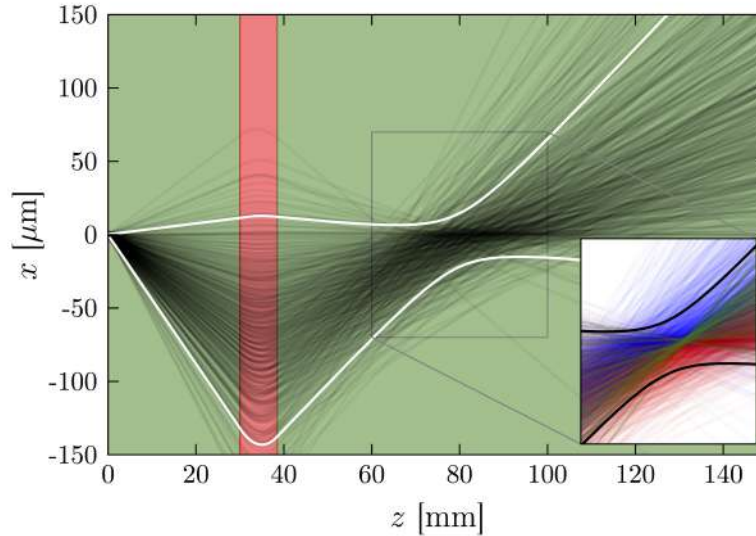


Figure 5.4.12: Electron trajectories and bunch waist through the setup. The inset shows the trajectories through the focal region, coloured according to the electron energy: $\gamma < \gamma_{\text{tar}}$ in blue, $\gamma = \gamma_{\text{tar}}$ in green, and $\gamma > \gamma_{\text{tar}}$ in red.

of a laser with $w_0 = 5 \mu\text{m}$ and $\tau = 4 \text{ ps}$ with the target focus of an electron bunch with an initial energy spread of $\sigma_\gamma/\gamma = 10 \%$ rms. A further reduction of the bunch energy spread to 12 % FWHM is obtained. As it was the case before, this bandwidth reduction comes at the cost of effective bunch charge and, thus, of photon yield which is reduced to 1.4×10^5 within the cone of $\pm 0.5 \text{ mrad}$.

The regarded rotation angle is small with respect to the distance from the plasma target. For future simulations the investigation of this technique at larger rotation angles of several degrees and/or larger distances from the plasma cell is required. Due to the changed setup and transversal focal chirp of the bunch, optimisation of the laser with respect to this configuration could lead to further improvements. One example is to introduce a laser of transversal chirp matched to the transversal chirp of the electron bunch. This could result in an increased yield at low bandwidth, rendering this scenario an interesting prospect for Thomson sources.

5.5 Conclusion

In this chapter, an electron bunch, as obtainable from laser-plasma acceleration was used for the Thomson scattering process. Two scenarios were investigated, firstly, the interaction at the plasma exit, and secondly, the interaction with an electron bunch focused via an active plasma lens.

The first scheme holds the advantage that no specific electron optical elements are installed. However, for head-on collisions close to the plasma exit, the Thomson laser is likely to enter the plasma cell at small size and thus high power, depending on the

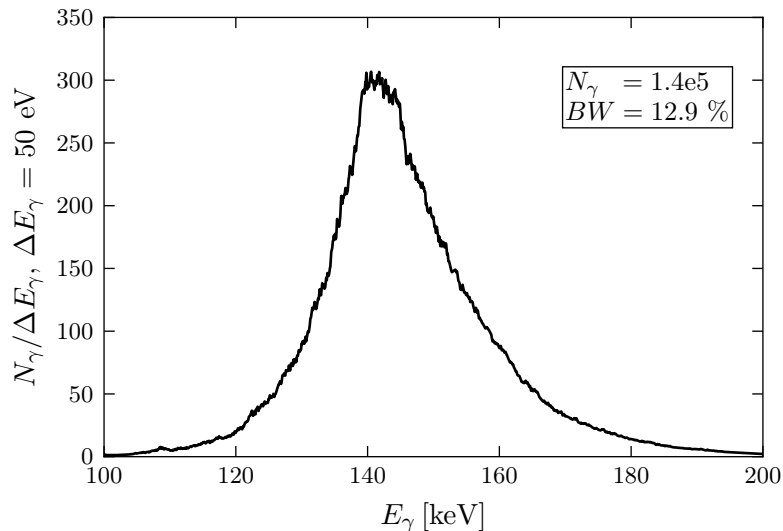


Figure 5.4.13: Thomson spectrum obtained from the head-on interaction with an electron bunch of $\sigma_\gamma/\gamma = 10 \%$ rms initial energy spread focused by a plasma lens rotated by 2 mrad. The laser is configured with respect to the propagation axis and focal point of the electrons at the target energy $\gamma = 156$.

distance between plasma exit and interaction centre. Furthermore, experimental setups might inhibit interactions too close to the target exit. Consequently, the dependence of the photon yield and bandwidth in dependence of the distance from the plasma exit, was investigated. As the electron bunch is divergent, its mean waist increases with increasing drift space. Furthermore, neither electron waist nor divergence are optimised according to the results from the design study in chapter 4. As a consequence, the photon yield decreases with increasing electron propagation distance, and drops to 50 % at a distance of 3 mm. The cone bandwidth is independent of the distance, and increases linearly with increasing electron energy spread. The limit of 15 % FWHM is reached for an electron energy spread of $\sigma_\gamma/\gamma = 2.5 \%$ rms. This interaction scheme is thus suitable for experimental setups allowing for small distances between the plasma exit and the Thomson interaction, and for electron bunches of low energy spread.

The second interaction scheme, employs a discharge-capillary active plasma lens to focus electrons of the target energy onto the design parameters. Consequently, for zero electron energy spread, the photon count is increased with respect to the first scheme by $\approx 20 \%$. With increasing electron energy spread, the longitudinal focal position, the waist and the divergence of bunch energy slices increasingly differs. As a consequence, the contribution to the Thomson spectrum, described by a response function, decreases for electrons with energies deviation from the target energy. This leads to a reduction of the effective bunch energy spread, so that the XFI bandwidth limit is reached for energy spreads of 3.5 % rms, a factor 1.4 in comparison to the first scheme without focusing optics.

Above $\sigma_\gamma/\gamma \approx 5 \%$ rms, the bandwidth saturates, as electrons at the far end of the

electron spectrum no longer contribute to the shape of the Thomson spectrum. Consequently, larger electron energy spreads are manageable via plasma-lens focusing, however, resulting in a reduced effective bunch charge, and thus, strongly diminishing the cone yield of the Thomson source. Therefore, in comparison to the first scenario, the plasma lens provides higher cone yields for bunch energy spreads below $\lesssim 5\%$ rms. Furthermore, it is the favourable scheme in case of large bunch energy spreads, despite the lower yield. Adjusting the saturation bandwidth to the XFI limit via a different bunch and laser parameter set (Ch. 4), there is no longer a limit on the required maximum energy spread of an electron bunch for the application.

Another feature of the plasma lens exploits the otherwise non-ideal energy spread of the electron bunch. Variation of the laser focus position and timing represents an option for tuning the source energy by ≈ 20 keV in the presented scenario, without significant yield reduction. The resulting source bandwidth, however, increases if the interaction centre deviates from the focus of electrons of mean energy.

The effect of pointing and positional electron jitter is negligible within the realistic values of 0.3 mrad and $6\ \mu\text{m}$, respectively. Larger pointing angles of up to 1.5 mrad have shown to result in a yield loss of 10%. Regarding the electron offset Δx_i , a 10% yield loss is the result of $\Delta x_i = 1.5\ \mu\text{m}$.

An approach to allow for head-on collisions without the threat of the Thomson laser entering the plasma target is to rotate the plasma lens, in order to obtain a bunch pointing angle in the focus. Thereby, the bunch obtains an additional transversal chirp. This allows for further bandwidth reduction via the effective electron energy spread, or via matching the laser chirp accordingly. The latter option might be of interest, as bandwidth reduction would not necessarily translate to yield loss. Therefore, design studies including a transversal laser chirp are an interesting prospect. For that, the application of the technique at larger rotation angles and/or distances from the plasma exit has to be investigated.

CHAPTER 6

APPLICATION-ORIENTED SOURCE DESIGN

In section 3.1, the required source parameters for the medical imaging via X-ray fluorescence are presented. So far, parameter scans and optimisation have been performed on the basis of a source energy of 150 keV. The optimum source energy is dependent on the geometry of the detector and of the imaging process. Recent results [9] showed that a source energy of 90 keV in a different detector setup would be more beneficial in terms of the signal quality and detection limit. In the following section, general guidelines for the design process are given, to enable design studies for different target source parameters. The optimisation technique is applied to the scenario of a 90 keV source and an outlook onto the consequences of the changed target energy is included.

6.1 Design Process

The design study for a 150 keV Thomson source showed that in general, a head-on collision is the favourable interaction geometry. Furthermore, the strength of the laser should be $a_0 < 1$, in order to avoid drastic bandwidth increase. From this, at first, the electron bunch energy necessary to achieve the target X-ray energy is determined:

$$\gamma = \sqrt{\frac{E_\gamma}{4E_L}} \quad (6.1.1)$$

for small¹ a_0 .

Thereupon, the optimum laser and electron parameters have to be determined. In order to avoid extensive parameter runs, due to the large number of electron and laser parameters, a previous finding is applied to minimise computation time. Here, it can be exploited that the yield maximisation favours a small width of the a_0 distribution at large values, thus leading to small bandwidths at the same time. Consequently, electron parameters for highest yield are approximately the same as for smallest bandwidth. Anal-

¹Higher values in a_0 reduce the maximum emitted photon energy. This effect can be neglected for small a_0 , as it is insignificantly small ($a_0 = 0.1 \Rightarrow$ factor of 1.002, for $a_0 = 0.3 \Rightarrow 1.01$).

ogous to section 4.4, this allows to assign one electron bunch configuration to each laser configuration. The numerical estimation of the optimum bunch waist is done numerically via equations (4.1.13) and (4.1.3)ff.

If, as in the presented application case, the bandwidth is the more crucial parameter, a theoretical first estimate is conducted, for each determined set of electron and laser parameters. In general, the theoretical estimate overestimates the actual bandwidth, as well as the photon yield in high- a_0 regions. Parameter regions where the bandwidth is dominated by large a_0 or large electron divergence are not well represented. For the limitation of the parameter region, section 4.4 can serve as an orientation. In order to reduce the contribution of higher harmonics, the laser strength parameter should be chosen small enough, as well (cp. Sec. 4.5). Consequently, few simulations of chosen scenarios should be performed to benchmark the theoretical results, including a laser chirp, if relevant, as this is not included in the theory. Thereupon, a suitable scenario is chosen.

Utilising the matrix formalism in section 5.2.1, the required plasma lens parameters, to achieve the necessary bunch focal waist and divergence, are determined. For the plasma lens simulations, an electron bunch of zero energy spread is propagated through the according lens via GPT. From this, the simulative focal electron waist and target focus position are determined. Thereupon, while keeping the laser and lens configurations identical, the interaction is simulated for different electron energy spreads. For the Thomson simulations, the laser focus for each laser configuration is set to the target focus, i.e. the focus of the zero energy-spread electron bunch. If the resulting Thomson bandwidth exceeds the requirement, a scenario of lower bandwidth should be chosen from the initial parameter scans.

If no plasma lens focusing is intended, the divergence and the distance-dependent mean electron waist are utilised for the scenario optimisation, and the actual electron energy spread can be included *ab initio*.

6.2 Thomson Source with $E_\gamma = 90$ keV

For a 90 keV Thomson source, as required for the GNP-based XFI according to recent findings [9], the target energy of the electron bunch is at $\gamma_{\text{tar}} = 120.48$. A consequence of a lower electron energy is a reduced yield within the collimation angle, as the synchrotron angle is larger ($1/\gamma$). Therefore, less photons are emitted into a cone of ± 0.5 mrad than for the 150 keV source with $\gamma = 156$. In general, cutting a smaller cone from the full $1/\gamma$ emission cone would also result in a bandwidth reduction. However, if the on-axis bandwidth is large enough - which is easily achieved from the energy spread and divergence of the bunch - there exists an optimum collimation angle. This angle is defined in such a way that a larger angle would result in an increased bandwidth, and a smaller angle in a reduced yield without further bandwidth reduction. For an on-axis bandwidth κ , the

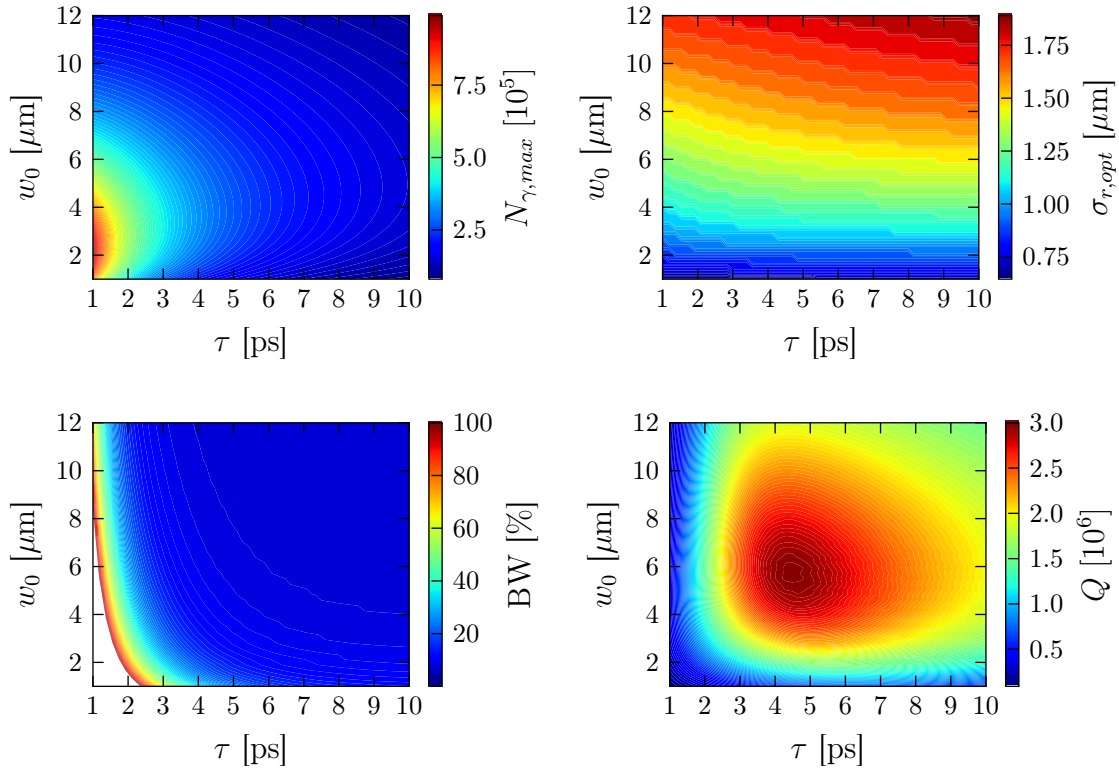


Figure 6.2.1: Maximum cone yield $N_{\gamma,\max}$ (top left), according electron waist $\sigma_{r,\text{opt}}$ (top right), cone bandwidth BW (bottom left), and resulting quality $Q = N_{\gamma,\max}/\text{BW}$ (bottom right), as functions of different laser-waist and -duration configurations for a laser of 0.5 J pulse energy. (For comparison to the 150 keV optimisation, see Fig. 4.4.2)

optimum collimation angle θ_c is [12]:

$$\theta_c = \sqrt{\kappa/\gamma^2} \quad (6.2.1)$$

Therefore, it is increased with decreasing γ . Assuming an on-axis bandwidth of 5 % FWHM, the optimum angle would be $\theta_c = 1.9$ mrad, thus exceeding the chosen cone angle by a factor of $\lesssim 4$. Consequently, a significant yield reduction without bandwidth reduction is obtained from the request of a high spatial resolution of the Thomson source in the medical application. This is true for $\gamma = 156$ (factor $\lesssim 3$), but even more crucial with decreasing γ . In case of an on-axis bandwidth of 15 % FWHM, as is the maximum acceptable bandwidth for the source, the optimum collimation angle is 3.2 mrad for $\gamma = 120.5$.

The region of interest in terms of laser duration and focal waist (τ , w_0) and optimum electron waist is estimated according to section 6.1. The results are shown in figure 6.2.1. In comparison to the optimisation process for $E_\gamma = 150$ keV (Fig. 4.4.1), the maximum achievable cone yield is reduced. Also, a stronger electron bunch focusing is required, while the optimum laser configuration is hardly changed. The highest quality is obtained for $\tau = 4.5$ ps and $w_0 \lesssim 6$ μm with a cone yield of 60 % with respect to the 150 keV scenario at approximately equal theoretical bandwidth of 10 % FWHM.

When regarding the plasma lens effect, the same relative energy spread σ_γ/γ results in a weaker longitudinal separation of the electron bunch. Consequently, the effective energy spread reduction is weaker.

In summary, a 90 keV Thomson source can be realised on similar design parameters, however, at a reduced cone yield and increased bandwidth. Further bandwidth reduction would result in a stronger yield decrease.

CHAPTER 7

CONCLUSIONS AND OUTLOOK

X-ray fluorescence imaging (XFI) of gold nanoparticles (GNP) requires an X-ray source of high quality and specific parameters, preferably at small spatial dimensions to enable the implementation at medical facilities. This thesis was therefore concerned with the design of a dedicated X-ray source for this application on the basis of an all-laser-driven setup combining laser-plasma acceleration (LPA) and Thomson scattering (TS). A possible source setup was proposed and the necessary design parameters were determined.

The target source parameters are an incident photon energy of 150 keV with a bandwidth below 15 % FWHM and a yield of 10^9 photons per line scan within a divergence of 1 mrad. The proposed source setup sets the electron- and laser-parameter boundaries for the design study. One issue is the limited laser pulse energy due to the single laser driving both, the electron acceleration and the X-ray generation. Moreover, the Thomson laser inherits the parameters of the driver laser. Consequently, appropriate beam optics were proposed, utilising chirped-pulse amplification, chirped mirrors and focusing elements in order to manipulate laser duration and focal waist. The electron bunch as obtained from the LPA is focused via a discharge-capillary active plasma lens. The investigation of the impact of this chromatic focusing element represent a main part of this thesis.

Though promoted with low divergences $\propto 1/\gamma$, the intrinsic small opening angle of Thomson radiation cannot be made use of. On the one hand, the target photon energy of 150 keV requires $\gamma = 156$ in a counter-propagating collision geometry, leading to an opening angle of 6 mrad. On the other hand, within the full opening angle of the radiation in forward direction, the bandwidth is intrinsically at ≈ 50 % FWHM. Consequently, a pin hole is required to collimate the Thomson radiation and thereby adjust the divergence and reduce the bandwidth.

A dedicated source design requires a fundamental understanding of the X-ray generation and the resulting spectrum. For that purpose, extensive parameter studies have been performed, including electron, laser, and geometrical parameters. A central aspect of

these studies was the special case of a confined observation cone, as required to obtain a low source divergence, and the impact of the electron bunch waist and divergence on the radiation spectrum, especially on the photon yield and bandwidth.

The geometrical tolerance and collision angle studies revealed the optimum interaction geometry to be a head-on collision with temporal and spatial coincidence of the bunch and laser foci. A deviation from the head-on collision by 5° results in a yield loss of $\lesssim 70\%$.

A narrow Thomson bandwidth is typically accompanied by a loss in the photon yield, as it is achieved either by collimation, i.e. discarding low-energy photons at large observation angles, or by reducing the laser strength to minimise spectral broadening. It was shown that geometrical bunch-parameter optimisation is able to increase the yield while decreasing the bandwidth within the confined cone, thus rendering electron focusing an important aspect in the source design. This effect is a consequence of the relation between the bunch and the laser waist, as well as of the electron divergence. In general, an increased photon emission is acquired from electron oscillation in high laser fields. The photon yield was found to be dependent on the mean laser strength parameter \bar{a}_0 . This broadens the applicability of theoretical formulae for the total Thomson yield to include interactions with a longitudinal focal mismatch. In case of a longitudinal focal delay, \bar{a}_0 is given simply by the mean bunch and laser waist during the interaction. Focusing the bunch in such a way as to obtain the most electrons within highest laser fields, simultaneously decreases the width of the a_0 distribution, as seen by the electrons, as the contribution from low a_0 values is diminished. The Thomson bandwidth is dependent on the shape of this distribution, rather than its maximum. A small bunch waist compared to the laser waist thus increases the yield while decreasing the bandwidth. The problems in analytical or numerical determination of the a_0 distribution renders simulation an important tool in the determination of the bandwidth.

The reduction of the bunch waist comes at the cost of an increase in divergence, rendering these to rivalling effects with respect to the cone yield and bandwidth. The cone yield is composed of two contributions, namely those arising from the overlap effect and those from the cone effect. The overlap effect aims at the lowest mean electron waist throughout the interaction with the laser, while the cone effect is solely dependent on the divergence, leading to a decreased yield with increasing divergence. Laser parameter variation showed that the overlap is highly affected by the laser waist and duration, so that there exists no global optimum for the electron waist and divergence.

In order to simulate an electron beam of non-zero energy spread, the propagation conditions have to be defined, so that according chromatic effects can be taken into account. The parameter scans showed that in principle, the energy spread has no influence on the cone yield, and leads to a symmetric spectral bandwidth broadening. Thus, a geometrical optimisation of the laser and electron parameters can be conducted with respect to the target electron energy, excluding an electron energy spread.

Exploiting the general idea of bunch parameter optimisation leading to yield maxi-

sation and bandwidth reduction at the same time, the optimisation process was performed as follows. For each possible laser configuration, the electron waist and divergence were optimised with regard to the maximum yield. Thereupon, the respective cone bandwidth was determined via simulation, and the configurations of highest quality, defined as the ratio of yield and bandwidth, were isolated.

The optimum laser and electron configuration depends on the energy spread of the bunch, as it determines the maximum acceptable bandwidth acquired from the laser and electron configuration. The highest quality was obtained by a laser of $a_0 = 0.3$, $w_0 = 7 \mu\text{m}$, and $\tau = 4 \text{ ps}$, and an electron bunch focal waist of $2 \mu\text{m}$ at a normalised emittance of $\varepsilon_n = 0.2 \text{ mm mrad}$. In this case, a cone yield of 5×10^5 is achieved for a bunch charge of 10 pC . The cone bandwidth excluding the bunch energy spread is 11% FWHM, hence allowing for an electron energy spread of 3% rms, in order to remain below the limit of 15% rms for XFI. A 10% gain in cone yield can be obtained for a laser waist of $5 \mu\text{m}$, however, at an increase in bandwidth. The resulting maximum tolerable bunch energy spread in this case is then 2.8% rms. At these configurations, the amount of photons within the second harmonic (300 keV) is less than 1% of the total cone yield. Space-charge effects were shown to be negligible within the regarded range of bunch charges up to 200 pC . Therefore, increasing the bunch charge to this value results in a cone yield of $\lesssim 10^7$ photons per shot. In case of a limited available laser pulse energy, to arrive at sufficient laser strength parameters a_0 , small focal waist of $< 10 \mu\text{m}$ are necessary which requires strong focusing. In general, such low waists are achievable by the according focusing optics. However, realising a head-on collision geometry at the according short focal lengths without impeding the different beam paths or damaging optical elements is an important issue in the experimental realisation.

The second main part of the thesis was the application of the parameter optimisation to the proposed source setup. Describing electron bunch propagation via the evolution of the Courant-Snyder parameters in the matrix formalism, allows to simulate a realistic electron bunch, including a finite energy spread.

A simplified setup without electron focusing optics makes use of the initial small bunch divergence and waist at the plasma exit. In this case, the distance of the Thomson interaction from the plasma exit is a crucial aspect. Experimental setups might require a certain distance from the target, and especially the Thomson laser should be hindered at entering the target plasma cell at high power. Furthermore, the distance has to be of the order of the interaction length, i.e. the laser pulse length.

Assuming an electron bunch of 0.2 mm mrad emittance and $1 \mu\text{m}$ initial waist yields a constant divergence of 1.3 mrad which exceeds the cone opening angle and thus leads to yield loss and bandwidth increase with respect to the results from an optimised bunch. While the bandwidth is dominated by the energy spread and nearly independent of the distance, the increasing bunch waist with increasing propagation length and the large

divergence lead to a significant cone yield loss of more than 50 % at only 3 mm distance from the plasma exit. Consequently, Thomson scattering at the plasma exit, if experimentally realisable, can be an alternative to the implementation of electron beam optics, as long as either small yield requirements are dictated by the application, or small distances $\lesssim 1$ mm are feasible. In terms of the bandwidth, this setup is limited to bunches with an energy spread of ≤ 2.5 % rms.

The implementation of electron-bunch focusing optics allows to impose the determined optimum parameters onto the bunch. A discharge-capillary active plasma lens enables symmetric focusing by a single optical element at small focal lengths. Due to the chromatic focusing of the lens, parameter optimisation can be accomplished for the target electron energy. Electrons of deviating energy experience different focusing forces, resulting in energy-dependent focal waist, divergence, and different focal lengths. The latter leads to a longitudinal bunch distribution according to the electron energy, i.e. a longitudinal chirp. Adjusting the laser timing and focal position to a certain part of this focal region, allows to enhance the contribution of the chosen target electron energy to the Thomson spectrum. At the same time, both, the parameters deviating from the optimum configuration, but predominantly the longitudinal focal delay of electrons of unfavourable energies reduces their contribution. Therefore, the plasma lens represents a means to achieve optimum electron parameters at the target electron energy, as well as to reduce the effective electron energy spread. The reduction of a 10 % rms energy spread to merely 3 % rms can be achieved. This comes at the cost of a decreased effective bunch charge, by the same factor, thus reducing the cone photon yield to 30 %. If the interaction centre coincides with the focus of the target electron energy, the effective energy spread of the bunch, and thereby the Thomson bandwidth, saturates for energy spreads above 5 % rms. This is due to the increasing distance of the focal lengths from the target focus with increasing deviation from the energy. Electrons with more than 5 % energy deviation do not contribute to the spectrum. In the regarded case, this limit is 17 % FWHM, but is further reducible via different electron and laser configurations. As a consequence, the method of reducing the effective energy spread by means of plasma-lens focusing is applicable to bunches of arbitrary large energy spreads.

Apart from the bandwidth reduction, the application of a plasma lens allows to change the peak Thomson energy by the variation of the laser focal position. An energy shift of 20 keV without significant yield loss and at small bandwidth increase is obtained by a longitudinal offset of 5 mm. The highly promoted tuneability of Thomson sources generally requires the change in electron energy, i.e. an alteration of the acceleration parameters. Alternatively, the observation angle or collision angle are proposed to be changed. This, however results in significant yield loss and bandwidth increase. In comparison, spectral tuning via the laser focusing in a plasma-lens setup is simpler and the quality degradation of the source is moderate. Furthermore, a finite bunch energy spread is not only tolerable, but a necessary feature for the tuneability.

Tolerance studies on this setup revealed that positional jitters of $\leq 1 \mu\text{m}$ and pointing jitters of $\leq 0.3 \text{ mrad}$, as achievable by LPAs, have a negligible effect on both the cone yield and bandwidth.

The difficulty to realise head-on collisions in an experiment, while this represents the favourable interaction geometry, is one of the major issues in experimental Thomson scattering experiments. An approach to deal with this problem is proposed, making use of the geometrical focusing properties of the plasma lens. In rotating the lens with respect to the electron propagation axis results in a change in the mean bunch propagation direction while the position coordinates of the bunch focus are maintained. At the same time, a transversal bunch chirp is obtained. A Thomson laser in respective head-on collision would thus not enter the plasma target cell. Furthermore, the transversal bunch chirp could be made use of. On the one hand, the mean propagation direction of electrons deviating from the target energy differs from the mean propagation axis. Consequently, their central emission is not directed into the centre of the pinhole, and the cone bandwidth of the source is further reduced. The pin-hole position can thus be used to select different target photon energies. On the other hand, a transversal laser chirp could be introduced to match the electron chirp and further reduce the cone bandwidth. A quantification of this setup with respect to larger rotation angles and/or distances of the Thomson interaction region from the plasma cell would be an attractive option for future design studies.

X-ray fluorescence imaging of gold nanoparticles is a current research project, and thus subject to parameter changes in the search for the optimum X-ray source. Furthermore, different source parameters enable the application in other research fields. Implying that, in general, a high yield at a low bandwidth and divergence are a prominent source requirement, the main aspect remains the source photon energy. For a different target source energy, the electron energy has to be adjusted. A different bunch energy has an impact on the electron waist and divergence relation for constant emittance, but also on the Thomson radiation cone, as well as the chromatic focusing via the plasma lens. Recent studies in X-ray fluorescence imaging revealed an improved signal quality for an incident photon energy of 90 keV [9]. A lower electron energy, as is thus required, results in a larger emission cone, so that less photons are emitted into a cone of 1 mrad divergence, without a reducing effect on the bandwidth. Moreover, for equal bunch waist, the electron divergence is increased, resulting in a further decrease of the cone yield at simultaneous bandwidth increase. In terms of plasma-lens focusing, shorter focal lengths are required. By that, for a given relative energy spread, the longitudinal separation is reduced. Consequently, a lower bunch energy reduces the chromatic effect of the lens focusing, and thus the effective bunch energy spread is increased. Requiring higher photon energies, and thus higher electron energies leads to smaller radiation cones. Consequently, the cone yield rises, but smaller collimation is necessary to reduce the bandwidth to the required value. Due to the quadratic dependence of the Thomson energy on the electron energy,

small changes in the target photon energy lead to even lower changes in the required electron energy.

LPA-based Thomson sources find application in many fields of research, so that the necessity for dedicated design studies is not limited to the medical application presented in this thesis. While for medical imaging, a moderate yield is required in order to obtain tolerable doses, applications in material science etc. might call for higher yields in a given time frame. Improving the photon yield per shot can be obtained either from a higher bunch charge, and/or from a higher pulse energy within the Thomson laser. The latter either requires a driver laser of higher pulse energy, or to separate the acceleration from the X-ray generation by applying two high-power lasers. If higher pulse energies for the Thomson laser are available, the demands on the focusing can be loosened, facilitating the laser beam optics path. A broader laser waist at equal a_0 and duration would also relax the conditions on electron focusing, allowing for even higher bunch charges in terms of space-charge effects.

Another approach is to increase the number of shots per time. This requires high-power lasers of kHz repetition rates, so that, for the medical application, a shot yield of 10^5 would be sufficient in terms of treatment time.

The setup, as proposed in this thesis, is able to be optimised to achieve the required divergence and bandwidth for GNP-based XFI. Future improvements on high-power laser techniques could increase the source photon yield and thus pave the way for numerous applications. This work can serve as a guide for respective source designs. Such high-quality X-ray sources at a small scale allow the installation at universities and medical facilities, and thus promote X-ray based research fields. In medical imaging, they enable improved specific imaging. In combination with the highly versatile GNP-based XFI, they allow for better understanding in the fields of cancer research, pharmacokinetics, neural damage, and many more.

APPENDIX A

A.1 Undulator Radiation

A.1.1 Emitted Wavelength, Bandwidth and Opening Angle

Via Bragg

The following derivation is adapted from reference [50].

The velocity of an electron in an undulator field consists of a contribution in transverse direction β_x and in longitudinal direction β_z with the relation to the original velocity βc : $\beta^2 = \beta_x^2 + \beta_z^2$, as the kinetic energy of the electron is constant. With

$$\beta_x = \frac{K}{\gamma} \cos\left(\frac{2\pi z}{\lambda_u}\right)$$

the velocity in z is

$$\beta_z = \sqrt{\beta^2 - \frac{K^2}{\gamma^2} \cos^2\left(\frac{2\pi z}{\lambda_u}\right)} \quad (\text{A.1.1})$$

Averaging the cosine term yields the average velocity in propagation direction:

$$\hat{\beta}_z = \sqrt{\beta^2 - \frac{K^2}{2\gamma^2}} \quad (\text{A.1.2})$$

An electron at $z = 0$ emits light of wavelength λ_γ at an angle θ . The same wavelength is emitted at a distance λ_u into the same angle. As the electron's velocity in z is smaller than that of the light it emits, there is a path distance between the emitted wavefronts.

The electron travels the distance λ_u with $v_e = \hat{\beta}_z c$ in the time

$$t_e = \frac{\lambda_u}{\hat{\beta}_z c}$$

In that time, the light will have travelled a distance $t_e \cdot c = \frac{\lambda_u}{\hat{\beta}_z}$ in the direction of θ . The

next wavefront is emitted at $\lambda_u \cos \theta$. Therefore, the distance between these wavefronts is:

$$\begin{aligned} d &= \frac{\lambda_u}{\hat{\beta}_z} - \lambda_u \cos \theta \\ n\lambda &= \frac{\lambda_u}{\hat{\beta}_z} - \lambda_u \cos \theta \end{aligned} \quad (\text{A.1.3})$$

With equation (A.1.2) and using $\frac{1}{1-x} \approx 1+x$, one obtains

$$n\lambda \approx \lambda_u \left(1 - \cos \theta + \frac{1}{2\gamma^2} + \frac{K^2}{4\beta\gamma^2} \right) \quad (\text{A.1.4})$$

For small emission angles θ the following approximation is applicable:

$$1 - \cos \theta = 2 \sin^2(\theta/2) \approx \theta^2 \quad (\text{A.1.5})$$

and thereby

$$n\lambda \approx \lambda_u \left(\frac{1}{2\gamma^2} + \frac{K^2}{4\beta\gamma^2} + \theta^2 \right) \quad (\text{A.1.6})$$

From this, the undulator equation is derived which defines the wavelength emitted by an undulator of λ_u and K by an electron of γ into the angle θ :

$$\lambda = \frac{\lambda_u}{2n\gamma^2} \left(1 + \frac{K^2}{2} + \gamma^2 \theta^2 \right) \quad (\text{A.1.7})$$

where n denotes the n^{th} harmonic.

The interference condition applied to the whole undulator device also has an effect on the bandwidth of the emitted wavelength or - analogously - the angular spread over which a certain wavelength will be observed. For constructive interference, the distance must be a whole number of wavelengths, fulfilling the Bragg condition. Each emitted wavefront at one oscillation must interfere constructively with a wavefront emitted at another period. This is given, if the distance is such that the first wavefront $N_i = 1$ interferes constructively with the one emitted at half the undulator length $N_i = N/2$, the wavefront from the $N_i = 2$ with the $N_i = N/2 + 1$ wavefront and so on.

$$Nn\lambda = N \frac{\lambda_u}{\hat{\beta}_z} - N\lambda_u \cos \theta = N \frac{\lambda_u}{\sqrt{\beta^2 - \frac{K^2}{2\gamma^2}}} - N\lambda_u \cos \theta$$

The condition for destructive interference is obtained by adding one wavelength over the whole undulator length, or, more descriptive, half a wavelength over half the undulator

length. The wavelength which interferes destructively is denoted as λ^* :

$$Nn\lambda^* + \lambda^* = N\frac{\lambda_u}{\hat{\beta}_z} - N\lambda_u \cos \theta = N\frac{\lambda_u}{\sqrt{\beta^2 - \frac{K^2}{2\gamma^2}}} - N\lambda_u \cos \theta$$

As the right part of the two equations are identical, the left sides can be set equal to one another

$$Nn\lambda = Nn\lambda^* + \lambda^*$$

This yields the destructively interfering wavelength, i.e. the first wavelength which is not observed at a fixed observation angle:

$$\lambda^* = \frac{Nn\lambda}{1 + nN}$$

Consequently, at a fixed angle θ one obtains the bandwidth of

$$\frac{\Delta\lambda}{\lambda} = \frac{\lambda - \lambda^*}{\lambda} = \frac{\lambda - \frac{Nn\lambda}{1+nN}}{\lambda} = \frac{1 + nN - nN}{1 + nN} = \frac{1}{1 + nN} \quad (\text{A.1.8})$$

The derivation, according to Fourier considerations is presented below.

Analogously, one can regard a fixed wavelength λ and determine the opening angle of this wavelength which gives

$$\theta^{*2} - \theta^2 = \frac{2\lambda}{N\lambda_u} \quad (\text{A.1.9})$$

For the on-axis radiation, i.e. at $\theta = 0$, we obtain an opening angle of

$$\Delta\theta = \frac{2\lambda}{N\lambda_u} = \frac{1}{\gamma} \sqrt{\frac{1 + K^2/2}{Nn}} \quad (\text{A.1.10})$$

In the undulator regime where $K \ll 1$, this gives the so-called undulator opening angle, defining the opening angle of the central, thus maximum, emitted wavelength

$$\Delta\theta = \frac{1}{\gamma\sqrt{N}} \quad (\text{A.1.11})$$

This theory is also applicable for a Thomson source with a constant-field laser.

Via Fourier

The derivation is in accordance with reference [69].

The length of the light signal of an undulator is $N_u\lambda_\gamma$, consequently the duration is

$$T_\gamma = \frac{N_u\lambda_\gamma}{c} = N_u 2\pi/\omega_\gamma$$

An ansatz for the amplitude of the radiation is

$$u(t) = \begin{cases} a \cdot e^{i\omega_\gamma t} & -T/2 \leq t \leq T/2 \\ 0 & \text{else} \end{cases}$$

A Fourier transform is the projection of an amplitude onto a plane wave.

The Fourier transform of the amplitude $u(t)$ is $\tilde{u}(\omega)$:

$$\begin{aligned} \tilde{u}(\omega) &= \frac{1}{\sqrt{2\pi}} \frac{1}{T} \int_{-T/2}^{T/2} u(t) e^{-i\omega t} dt \\ &= \frac{a}{\sqrt{2\pi T}} \int_{-T/2}^{T/2} e^{i(\omega_\gamma - \omega)t} dt \\ &= \frac{a}{\sqrt{2\pi T}} \frac{1}{i(\omega_\gamma - \omega)} [e^{i(\omega_\gamma - \omega)t}]_{-T/2}^{T/2} \\ &= \frac{a}{\sqrt{2\pi T}} \frac{1}{i(\omega_\gamma - \omega)} [\cos(\omega_\gamma - \omega t) + i \sin(\omega_\gamma - \omega t)]_{-T/2}^{T/2} \\ &= \frac{2a}{\sqrt{2\pi T}} \frac{1}{(\omega_\gamma - \omega)} \sin[(\omega_\gamma - \omega) \frac{T}{2}] \\ &= \frac{a}{\sqrt{2\pi}} \frac{\sin(\Delta\omega T/2)}{\Delta\omega T/2} \\ &= \frac{a}{\sqrt{2\pi}} \frac{\sin(N_u \pi \frac{\Delta\omega}{\omega_\gamma})}{N_u \pi \frac{\Delta\omega}{\omega_\gamma}} \end{aligned}$$

The emitted intensity at frequency ω is thus

$$I(\omega) \propto |\tilde{u}(\omega)|^2 = \frac{a^2}{2\pi} \text{sinc}^2(N_u \pi \frac{\Delta\omega}{\omega_\gamma})$$

Consequently, one obtains the FWHM bandwidth of the frequency spectrum:

$$2\Delta\omega/\omega_\gamma = 0.886/N_u$$

A.2 Thomson Bandwidth

Collision Angle

A divergence of the electron bunch and/or the laser lead to different interaction angles α .

The laser divergence in terms of the wavelength and the focal waist $w_0 = 2\sigma_l$ is

$$\sigma_{\theta,l} = \frac{1}{2} \arctan\left(\frac{\lambda}{\pi w_0}\right)$$

The rms divergence of the electron bunch in terms of the normalized emittance and the rms transversal bunch size reads

$$\sigma_{\theta,e} = \frac{\epsilon_n}{\gamma\sigma_e}$$

where $\Delta\alpha$ is estimated from the divergences as

$$\Delta\alpha = 2\sqrt{2\ln(2)}\sqrt{\sigma_{\theta,l}^2 + \sigma_{\theta,e}^2}$$

Theoretical Modeling of a_0

The normalised 1D Gaussian distribution of the electron bunch is defined as

$$N_{e,\text{norm},1\text{D}}(\sigma_r) = \frac{1}{\sqrt{2\pi\sigma_r^2}} \exp\left(\frac{-x^2}{2\sigma_r^2}\right)$$

The 1D distribution for the laser strength parameter reads

$$a_{0,1\text{D}} = a_{0,\text{max}} \exp\left(\frac{-x^2}{2(w_0/2)^2}\right)$$

From these, the according 2D distributions are obtained:

$$N_{e,\text{norm},2\text{D}}(\sigma_r) = N_{e,\text{norm},1\text{D}}(\sigma_r) \cdot N_{e,\text{norm},1\text{D}}^T(\sigma_r)$$

$$a_{0,2\text{D}} = a_{0,2\text{D}} \cdot a_{0,2\text{D}}^T / a_{0,\text{max}}$$

The yield is quadratically proportional to a_0 , so that the quadratic mean a_0 for the whole bunch in dependence of the waist is

$$a_{0,\text{quadmean}}(\sigma_r) = \sqrt{\frac{\sum(N_{e,\text{norm},2\text{D}}(\sigma_r) \cdot a_{0,2\text{D}}^2)}{\sum N_{e,\text{norm},2\text{D}}(\sigma_r)}}.$$

In order to obtain the a_0 distribution, not the 2D a_0 distribution is utilised for the calculation, but the single a_0 values are determined for equidistant time steps and transversal coordinates during the interaction time. The 2D bunch distribution renders the weighting for the single values. Thereupon, the distribution is determined.

A.3 Supplementary plots

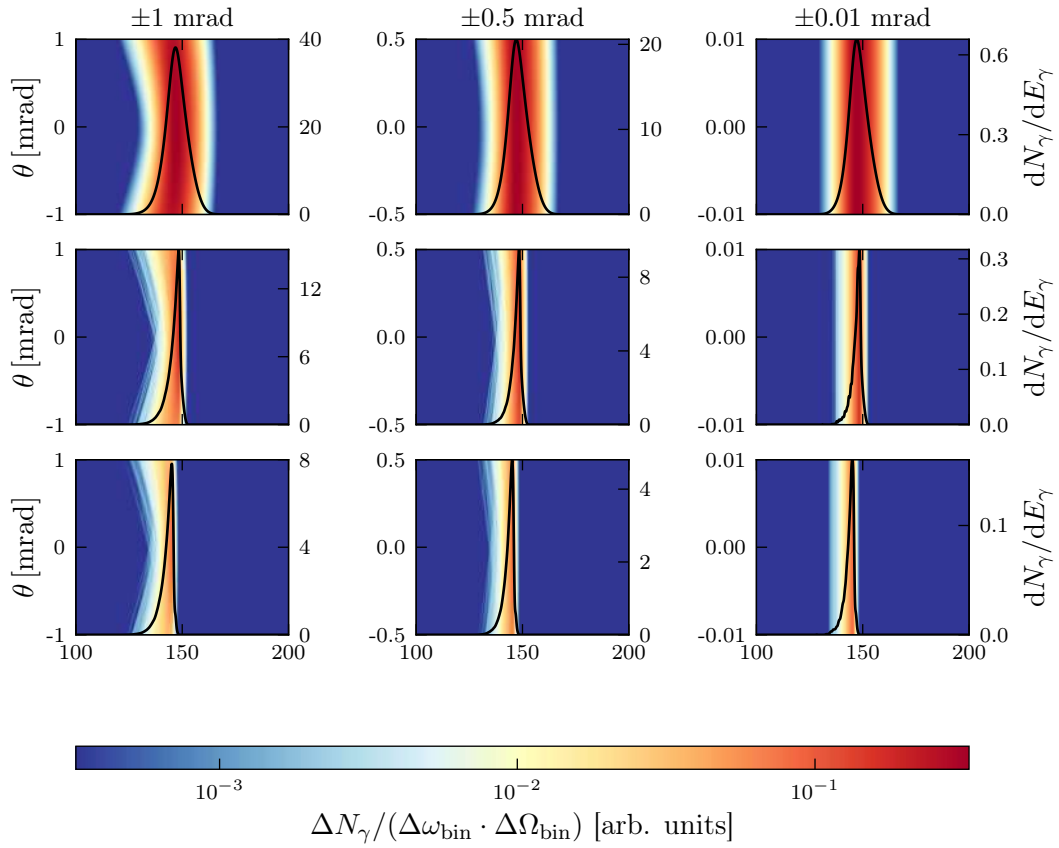


Figure A.3.1: Line spectra for a divergent electron beam without energy spread in a chirped laser for different collision angles deviating from the head-on geometry $\alpha = 180^\circ$: $\Delta\alpha = 0$ (first row), $\Delta\alpha = 10^\circ$ (second row), and $\Delta\alpha = 20^\circ$ in the third row. The columns show the line spectra in an observation angle of ± 1 mrad (left), ± 0.5 mrad (centre), and ± 0.01 mrad (right).

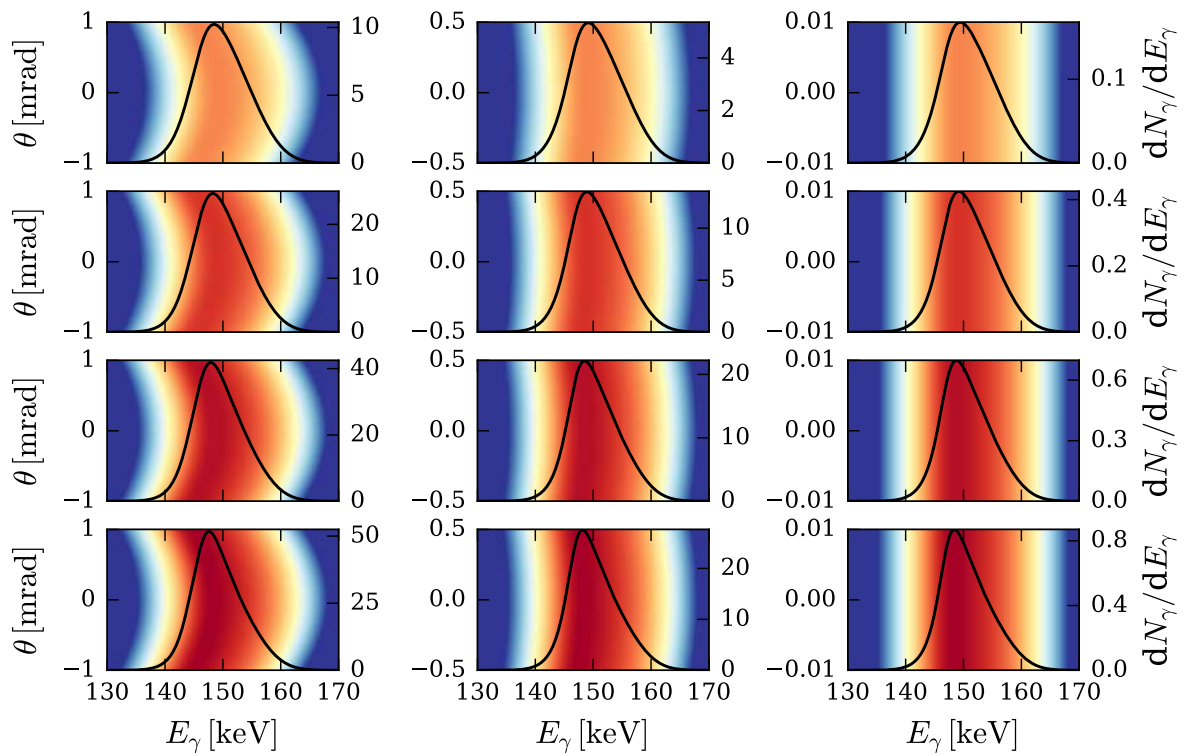


Figure A.3.2: Line spectra for a non-divergent zero energy spread electron bunch in a linearly chirped Gaussian laser of $\Delta\lambda = 60$ nm, $\tau = 4$ ps and $w_0 = 12$ μm . The electron bunch waist is varied. From top to bottom: $\sigma_r = 12$ μm , 6 μm , 3 μm , 1 μm . Left column: Opening angle of 1 mrad, centre: 0.5 mrad, right: 0.01 mrad.

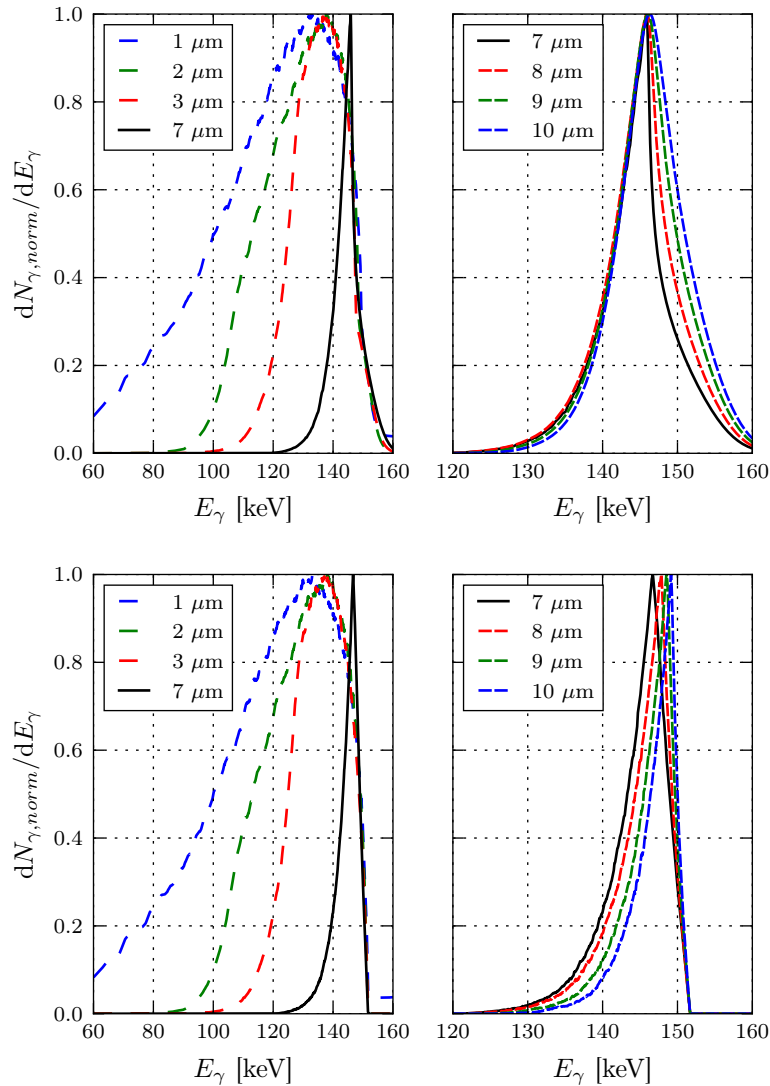


Figure A.3.3: Thomson spectra within a cone of ± 0.5 mrad. The laser duration is constant at $\tau = 4$ ps, while the waist (and a_0 accordingly) is varied. Top: laser with linear chirp, bottom: Laser without chirp. Below $w_0 = 7 \mu\text{m}$, the bandwidth increase arises from the increasing a_0 which leads to a broadening on the low-energy side of the spectrum. For increasing waist $w_0 \geq 7 \mu\text{m}$, the results depend on the laser chirp. With a linear laser chirp, only the high-energy side of the spectra is increased, the peak energy is constant. This is due to low- a_0 cutting from the effective distribution, as seen by the electrons. In the unchirped case, the peak energy increases with the duration and the low-energy side (dominated by larger a_0 values) is further reduced.

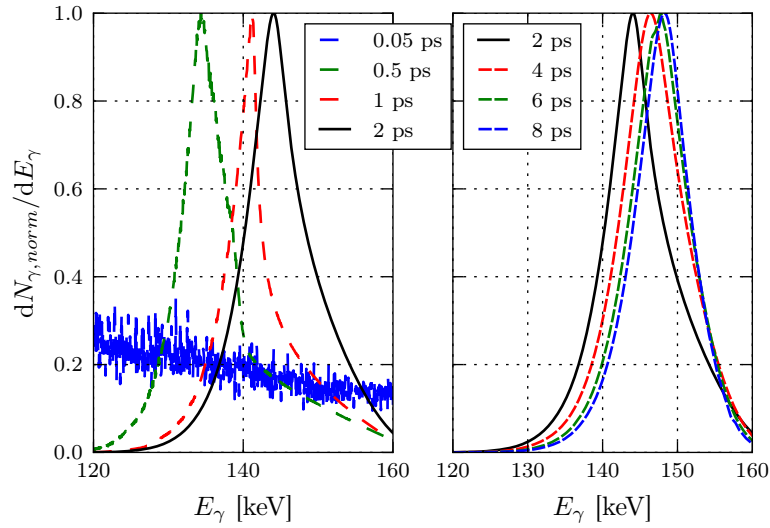


Figure A.3.4: Thomson spectra within a cone of ± 0.5 mrad. The laser waist is constant at $w_0 = 10.45 \mu\text{m}$, while the duration (and a_0 accordingly) is varied. The laser has a longitudinal chirp. With increasing duration, the peak energy shifts to lower values, as the mean a_0 is reduced.

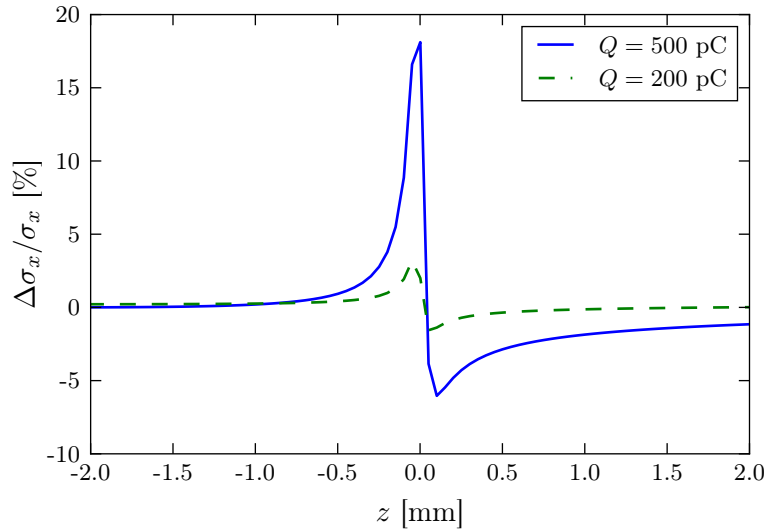


Figure A.3.5: Relative bunch waist $\Delta\sigma_x/\sigma_x$ with respect to the bunch waist at $Q = 10$ pC as a function of the distance from the electron and laser foci at $z = 0$. The target bunch focus in the simulation is $\sigma_r = 0.2 \mu\text{m}$. In the drift, the bunch waist is hardly effected. In approaching its focus, the electron bunch waist decreases, thus increasing the space-charge effects. At the laser focus, the bunch waist of the 500 pC bunch is 18 % larger than the waist of the 10 pC bunch. However, at such low bunch waists, the effect on the Thomson bandwidth and yield is negligible. Values of $\Delta\sigma_x/\sigma_x < 0$ are explained by the shift of the bunch focus to larger z coordinates with increasing bunch charge and thus increasing space-charge effects.

LIST OF FIGURES

2.1.1	Gaussian laser profile.	8
2.1.2	Figure eight motion.	10
2.3.1	Hertzian dipole and angular radiation intensity distribution.	15
2.3.2	Schematic of an undulator.	16
2.3.3	Schematic Thomson interaction.	18
2.3.4	Origin of the on-axis spectral oscillations.	22
3.1.1	Au attenuation coefficient.	24
3.1.2	XFI dose-normalised signal-to-noise ratio as a function of the incident photon energy.	25
3.2.1	Possible LPA-driven Thomson-source setup.	26
4.1.1	Typical angular energy and intensity distribution of a Thomson source and the source collimation effect.	35
4.1.2	Ideal Thomson spectrum.	36
4.1.3	Angular intensity distribution in x and y .	40
4.1.4	Wavelength-dependent angular intensity.	41
4.1.5	Thomson bandwidth in dependence of the cone size and the number of laser periods.	42
4.1.6	Graphic presentation of the theoretical bandwidth contributions.	44
4.2.1	Rayleigh and interaction length as functions of the laser waist.	48
4.2.2	Thomson photon yield within a cone as a function on the electron waist for a non-divergent zero energy spread electron bunch.	50
4.2.3	Effective a_0 as a function on the electron waist for a non-divergent zero energy spread electron bunch.	50
4.2.4	Cone spectra of non-divergent zero energy spread electron bunches of different waist.	51
4.2.5	Line spectra for a non-divergent zero energy spread electron bunch.	52
4.2.6	FWHM cone bandwidth as a function of the bunch waist for a non-divergent zero energy spread electron bunch.	54
4.2.7	a_0 distributions as experienced by the electrons, and according energy spectra.	56

4.2.8	Line spectra for a non-divergent zero energy spread electron bunch in a linearly chirped Gaussian laser.	58
4.2.9	Cone spectra for different electron waist and laser bandwidths.	59
4.2.10	Normalised cone spectra for different cone angles and laser bandwidths.	59
4.2.11	Cone bandwidth as a function of the electron laser waist ratio for the interaction with a chirped laser.	60
4.2.12	Line spectra for a non-divergent electron beam with 1 % and 5 % rms energy spread in an zero chirp Gaussian laser beam.	61
4.2.13	Bandwidth within a cone of 0.5 mrad as a function of the electron waist for different electron energy spreads.	62
4.2.14	Line spectra for a divergent electron beam without energy spread in an zero chirp Gaussian laser beam.	63
4.2.15	Normalized energy spectra within a 0.5 mrad cone for different electron bunch waists for non-zero emittance.	64
4.2.16	Total and cone yield as functions of the electron divergence	65
4.2.17	FWHM Thomson bandwidth as a function of the electron divergence.	66
4.2.18	Yield and bandwidth as functions of the spatial longitudinal electron focus delay.	67
4.2.19	Cone spectra, yield and bandwidth in dependence of a temporal electron focus delay.	68
4.2.20	Cone spectra, yield and bandwidth in dependence of a transversal electron focus offset.	69
4.2.21	Cone spectra, yield, and bandwidth in dependence of the collision angle for a chirped and a zero chirp laser.	71
4.3.1	Cone yield as function of the laser-electron waist relation and of the electron divergence for different parameter sets.	74
4.3.2	Cone yield as a function of the waist relation and electron divergence for different electron emittances.	75
4.3.3	Laser strength parameter for different waist and duration configurations of a laser with pulse energy $E_p = 0.5$ J.	76
4.3.4	Cone yield as a function of the waist relation and electron divergence for equal a_0 .	76
4.3.5	$a_{0,\text{eff}}^2 N_0$ as a function of the electron waist.	78
4.3.6	Cone yield as a function of the waist relation and electron divergence for different a_0 .	78
4.3.7	Relative cone yield as a function of the electron divergence and of the electron-laser-waist ratio.	79
4.3.8	Overlap effect on the total yield for a divergent electron beam.	81
4.3.9	Overlap functions $F(x)$ and ξ as functions of the waist relation.	82

4.3.10	Emittance influence on the optimum electron-laser waist relation and on the optimum electron divergence.	83
4.3.11	Cone bandwidth as functions of the electron waist and of the electron divergence for the different parameter sets.	84
4.3.12	Quality as a function of the electron divergence.	85
4.4.1	Maximum yield and according optimum electron waist for different laser parameter configurations.	86
4.4.2	Theoretical bandwidth and quality for different laser parameter configurations.	87
4.4.3	Yield, bandwidth, and quality for the laser parameter scans.	88
4.5.1	Line spectra including second harmonic contribution.	91
4.5.2	Percentage of photons within the second harmonic and quality criterion including the second harmonic contribution.	92
4.6.1	Space-charge effect on cone yield and bandwidth for different bunch charges.	93
5.1.1	Schematic display of a discharge capillary and chromatic dependence of the focal length.	98
5.1.2	Radial dependence of the magnetic field within a capillary.	99
5.2.1	Active plasma lens focusing setup.	100
5.2.2	Influence of the plasma lens parameters on focal length and waist.	104
5.2.3	Energy dependence of the plasma-lens focusing.	105
5.2.4	Electron bunch size as function of the distance from the plasma target, focal length and waist for different electron energy spreads.	106
5.2.5	Chromatic emittance growth within the capillary for different electron bunch energy spreads.	107
5.3.1	Cone yield and bandwidth as a function of the electron bunch energy spread, and of the distance from the plasma target exit.	108
5.4.1	Electron trajectories and bunch waist evolution through the setup for different energy spreads.	111
5.4.2	Focal chromatic effect for a 10 % rms energy spread bunch.	112
5.4.3	Electron spectra and response function for an energy-independent focus of a non-zero energy spread bunch.	113
5.4.4	Response functions of interaction at the total and target electron focus.	114
5.4.5	Initial and effective electron spectra, and the resulting Thomson spectra.	115
5.4.6	Cone photon yield (blue) and bandwidth (green) as functions of the APL-focused electron bunch's initial energy spread.	116
5.4.7	Electron transversal offset effect on the propagation through the setup and the electron focus position with respect to the laser focus.	118
5.4.8	Focus offset, pointing angle and bunch waist after APL focusing as a function of the initial electron bunch offset.	119

5.4.9 Thomson yield and bandwidth after APL focusing as a function of an initial electron bunch offset.	119
5.4.10 Pointing angle effect on the bunch propagation and waist evolution through the APL setup.	120
5.4.11 Thomson spectra, photon yield and bandwidth after APL focusing as a function of an initial electron bunch pointing angle.	121
5.4.12 Electron trajectories and bunch waist through a setup with a rotated plasma lens.	122
5.4.13 Thomson spectrum with rotated plasma lens.	123
6.2.1 Optimisation for 90 keV target source energy.	127
A.3.1 Line spectra for a divergent electron beam without energy spread in a chirped laser for different collision angles.	140
A.3.2 Line spectra for a non-divergent zero energy spread electron bunch in a linearly chirped Gaussian laser of $\Delta\lambda = 60$ nm	141
A.3.3 Thomson spectra at constant $\tau = 4$ ps for varying waist and a_0	142
A.3.4 Thomson spectra at constant $w_0 = 10.45$ μm for varying duration and a_0	143
A.3.5 Space-charge induced bunch waist increase	143

LIST OF TABLES

3.1.1 Target design parameters for the X-ray source. 26

3.2.1 Laser and Electron parameters as obtained from the proposed setup. 27

4.1.1 Angular and energetic contributions to the bandwidth. 43

4.1.2 Typical parameter ranges and according contributions to the Thomson
bandwidth. 44

4.3.1 Maximum yield and respective electron waist, waist relation, and electron
divergence for different scenarios. 74

5.3.1 Parameter sets and photon yield and bandwidth within a ± 0.5 mrad cone
for a Thomson interaction behind the plasma target. 108

BIBLIOGRAPHY

- [1] W. C. Röntgen. On a new kind of rays. *Science*, 1896.
- [2] D. J. Gibson, S. G. Anderson, C.P J Barty, S. M. Betts, R. Booth, W. J. Brown, J. K. Crane, R. R. Cross, D. N. Fittinghoff, F. V. Hartemann, J. Kuba, G. P. Le Sage, D.R. Slaughter, A. M. Tremaine, A. J. Wootton, E. P. Hartouni, P. T. Springer, and J. B. Rosenzweig. PLEIADES: A picosecond compton scattering x-ray source for advanced backlighting and time-resolved material studies. In *Physics of Plasmas*, 2004.
- [3] D. J. Gibson, F. Albert, S. G. Anderson, S. M. Betts, M. J. Messerly, H. H. Phan, V. A. Semenov, M. Y. Shverdin, A. M. Tremaine, F. V. Hartemann, C. W. Siders, D. P. McNabb, and C. P.J. Barty. Design and operation of a tunable MeV-level Compton-scattering-based γ -ray source. *Physical Review Special Topics - Accelerators and Beams*, 2010.
- [4] S. Cheong, B.L. Jones, A.K Siddiqi, F. Liu, N. Manohar, and S. H. Cho. X-ray fluorescence computed tomography (XFCT) imaging of gold nanoparticle-loaded objects using 110 kVp x-rays. *Physics in medicine and biology*, 55(3):647–62, feb 2010.
- [5] L. Ren, D. Wu, Y. Li, G. Wang, X. Wu, and H. Liu. Three-dimensional x-ray fluorescence mapping of a gold nanoparticle-loaded phantom. *Medical Physics*, 41(3):31902, 2014.
- [6] N. Manohar, F.J. Reynoso, P. Diagaradjane, S. Krishnan, and S. H. Cho. Quantitative imaging of gold nanoparticle distribution in a tumor-bearing mouse using benchtop x-ray fluorescence computed tomography. *Scientific Reports*, 6(October 2015):22079, 2016.
- [7] F. Schulz, D. Lutz, N. Rusche, N. G. Bastús, M. Stieben, M. Höltig, F. Grüner, H. Weller, M. Schachner, T. Vossmeier, and G. Loers. Gold nanoparticles functionalized with a fragment of the neural cell adhesion molecule L1 stimulate L1-mediated functions. *Nanoscale*, 5(21):10605–17, 2013.
- [8] J. F. Dorsey, L. Sun, D. Y. Joh, A. Witztum, G. D. Kao, M. Alonso-Basanta, S. Avery, S. M. Hahn, A. Al Zaki, and A. Tsourkas. Gold nanoparticles in radiation

- research: potential applications for imaging and radiosensitization. *Translational Cancer Research*, 2013.
- [9] F. Grüner. manuscript in preparation. 2017.
- [10] O. Schmutzler. private communication, 2016.
- [11] N. D. Powers, I. Ghebregziabher, G. Golovin, C. Liu, S. Chen, S. Banerjee, J. Zhang, and D. P. Umstadter. Quasi-monoenergetic and tunable X-rays from a laser-driven Compton light source. *Nature Photonics*, 8(1):28–31, 2013.
- [12] S. G. Rykovanov, C. G. R. Geddes, J. L. Vay, C. B. Schroeder, Eric Esarey, and W. P. Leemans. Quasi-monoenergetic femtosecond photon sources from Thomson Scattering using laser plasma accelerators and plasma channels. *Journal of Physics B: Atomic, Molecular and Optical Physics*, 47(23):234013, 2014.
- [13] K. Khrennikov, J. Wenz, A. Buck, J. Xu, M. Heigoldt, L. Veisz, and S. Karsch. Tunable all-optical quasimonochromatic Thomson X-ray source in the nonlinear regime. *Physical Review Letters*, 114(19):1–5, 2015.
- [14] K. Chouffani, D. Wells, F. Harmon, J. Jones, and G. Lancaster. Laser-Compton scattering from a 20 MeV electron beam. *Nuclear Instruments and Methods And Methods in Physics Research A*, 495:95–106, 2002.
- [15] A. Jochmann, A. Irman, M. Bussmann, J. P. Couperus, T. E. Cowan, A. D. Debus, M. Kuntzsch, K. W D Ledingham, U. Lehnert, R. Sauerbrey, H. P. Schlenvoigt, D. Seipt, Th Stöhlker, D. B. Thorn, S. Trotsenko, A. Wagner, and U. Schramm. High resolution energy-angle correlation measurement of hard x rays from laser-Thomson backscattering. *Physical Review Letters*, 111(11):1–5, 2013.
- [16] F. Hartemann, D. Gibson, W. Brown, a. Rouse, K. Phuoc, V. Mallka, J. Faure, and a. Pukhov. Compton scattering x-ray sources driven by laser wakefield acceleration. *Physical Review Special Topics - Accelerators and Beams*, 10(1):011301, jan 2007.
- [17] A. Debus. *Brilliant Radiation Sources By Laser-Plasma Accelerators And Optical Undulators*. PhD thesis, Technische Universität Dresden, 2012.
- [18] S. Chen, N. D. Powers, I. Ghebregziabher, C. M. Maharjan, C. Liu, G. Golovin, S. Banerjee, J. Zhang, N. Cunningham, a. Moorti, S. Clarke, S. Pozzi, and D. P. Umstadter. MeV-Energy X Rays from Inverse Compton Scattering with Laser-Wakefield Accelerated Electrons. *Physical Review Letters*, 110(15):155003, apr 2013.
- [19] M. Jacquet and P. Suortti. Radiation therapy at compact Compton sources. *Physica Medica*, 31(6):596–600, 2015.

- [20] R. Kuroda, E. Yamaguchi, Y. Taira, E. Miura, M. Koike, H. Toyokawa, K. Yamada, and M. Kumaki. Development of Multi-Collision Laser Compton Scattering X-Ray Source on the Basis of Compact S-Band Electron Linac Single Collision Lcs for Imaging X-Ray Source. pages 4139–4141, 2012.
- [21] J. M. Cole, J. C. Wood, N. C. Lopes, K. Poder, R. L. Abel, S. Alatabi, J. S. J. Bryant, A. Jin, S. Kneip, K. Mecseki, D. R. Symes, S. P. D. Mangles, and Z. Najmudin. Laser-wakefield accelerators as hard x-ray sources for 3D medical imaging of human bone. *Scientific reports*, 5:13244, 2015.
- [22] S. K. Ride, E. Esarey, and M. Baine. Thomson scattering of intense lasers from electron beams at arbitrary interaction angles. *Physical Review E*, 52(5):5425–5442, 1995.
- [23] E. Esarey, P. Sprangle, A. Ting, and S. K. Ride. Laser synchrotron radiation as a compact source of tunable, short pulse hard X-rays. *Nuclear Inst. and Methods in Physics Research, A*, 331(1-3):545–549, 1993.
- [24] K. Y. Ng. The Equivalence of Inverse Compton Scattering and the Undulator Concept. 2009.
- [25] C. Sun and Y. K. Wu. Theoretical and simulation studies of characteristics of a Compton light source. *Physical Review Special Topics - Accelerators and Beams*, 14(4):1–17, 2011.
- [26] I. Ghebregziabher, B. A. Shadwick, and D. Umstadter. Spectral bandwidth reduction of Thomson scattered light by pulse chirping. *Physical Review Special Topics - Accelerators and Beams*, 16(3), 2013.
- [27] S. G. Rykovanov, C. G. R. G R Geddes, C. B. Schroeder, E. Esarey, and W. P. P Leemans. Controlling the spectral shape of nonlinear Thomson scattering with proper laser chirping. *Physical Review Accelerators and Beams*, 19(3):030701, 2016.
- [28] O. Lundh, J. Lim, C. Rechatin, L. Ammoura, A. Ben-Ismaïl, X. Davoine, G. Gallot, J-P. Goddet, E. Lefebvre, V. Malka, and J. Faure. Few femtosecond, few kiloampere electron bunch produced by a laser-plasma accelerator. *Nature Physics*, 2011.
- [29] A. Buck, M. Nicolai, K. Schmid, C. M. S. Sears, A. Sävert, J. M. Mikhailova, F. Krausz, M. C. Kaluza, and L. Veisz. Real-time observation of laser-driven electron acceleration. *Nature Physics*, 2011.
- [30] F. Grüner, S. Becker, U. Schramm, T. Eichner, M. Fuchs, R. Weingartner, D. Habs, J. Meyer-Ter-Vehn, M. Geissler, M. Ferrario, L. Serafini, B. Van Der Geer, H. Backe, W. Lauth, and S. Reiche. Design considerations for table-top, laser-based VUV and X-ray free electron lasers. *Applied Physics B: Lasers and Optics*, 2007.

- [31] A. R. Maier, A. Meseck, S. Reiche, C. B. Schroeder, T. Seggebrock, and F. Grüner. Demonstration scheme for a laser-plasma-driven free-electron laser. *Physical Review X*, 2012.
- [32] W. P. Leemans, B. Nagler, a. J. Gonsalves, Cs. Tóth, K. Nakamura, C. G. R. Geddes, E. Esarey, C. B. Schroeder, and S. M. Hooker. GeV electron beams from a centimetre-scale accelerator. *Nature Physics*, 2006.
- [33] D. Strickland and G. Mourou. Compression of Amplified Chirped Optical Pulses. *Optics Communications*, 55(6):447–449, 1985.
- [34] M. Fuchs, R. Weingartner, A. Popp, Z. Major, S. Becker, J. Osterhoff, I. Cortrie, B. Zeitler, R. Hörlein, G. D. Tsakiris, U. Schramm, T. P. Rowlands-Rees, S. M. Hooker, D. Habs, F. Krausz, S. Karsch, and F. Grüner. Laser-driven soft-X-ray undulator source. *Nature Physics*, 5(11):826–829, 2009.
- [35] J. Van Tilborg, S. Steinke, C. G R Geddes, N. H. Matlis, B. H. Shaw, A. J. Gonsalves, J. V. Huijts, K. Nakamura, J. Daniels, C. B. Schroeder, C. Benedetti, E. Esarey, S. S. Bulanov, N. A. Bobrova, P. V. Sasorov, and W. P. Leemans. Active Plasma Lensing for Relativistic Laser-Plasma-Accelerated Electron Beams. *Physical Review Letters*, 115(18):1–5, 2015.
- [36] LUX. <http://lux.cfel.de>.
- [37] E. Esarey, S. K. Ride, and P. Sprangle. Nonlinear Thomson scattering of intense laser pulses from beams and plasmas. *Physical Review E*, 48(4), 1993.
- [38] E. Esarey, C. B. Schroeder, and W. P. Leemans. Physics of laser-driven plasma-based electron accelerators. *Reviews of Modern Physics*, 81(3):1229–1285, aug 2009.
- [39] S. Bulanov, N. Naumova, F. Pegoraro, and J. Sakai. Particle injection into the wave acceleration phase due to nonlinear wake wave breaking. *Physical Review E*, 58(5):1–4, 1998.
- [40] J. Faure, C. Rechatin, A. Norlin, A. Lifschitz, Y. Glinec, and V. Malka. Controlled injection and acceleration of electrons in plasma wakefields by colliding laser pulses. *nature*, 444(December):737–739, 2006.
- [41] V. Malka, J. Faure, C. Rechatin, J. K. Lim, and X. Davoine. Laser-driven accelerators by colliding pulses injection : A review of simulation and experimental results. *Physics of Plasmas*, 16(056703), 2009.
- [42] B. Zeitler, I. Dornmair, T. Gehrke, M. Titberidze, A. R. Maier, B. Hidding, Klaus Flöttmann, and Florian Grüner. Merging conventional and laser wakefield accelerators. *SPIE*, page 877904, 2013.

- [43] <http://regae.desy.de>.
- [44] K. Floettmann. Some basic features of the beam emittance. *Physical Review Special Topics - Accelerators and Beams*, 6(3):80–86, 2003.
- [45] M. B. Reid. Electron beam emittance growth in thin foils: A betatron function analysis. *Journal of Applied Physics*, 70(11):7185–7187, 1991.
- [46] E. D. Courant and H. S. Snyder. Theory of the Alternating-Gradient Synchrotron. *Annals of Physics*, 3(1):1–48, 1958.
- [47] T. Mehrling, J. Grebenyuk, F. S. Tsung, K. Floettmann, and J. Osterhoff. Transverse emittance growth in staged laser-wakefield acceleration. *Physical Review Special Topics - Accelerators and Beams*, 15(11):1–7, 2012.
- [48] I. Dornmair, K. Floettmann, and A. R. Maier. Emittance conservation by tailored focusing profiles in a plasma accelerator. *Physical Review Special Topics - Accelerators and Beams*, 18(4):1–6, 2015.
- [49] K. Floettmann. Adiabatic matching section for plasma accelerated beams. *Physical Review Special Topics - Accelerators and Beams*, 17(5):1–7, 2014.
- [50] J. A. Clarke. *The science and technology of undulators and wigglers*. Oxford University Press Inc, Oxford, 2004.
- [51] P. Schmüser, M. Dohlus, J. Rossbach, and C. Behrens. *Free-Electron Lasers in the Ultraviolet and X-ray Regime*. Springer, 2 edition, 2014.
- [52] K. Floettmann. ASTRA: A Space Charge Tracking Algorithm, <http://www.desy.de/~mpyflo/>.
- [53] H. Wiedemann. *Particle accelerator physics: Third edition*. Springer, Berlin, Heidelberg, 2007.
- [54] C. A. Brau. Oscillations in the spectrum of nonlinear Thomson-backscattered radiation. *Physical Review Special Topics - Accelerators and Beams*, 7(2):1–9, 2004.
- [55] M.J. Berger, J.H. Hubbell, S.M. Seltzer, J. Chang, J.S. Coursey, R. Sukumar, D.S. Zucker, and K. Olsen. XCOM: Photon Cross Sections Database, <http://www.nist.gov/pml/data/xcom/>, 2010.
- [56] H. Jadvar and J. A. Parker. *Clinical PET and PET/CT*. Springer, 2005.
- [57] F. Peyrin and M. Dahlbom. *Handbook of Particle Detection and Imaging*. Springer, 2012.

- [58] R. Weingartner, S. Raith, A. Popp, S. Chou, J. Wenz, K. Khrennikov, M. Heigoldt, A. R. Maier, N. Kajumba, M. Fuchs, B. Zeitler, F. Krausz, S. Karsch, and Florian Grüner. Ultralow emittance electron beams from a laser-wakefield accelerator. *Physical Review Special Topics - Accelerators and Beams*, 15(11):111302, 2012.
- [59] G. R. Plateau, C. G R Geddes, D. B. Thorn, M. Chen, C. Benedetti, E. Esarey, A. J. Gonsalves, N. H. Matlis, K. Nakamura, S. Rykovanov, C. B. Schroeder, S. Shiraishi, T. Sokollik, J. Van Tilborg, Cs Toth, S. Trotsenko, T. S. Kim, M. Battaglia, Th Stöhler, and W. P. Leemans. Low-emittance electron bunches from a laser-plasma accelerator measured using single-shot X-ray spectroscopy. *PRL*, 109, 06480(August), 2012.
- [60] A. R. Maier. private communication, 2017.
- [61] S. Steinke, J. van Tilborg, C. Benedetti, C. G. R. Geddes, C. B. Schroeder, J. Daniels, K. K. Swanson, A. J. Gonsalves, K. Nakamura, N. H. Matlis, B. H. Shaw, E. Esarey, and W. P. Leemans. Multistage coupling of independent laser-plasma accelerators. *Nature*, 530(7589):190–3, 2016.
- [62] R. Pausch, A. Debus, R. Widera, K. Steiniger, A. Huebl, H. Burau, M. Bussmann, and U. Schramm. How to test and verify radiation diagnostics simulations within particle-in-cell frameworks. *Nuclear Instruments and Methods in Physics Research, Section A: Accelerators, Spectrometers, Detectors and Associated Equipment*, 740:250–256, 2014.
- [63] S. B. van der Geer and M. J. de Loos. General Particle Tracer, <http://www.pulsar.nl/gpt>, 2017.
- [64] J. D. Jackson. *Classical Electrodynamics*. Wiley, 1998.
- [65] F. Grüner, C. B. Schroeder, A. R. Maier, S. Becker, and J. M. Mikhailova. Space-charge effects in ultrahigh current electron bunches generated by laser-plasma accelerators. *Physical Review Special Topics - Accelerators and Beams*, 12(2):1–11, 2009.
- [66] N. A. Bobrova, P. V. Sasorov, C. Benedetti, S. S. Bulanov, C. G R Geddes, C. B. Schroeder, E. Esarey, and W. P. Leemans. Laser-heater assisted plasma channel formation in capillary discharge waveguides. *Physics of Plasmas*, 20(2), 2013.
- [67] B. Schmidt. Accelerator Physics Lecture Notes (WiSe 2013/14). Technical report, 2014.
- [68] S. Y. Lee. *Accelerator Physics*. Singapore: World Scientific Publishing Co. Pte. Ltd, Singapore, 2 edition, 2004.

- [69] F. Grüner. "Physik und Anwendung von Laser-Plasma-Beschleunigern: Von medizinischer Bildgebung bis Hochenergiephysik", (WiSe12/13), 2012.

ACKNOWLEDGEMENTS

At last, I would like to express my gratitude to the many people whose support was of vital importance in the years of my PhD work.

I would like to thank **Prof. Florian Grüner**, first of all, for the opportunity to work in his group and on this topic, but most of all for his great support in the last months of my PhD. I am grateful for his constant availability and the constructive input.

Furthermore, I thank **Prof. Wolfgang Hillert** for his interest and spontaneous acceptance of being the second referee of my thesis.

I am indebted to the **simulation crew** of Michael Bussmann at the HZDR in Dresden, especially **Dr. Alexander Debus** who introduced me to Clara. His patience concerning my many questions, but more so his enthusiasm for the simulation of classical radiation were a great physical and moral support, and made my frequent trips to Dresden really worthwhile! Moreover, I would like to thank **Richard Pausch** for his support concerning Clara2. Many thanks to the **Computational Radiation Physics group** who made me feel like part of their group. Also, I thank the people of the **HZDR cluster support** without whom the many simulations for this thesis would not have been possible.

In Hamburg, my immediate group was the **medical team**, and I would like to thank its former and present PhD students, **Martin Stieben**, **Florian Blumendorf**, and **Oliver Schmutzler** for many interesting conversations.

I also would like to thank **Andreas Maier** for his always honest and direct way, for always making time for me, when there was none, and for welcoming me to the circle of the **members and friends of the LUX group**. Among the many members, special thanks go to **Irene Dornmair**, **Benno Zeitler**, and **Niels Delbos** whose doors were always open, for many helpful and fruitful, and really enjoyable non-work-related discussions. I want to thank the whole group for the great atmosphere, the coffee breaks and lots of cake over the past years. Furthermore, I would like to thank **Klaus Flöttmann** for his help with the ASTRA laser tool and his interest in problems of all kinds. Many thanks go to **Heike Kaminski** and **Fenna Reinholdt**, the team assistants, who always offer a smile and help for anything. I cannot imagine what this group would do without them!

I am thankful to **Milan Zvolisky**, **Florian Blumendorf**, **Oliver Schmutzler**, **Benno Zeitler**, **Niels Delbos**, and **Sören Jalas** for proof-reading my thesis.

I would like to express my gratitude to **Irmgard Flick** for her effort and involvement in supporting me in the final part of this thesis.

Furthermore, I am obliged to the **Gleichstellungsfonds der Universität Hamburg** for the scholarship supporting the completion of my thesis.

Finally, I am deeply grateful to my **parents** for their love, their infinite belief in me, and constant support. Thank You, **Milan**, for always supporting me, for motivating me, for understanding me. Thank You, **Nela**, for allowing me to write this thesis, and for always being able to lighten my mood, take my mind off work, and make me recognise the important things in life. I am thankful for my invaluable **family and friends**. I am very lucky to have such great people in my life. You are truly the source of my strength!

Eidesstattliche Versicherung / Declaration of oath

Hiermit versichere ich an Eides statt, die vorliegende Dissertationsschrift selbst verfasst und keine anderen als die angegebenen Hilfsmittel und Quellen benutzt zu haben.

Die eingereichte schriftliche Fassung entspricht der auf dem elektronischen Speichermedium.

Die Dissertation wurde in der vorgelegten oder einer ähnlichen Form nicht schon einmal in einem früheren Promotionsverfahren angenommen oder als ungenügend beurteilt.

Hamburg, den